FOSSIL ENERGY

#340
4/30/80

DR. 1304

FE-15529-2

MHD ELECTRODE DEVELOPMENT

Quarterly Report for January—March 31, 1979

By

John W. Sadler
Jeff Bein
David L. Black
Laurence H. Cadoff
James A Dilmore
Alfred G. Eggers
Edsel W. Frantti
Edgar L. Kochka
Jack A. Kuszyk
S. K. Lau
Joseph Lempert
Barry R. Rossing
Stephen J. Schneider
James R. Schornhorst

May 1979

Work Performed Under Contract No. AC01-79ET-15529

Westinghouse Electric Corporation
Advanced Energy Systems Division
Pittsburgh, Pennsylvania

U. S. DEPARTMENT OF ENERGY

DISCLAIMER

Available from the National Technical Information Service, U. S. Department of Commerce, Springfield, Virginia 22161.

Price: Paper Copy $12.00
Microfiche $3.50

FE-15529-2
Distribution Categories UC-90g and UC-93

MHD ELECTRODE DEVELOPMENT

Quarterly Report for the Period

JANUARY-MARCH 31, 1979

John W. Sadler
Jeff Bein
David L. Black
Laurence H. Cadoff*
James A. Dilmore*
Alfred G. Eggers
Edsel W. Frantti
Edgar L. Kochka
Jack A. Kuszyk
S. K. Lau
Joseph Lempert**
Barry R. Rossing*
Stephen J. Schneider*
James R. Schornhorst

*Westinghouse Research & Development Center
**Consultant

WESTINGHOUSE ELECTRIC CORPORATION
Advanced Energy Systems Division
P. O. Box 10864
Pittsburgh, Pa. 15236

MAY, 1979

PREPARED FOR THE
UNITED STATES DEPARTMENT OF ENERGY

Under Contract No. DE-AC-01-79-ET-15529

APPROVED:

J. W. Sadler, Project Manager
Advanced Energy Systems Division

TABLE OF CONTENTS

TABLE OF CONTENTS (Continued)

LIST OF FIGURES

LIST OF FIGURES (Continued)

LIST OF FIGURES (Continued)

LIST OF FIGURES (Continued)

LIST OF FIGURES (Continued)

LIST OF FIGURES (Continued)

LIST OF FIGURES (Continued)

LIST OF TABLES

I. ABSTRACT

Technical progress under DOE Contract DE-AC-01-79-ET-15529 during the January to March 1979 quarter is reported.

Zirconia based electrode compositions have been selected for inclusion in the up-coming non-slagging super-hot WESTF Test 42. Fabrication and processing details for these materials are presented. The hafnia based materials to be included in this test have not yet been identified by Battelle Northwest Laboratory. Results of slag compatibility tests for a number of candidate ceramic insulating materials are presented. These test results have been used to rank these materials as candidates for use under the slagging hot or non-slagging super-hot operating modes.

Laboratory screening tests, including electrochemical and anode arc erosion tests, have continued. A comprehensive analytical model has been derived which permits detailed analysis of the role of slag properties as well as electrode-slag polarization on the nature of electrochemical reactions under hot slagging conditions. Anode arc erosion tests have been extended to provide preliminary data on the effect of potassium carbonate/slag versus potassium sulfate/slag mixtures on the arc erosion of copper and platinum clad copper anode samples. The results indicate increased arc damage for the sulfate/slag mixture.

Test planning and detail experiment design activities have continued in support of the upcoming WESTF tests. Parametric analyses were completed to define electrode and insulator material coupons for WESTF Test 42/44, non-slagging super-hot operating mode; design activities in support of WESTF Test 43, Pt-Fe, were similarly completed.

Following completion of the final two runs of WESTF Test 40, bare copper electrodes, WESTF Test 41, AVCO reference electrodes, was initiated. This run

was terminated after approximately 14 hours at conditions due to a test section leak. The electrodes are being incorporated in a rebuilt test section which will reflect a number of insulating wall design improvements. Certain WESTF area layout modifications, which are a part of the overall modifications necessary to provide for installation of the magnet in WESTF, have been initiated. Modification of the existing WMTF conventional 3 tesla magnet for use in WESTF is planned.

II. OBJECTIVE AND SCOPE OF WORK

In continuation of the program to develop MHD power generation to commercial feasibility, Westinghouse is conducting a program to develop improved electrode designs for open-cycle, coal-fired, MHD generator applications. The program includes the link between basic and supportive materials development and testing in an engineering test rig that offers an adverse MHD environment for extended periods of time.

Specific development activities of this program are as follows:

(a) Laboratory screening tests to provide preliminary electrochemical stability data on selected advanced or modified ceramic candidate electrode and insulation materials.

(b) Laboratory screening tests to evaluate the resistance of selected candidate anode materials to simulated arc impingements under a representative range of chemical and thermal conditions.

(c) Engineering rig tests of preferred electrode designs, selected on the basis of the screening test results and/or pertinent outside data, under simulated open-cycle coal-fired MHD operating conditions.

(d) Preparation and fabrication of experimental electrode materials, as warranted by favorable laboratory screening test results, to provide samples for engineering rig tests.

In addition to these four main development activities, this project includes providing such laboratory, design, test and analytical support as necessary to characterize test materials, and to determine such essential physical and chemical properties as are required to properly design the test specimens and to interpret and analyze test data. Dependent on development results, preferred electrode materials will be prepared for advanced testing in other DOE contractor facilities.

These objectives are being pursued in accordance with a statement of work which is consistent with the National Plan for MHD Development formulated by DOE.

The major elements of the program are presented in a Work Breakdown Structure which is presented in Table 1. The Level I effort is the MHD Electrode Development Contract, and Level II consists of the following four tasks.

WBS 1.1 ELECTRODE AND INSULATOR MATERIALS
WBS 1.2 ENGINEERING TESTS
WBS 1.3 WESTF MODIFICATION
WBS 1.4 PROJECT MANAGEMENT AND DOCUMENTATION

WBS 1.1 - ELECTRODE AND INSULATOR MATERIALS

The objective of this task is to provide for the development, laboratory evaluation and fabrication of electrode and insulator materials. All necessary experimental material preparation, as well as fabrication of test samples for laboratory screening tests, engineering rig tests in the Westinghouse Electrode System Test Facility, WESTF (WBS 1.2), or other tests will be completed under this task. This task also includes supporting pre-test material characterization and laboratory screening tests used to evaluate the relative performance of candidate materials. These screening tests include electrochemical and anode arc impingement tests.

WBS 1.2 - ENGINEERING TESTS

The objective of this task is to provide for the engineering tests of promising electrode/insulator materials resulting from the WBS 1.1 activity. In particular, this task provides for the supporting design, test and post-test analysis effort as well as maintenance, operation and modification of the engineering test rig, WESTF. Table 2 summarizes WESTF test capabilities.

This task incorporates the elements of planning, experiment design, test operations and post-test analysis and provides the close engineering design and test discipline necessary to effect successful electrode/insulating wall system development. In addition, final fabrication and assembly operations necessary to incorporate electrode and interelectrode insulating elements fabricated under WBS 1.1 into a complete assembly ready for testing in WESTF

TABLE 1

WORK BREAKDOWN STRUCTURE

(SUBELEMENTS TO DOE WBS 2.2.2)

- WBS 1.0 MHD ELECTRODE DEVELOPMENT
  - WBS 1.1 ELECTRODE AND INSULATOR MATERIALS
    - WBS 1.1.1 EXPERIMENTAL MATERIALS FABRICATION
      - MATERIAL DEVELOPMENT
      - MATERIAL CHARACTERIZATION
      - MATERIAL FABRICATION
    - WBS 1.1.2 LABORATORY SCREENING TESTS
      - ELECTROCHEMICAL TESTS
      - ANODE ARC TESTS
  - WBS 1.2 ENGINEERING TESTS
    - WBS 1.2.1 TEST ENGINEERING
      - DEVELOPMENT REQUIREMENTS
      - EXPERIMENT DESIGN
      - POST-TEST ANALYSIS
    - WBS 1.2.2 TEST ASSEMBLY FABRICATION
    - WBS 1.2.3 WESTF OPERATIONS
      - PRE-TEST ACTIVITY
      - TEST OPERATIONS
  - WBS 1.3 WESTF MODIFICATION
  - WBS 1.4 PROJECT MANAGEMENT AND DOCUMENTATION

I II III - SYSTEMS LEVEL

TABLE 2

WESTF TEST CAPABILITIES

Mass Flow	To 0.5 lb/sec
Combustion Temperature	To 2850^{o}K
Combustor Pressure	1 to 5 atm
Channel Velocity	Subsonic, 500 to 800 m/sec
Seeding	K_2CO_3 or K_2SO_4 wet with ash or char additions (Rosebud)
B Field	3 tesla, nominal - 3.3 tesla, objective
Fuel	Toluene/#2 Fuel Oil
Oxidant	Preheated air with oxygen enrichment
Data Collection	240 channels coupled with minicomputer
Test Duration	Up to 100 hours
Test Frequency	Up to 2 per month
Channel Configuration	12.5 cm^2 flow cross section
Startup Ramp, Minimum	$\approx$25^{o}K/min

will be provided under this task. Required test documentation and facility operating procedures will also be prepared.

WBS 1.3 - WESTF MODIFICATION

This task has been established to provide for the planned modification of WESTF. The primary element of this task is the addition of a conventional 3.0 tesla magnet.

WBS 1.4 - PROJECT MANAGEMENT AND DOCUMENTATION

This centralized management task provides the focal point for directing the activities which comprise the full project effort. The Project Manager is responsible for the proper definition, integration and implementation of the technical, schedule, contractual, and financial aspects of the program. Coordination of the preparation of required documentation will also be completed under this task.

III. SUMMARY OF PROGRESS TO DATE

Figure 1 summarizes the overall program schedule and status based on the Project Management Summary Baseline Report currently being revised for submittal.

During the January to March 1979 quarter, the principal areas of activity were as follows:

- Continuation of electrode and insulator material development.
- Derivation of a comprehensive analytical model which permits analysis of the role of slag properties as well as electrode polarization under hot slagging conditions.
- Continuation of anode arcing laboratory tests.
- Completion of WESTF Test 40 (runs 3 and 4) and initiation of WESTF Test 41.
- Continuation of engineering activities in support of the WESTF test series.
- Initiation of activities to support the installation of the modified 3 tesla magnet in WESTF.

Table 3 summarizes the WESTF tests completed and currently planned.

1.0 WBS 1.1 - ELECTRODE AND INSULATOR MATERIALS

In support of WESTF Tests 42 and 44 (non-slagging super-hot electrodes) definition of the processing for the zirconia based electrodes as well as material characterization has been completed. The relative ranking of insulator materials based on slag corrosion resistance has been completed and seven materials have been identified for inclusion in WESTF 42/44. A method for fabricating synthetic Kalsilite (K_2O-Al_2O_3-$2SiO_2$) is defined; further laboratory testing of this material will be required to determine its suitability for use under slagging conditions. Details relative to the above are presented in Section IV - 1.1.

U.S. DEPARTMENT OF ENERGY

DOE Form CR-535
(1-78)

MILESTONE SCHEDULE AND STATUS REPORT

1 Contract Identification: MHD ELECTRODE DEVELOPMENT PROGRAM		2 Reporting Period through 3/30/79	3 Contract Number: DE-AC-01-79-ET-15529
4 Contractor (name, address): WESTINGHOUSE ELECTRIC CORPORATION ADVANCED ENERFY SYSTEMS DIVISION P. O. Box 10864 Pittsburgh, Pa. 15236			5 Contract Start Date: April 23, 1979 6 Contract Completion Date: September 30, 1980

7 Identification Number WBS	8 Reporting Category (e.g. contract line item or work breakdown structure element)	9 Fiscal Years and Months: 79 (O N D J F M A M J J A S) 80 (10 20 30 40)	10 Percent Complete (a) Planned	(b) Actual
1.1	ELECTRODE AND INSULATOR MATERIALS			
1.1.1	EXPERIMENTAL MATERIALS FABRICATION			
1.1.2	LABORATORY SCREENING TESTS			
1.2	ENGINEERING TESTS			
1.2.1	TEST ENGINEERING			
1.2.2	TEST ASSEMBLY FABRICATION			
1.2.3	WESTF OPERATIONS			
1.3	WEST. MODIFICATION			
1.4	PROJECT MANAGEMENT AND DOCUMENTATION			

11 Remarks

12 Signature of Contractor's Project Manager and Date	13 Signature of Government Technical Representative and Date
John W. Sadler	

Figure 1. Program Schedule and Status

TABLE 3

WESTF TEST SUMMARY

OPERATING MODE	SLAG COLD	SLAG COLD	SLAGGING	NON-SLAG-SH	SLAG HOT	NON-SLAG-SH	SLAG HOT	NON-SLAG-SH	SLAG HOT
Facility	WESTF	WESTF	WESTF	WESTF	WESTF	WESTF	WESTF	WESTF	WESTF
Test ID	W-40	W-41	D-9	W-42	W-43	W-44	TBD	TBD	TBD
Approx. Date	11/78-1/79	3/79-6/79	6/79	6/79	8/79	9/79	TBD	TBD	TBD
Electrode Material	Cu	Cu-Pt (+) Cu-W/Cu (-)	NA	ZrO_2 Based(1) HfO_2 Based Perovskite	Pt (+) Fe (-)	ZrO_2 Based(1) HfO_2 Based Perovskite	SiC	ZrO_2 Based HfO_2 Based Perovskite	$MgCr_2O_4$
Insulator Material	$MgAl_2O_4$	BN	NA	NA	$MgAl_2O_4$ Al_2O_3	NA	Si_3N_4	NA	$MgAL_2O_4$ Al_2O_3
T_E, ^oC	150/275	150	NA	1700-1900	1000-1300	1700-1900	1000-1300	1700-1900	1000-1400
J, amp/cm^2	To 1.25	0.9	NA	NA	To 1.25	NA	To 1.25	To 1.25	To 1.25
$\dot{Q}$, w/cm^2	~125	~125	NA	<60	~80	<60	~80	<60	~80
Axial Field, Kv/m	Yes	Yes	NA	NA	Yes	NA	Yes	TBD	Yes
Coal Type	Eastern	Eastern	Rosebud	Rosebud	Rosebud	Rosebud	Rosebud	Rosebud	Rosebud
Duration-Hrs.(2)	15	20+	NA	8/Increm.	~20	8/Increm.	~20	8/Increm.	~20
Status	Complete	In Process							

(1) Coupons

(2) Seen On to Seed Off

A comprehensive analytical model has been derived which permits detailed analysis of the role of slag properties as well as electrode-slag polarization on the nature of electrochemical reactions under hot slagging conditions. Section IV - 1.2.1 presents the model and discusses criteria for the selection of slagging MHD electrode materials. Section IV - 1.2.2 presents the results of the continuing laboratory anode arc erosion studies. In particular the relative effect of potassium carbonate versus potassium sulfate seed on copper and platinum clad copper electrode materials is discussed.

2.0 WBS 1.2 - ENGINEERING TESTS

Test Specification addenda and revisions have been issued for WESTF Test 40 (bare copper electrodes) and WESTF Test 41 (AVCO reference electrodes). Summaries of the above are presented in Section IV - 2.1.1. The revision to the WESTF Test 41 specification reflects those changes made to correct for the test section leak which resulted in premature shutdown of the test and to implement a number of improvements in the electrical isolation characteristics of the insulating walls.

Appropriate supporting design and post-test analysis activities for WESTF tests 40 through 43 are presented in Sections IV - 2.1.2 and 2.1.3. Fabrication activities relating to the rebuilding of the WESTF Test 41 test section for Run 2 are presented in Section IV - 2.2.

Following the successful completion of the final two runs WESTF Test 40 (slagging cold electrodes - bare copper) the WESTF Test 41 test section (AVCO reference electrodes) was installed and operated in WESTF. Summaries of the test operations are presented in Section IV - 1.2.3. WESTF Test 41 operations were terminated prematurely after approximately 15 hours at conditons due to a test section leak. As discussed elsewhere, design modifications have been defined and rebuilding of the test section (incorporating the electrodes used in Run 1) is in progress. WESTF Test 41-Run 2 will be initiated as soon as practicable.

As of the end of this quarter, the total operating time of WESTF, defined as the cumulative time interval from combustor on to combustor off, is 286.8 hours.

This total time covers WESTF Test 35 through WESTF Test 41 - Run 1. Of this total time 187.4 hours were accumulated under clean firing conditions while 99.4 hours were accumulated under slagging conditions.

3.0 WBS 1.3 - WESTF MODIFICATION

As presented in Section IV - 3.0, planning activities were continued in support of the addition of a 3.0 tesla conventional magnet to WESTF. Westinghouse recommended, and DOE concurred, that the Waltz Mill magnet be modified for this use. Selected facility modifications have been initiated.

4.0 WBS 1.4 - PROJECT MANAGEMENT AND DOCUMENTATION

Significant project documentation issued included the following:

- Quarterly Report - October-December 1978.

The Project Management Summary Baseline Report is being revised consistent with programmatic changes being identified during contract negotiations.

IV. DETAILED DESCRIPTION OF TECHNICAL PROGRESS

1.0 WBS 1.1 ELECTRODE AND INSULATOR MATERIALS

1.1 WBS 1.1.1 - Experimental Materials Fabrication

1.1.1 Material Development

Zirconia - Based Electrodes

WESTF-42 and 44 will consist of 'coupons' of electrode materials suitable for use under non-slagging super-hot conditions in the absence of electrical or magnetic fields. ZrO_2 and HfO_2-based electrode compositions have been identified as promising candidate materials. The ZrO_2-based electrodes are to be processed and fabricated by Westinghouse while the HfO_2-based electrodes will be supplied by Battelle Northwest Laboratories (BNW). WESTF-42 will tentatively consist of one wall of ZrO_2-based electrodes and the other wall of the HfO_2-based materials supplied by BNW. Two ZrO_2 compositions have been identified for the test and will be positioned in the channel wall to achieve three different surface temperatures. Specifically, the compositions are:

(1) 85 m/o ZrO_2 - 15 m/o $(Mg_{.625}Ca_{.375})O$
(2) 88 m/o ZrO_2 - 12 m/o Y_2O_3
(3) 88 m/o ZrO_2 - 12 m/o Y_2O_3 (Phase I U-02 Electrode)

The virgin Yttria-stabliized electrodes from the U-02 Phase I program will be run as a comparison with the newly processed electrodes. The fabrication details for all of the ZrO_2-based electrodes are presented in the following discussion.

The processing and characterization scheme for fabricating the ZrO_2-based electrodes is shown in Figure 2. All of the starting powders were of very pure quality and very fine grain size. They were all obtained commercially from the following sources: ZrO_2 from UGE Kuhlmann, Paris, France; CeO_2,

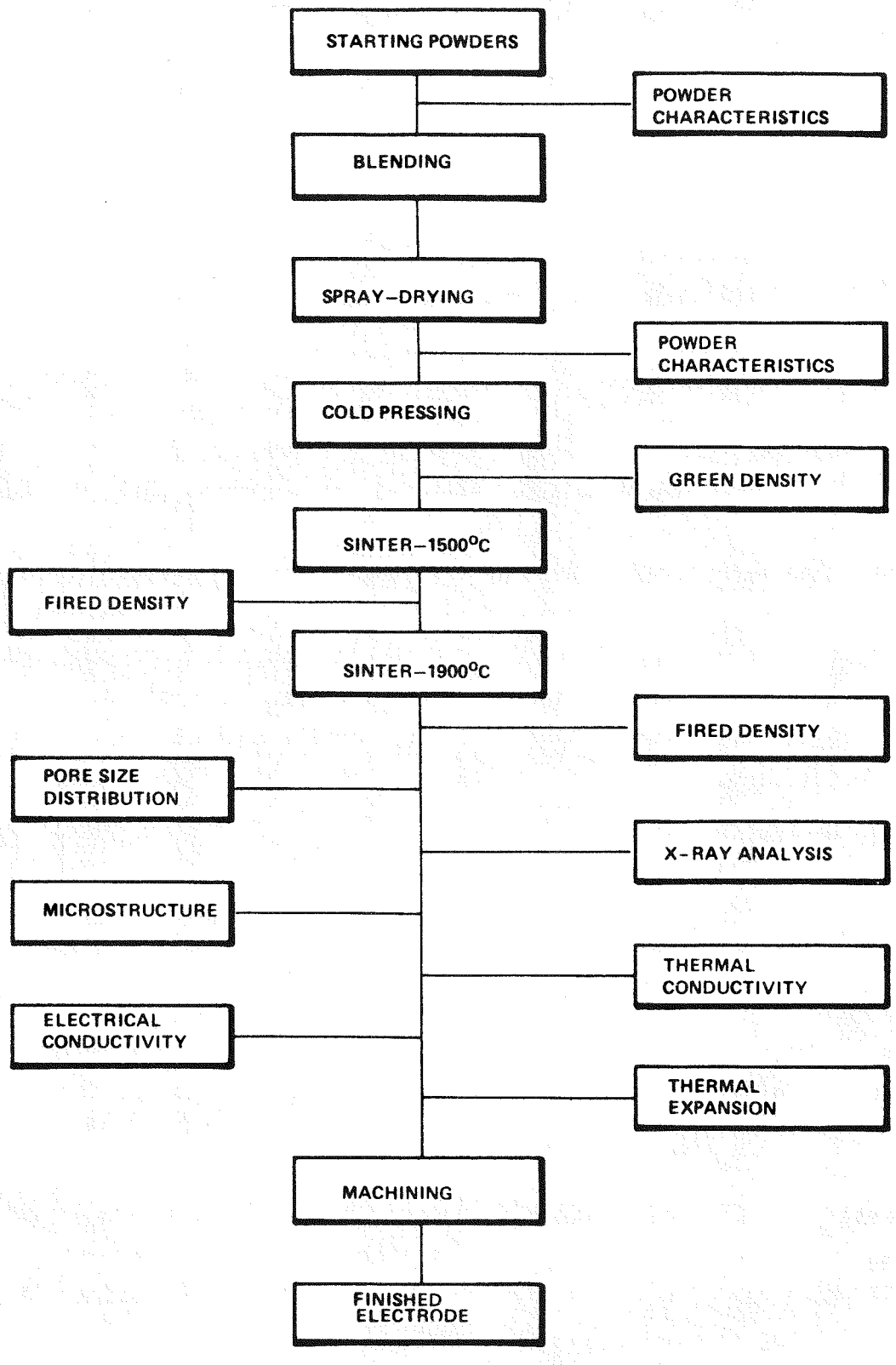

Figure 2. Flow Chart of ZrO_2-Based Electrode Fabrication and Characterization

Y_2O_3 and Nd_2O_3 from Research Chemicals, Phoenix, Arizona; MgO from Fisher Scientific, Fair Lawn, New Jersey; and $CaCO_3$ from ALFA Div., Danvers, Massachusetts. Each supplier claimed a purity of greater than 99.9%. Emission spectroscopic analysis of powders from these sources in previous investigations have also shown limits of 100 ppm of either Fe_2O_3 or SiO_2. Average particle sizes of the starting powders were determined from scanning electron micrographs. Values for ZrO_2, $CaCO_3$, Y_2O_3, CeO_2, MgO, and Nd_2O_3 were 1.5, 4.0, 4.5, 6.0, 10.0, and 15 micrometers, respectively.

The individual powders were blended together to a specific molar composition in a large V-blender until a good mechanical mixture was obtained. Each of these batches of 2300 grams was then combined with a mixture of distilled water, polyvinyl alcohol, and carbowax to form a slurry. Homogeneity was achieved by milling these constituents together for four hours in a rubber lined ball mill using yttria-stabilized zirconia balls. The slurry was then introduced into a centrifugal disk type spray dryer to produce free flowing spherical powder. SEM photomicrographs of four ZrO_2-based compositions after spray-drying are shown in Figures 3 through 6. All show an agglomeration of the different oxide constituents into spherical particles. A bimodal distribution of these spheres is observed in some cases, presumably due to the large particle size difference between some of the starting powders. Analysis of the surface areas of these ZrO_2-based powders was also performed using a Micromeritics Surface Area Analyzer. The values are shown below:

Composition	Surface Area (m^2/gm)
82 m/o ZrO_2 - 18 m/o CeO_2	8.78
88 m/o ZrO_2 - 12 m/o Y_2O_3	11.2
85 m/o ZrO_2 - 15 m/o $(Mg_{.625}Ca_{.375})O$	6.82
88 m/o ZrO_2 - 4 m/o Y_2O_3 - 8 m/o Nd_2O_3	7.70

All of the ZrO_2 powders were cold pressed at 30,000 psi into 50 gm bars approximately 9 cm x 1.2 cm x 1.2 cm. They were subsequently sintered for 10 hours at 1500°C and then at 1900°C for 2.5 hours. 12 m/o Y_2O_3 - 88 m/o ZrO_2 electrodes used in the U-02 Phase I program were also fired at 1900°C to

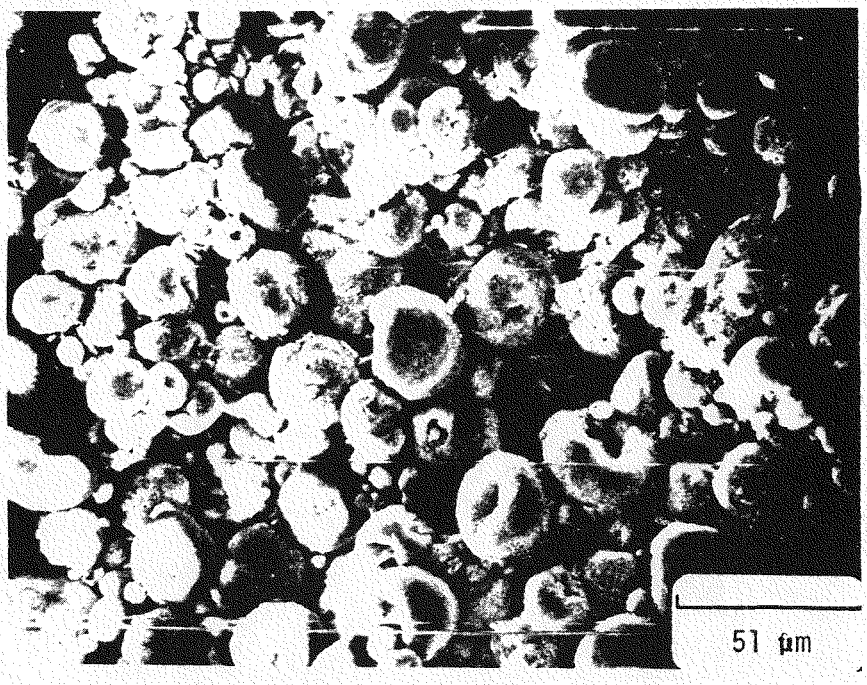

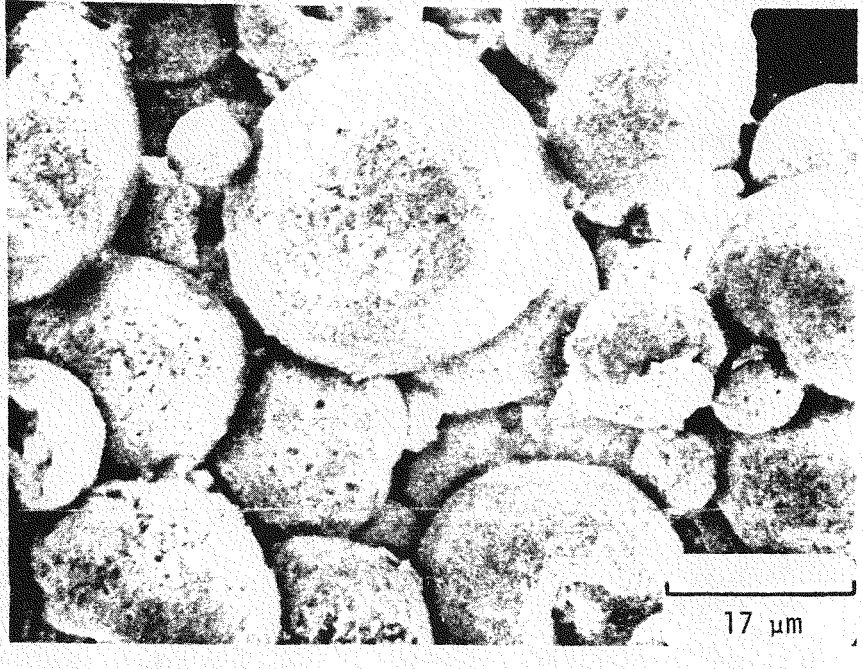

Figure 3. SEM Microphotographs of 88 m/o ZrO_2 - 4 m/o Y_2O_3 - 8 m/o Nd_2O_3 Powder after Spray-Drying

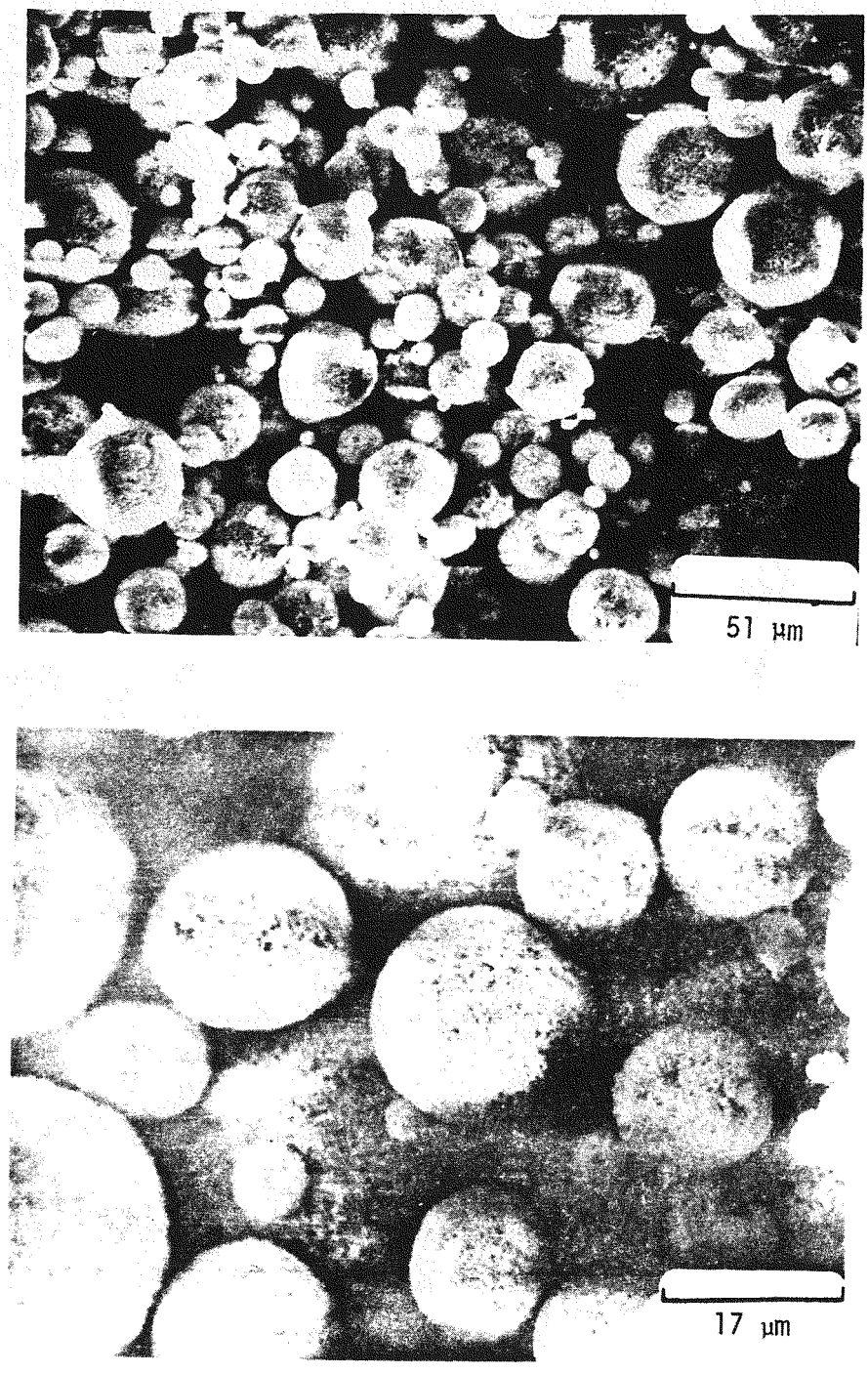

Figure 4. SEM Microphotographs of 85 m/o ZrO_2 - 15 m/o $(Mg_{.625}Ca_{.375})$ Powder after Spray-Drying

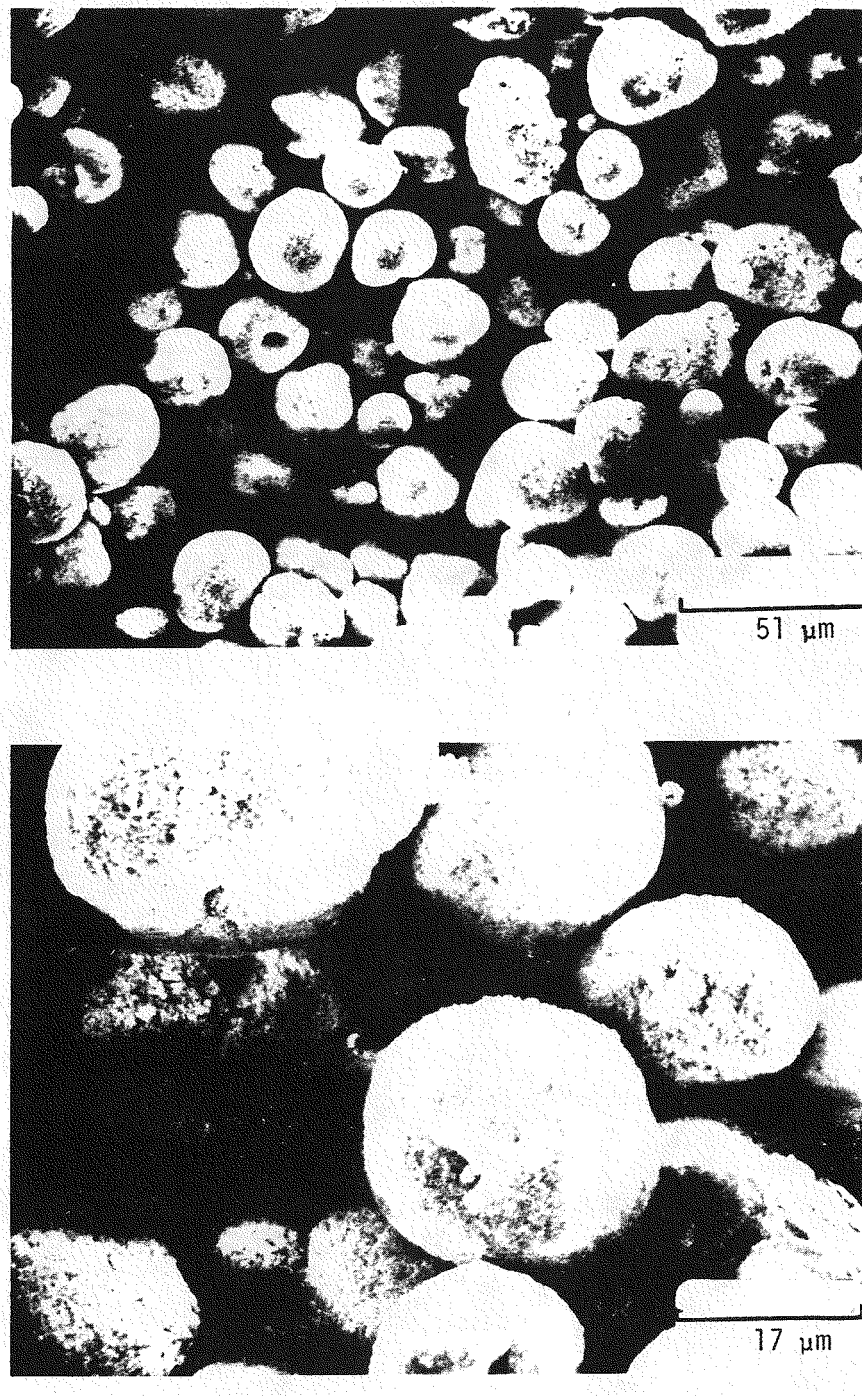

Figure 5. SEM Microphotographs of 88 m/o ZrO_2 - 12 m/o Y_2O_3 Powder after Spray-Drying

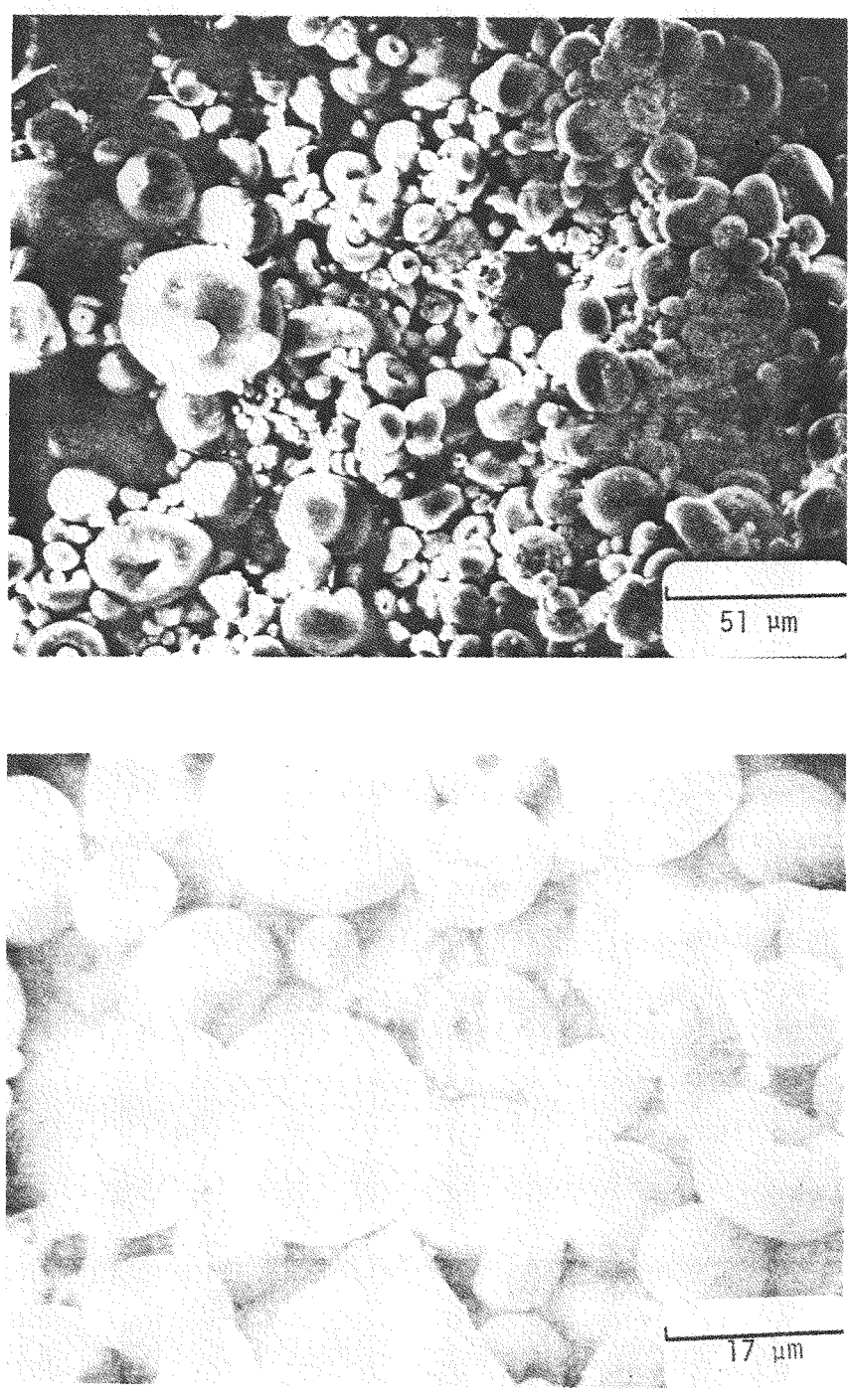

Figure 6. SEM Microphotographs of 82 m/o ZrO_2 - 18 m/o CeO_2 Powder after Spray-Drying

further increase their density. Linear shrinkage was measured at 8-10% for all of the compositions. Finally, the bars will be machined to the proper design dimensions using diamond cutting tools. X-ray analysis, along with densities, porosities, pore size distribution, microstructure, thermal and electrical properties of the ZrO_2 based electrodes are described in Section 1.1.2.

General Insulating Materials

Tests were completed on the slag corrosion resistance of fourteen ceramic insulators deemed suitable for use in slagging hot or non-slagging super-hot generators. These insulators were of varying compositions, densities and processing histories. It was believed that from this slag compatibility test it would be possible to ascertain whether certain chemical or microstructural features were more favorable in combating the corrosive nature of a Western coal slag.

A simple static immersion test was used to evaluate, relative slag corrosion resistance. Cubic samples of the insulating materials, approximately 1.2 cm on a side, were cut and then a cavity approximately 1 cm in diameter was drilled in one end three quarters of the way through. The cavity was filled with ground homogeneous Montana Flyash/K_2CO_3, and then each "mini-crucible" was placed in a high temperature furnace. A temperature of 1400°C (semi-viscous slag state) was maintained for 20 hours and then slowly cooled. The crucibles were then sectioned to expose the slag/insulator interface at the bottom of the cavity. The exposed surfaces were cold mounted, ground, and polished for microstructural examination and evaluation of the insulator's compatibility with the slag.

Photographs of the fourteen sectioned insulators are shown in Figures 7 to 13 Macrophotographs of the sectioned "mini-crucibles" are shown on the left side of the pages along with higher magnification photos of the insulator/slag interface on the right-hand side. Table 4 lists the fourteen insulators along with their density, source, processing history and relative observations of their corrosion resistance. Our determination of how well an insulator fares in a corrosive slag environment is based on its ability to resist:

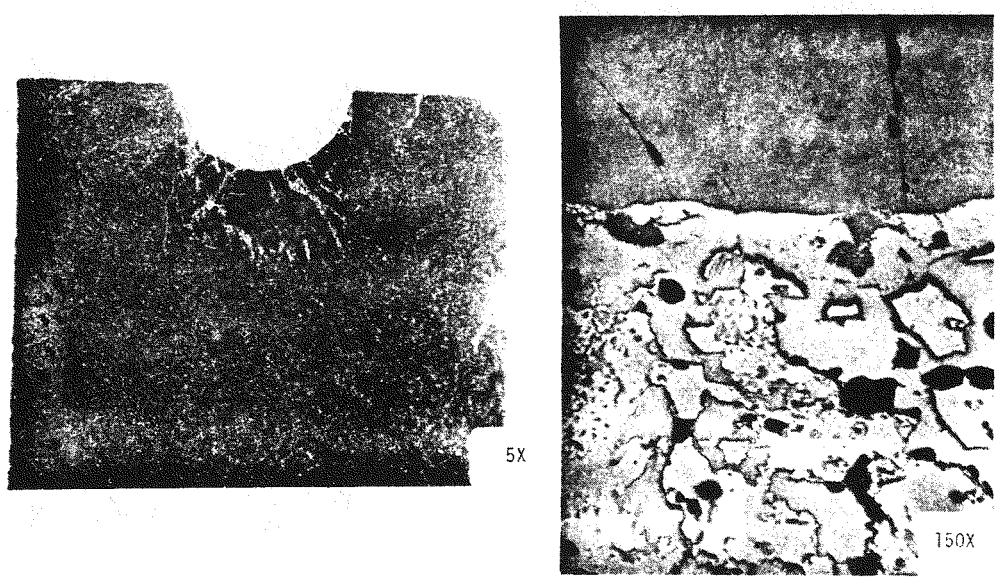

(A)

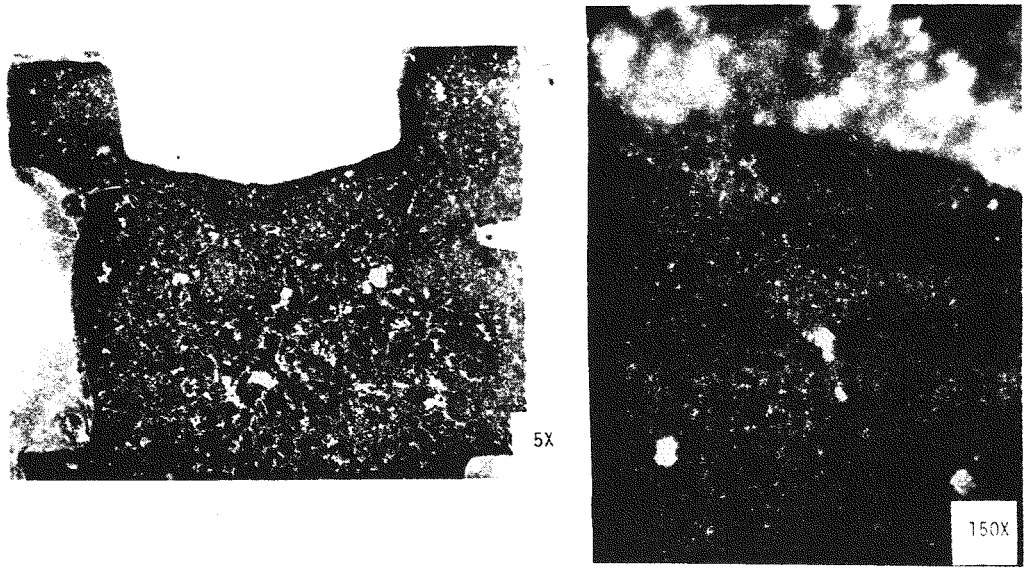

(B)

Figure 7. Appearance of (A) Al_2O_3-Cr_2O_3 (Fused Cast) from Carborundum, (B) $MgAl_2O_4$-Cr_2O_3 (Fused Cast) from Carborundum after Exposure to Western Coal Slag at 1400°C for 20 Hours

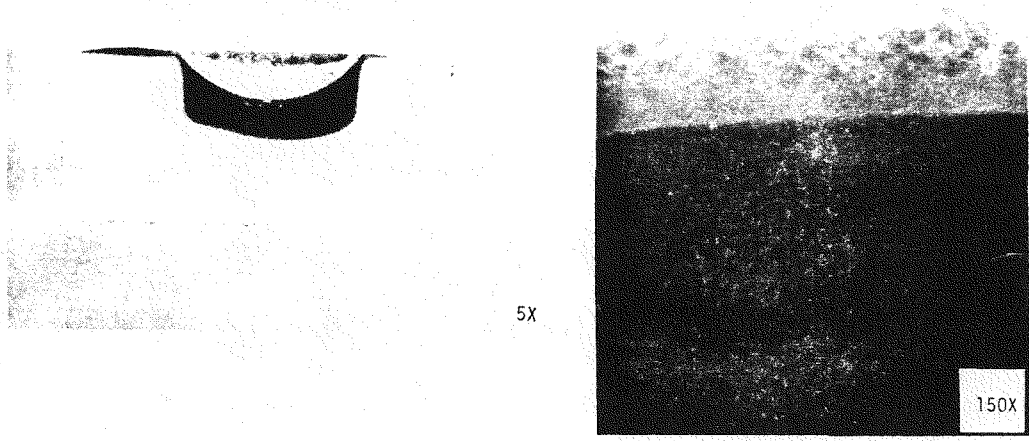

(A)

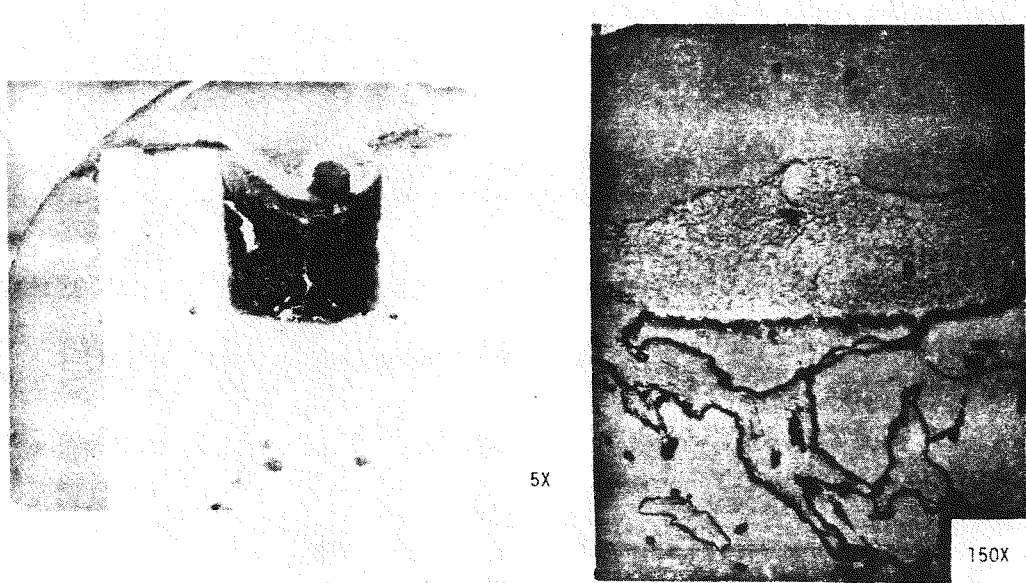

(B)

Figure 8. Appearance of (A) Al_2O_3 (high sintered) from Trans-Tech, (B) Al_2O_3 (Fused Cast) from Carborundum after Exposure to Western Coal Slag at 1400°C for 20 Hours

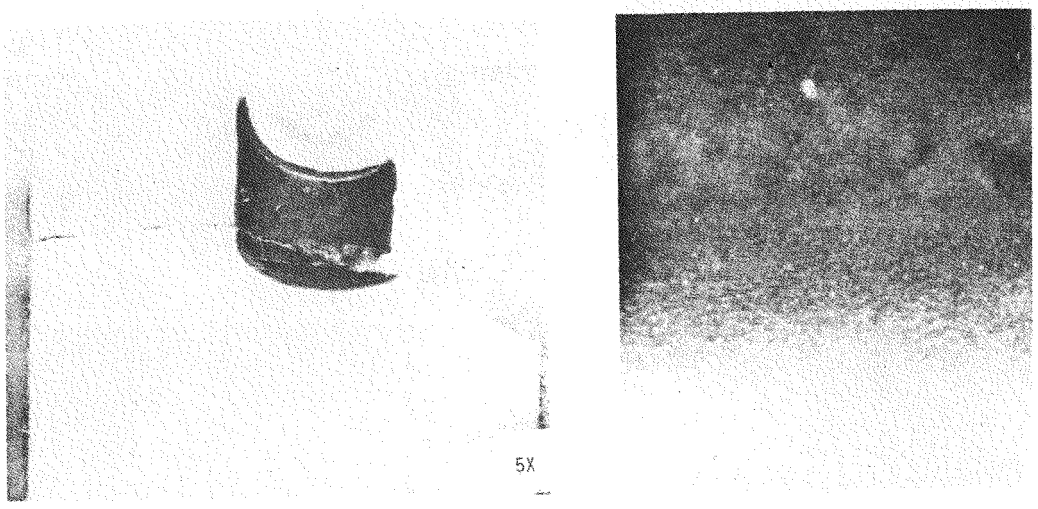

(A)

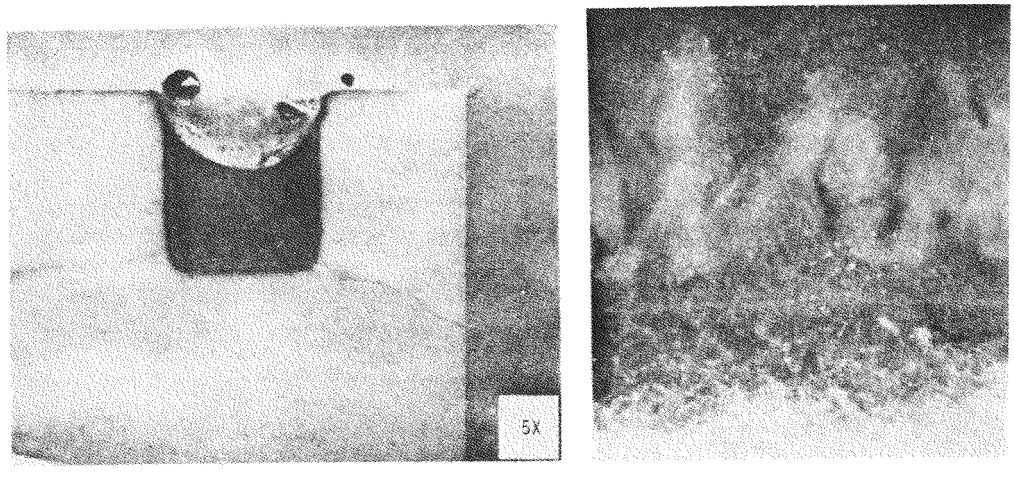

(B)

Figure 9. Appearance of (A) MgO (high sintered) from Trans-Tech. (B) MgO (reaction bonded, fused grain) from Norton after Exposure to Western Coal Slag at 1400°C for 20 Hours

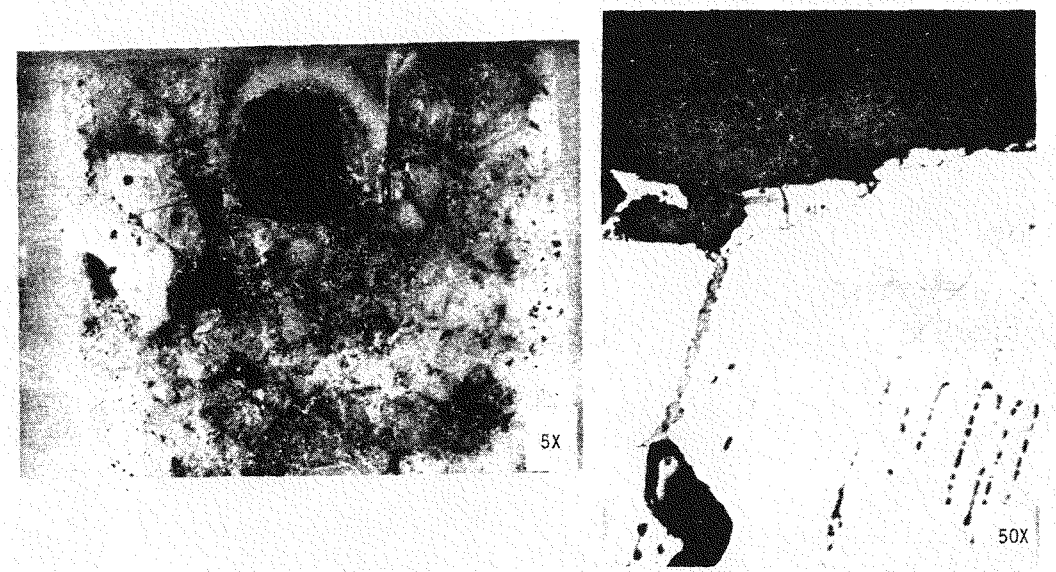

(A)

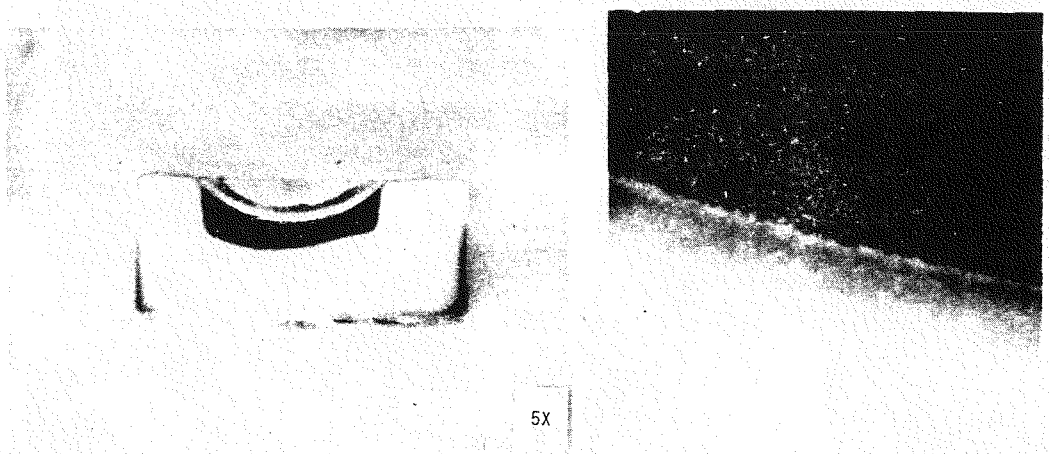

(B)

Figure 10. Appearance of (A) $MgAl_2O_4$ (commercial sintered product) from Norton, (B) $MgAl_2O_4$ (high sintered) from Trans-Tech after Exposure to Western Coal Slag at 1400°C for 20 Hours

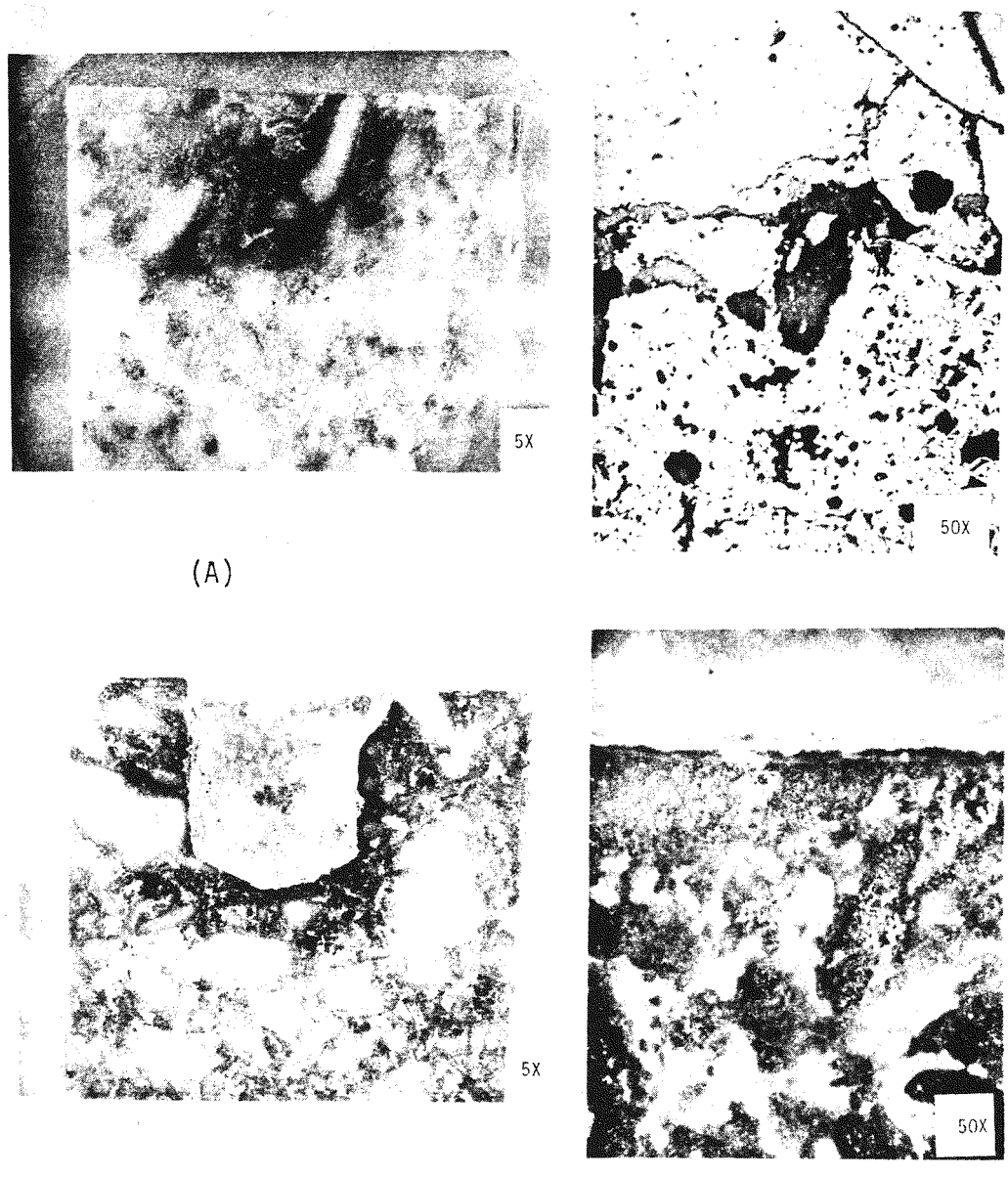

Figure 11. Appearance of (A) MgO (commercial sintered product) from Harbison-Walker, (B) MgO (high sintered) from Harbison-Walker after Exposure to Western Coal Slag at 1400°C for 20 Hours

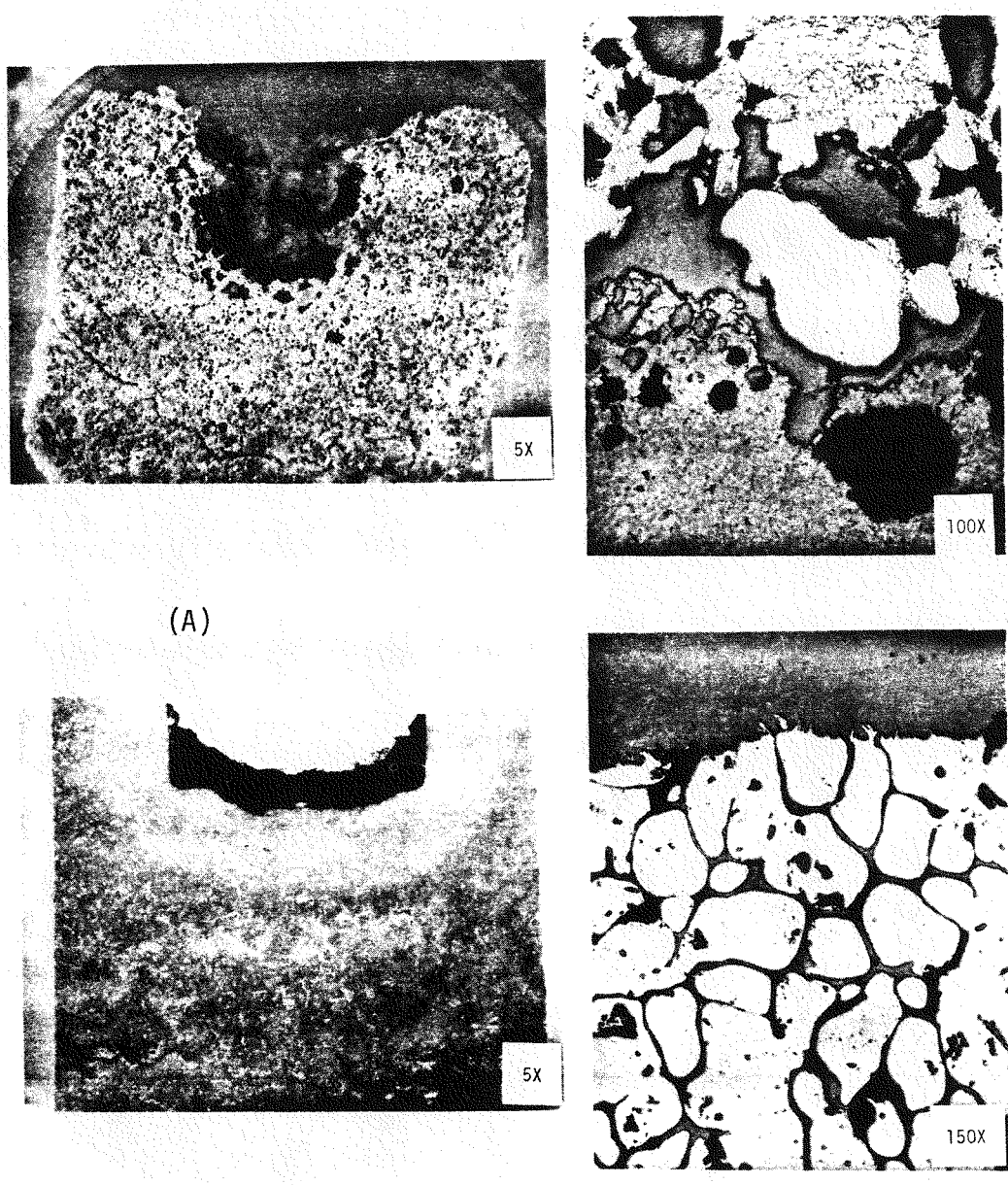

Figure 12. Appearance of (A) ZrO_2 (castable ceramic) from Zircoa, (B) ZrO_2 (fused cast) from Carborundum after Exposure to Western Coal Slag at 1400°C for 20 Hours

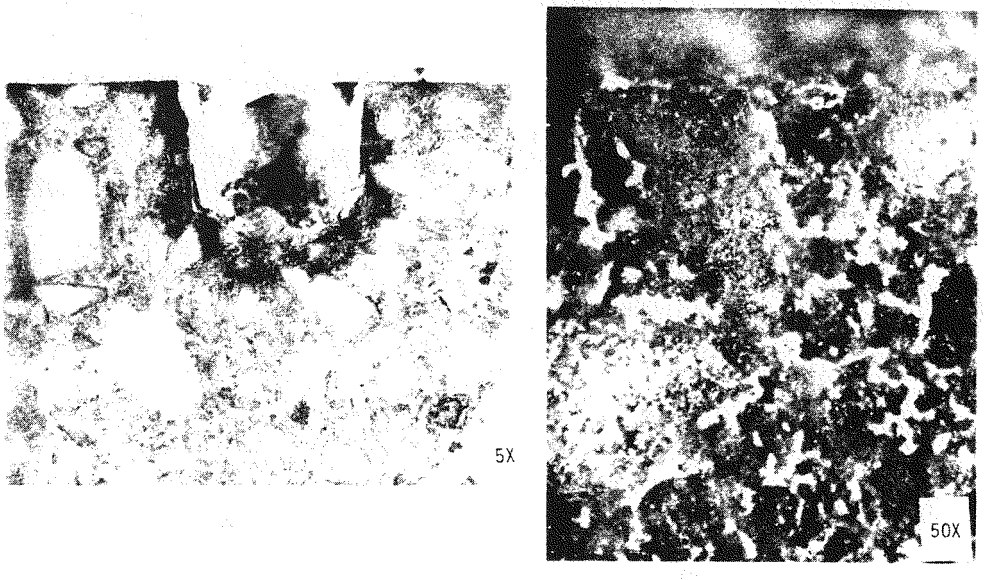

MgO (commercial sintered product)
Kaiser (A)

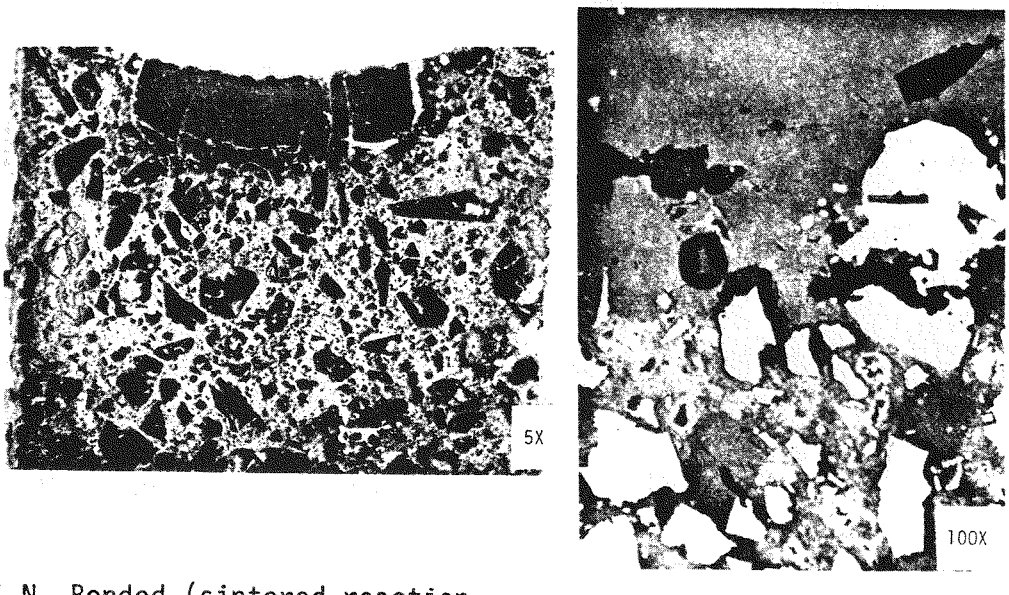

SiC/Si_3N_4 Bonded (sintered reaction bonded) (B)

Figure 13. Appearance of (A) MgO (commercial sintered product) from Kaiser, (B) SiC/Si_3N_4 Bonded (sintered, reaction bonded) after Exposure to Western Coal Slag at 1400°C for 20 Hours

TABLE 4

COMPATIBILITY OF CERAMIC INSULATORS WITH WESTERN COAL SLAG* (MINI-CRUCIBLE TEST @ 1400°C FOR 20 HOURS)

Material	% Theoretical Density	Source	Processing History	Relative Observations
MgO	88	Harbison-Walker	Exp. Hi density, 99% MgO High Purity Sintered	Surface exposed to slag has been wet - and penetration is observed to ~ 1/2 cm in all directions, penetration is only in and around large MgO grog grains, possible chemical interaction in bonding phase although structure is still intact, penetration depth is noted by brownish color.
MgO	82	Kaiser	98% MgO, Commercial Sintered Product	Surface exposed to slag is wet - and penetration is noted to depth of ~ 1/4 cm, again penetration is concentrated in bonding phase - not large grog grains, brownish color distinguishes slag penetration, no structural degradation as yet but strength of exposed material should have been weakened.
MgO	83	Harbison-Walker	98% MgO, Commercial Sintered Product	Exposed surface is wet and penetrated to a depth of 1/2 cm mainly through bonding phase - note MgO grog grains brownish color distinguishes penetration, some structural damage, where there is release of grog grains due to bonding phase damage.
MgO	85	Norton	Hot-Pressed, Fused Grain Material	Slag has wet the surface and penetrated to a depth of 1/4 mm, penetrated layer observed to be bright light brown color, 1/4 mm layer of slag interfaced with the insulator shows dull tan coloration as opposed to dark black slag hue, structurally intact, relatively good compatibility of insulator, tannish phase possibly possibly potassium phase since not seen in K-free sample
MgO	98	Trans-Tech	High Temperature Sintering of Pure Product	Slag has wet surface and penetrated 1/4 mm into insulator, identical pattern as Norton MgO, penetrated layer is bright light brown, no structural damage minimal chemical interaction.
Al_2O_3	98	Trans-Tech	High Temperature Sintering of Pure Powders	Slag has wet surface and penetrated 1/4 mm into insulator, reaction zone has light greenish-gray hue no structural degradation and overall good chemical compatibility.
Al_2O_3	99	Carborundum	Fused-Cast High Density Product	At the exposed surfaces only slight greyish while reaction zones are present, the zones are not continuous and only 1/8 mm in thickness, some pieces of refractory observed floating in slag-not due to chemical interaction but from thermal shock from quenching - refractory has crackled, glassy appearance, chemical compatibility appears very good.
$MgAl_2O_4$	82	Norton	Commercial Sintered Refractory	Where the refractory has been exposed a penetration of 1/2 cm into the insulator is observed, penetration is mainly through the bonding phase, not $MgAl_2O_4$ grog grains, light brownish pigment marks extent of penetration, very crazed appearance reveals some thermal shock from quenching, and loss of strength - could lead to loss of material through pullout.
$MgAl_2O_4$	98	Trans-Tech	High Sintered, High Purity Product	Material is wet by slag, but only 1/10 mm layer is reacted, reaction layer is of a light-greyish white color, excellent compatibility with slag.
Al_2O_3-Cr_2O_3	96	Carborundum	Fused-Cast High Density Product	Insulator appears wet by slag but there is no attack zone or boundary layer, no signs of any degradation, sharp distinction between slag and insulator at interface, excellent performance with Western slag.
ZrO_2	80	Zircoa	ZrO_2 - Phosphate Bonded Castable	Due to high amount of open porosity insulator has been penetrated extensively through the porosity causing fluxing away of individual ZrO_2 grains, at least 1 mm of material has been eroded away in process.
ZrO_2	98	Carborundum	Fused-Cast High Density Product	Intensive penetration of slag-whitish discoloration band extends 4 mm from slag/insulator interface, at interface a few ZrO_2 grains are shown in the slag pool-due to corrosion around ZrO_2 grains causing pullout and structural damage, definite chemical activity at grain boundaries.
$MgAl_2O_4$-Cr_2O_3	95	Carborundum	Fused-Cast High Density Product	Material shows excellent resistance to slag, no detectable penetration, in fact minimal wetting of surface.
SiC/Si_3N_4 Bonded	85	Carborundum	Sintered SiC Grain, Nitrided System	Appearance of slag is very milky - indicating fluxing of material from insulator, insulator is wet by slag and appears penetrated into bonding region to depth of 2 mm. This bonding region appears glassy and murky white - when bond is weakened SiC grains are then succeptible to structural breakdown and floating away.

*Montana Flyash/K_2CO_3

(1) Wetting of the surface by the slag;
(2) Penetration of the slag into any open pores;
(3) Chemical interaction with the slag and the resulting loss of structural integrity (recession rate).

All fourteen insulators show some degree of wetting of their surface by the semi-viscous slag. It does not seem to matter whether the material is of a high density or of what chemical composition it is comprised. Adherence of the slag to the insulators appears universal and fairly uniform. Penetration of the slag through the surface of the insulators, though, definitely does appear dependent on the amount of open porosity present in the material. All of the refractories with porosities greater than six percent, with the exception of the MgO, fused grain (Norton), show a substantial amount of slag penetration, predominantly by way of the more susceptible grain boundaries. The liquid slag then has a chance to react with any impurities (such as SiO_2, Fe_2O_3, CaO) that tend to concentrate in the grain boundaries, and form lower melting eutectic compositions. Even if the impurity level is low, a large level of porosity increases the availability of surface area for reaction or dissolution by the molten alumino-silicate phases in the slag. This in turn eventually leads to a loss of structural integrity. The MgO(fused grain) refractory from Norton, which was only 85% dense, did not display the same substantial amount of penetration as the other low density materials presumably because of its much higher purity and the smaller pore size.

The two ZrO_2 refractory entries did not perform particularly well in spite of their two completely different processing histories. The ZrO_2 castable (with a large amount of open porosity) and the fused cast entry (with only 1% total porosity) both showed a great amount of slag infiltration through the grain boundaries and fluxing away of individual ZrO_2 grains. The Si_3N_4 bonded SiC also was observed to have the identical problem - intrusion of the slag at the grain boundaries causing the loss of the SiC grog grains. The materials which displayed excellent compatibility with the slag were the Al_2O_3, Al_2O_3-Cr_2O_3 and $MgAl_2O_4$-Cr_2O_3 fused cast entries from carborundum and $MgAl_2O_4$ from Trans-Tech. These four refractories showed little evidence of penetration, let alone

any chemical interaction with the molten slag. Close behind these four materials were three refractories which showed a slight interaction or boundary zone with the slag. These included the Al_2O_3 and MgO from Trans-Tech and MgO (fused grain) from Norton. These seven materials would naturally be the recommended refractories for upcoming WESTF tests as shown in Table 5. Additional promising insulators will be tested for slag compatibility in the near future.

Kalsilite ($KAlSiO_4$)

An investigation was initiated into the synthesis and fabrication of dense synthetic $KAlSiO_4$ for use as a possible refractory material for coal-fired MHD components. Investigators, Reference 1 & 2 have found that the major water insoluble crystalline phase found in the coal slag deposited in MHD generators is Kalsilite. Bowen, Reference 3, has reasoned that electrode (and insulator) compositions which are in equilibrium with a coal slag have lower rates of corrosion. This led to his synthesis and use of hercynite ($FeAl_2O_4$) as an electrode material in a number of MHD test channels. It is hoped that Kalsilite would also display the same equilibrium solubility with the slag and perform as an acceptable insulating material.

Kalsilite ($KAlSiO_4$) was synthesized by an organo-metallic method developed by Yoldas, Reference 4. This technique for the preparation of monolithic oxide materials allows (1) polymerization of the oxide constituents at low temperatures (2) homogeneity at the molecular level, and (3) reaction of the constituents before crystallization or any other phase transformation takes place in the individual oxide constituents. A clean alumina sol capable of producing a transparent monolithic alumina was prepared from $Al(OC_2H_5)_3$ aluminum-secondary-butoxide by peptization with HNO_3. This in turn was reacted with a silonol complex prepared from $Si(OC_2H_5)_4$ tetraethyl-silicate and K(COOH) potassium formate. The resultant powder was then fired to 1200° for several hours prior to obtaining an x-ray analysis. X-ray diffraction results showed the material consisted of two phases - a high temperature orthorhombic $KAlSiO_4$ ($\sim$ 80 w/o) and a tetragonal $K_{1+x}Al_{1+x}Si_{1-x}O_4$ ($\sim$ 20 w/o). The whitish crystalline powder was then milled for several hours to obtain a particle size of less than 325 mesh.

TABLE 5

RANKING* OF CANDIDATE INSULATORS
FOR USE IN SLAGGING HOT OR NON-SLAGGING SUPER-HOT GENERATORS

Strongly recommended for use in future WESTF tests

Al_2O_3	Fused Cast	Carborundum
$MgAl_2O_4$	High Sintered	Trans-Tech
Al_2O_3-Cr_2O_3	Fused-Cast	Carborundum
$MgAl_2O_4$-Cr_2O_3	Fused-ast	Carborundum

Acceptable for use in future tests

MgO	Fused grain	Norton
MgO	High Sintered	Trans-Tech
Al_2O_3	High Sintered	Trans-Tech

Not recommended for tests of long duration

MgO	Exp. High Sintered	Harbison-Walker
MgO	Commercial Sintered	Harbison-Walker
MgO	Commercial Sintered	Kaiser
$MgAl_2O_4$	Commercial Sintered	Norton
ZrO_2	Castable	Zircoa
ZrO_2	Fused Cast	Carborundum
SiC/Si_3N_4	Sintered, reaction bonded	Carborundum

*Ranking is based on slag compatibility test.

The Kalsilite powder was fabricated into monolithic disks of two different densities (82% and 98% of theoretical) by hot-pressing. A radio frequency generator was used to heat the powder in a static nitrogen atmosphere. Graphite components were used exclusively to hold the powder charge. A temperature of 1600°C and several different pressing pressures were needed to obtain the desired billets. Characterization of the Kalsilite, which included x-ray analysis, thermal expansion, electrical conductivity, microstructure and slag corrosion resistance was achieved from samples diamond cut from the 2" dia x 0.5" high billets.

X-ray diffraction measurements on the solid billets of $KAlSiO_4$ revealed two phases - the major phase being a high temperature orthorhombic $KAlSiO_4$ (94 w/o) and a minor phase $K_{1+x}Al_{1+x}Si_{1-x}O_4$ (6 w/o). Fractured surfaces of the two different density billets are displayed in Figure 14. The more porous $KAlSiO_4$ shows a very 'feathery' open type surface, with a great deal of surface area open to any outside elements. The denser material, in contrast, displays very little noticeable open porosity. In both cases the predominant mode of fracture is intergranular. The thermal expansion of $KAlSiO_4$ was determined using a standard dilatometer setup from room temperature to 1500°C. The data is shown in Figure 15. It is apparent that the relatively high thermal expansion coefficient of Kalsilite could present a problem e.g., fracturing or spalling, if large thermal gradients were imposed in the material during an MHD generator test. This may be somewhat alleviated if it is found that the material has relatively low creep resistance. Increased investigation into Kalsilites thermal shock resistance is definitely needed in the near future. The electrical resistivity of $KAlSiO_4$ at various temperatures is shown in Figure 16. It has been determined that to maintain adequate electrical insulation between electrodes an electrical resistivity of greater than 100 ohm-cm in the insulation is required. In looking at the resistivity curve for Kalsilite it appears that temperatures up to 1400°C can be reached without the possibility of exceeding the 100 ohm-cm resistivity value. Preliminary slag corrosion studies in Western coal slag were completed for both the 82 and 98% dense $KAlSiO_4$ materials. A comparison of the corrosion rate was made between the Kalsilite samples and a dense spinel ($MgAl_2O_4$), which has shown the best overall corrosion performance of the insulators tested to date. This initial study was

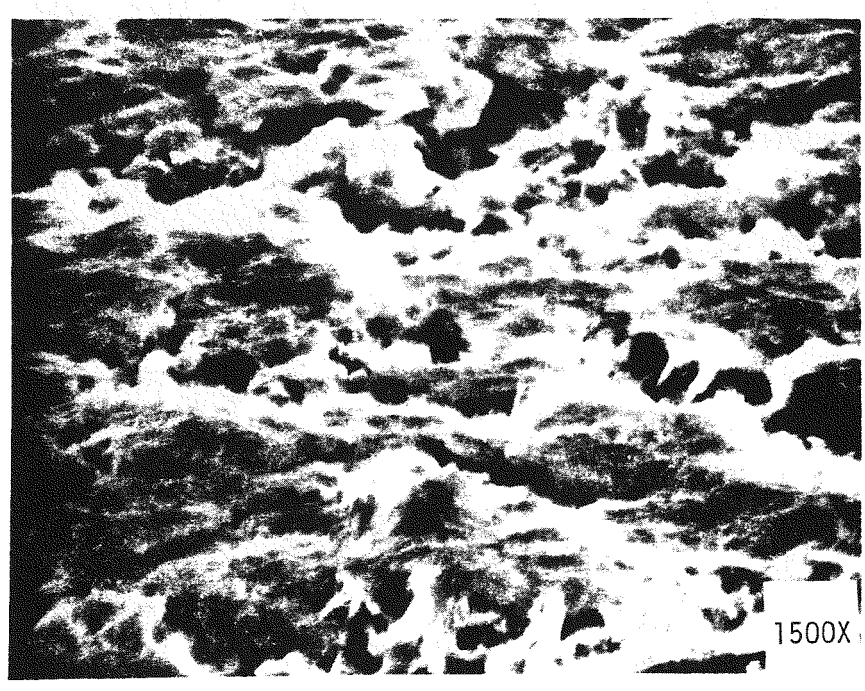

(A)

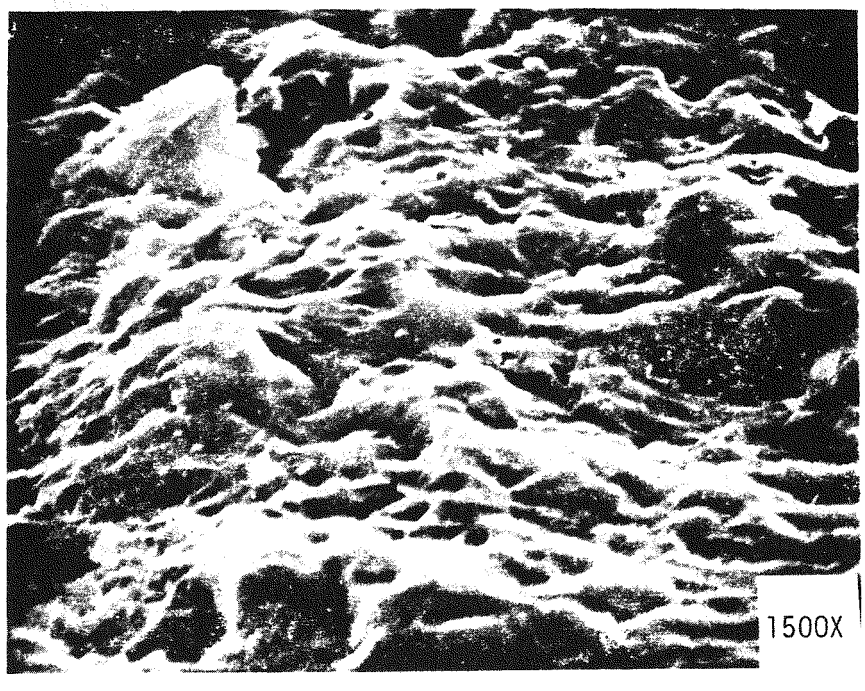

(B)

Figure 14. SEM Microphotographs of Fractured Surfaces of (A) 82% Dense KAl SiO_4, (B) 98% Dense Kalsilite

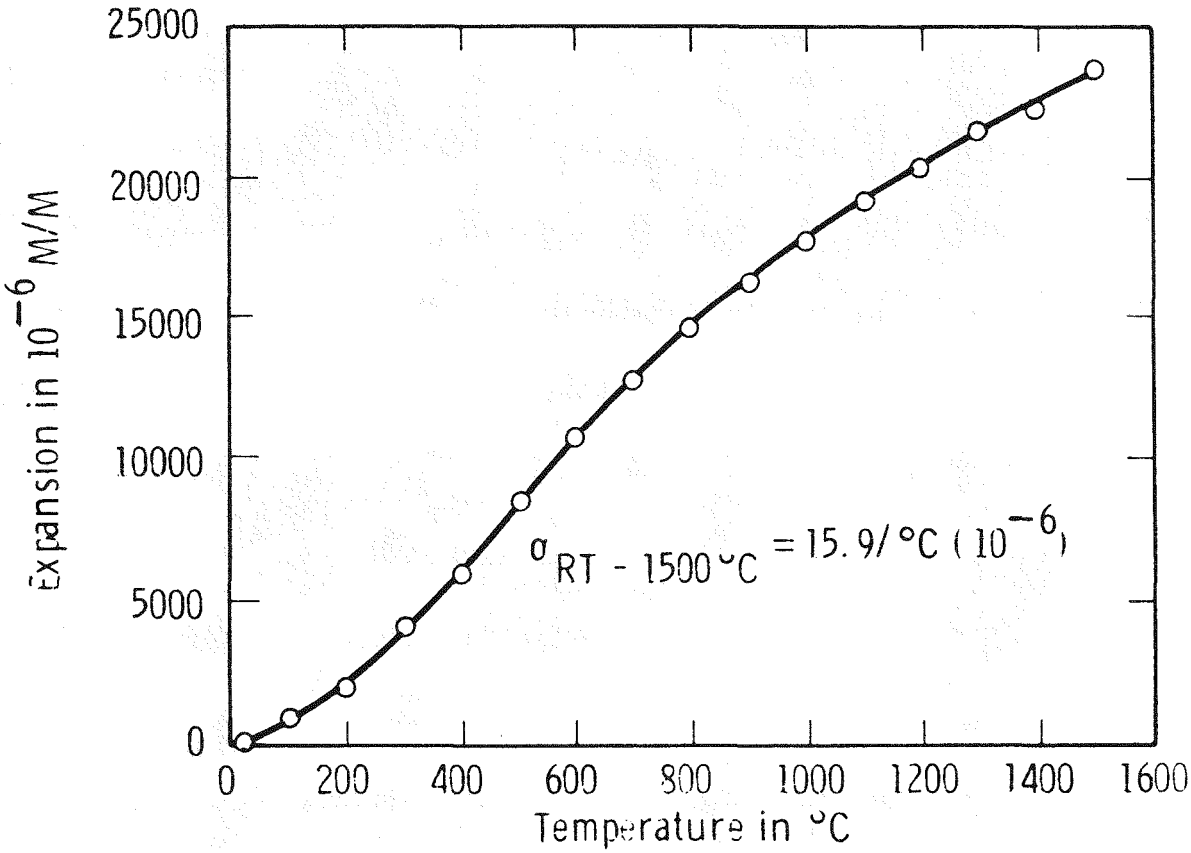

Figure 15. Thermal Expansion of Kalsilite ($KAlSiO_4$)

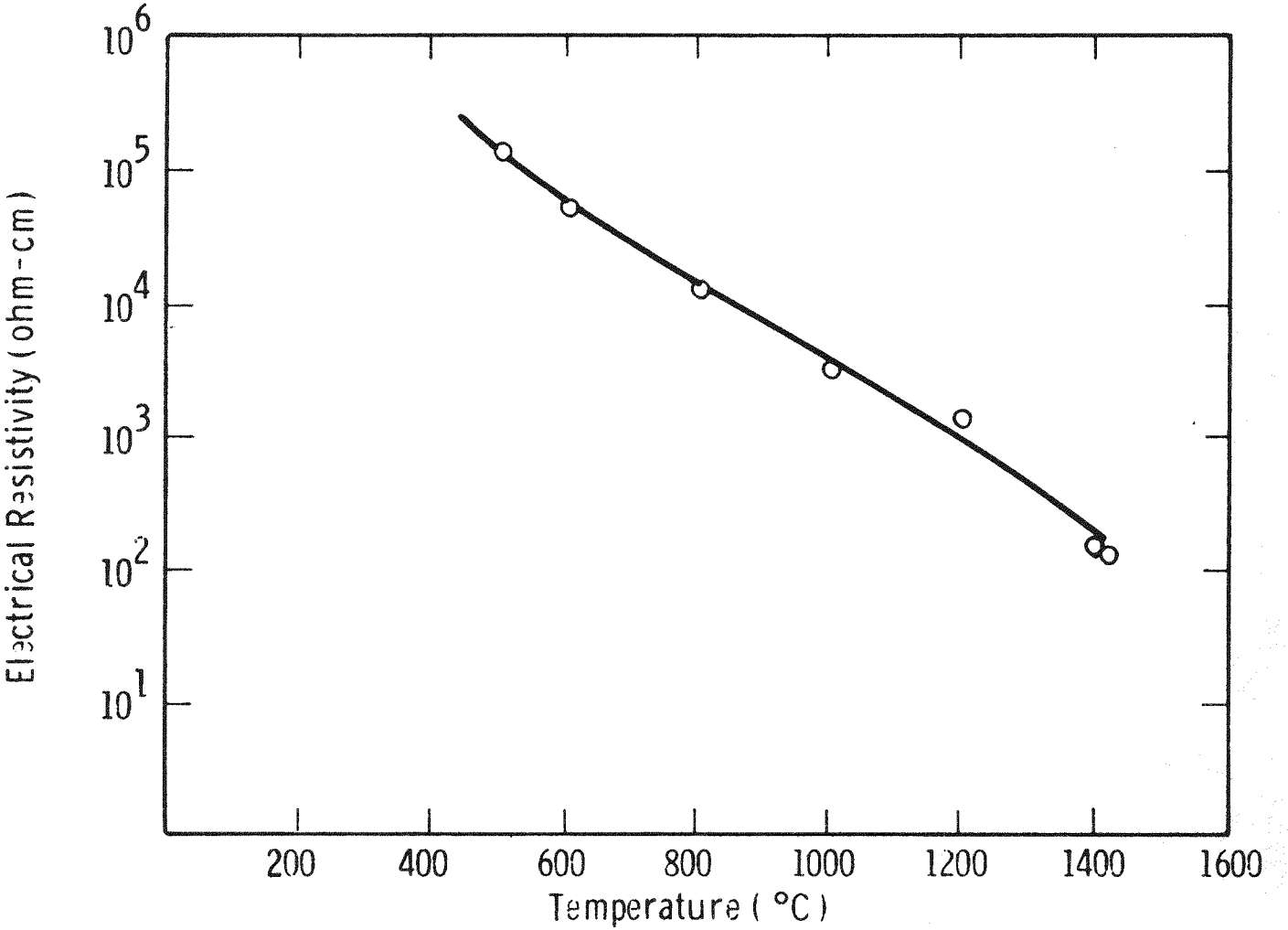

Figure 16. Electrical Resistivity of Kalsilite ($KAlSiO_4$)

basically a static immersion test, where samples 0.25" x 0.25" x 0.75" of each of the materials were hung with platinim wire from the top of small high alumina crucibles that were filled with a homogeneous mixture of Montana Flyash and K_2CO_3. The crucibles were then positioned in a high temperature globar furnace at 1400°C for several immersion times. The crucibles were then sliced in half to expose the slag/insulator interface and the percent of thickness reduction was measured. Figure 17 presents the findings. From these initial test results the spinel insulator shows the best corrosion rate. The dense $KAlSiO_4$ displays a corrosion rate 2-3 times greater than the spinel but a rate of half as great as the more porous $KalSiO_4$. More comprehensive corrosion tests will be undertaken in the next quarter.

1.1.2 Material Characterization

Zirconia-Based Electrodes

ZrO_2-based electrodes which were processed for consideration in WESTF 42 or 44 were characterized for a number of material properties. This pre-test analysis is undertaken to properly evaluate the performance of these electrodes under the design conditions. Small samples were cut from the as-processed sintered bars for the analyses.

Densities and Porosities

The densities and porosities of the candidate ZrO_2-based electrodes are shown in Table 6. The green density of each, after cold pressing, is displayed along with the density and percent of open porosity after each of the two firings. It is noted that there is an increase (3-8%) in density from the 1500°C firing to the 1900°C firing in all cases. Additionally, the percent of open porosity for every composition has dramatically decreased after the higher temperature sintering. The pore size distribution of the ZrO_2-based compositions, as determined using a commercial mercury penetration porosometer, is shown in Figure 18. Sample volumes of approximately 30cm were infiltrated with mercury at various pressures. The volume of mercury penetrating the sample increased with increasing pressure as smaller and smaller open pores were filled. From this volume, the pore size distribution was obtained.

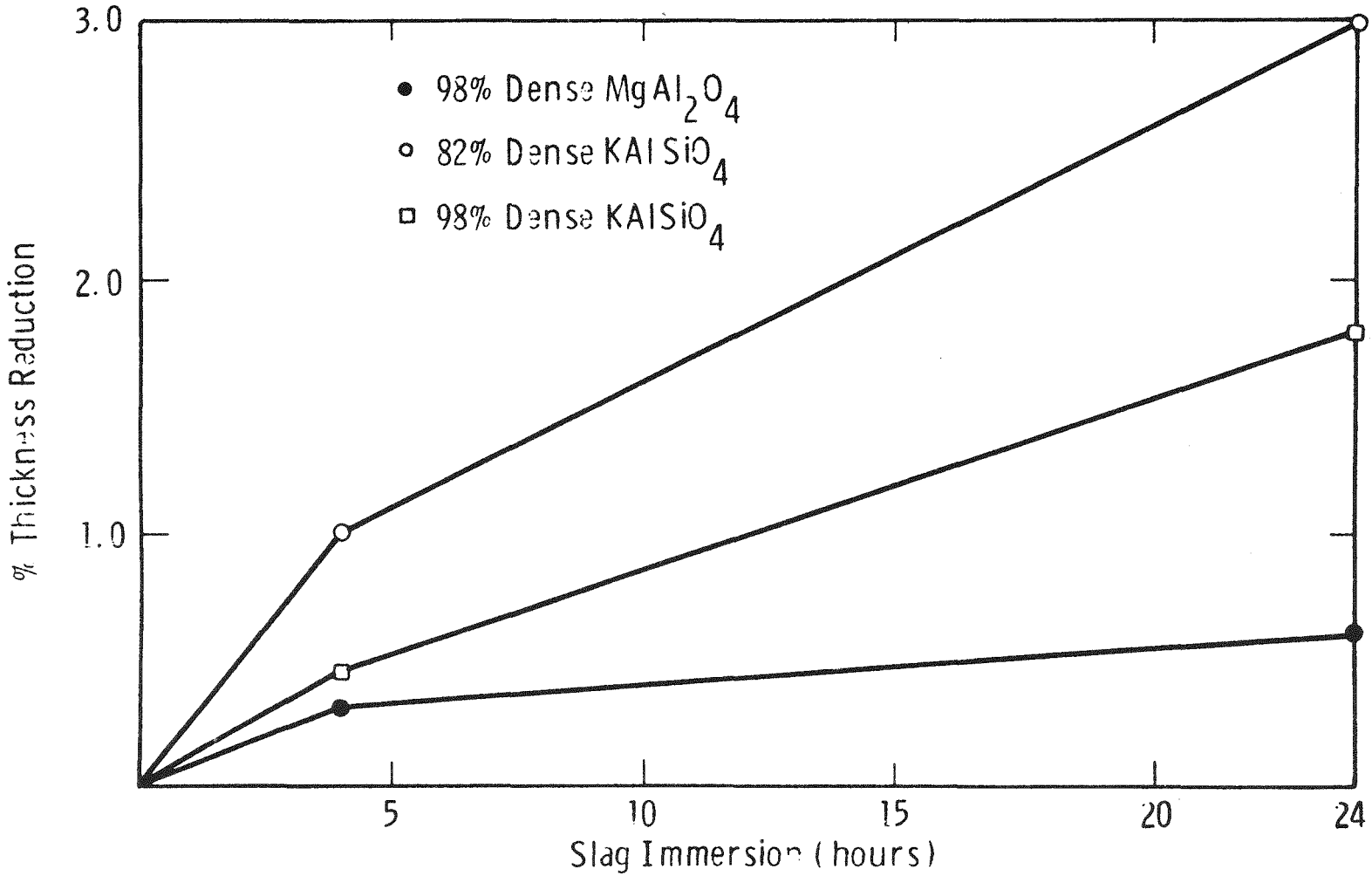

Figure 17. Corrosion Rate of Spinel and Kalsilite ($KAlSiO_4$) in Western Coal Slag

TABLE 6

DENSITIES AND POROSITIES OF ZrO_2-BASED ELECTRODES

Composition	Green Density	% Theoretical	1500°C Fired Density	% Theoretical	% Open Porosity	1900°C Fired Density	% Theoretical	% Open Porosity
85 m/o ZrO_2-15 m/o $(Mg_{.625}Ca_{.375})O$	2.68	--	4.78	--	2.05	5.02	--	.03
88 m/o ZrO_2-12 m/o Y_2O_3	3.11	54	4.73	82	4.91	4.92	85	.8
88 m/o ZrO_2-4 m/o Y_2O_3 8 m/o Nd_2O_3	3.05	--	4.75	--	3.06	5.01	--	.56
82 m/o ZrO_2-18 m/o CeO_2	3.25	52	5.51	87	1.03	5.77	91	.46
88 m/o ZrO_2-12 m/o Y_2O_3 (Phase I Test)	--	--	4.76	82	--	5.19	90	.10

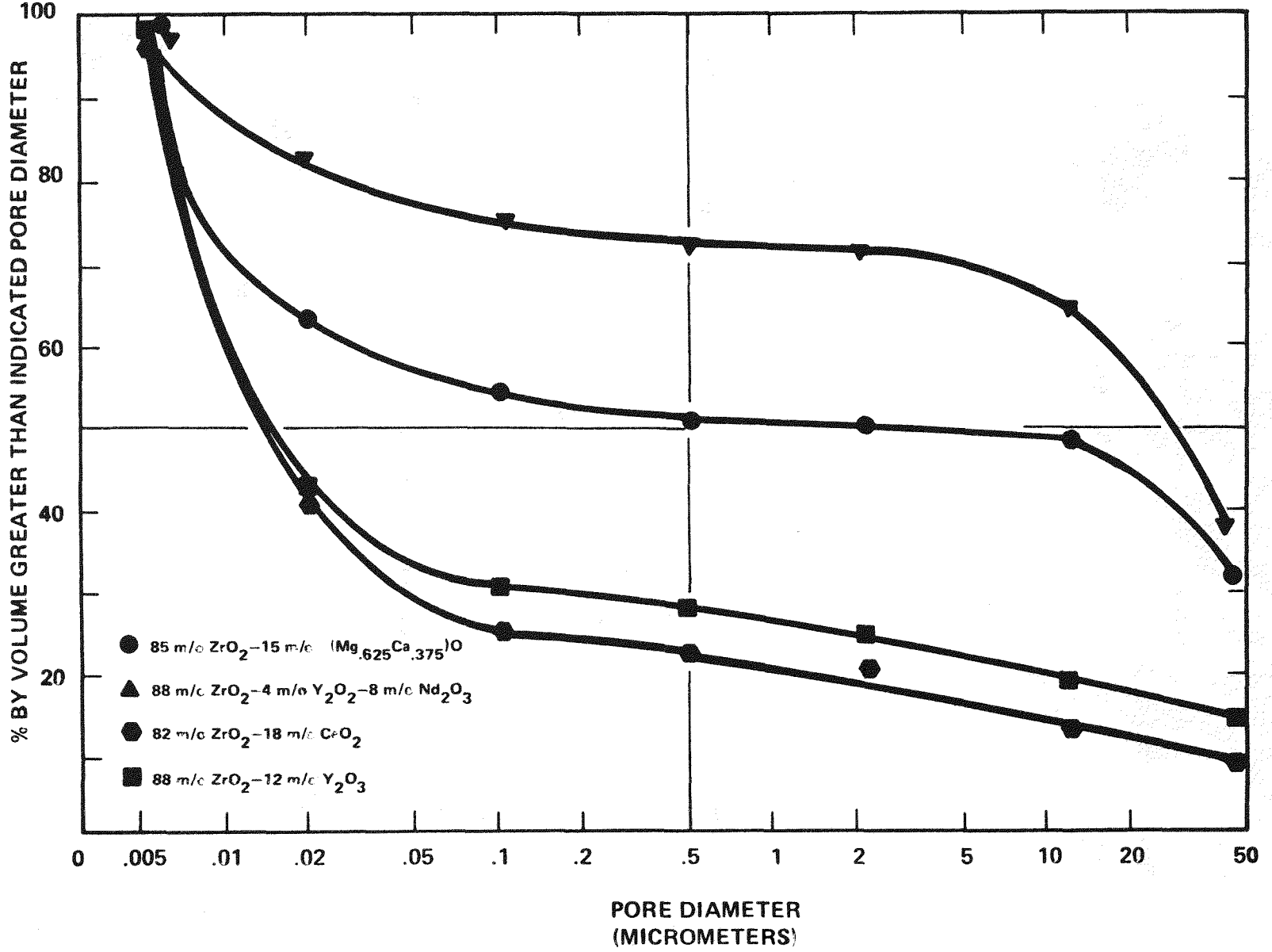

Figure 18. Pore Size Distribution of ZrO_2-Based Electrode Materials

Phase Analysis

X-ray diffraction methods were employed for determining the phases present, the crystallinity, and the lattice parameters of the ZrO_2-based electrodes. Table 7 presents the findings. All of the compositions are observed to have good crystallinity and a face centered cubic structure except for the 82 m/o ZrO_2-18 m/o CeO_2 material. It showed very poor crystallinity and a tetragonal crystal structure. A trace of the monoclinic crystal structure was detected in every case but the 12 m/o Y_2O_3-88 m/o ZrO_2 composition, run in the U-02 Phase I program.

Microstructure

The microstructure of the ZrO_2-based electrodes were evaluated from both fracture surface samples and from samples which had been mounted and polished. Figures 19 through 22 depict scanning electron micrographs of the electrodes' fractured surfaces and Figures 23 and 24 display optical metallographic photographs of as polished electrode samples. The SEM photographs reveal predominately a transgranular mode of fracture for the electrodes. The porosity mainly consists of isolated spherical or elongated eliptical cavities of fairly uniform size, which usually denotes little open porosity. The 85 m/o ZrO_2-15 m/o $(Mg_{.625}Ca_{.375})O$ composition shows very rounded smooth fracture edges in contrast to the other electrodes' sharp well defined lines. This suggests some possible deformation has taken place during the sintering cycle.

Electrical Conductivity

The electrical resistivity as a function of temperature of several ZrO_2-based electrodes are shown in Figure 25. The data was obtained in air using a 2 point probe method of measurement that utilizes a logthrithmic a. c. voltage response apparatus as described by Bottelberghs (Reference 1). The conductivity of the three measured compositions at the higher temperatures ($>1400°C$) should be adequate enough for their consideration as MHD electrodes in a super hot non-slagging operation mode.

TABLE 7

X-RAY ANALYSIS OF ZrO_2-BASED ELECTRODE MATERIALS

Composition	Sample Designation	Crystallinity	Major Phase	Minor Phase
85 m/o ZrO_2-15 m/o $(Mg_{.625}Ca_{.375})O$	ZC-WE01	Very Good	Cubic $a = 5.096$ Å	Trace of Monoclinic
88 m/o ZrO_2-4 m/o Y_2O_3-8m/o Nd_2O_3	YZ-WE02	Good	Cubic $a = 5.176$ Å	Trace of Monoclinic
82 m/o ZrO_2-18m/o CeO_2	CZ-WE03	Poor	Tetragonal $a = 5.10$ Å, $c = 5.20$ Å	Trace of Monoclinic
88 m/o ZrO_2-12 m/o Y_2O_3	YZ-WE01	Very Good	Cubic $a = 5.152$	Trace of Monoclinic
88 m/o ZrO_2-12 m/o Y_2O_3 (Phase I Electrode)	RZY-1	Good	Cubic $a = 5.151 \pm .002$ Å	None

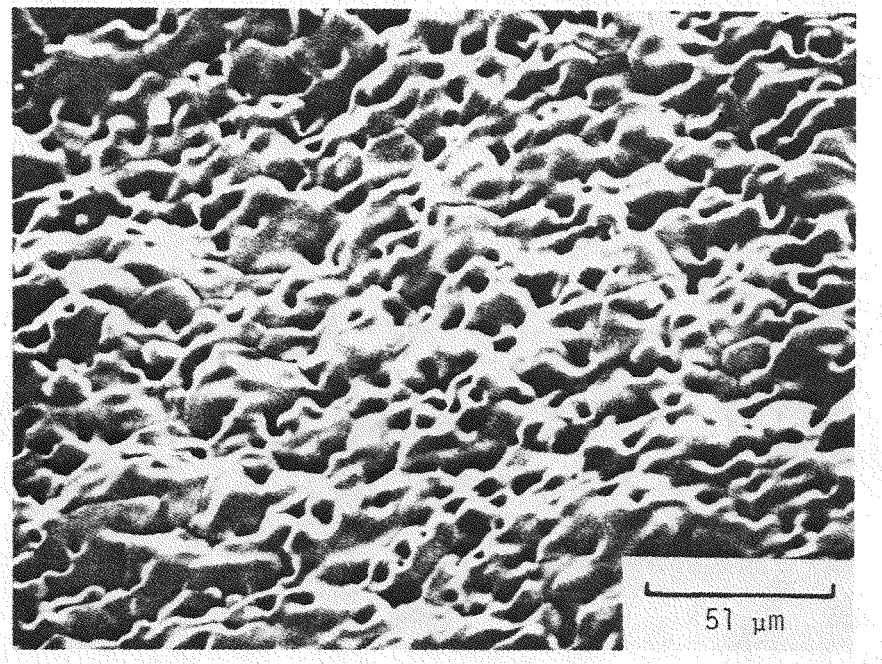

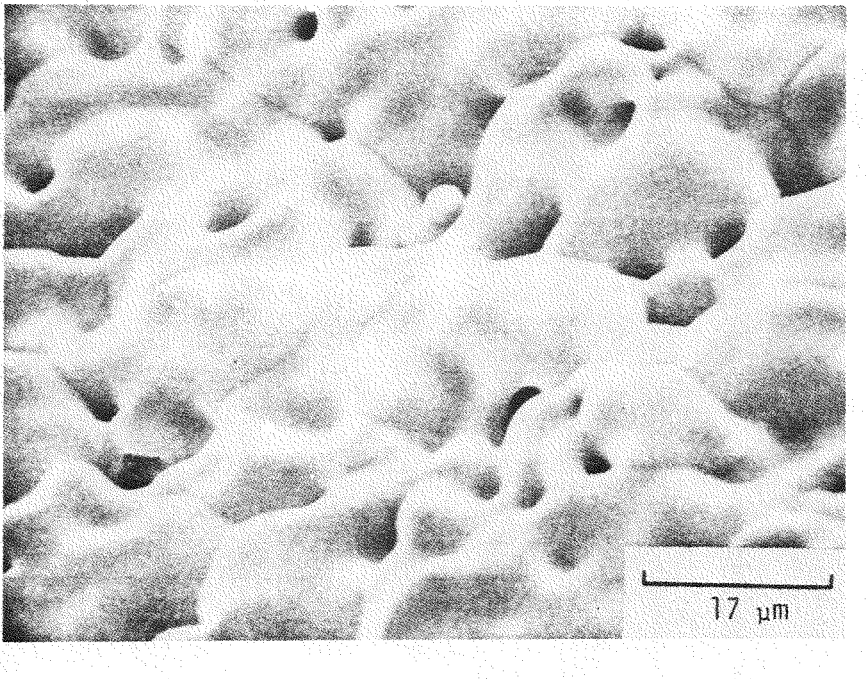

Figure 19. SEM Microphotographs of Fractured Surface of 85 m/o ZrO_2 - 15 m/o $(Mg_{.625}Ca_{.375})O$

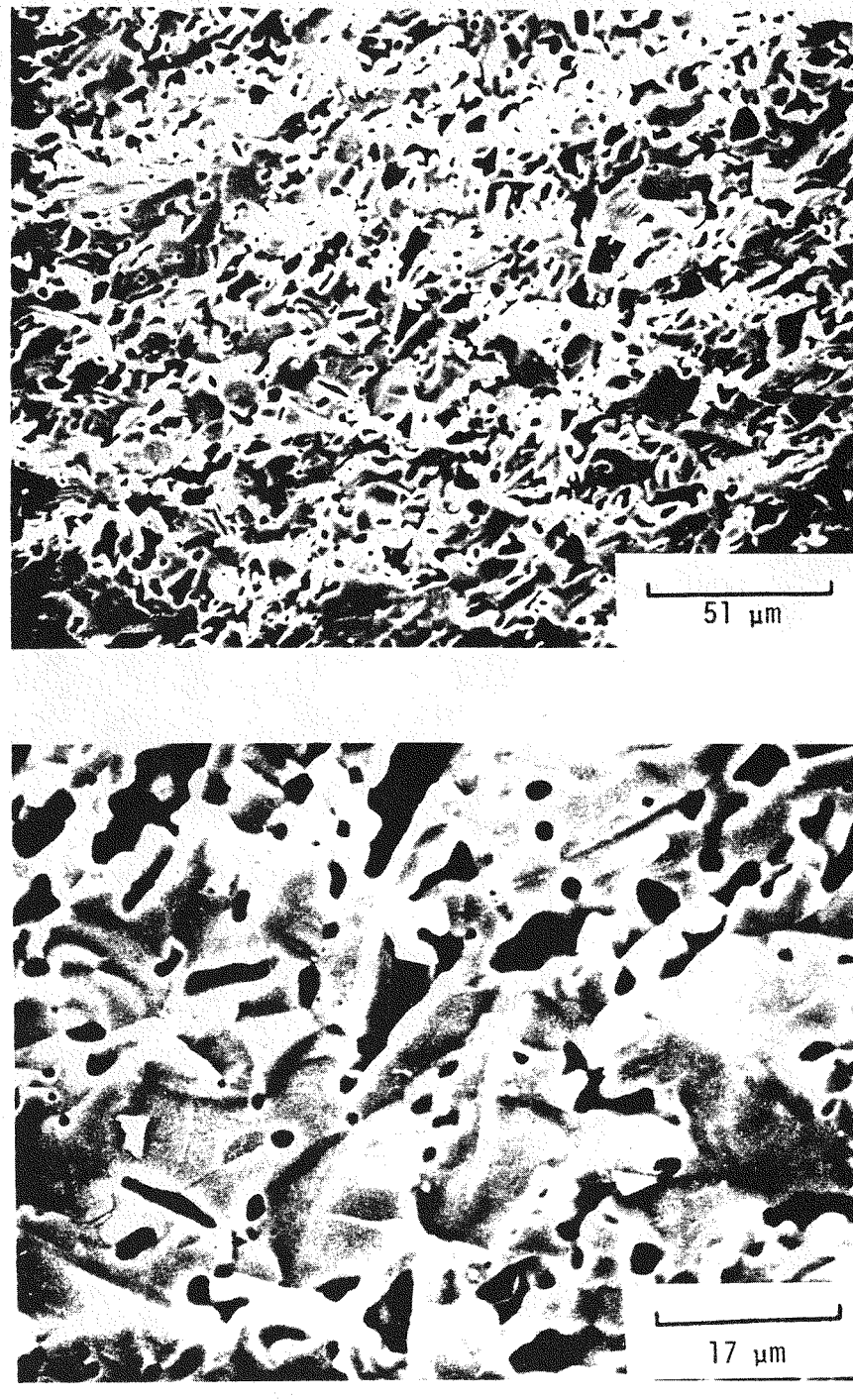

Figure 20. SEM Microphotographs of Fractured Surface of 88 m/o ZrO_2-12 m/o Y_2O_3

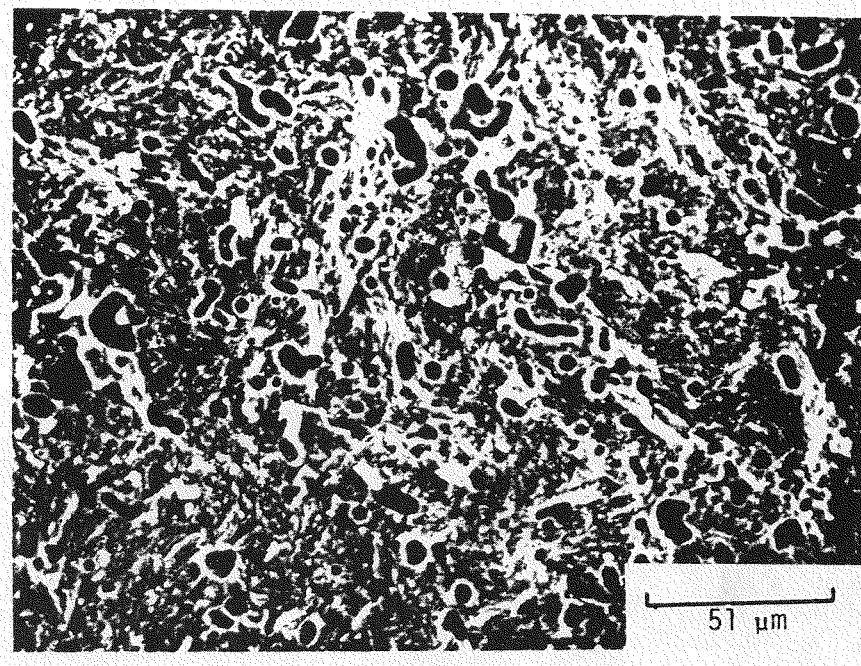

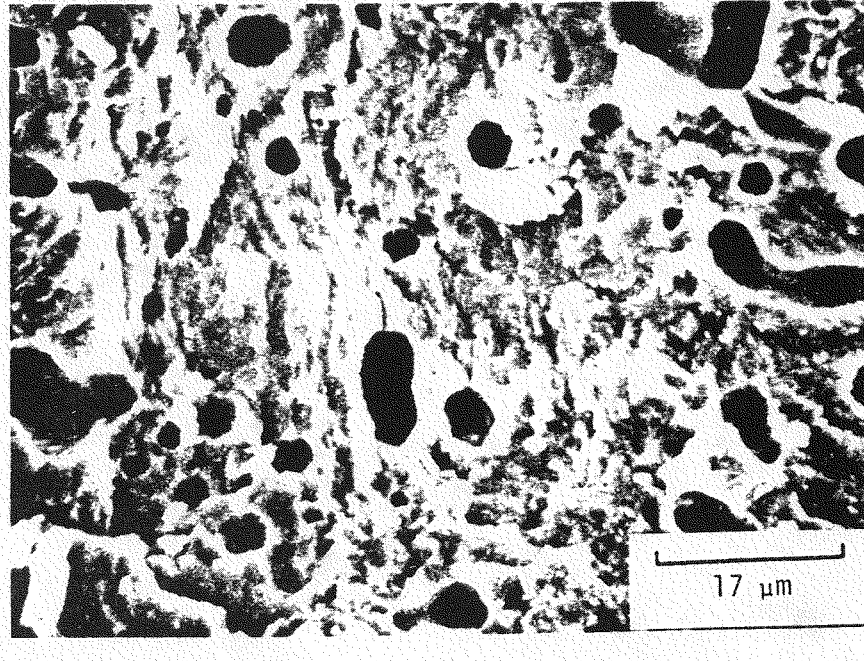

Figure 21. SEM Microphotographs of Fractured Surface of 82 m/oZrO_2-18 m/o CeO_2

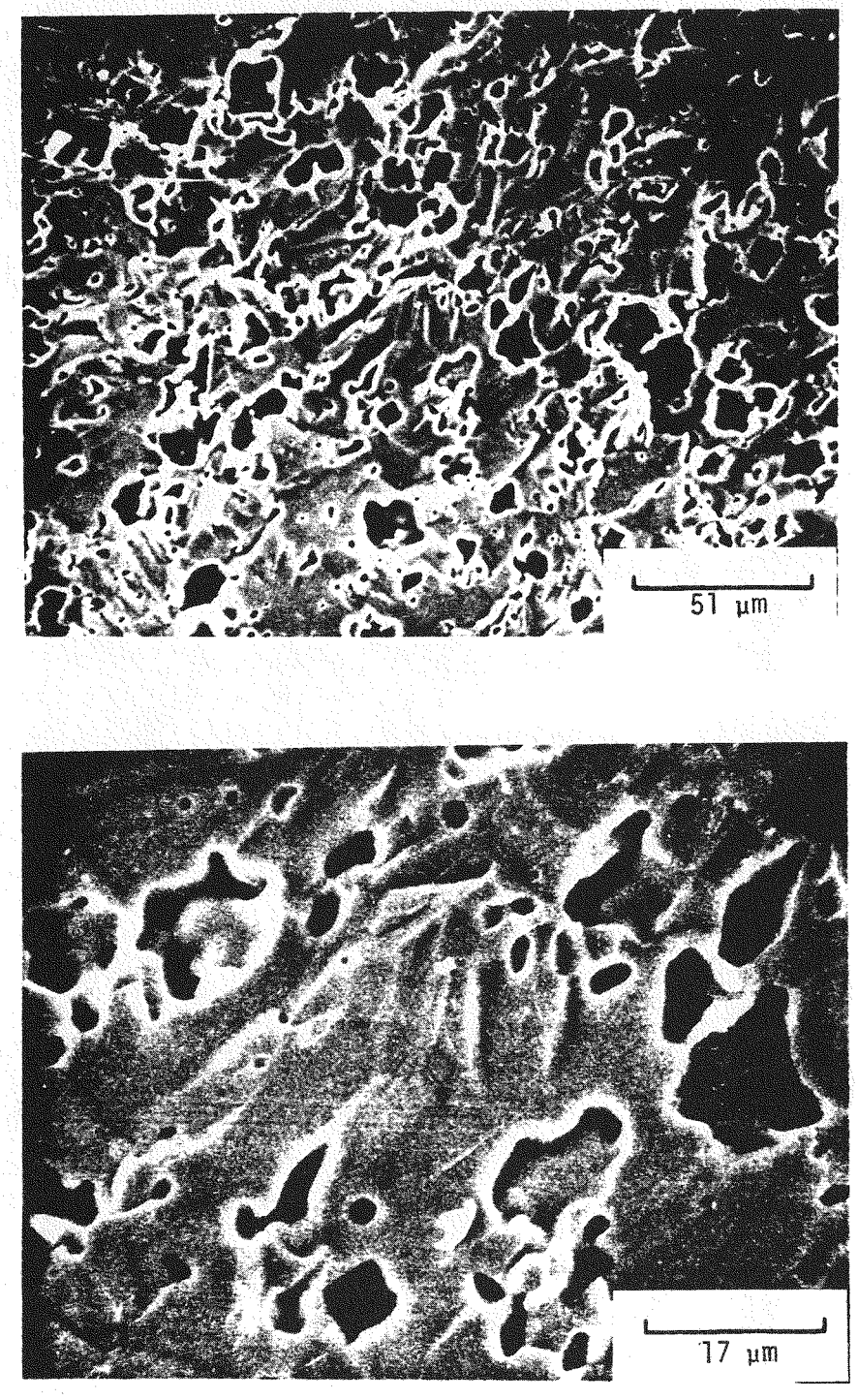

Figure 22. SEM Microphotographs of Fractured Surface of 88 m/o ZrO_2-4 m/o Y_2O_3 - 9 m/o Nd_2O_3

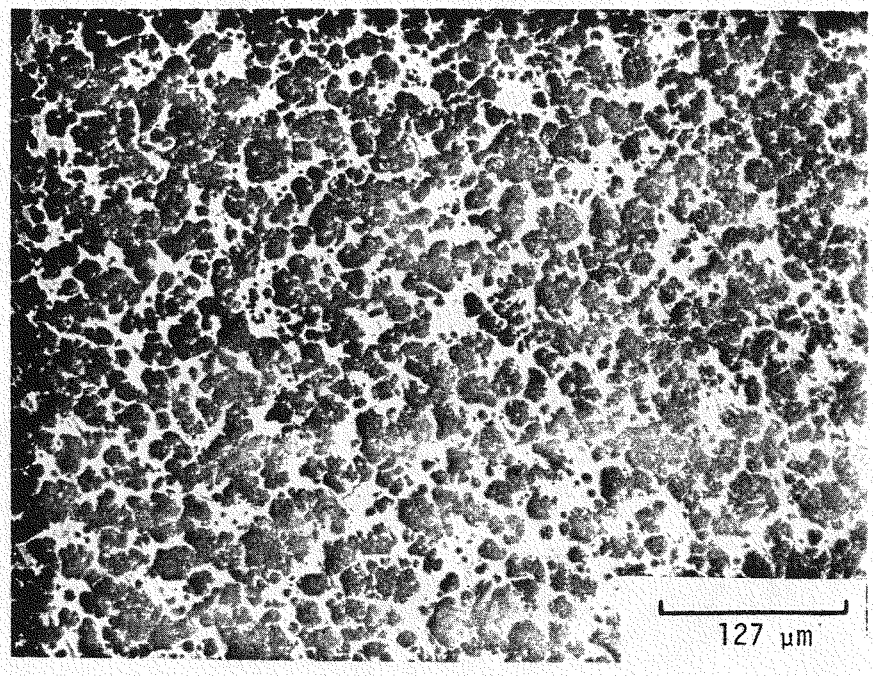

(A)

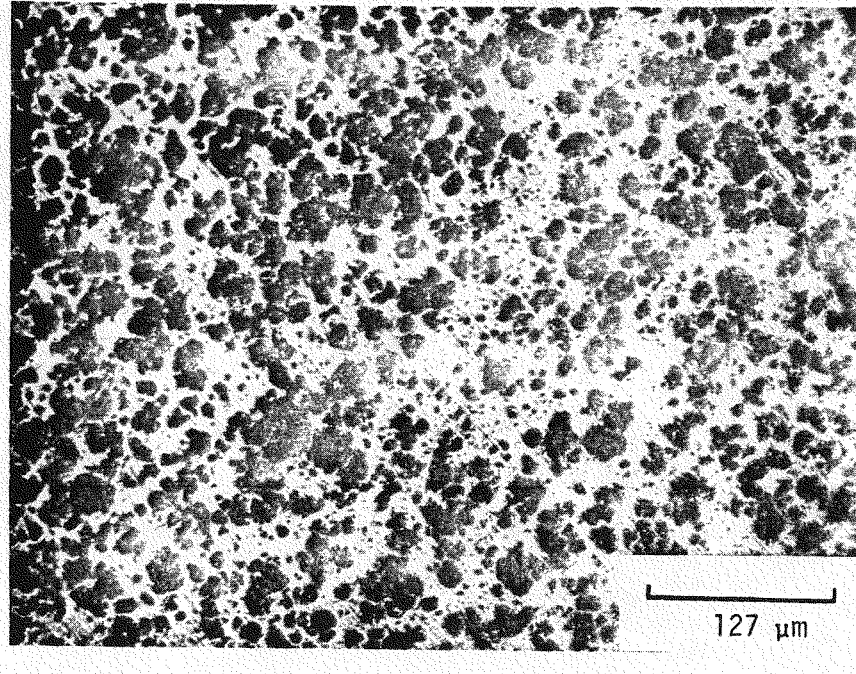

(B)

Figure 23. Microstructures of ZrO_2-Based Electrodes: (A) 85 m/o ZrO_2 - 15 m/o $(Mg_{.625}Ca_{.375})O$; (B) 88 m/o ZrO_2 - 12 m/o Y_2O_3

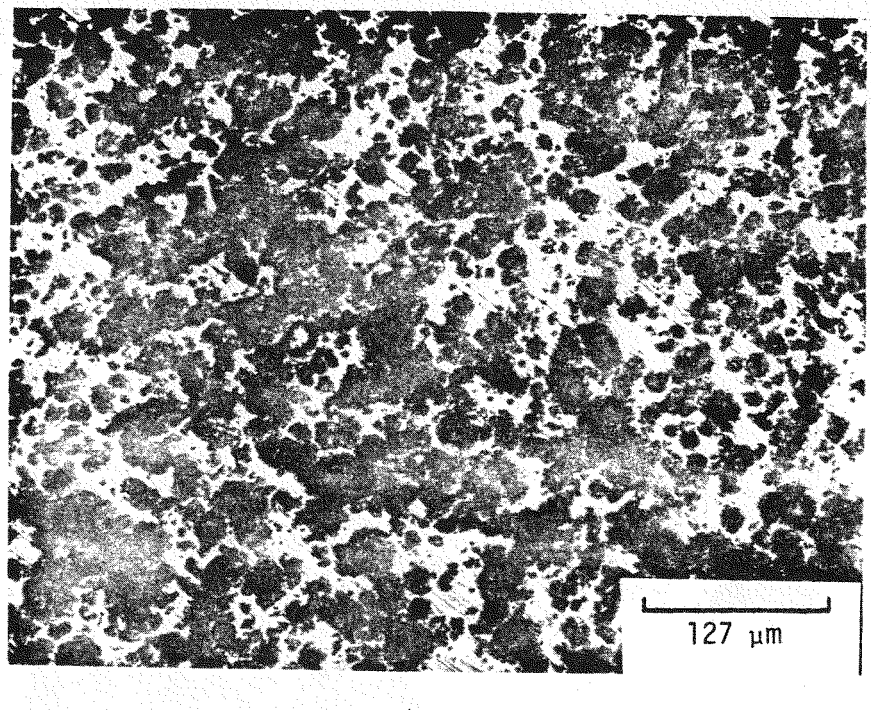

(A)

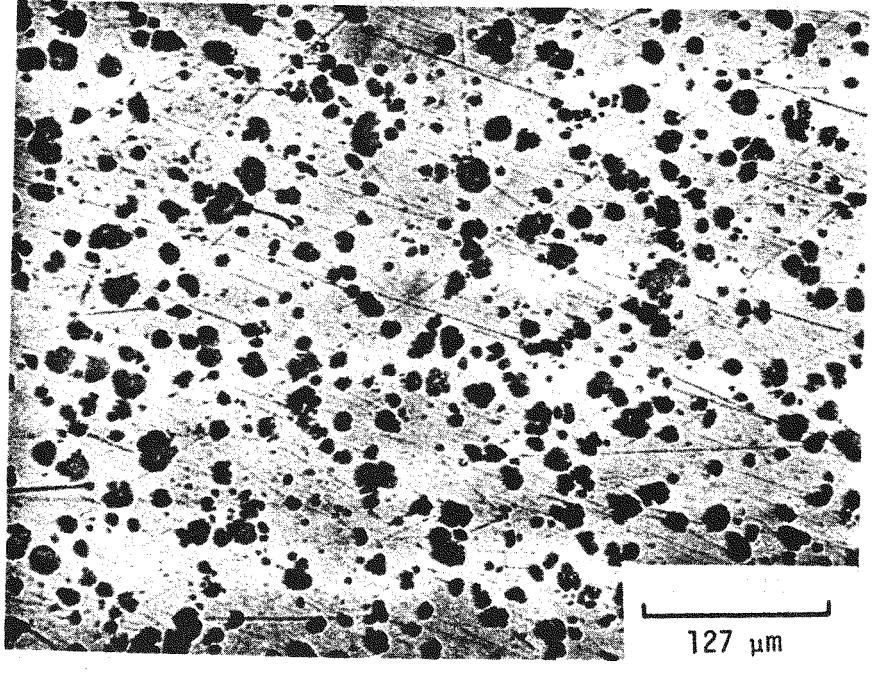

(B)

Figure 24. Microstructures of ZrO_2-Based Electrodes: (A) 88 m/o ZrO_2 - 4 m/o Y_2O_3 - 8 m/o Nd_2O_3; (B) 82 m/o ZrO_2 - 18 m/o CeO_2

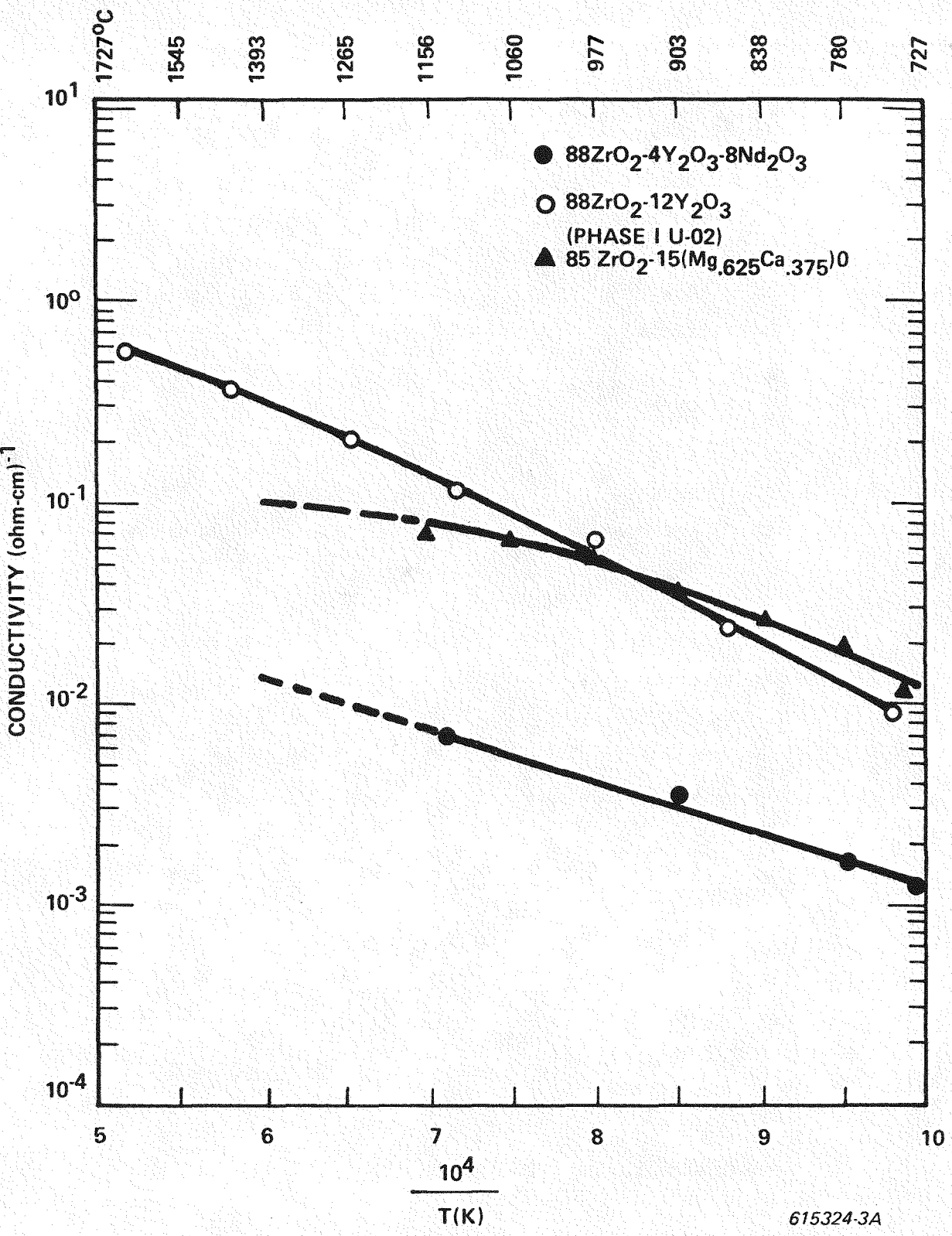

Figure 25. Electrical Conductivity of ZrO_2 Based Electrodes Taken in Air

1.2 WBS 1.1.2 - Laboratory Screening Tests

1.2.1 Electrochemical Corrosion

In this period a comprehensive analytical model has been derived which permits detailed analysis of the role of slag properties as well as electrode-slag polarization on the nature of electrochemical reactions under hot slagging conditions. In the following section, we will present this model and will also discuss criteria for selection of slagging MHD electrode materials.

Electrochemical Reaction Model

Earlier experiments with ZrO_2 materials (References 5 & 6) point to the interrelationship between the nature of electrochemical reactions that occur at anode and cathode and the mode of current transfer both in the electrodes and in the slag. It is unfortunate that at this time, conduction mechanisms in slag are poorly understood. It is generally conceded that coal slags exhibit mixed electronic-ionic conduction and that increasing iron content raises the total conductivity by increasing the electronic contribution. Electronic conduction is attributed to an electron hopping or exchange mechanism between Fe^{+2} and Fe^{+3} ions and increases with the Fe^{+2}/Fe^{+3} ratio. The electronic conductivity is not dependent on movement of iron ions. Early studies on metallurgical slags (Reference 7, 9) suggest that Fe or Ca are the predominant ion current carriers but this is because of a priori assumptions that anions do not move and not to experimental fact. Evidence from electrochemical studies (References, 10, 11, 22), do suggest some cation movement as evidenced by cation depleted or enriched zones of slag at anode and cathode interfaces, respectively. However, results from the above experiments on ZrO_2(Y)/slag cells suggest that perhaps it is the anions and not the cations that are the major ion current carriers. These experiments indicate that the O^{-2} ions in Rosebud slag move at a rate nearly equal to that in ZrO_2(Y). Since it is generally acknowledged that the O^{-2} diffusivity in ZrO_2 at elevated temperatures (i.e., 1400°C) is greater than the diffusivities of either anions or cations in most other ceramic oxide solids or melts, it may not be unreasonable to conclude that O^{-2} is a major if not the dominant ion charge carrier in coal slags. Studies on diffusion in CaO-SiO_2-Sl_2O_3 melts (Reference 12) tend to support this hypothesis.

If the above hypothesis is true, it becomes necessary to propose how O^{-2} ions are formed in the liquid slag at the cathode interface, especially when non-oxide or electronically conducting electrodes are used in an electrochemical cell or in an MHD channel.* Several possible reactions are:

(a) $FeO + 2e^- \rightarrow Fe + O^{-2}$,

(b) $SiO_2 + 2e^- \rightarrow SiO\uparrow + O^{-2}$, and

(c) $SiO_2 + 4e^- \rightarrow Si + 2O^{-2}$**.

Evidence for all these reactions exist--for example, metallic iron has been found at cathode/slag interfaces by investigators (References 10, 11, 13, 22) (reaction (a)), gas bubbles at the cathode slag/interface, perhaps SiO, have been reported (References 13, 14) and suggest reaction (b) and finally, the presence of Si in the metallic Fe which is discharged at the cathode from Western slags (References 14, 15) suggest reaction (c). It is possible that all reactions occur with reaction (a) being dominant in high iron containing slags, while reactions (b) and (c) are more important in low iron slags (Western coal slags).

To simplify the exposition of the following electrochemical model and the subsequent discussion, we will consider that only O^{-2} ions transfer the ionic portion of current in liquid slags. It is important to note, however, that the model is completely general and will apply to any anion or cation species that transfers current.

When a direct current is applied across electrodes attached to a homogeneous mixed ionic-electronically conducting ceramic or liquid slag, a current will flow due to the movement of electrons and ions within the sample. Anions will migrate to the positive electrode while cations accumulate at the negative electrode. When this occurs, the sample is no longer homogeneous but instead it is "polarized". The net result of these differences in ion concentration is to give rise to internal polarization voltages which are in opposition to the applied field. If the electrodes can block the movement of all ions out of the ceramic or slag, the opposing voltage becomes greater and greater until

*Note that for a ZrO_2 cathode, O^{-2} pass directly from electrode into the slag. For a metallic cathode this is not possible, and O^{-2} ions must be generated.

**In high potassium containing slag, $K_2O \rightarrow 2K + O^{-2}$ may occur.

the flow of ionic current (but not the electronic current) is completely stopped. If the electrodes are not completely blocking but can accept or transfer the moving ions into or out of the slag to some degree, the opposing voltage will not build to a value sufficient to halt ion migration and, therefore, some ionic current will flow.

Patterson (Reference 16) has shown a simple method of representing the conditions in an electrochemical cell similar to that described above through use of an equivalent electrical circuit diagram such as shown in Figure 26. Referring to Figure 26, an external voltage, E_x, causes a current to flow in the external metal circuit, I_x. Since the slag of thickness, ℓ, has both ionic and electronic conduction, the external current passes through the electrodes and partitions into an ionic component, I_i, and an electronic component, I_e, (i.e., $I_x = I_i + I_e$). R_i and R_e refer to the resistance of the slag to ionic and electronic current transfer, respectively. E_{oc} is the back or bucking EMF generated in the ionic leg of the circuit due to the establishment of a concentration gradient of ions between the anode and cathode electrodes.

If it is assumed that: the system is at constant temperature, the electrodes are in chemical equilibrium with the slag electrolyte, local equilibrium exists between ionic, electronic and neutral species in the slag, and if we neglect the resistance of the electrodes and external circuit, we can apply Kirchoff's law to the circuit in Figure 26 to obtain the following relationships:

$$I_x = I_i + I_e \tag{1}$$

$$E_x = - I_e R_e \qquad \text{and} \tag{2}$$

$$E_x = - I_i R_i + E_{oc} \tag{3}$$

where E_{oc} = the open circuit bucking voltage (i.e., $I_x=0$) which for oxygen equals

$$E_{oc} = \frac{-\Delta G}{nF} = RT \ln \frac{P_{O_2}{}^{A}}{P_{O_2}{}^{C}} \tag{4}$$

where $P_{O_2}{}^{A}$, $P_{O_2}{}^{C}$ = the partial pressure of oxygen at the slag/anode and slag/cathode interfaces, respectively.

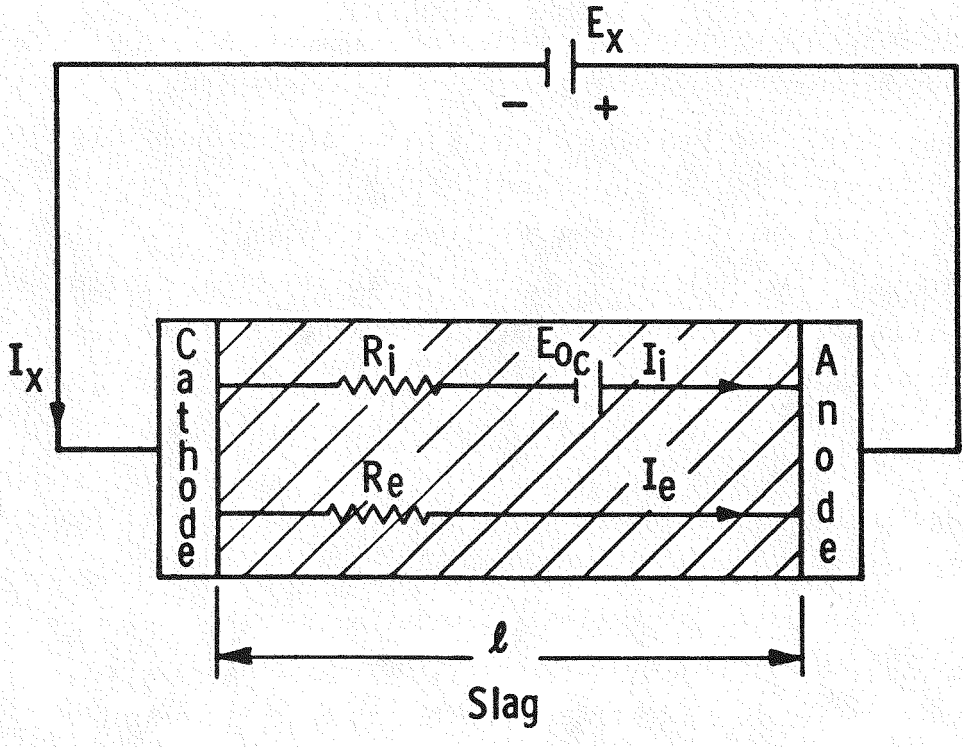

Figure 26. Electrical Analog Circuit for an Electrochemical Test Cell

F = Faraday constant

n = Valency

To simplify the above relationships, a relative polarization factor, r*, is introduced where

$$r^* = (\frac{I_i}{I_e})/(\frac{\bar{t}_i}{\bar{t}_e}) \tag{5}$$

and $\bar{t}_e$, $\bar{t}_e$ = average ionic and electronic transference numbers in the slag ($\bar{t}_i + \bar{t}_e = 1$) and

$$\bar{t}_i = \sigma_i/\sigma_T \text{ and } \bar{t}_e = \sigma_e/\sigma_T \tag{6}$$

where σ_i, σ_e, σ_T, = ionic, electronic and total conductivity of the slag ($\sigma_T = \sigma_i + \sigma_e$), and

$$\sigma_i = \ell/\rho_i A, \quad \sigma_e = \ell/\rho_e A \tag{7}$$

where ℓ, A = slag thickness and cross-sectional area, respectively.

The relative polarization factor, r*, is a measure of the ratio of how the total current partitions between ionic and electronic modes of transfer in a <u>real</u> system where ion blocking or polarization occurs at the electrodes (I_i/I_e) to how the current would partition in an <u>ideal</u> system where the electrodes are completely reversible ($\bar{t}_i/\bar{t}_e$). r* is not an unbounded function. For the system under consideration:

$$0 \leq r^* < 1 \tag{8}$$

When r* = 0, the electrodes are totally blocking and the slag is polarized to the maximum extent ($I_i = 0$). When $r^* \rightarrow 1$, the electrodes become non-blocking and polarization (and concentration gradients) in the slag approaches zero.

If equations (4) thru (7) are substituted into equations (1) thru (3), one obtains, upon rearrangement, expressions for the dependence of the ratio of oxygen partial pressures at the anode to that at the cathode resulting from the passage of a given current I_x (or current density, J_x) or an applied voltage, E_x.

$$\frac{P_{O_2}^{A}}{P_{O_2}^{C}} = \exp \left| \frac{4F\, J_x\, \ell(1-r^*)}{RT\, \sigma_T\, (\bar{t}_i\, r^* + \bar{t}_e)} \right| \tag{9}$$

and

$$\frac{P_{O_2}^{A}}{P_{O_2}^{C}} = \exp \left| \frac{4F\, E_x\, (1-r^*)}{RT} \right| \tag{10}$$

As Cannon suggests, Reference 17, $P_{O_2}^{A}/P_{O_2}^{C}$ is the electrochemical stress (ECS) in the system. The greater this ratio, the more likely it is for the slag to be electrolyzed giving rise to all those reactions that are inimical to long electrode life and to successful operation of MHD channels, i.e., O_2 gas erosion and polarization, metallic iron formation, and oxidation-reduction of electrodes. In agreement with Cannon, et al's model, equations (9) and (10) show that the ECS varies exponentially with current density, thickness of the slag layer and with the total electrical resistivity of the slag ($\rho_T = 1/\sigma_T$). More significantly, however, these equations also relate the ECS to the transference numbers--, $\bar{t}_i$ and $\bar{t}_e$,-- of the slag and to the relative polarization of the slag, r*. It can be seen by inspection of equation (9) that increasing the electronic transference number and/or increasing r* (i.e., reducing polarization) will serve to minimize the ECS.

Figure 27 shows the interrelationship between ECS and the relative polarization factor, r*. Calculations were made at 1700 K for a typical Eastern (σ_T = 1.1 x 10^{-1} $(\Omega\text{-cm})^{14}$ and Western (σ_T = 3.25 x $10^{-2}/\Omega\text{-cm})^{14}$ coal slag for a variety of ionic transference numbers, $\bar{t}_i$, assuming a 1mm thick slag layer and a current density, J_x, of 1 amp/cm^2. Superimposed on this figure are horizontal lines which represent the values of ECS at which the FeO and SiO_2 components of the slag will decompose to their constituent elements. The curves in Figure 27 illustrate how sensitive ECS is to slag conductivity. For example, although σ_T (Eastern) is a little over three times greater than σ_T (Western), the ECS rises from $\approx 10^{18}$ for the Eastern slag to $\approx 10^{56}$ for the Western slag when t_i = .4. Similar increases in slag thickness and/or current density will also

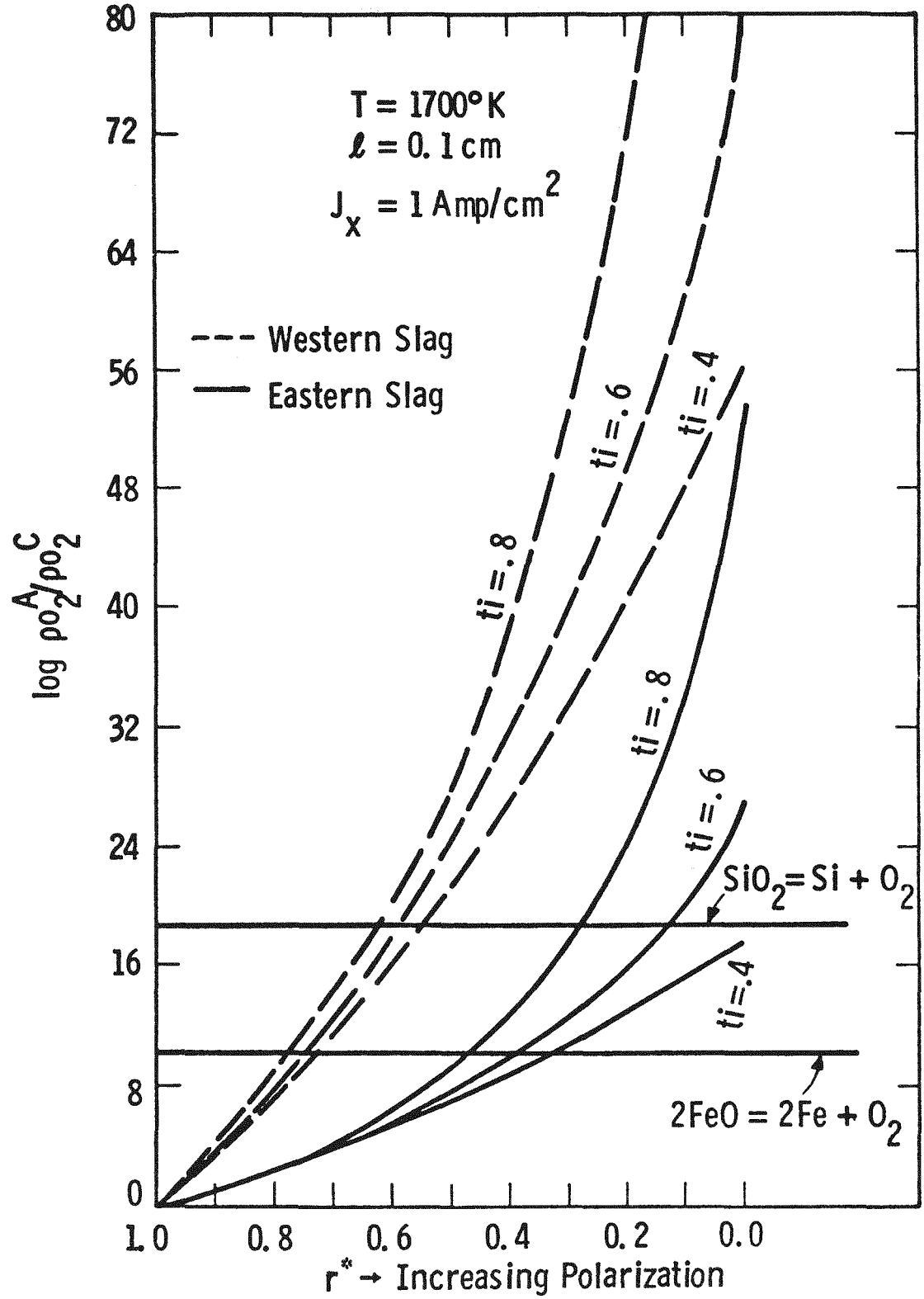

Figure 27. The Calculated Dependence of ECS (Po_2^A/Po_2^C) on Relative Polarization, r*, for Eastern and Western USA Coal Slags at 1700 K

be manifested by an exponential increase in ECS. As might be expected, the more ionic the slag, the greater the ECS. However, $\bar{t}_{i\uparrow}$ is an important term only when the slag is very highly polarized (i.e., $r^* \rightarrow 0$). When r^*, the relative polarization factor exceeds about 0.6, the effect of transference number on ECS becomes relatively small. ECS exhibits an extremely strong dependence on r^*. As can be seen in Figure 27 as the amount of slag polarization decreases, the ECS becomes smaller, until at values of r^* between $\approx$0.35 - 0.48 for the Eastern slag and $\approx$0.73 - 0.78 for the Western slag, these curves fall below the horizontal line for the decomposition of FeO. At these points, electrolysis reactions can no longer occur and the system will transfer current in a stable manner. Slag depolarization is the basic reason as to why the ionically conducting $ZrO_2(Y)$ electrodes were so effective in preventing slag electrolysis in the experiments described earlier. $ZrO_2(Y)$ is reversible to the moving O^{-2} ion in the slag so that little or no concentration gradient can build up at the cathode/slag or anode/slag interface. Without such concentration gradients, polarization will be minimal ($r^* \rightarrow 1$) and electrolysis is impossible. Any electrode material that is non-blocking or reversible to the moving ion in the slag will perform similarly.

The model presented above can be readily applied[/] to the physical boundary conditions existent in an MHD channel. In a channel there are two separate electrochemical cells operating in series--these can be presented as:

$$\text{cathode (-)} \;\Big|\text{slag}\Big|\; (P_{O_2}^{\text{plasma}} = 10^{-3}\ \text{atm}) \qquad \text{(I)}$$

$$(P_{O_2}^{\text{plasma}} = 10^{-3}\ \text{atm}) \;\Big|\text{slag}\Big|\; \text{anode (+)} \qquad \text{(II)}$$

Here, the electronically conducting plasma itself will function as an electrode supplying or accepting O^{-2} ions and electrons to or from the slag. In cell (I), the plasma functions as an anode while in cell (II), the plasma is the cathode.

/This would require the numerical solution of equation (9) taking into account the thermal gradients across the slag layer and the variation of slag properties with temperature.

Because of high temperatures at the plasma/slag interfaces (>1800 K) it is reasonable to assume that the plasma will function as a reversible electrode. Hence the P_{O_2} in the slag at the plasma interfaces will be equivalent to that in the plasma, i.e., 10^{-3} atm. It is important to note that, theoretically, electrolysis (i.e. $O_2\uparrow$) will occur in the anode slag when P_{O_2} at the slag/anode interface equals 1 atm., while electrolysis (Fe^0 formation) at the slag/cathode interface will require that P_{O_2} be $\approx 10^{-10}$ atm, at about 1700 K. Thus in a real channel there is an asymmetry in ECS, and in general, the ECS needed for electrolysis will be lower at the anode than at the cathode, presuming all other factors such as σ_T, ℓ, and T are the same at both walls. In the above example, the ECS is 10^3 and 10^7 in the anode and cathode slags, respectively. The current density needed to electrolyze the slag, J_{xe}, at each wall can be calculated as a function of temperature and for a range of values[/] of relative polarization factor, r* through the use of equation (9). Results are shown in Figure 28 for an Eastern slag assuming ℓ = .1 cm, t_i = .6 and $\sigma_T = 2.4 \times 10^5 \exp[-2.5\times10^{-4}/T]$ (Reference 14). It may be readily seen that for comparable r* factors, J_{xe}, is considerably less at the anode than at the cathode. For real channel operation (where the current is constant across each slag layer), the above result implies that slag electrolysis (O_2 gas production) will occur at the anode wall before slag decomposition and metal formation occurs at the cathode wall. Since oxygen bubbles can very effectively block passage of diffuse current, it follows simply from polarization arguments that arcing phenomena will be more severe at the anode than at the cathode. Other factors which tend to promote anode slag decomposition and arcing are the decrease in σ_T and the increase in t_i in the segregated slag at the anode interface due to preferential diffusion of cations away from this zone. As shown in Figure 28, the most effective way of increasing J_{xe} and hence of reducing the chance for anode arc discharge is to depolarize the slag through the use of highly reversible anode electrode materials; the best examples being ZrO_2 or HfO_2 based ceramics. Another less satisfactory method of depolarization is to use a sacrificial anode material such as iron. The concept of pumping selected ions into the slag at the anode/slag interface to depolarize the slag or increase its electrical

[/] r* = 0, 0.3, 0.9 correspond to conditions in the slag of total polarization, partial polarization and nearly total depolarization, respectively.

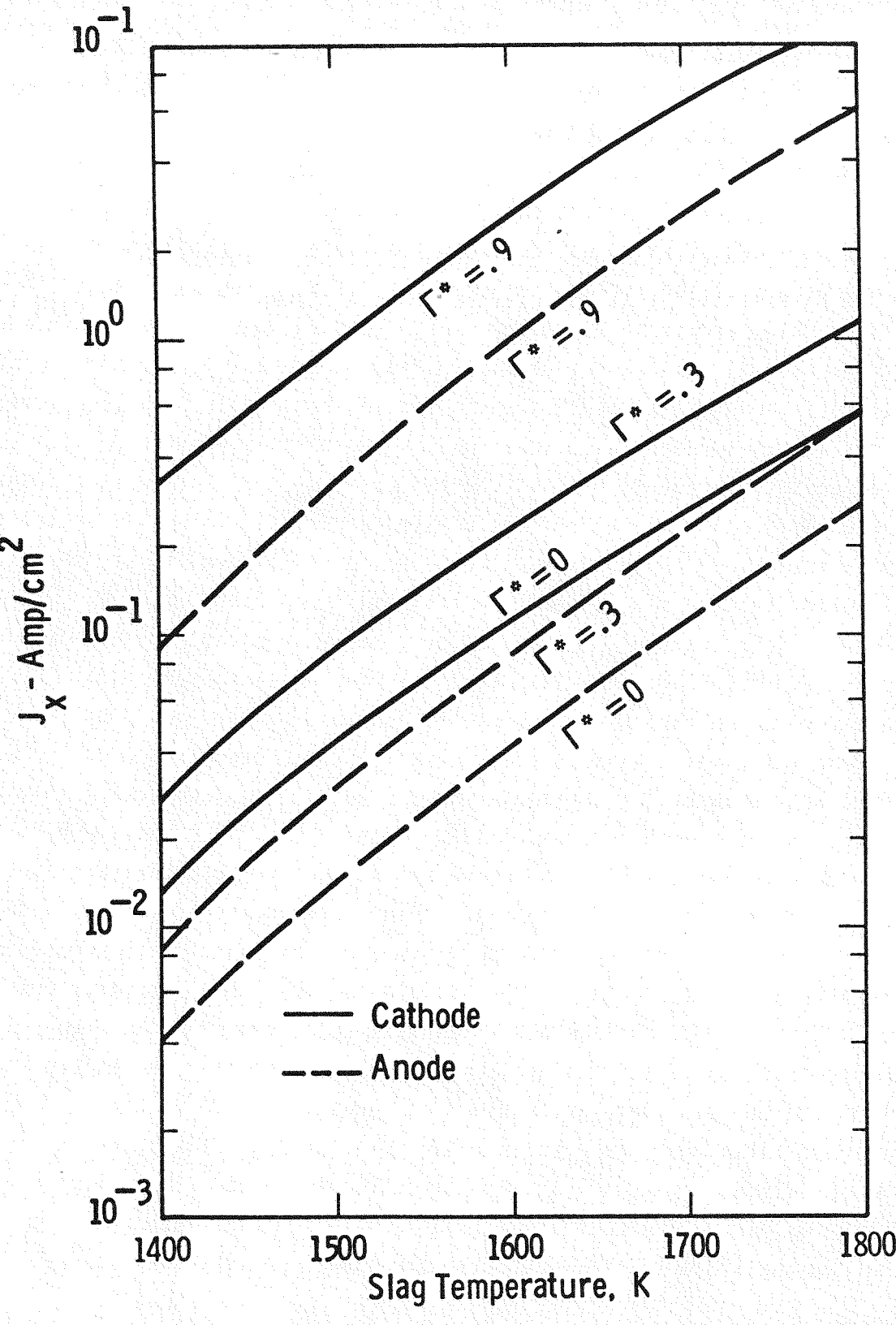

Figure 28. Calculated Temperature Dependence of Current Density, J_x, to Electrolyze a 1 mm Layer of Eastern Slag on Anode and Cathode Walls of a Channel for Various Values of Relative Polarization, r*

conductivity is possible on a laboratory scale but would be difficult in practice for large MHD generators.

Implications of the Electrochemical Model

The principal implication of this study is that in order to insure satisfactory performance of MHD channels and long electrode life under semi-hot wall slagging conditions, it is essential that the electrochemical stress, ECS ($P_{O_2}^{A}/P_{O_2}^{C}$), across the slag layer be minimized to such an extent that slag electrolysis reactions will not occur. From equation (9) it is clear that a reduction in ECS can be achieved in only two practical ways. These include: 1) modifying the properties of the slag to minimize t_i and ℓ, and to maximize σ_T, and 2) modifying the properties of the electrodes to minimize the polarization in the slag (i.e., maximize r*).

The first approach is potentially an extremely effective way of reducing electrochemical reactions. For example, if it were possible through the use of additives to make the slag completely electronic, $t_e = 1$, there would be no electro-chemical effects and the only criteria for electrode material selection would simply be intrinsic corrosion resistance. Realistically, it is improbable that coal slags could be doped to obtain a value of t_e greater than 0.8. However, achieving even this goal should drastically improve corrosion resistance of electrode materials. Marchant (Reference 14), and Cadoff, (Reference 19), show that increasing the Fe_2O_3 content of slags can significantly reduce electrode corrosion. Of course, raising the iron content in slags increases the total electrical conductivity as well as t_e, so that in this case two factors are operating in tandem to reduce the ECS. Additives such as K which are known to increase σ_T, at least for Western coal slags (Reference 20), have also been experimentally shown to decrease electrode corrosion (Reference 21). An avenue of approach that could prove fruitful is to find effective additives that will minimize slag viscosity so as to reduce slag layer thickness, ℓ. If this additive were cost effective and if it could also reduce t_i and increase σ_T, major improvements in electrode performance could be envisioned.

The second approach involves selection of electrode materials with electrical properties compatible with that of the slag. This implies that the electrode be completely reversible or non-blocking ($r^* \rightarrow 1$) to the principal conducting ion in the slag. Only in this way can high polarization voltages and electrolysis be prevented. New theoretical studies, reported herein suggest that for the ideal electrode, both t_3, t_i and the conducting ion species be identical with that of the slag. If O^{-2} is the predominant diffusing ion, then metals will, in general, be poor choices as electrode materials. At the cathode all metals are blocking to O^{-2} and, hence, will give rise to electrolysis reactions. At the anode, noble metals are nearly completely blocking ($r^* \rightarrow 0$). This will result in O_2 gas evolution with accompanying arc discharges. Reactive metal anodes such as iron are completely nonblocking to O^{-2} ion and can depolarize the anode slag. Unfortunately, reactive metal anodes corrode so rapidly (i.e., $Fe + O^{-2} \longrightarrow FeO = 2e^-$) that they are of little practical use. The above remarks also apply to the use of non-oxide ceramic electrodes. Only oxide materials and more particularly, only those oxides whose oxygen ions transference number and electronic transfer number closely matches that of the slag should be seriously considered as electrode materials.

The same general criteria for electrode material selection as discussed above would apply if investigations demonstrate that another ion, for example, K^+, is the most mobile current carrying species in high potassium slags. In this case, one must select electrodes on the basis of reversibility with respect to K^+ ions. Equation (9) would still be applicable, provided P_K is inserted for P_{O_2}.

Our experiments have shown that $ZrO_2(Y)$ or $ZrO_2(Ca)$ and perhaps by extrapolation HfO_2, are serious candidate materials, especially for use as hot slagging anode wall electrodes with Montana Rosebud slag. They are less suitable for use as cathode wall materials since they tend to blacken and electrolyze at high current densities.

1.2.2 Anode Arc Erosion Studies

If either the slag layer or plasma boundary layer is electrically resistive, current will no longer be able to pass in the normal or 'diffuse' mode and instead will be carried by 'arc columns' which are local regions of high current density

capable of releasing large amounts of heat. The localized heating of electrode surfaces can produce excessive loss of material through vaporization, melting, erosion, oxidation and chemical/ electrochemical reactions. This resultant loss of material, in turn, will limit the lifetime of electrodes. The loss of material due to arc related degradation mechanisms (which will be labeled under the general term 'arc erosion' for ease of discussion) is much more significant for anodes than for cathodes. This fact is attributed to cathode erosion being related to only thermal effects, i.e., vaporization and melting in metals, while anode erosion is due to a combination of thermal effects and chemical (or electrochemical attack (References 23,24). The presence of a slag layer reduces the cathode thermal effects and promotes anode chemical/electrochemical reactions (Reference 24, 25). Thus, the lifetime of coal fired, slagging MHD generators operating under arcing conditions is limited by anode materials. There is need of an experimental arrangement to systematically evaluate various candidate materials over wide range of test conditions. Since this would require a large number of individual tests it would be desirable to use a laboratory test that would be as simple as possible and would have a short turnaround time. The following section describes the test apparatus that fulfills these requirements, along with results obtained to date.

Description of Anode Arc Erosion Apparatus

A commercial plasma needle jet welder having the circuit diagram shown in Figure 29, was utilized to generate an arc discharge. In the test set-up a plasma discharge was initiated between the two internal sections of the cathode shown in Figure 29 and then transferred to the anode test piece by applying the impressed voltage between the internal cathode electrode and the anode. Argon was used as shielding and focusing gas.

The anode test samples, having a 2.5 cm O.D. and 1.8 cm height, are rotated under the arc jet in order to simulate arc mobility. Most of the back side of the sample is milled out to reduce thermal mass. The measurement of temperature is accomplished by insertion of E-type thermocouples to a position .010" distant from the anode surface exposed to the plasma. Sample temperature is controlled by varying the amount of air cooling directed against the sample. Temperatures of 200-600^{o}C are easily obtained using this technique.

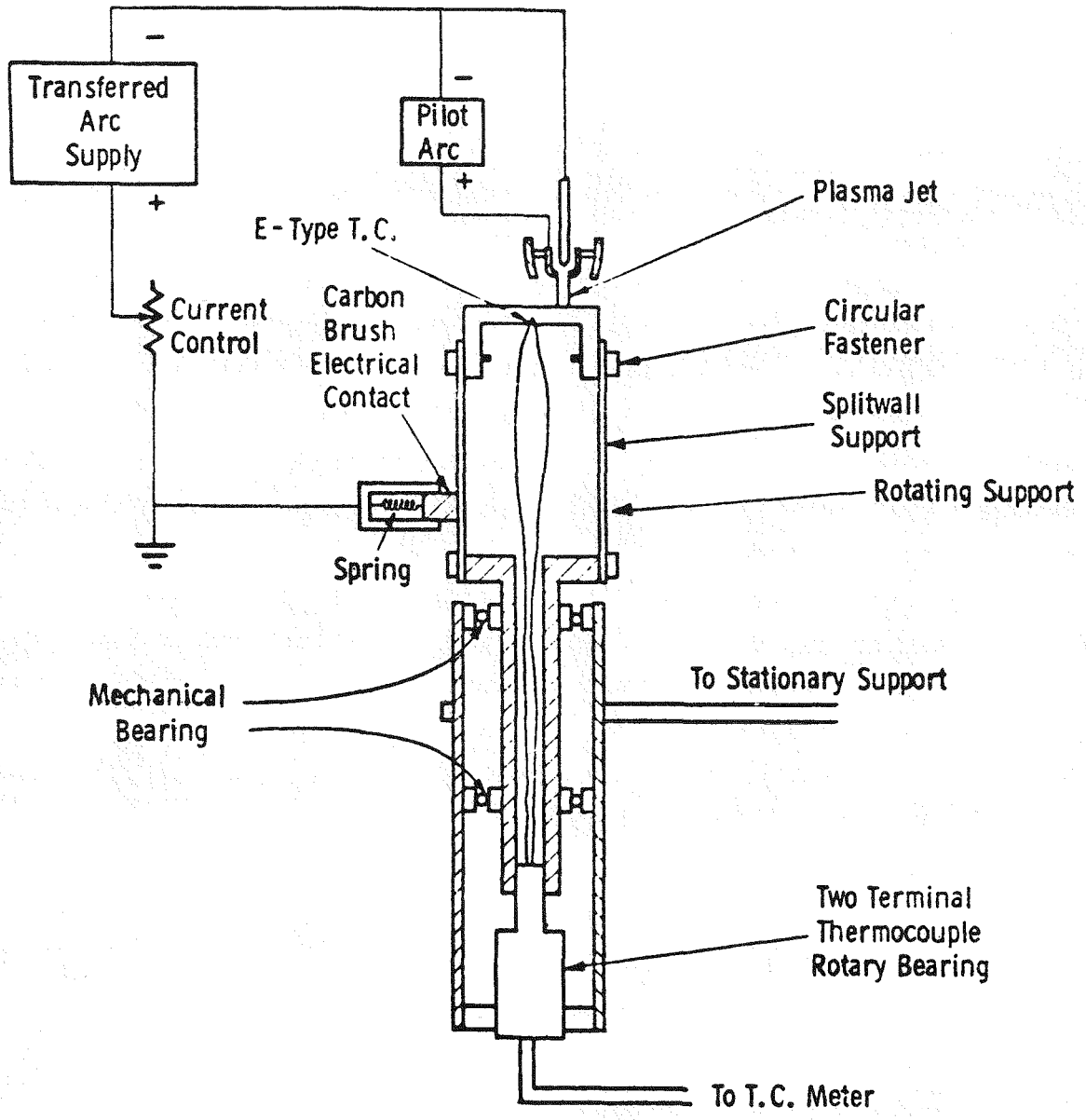

Figure 29. Schematic of Anode Arc Test Using Plasma Needle Arc Welder

Several methods were tried to produce a slag layer; the most satisfactory results were obtained using a thick water slurry of the slag-seed mixture which was applied by brushing. A slag-seed composition 2/3 slag and 1/3 seed by weight was chosen as a reasonable approximation of the composition found in MHD channels. Two coal fly ashes were used; Rosebud which was obtained from a Montana power plant and an Eastern fly ash used by AVCO in the Mark VI and obtained from the New Hampshire power plant. Chemical analysis of these fly ashes are found elsewhere (References 24,26).

Tests to date have been conducted using 5.5 amperes; this current is in the range observed for arcs in MHD channels (Reference 23). At this loading the voltage drop between the cathode and anode is generally 20 to 30 volts. The rotational speed of one RPM, selected for these, tests simulated an arc velocity of approximately 5 cm/min.

Some general observations can be made as to arcing characteristics. First, as the temperature of the anode substrate increased from the order of 200°C to temperatures of the order of 450°C, the arc became much less constricted. Secondly, the discharge would frequently depart from its normal trajectory, i.e., perpendicular to the anode, and maintain preferred landing sites on the anode until the gradual rotation of the samples took the favored anode landing spot out of range of the discharge. This tendency for the arc to favor certain spots increases with substrate temperature and test duration. Finally, high speed motion pictures showed that the slag near the arc had been brought to the boiling point.

Materials Evaluation

The erosion of various materials by arcs is very dependent upon the local temperatures near the arc root. This temperature, in turn, is dependent upon the amount of heat available from the arc, the residence time of the arc and material properties. The time required to bring a localized anode area under an anode arc spot of constant power to a given temperature is proportional to $K\rho C$ where K is the anode thermal conductivity, ρ is the anode density and C is the anode specific heat. Since the usual MHD arcs are mobile, the factor $K\rho C$

can be considered a figure of merit. If $K\rho C$ is large enough and the arc dwell time short enough, little or no arc erosion will be experienced. To minimize temperature excursions and to most fairly compare candidate materials, tests are conducted on thin sheets of test materials brazed to copper. In this configuration the thermal properties of the composite approach that of copper.

The objective of tests to date has been to establish whether this test setup can truely simulate arc damage phenomena found in MHD channels. These tests have been restricted to copper and platinum--as these materials have been subjects of a number of previous anode tests (References 23, 25, 27, 29). The arc erosion of these materials has been studied as a function of anode surface temperature and slag layer chemistry. The amount of erosion is measured by the weight change before and after testing (corrected for oxidation). Erosion rates are calculated on the basis of weight loss per coulomb of current passed. Tests were generally two hours duration. Duplicate samples were also run for metallographic and SEM/EDAX examination.

The erosion rates of copper and platinum with various slag-K_2CO_3 coatings are shown as a function of temperature in Figure 30. The erosion rate versus substrate temperature curves all display minimums in the 250-400°C range. This type of behavior usually suggests a change in erosion mechanism with temperature. At temperatures below the minimum, increased erosion rates could be due to electrolytic corrosion due, in turn, to the presence of high concentrations of water from the slag-seed slurry or to the more constricted nature of the arc at low temperatures. Incomplete results using dry slag-seed mixtures suggest that much of the increased erosion is due to the former. Heywood and Womack (Reference 23) reported enhanced erosion was experienced at low temperatures due to condensation of water and electrolytic corrosion of aqueous deposits.

At temperatures above 300°C erosion rates also increase rapidly. This increase could be due to increased chemical or electrochemical attack or to changes in the thermal effects produced by the arc with changing substrate temperature. It is apparent that some of these erosion losses are due to the tendency of the arc to 'hang up' on certain surface sites at higher temperatures. This tendency would produce higher local temperatures, more melting and vaporization. Optical

microscopy and SEM examination indicate that the number of arc damage sites decreases with increasing temperature but that the loss of material per damage site increases significantly with temperature. The localized hot spots appear as molten drops on substrate surfaces. Weight losses can occur as vaporization losses and/or as molten metal droplet entrainment into the slag layer. Bates (Reference 30) noted platinum droplets in the slag layer adjacent to the platinum anodes in the AVCO 250 hour test.

Figure 30 also indicates that copper anode erosion rates are higher than corresponding erosion rates for platinum and that erosion rates are higher for the Eastern New Hampshire slag as compared to the Western Rosebud slag. The former result was anticipated; however, it was expected that platinum would have an erosion rate at least an order of magnitude lower than copper.

Figure 31 compares the anode erosion rates in this study with those obtained in various MHD generators and in the Westinghouse Electrode Systems Test Facility on copper and platinum. AVCO data (Reference 24) for slag-K_2CO_3 operation shows that platinum erosion rates are at least an order of magnitude lower than copper. Earlier British studies (Reference 23) also show that the erosion rate for platinum is well over two orders of magnitude lower than copper. The anode arc test erosion rates for copper are lower by a factor of about three than AVCO's results, while the platinum arc test erosion rates are higher than Mark VI test results. Clearly this is an area that needs to be sorted out before this test can be used in a quantitative fashion. The low temperature electrolytic effects need to be assessed along with investigation of the effect of arc voltage and current and arc velocity on erosion rates. Also it must be recognized that for the same heat input the temperature rise for platinum is approximately 2.5 times that of copper. While thin sheets of platinum have been used to minimize the differences in thermal properties, further attention will be given to sample thermal design.

The effect of using seed in the sulfate form on the erosion rate of platinum is shown in Figure 32. The use of K_2SO_4 increases erosion by a factor of at least two when compared to the use of K_2CO_3. Again, Figure 31 shows that previous

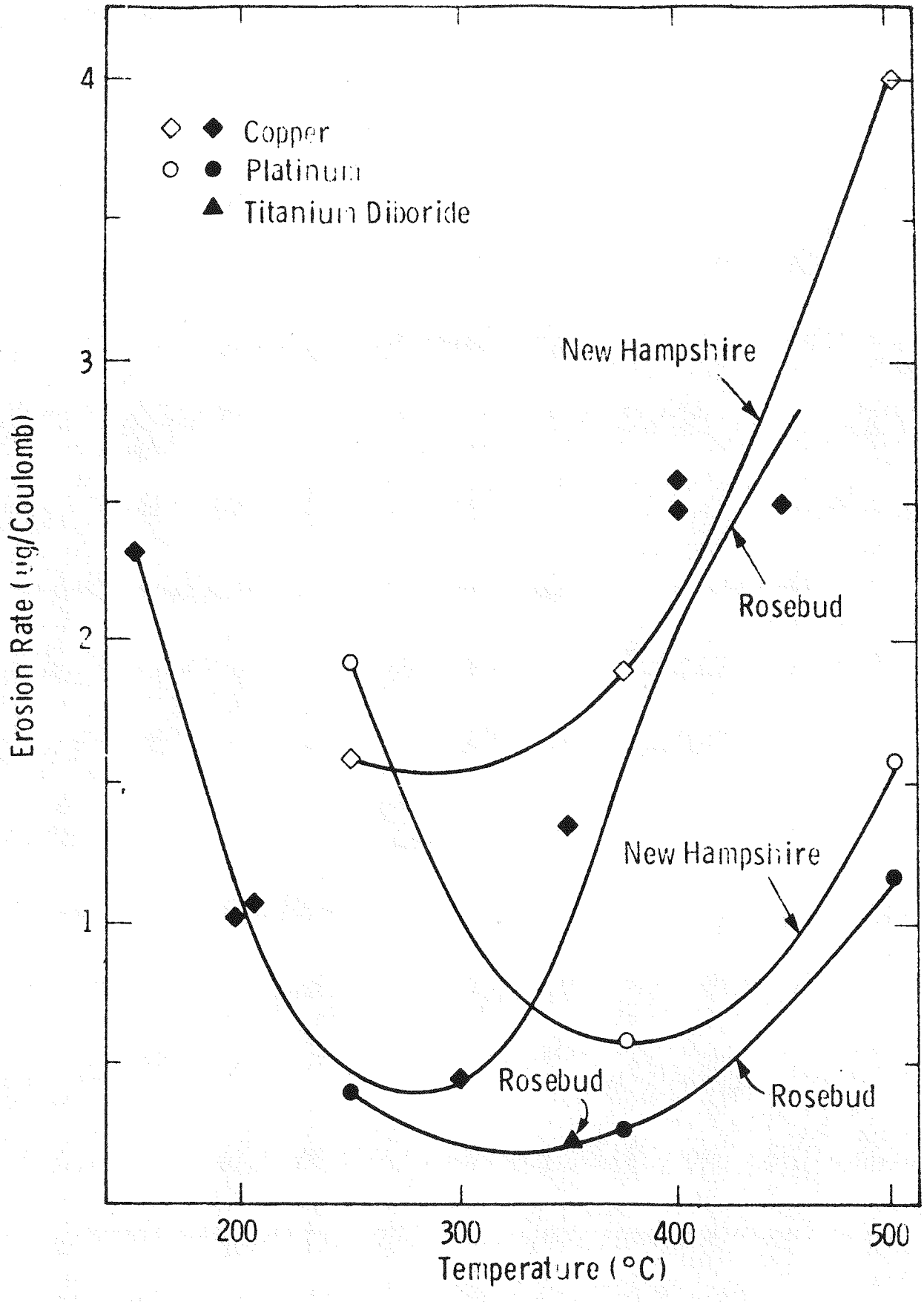

Figure 30. Erosion Rates of Coal Ash-K_2CO_3 Coated Anodes Versus Temperature

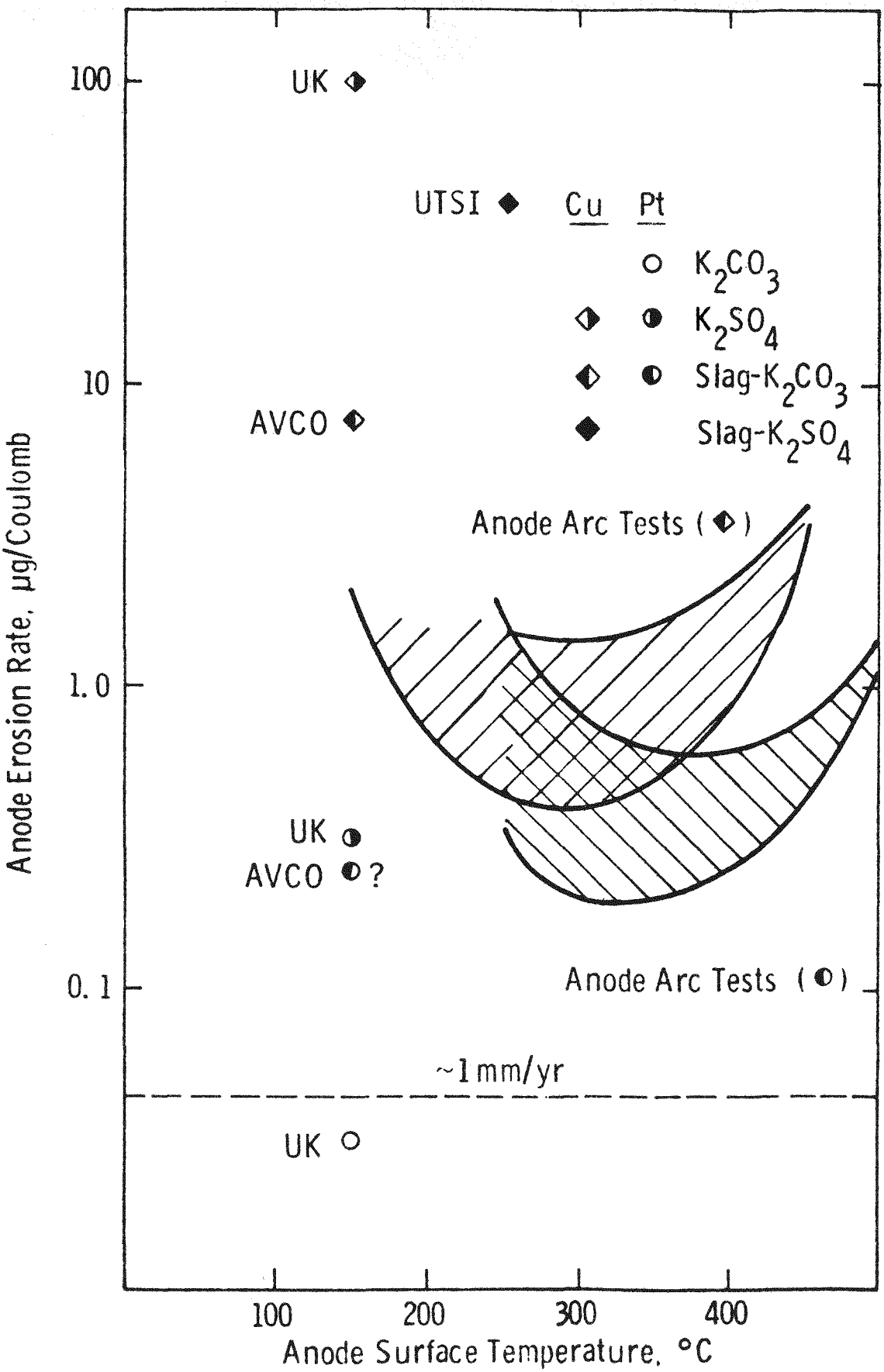

Figure 31. Comparison of Anode Erosion Rates From Laboratory and MHD Generator Tests

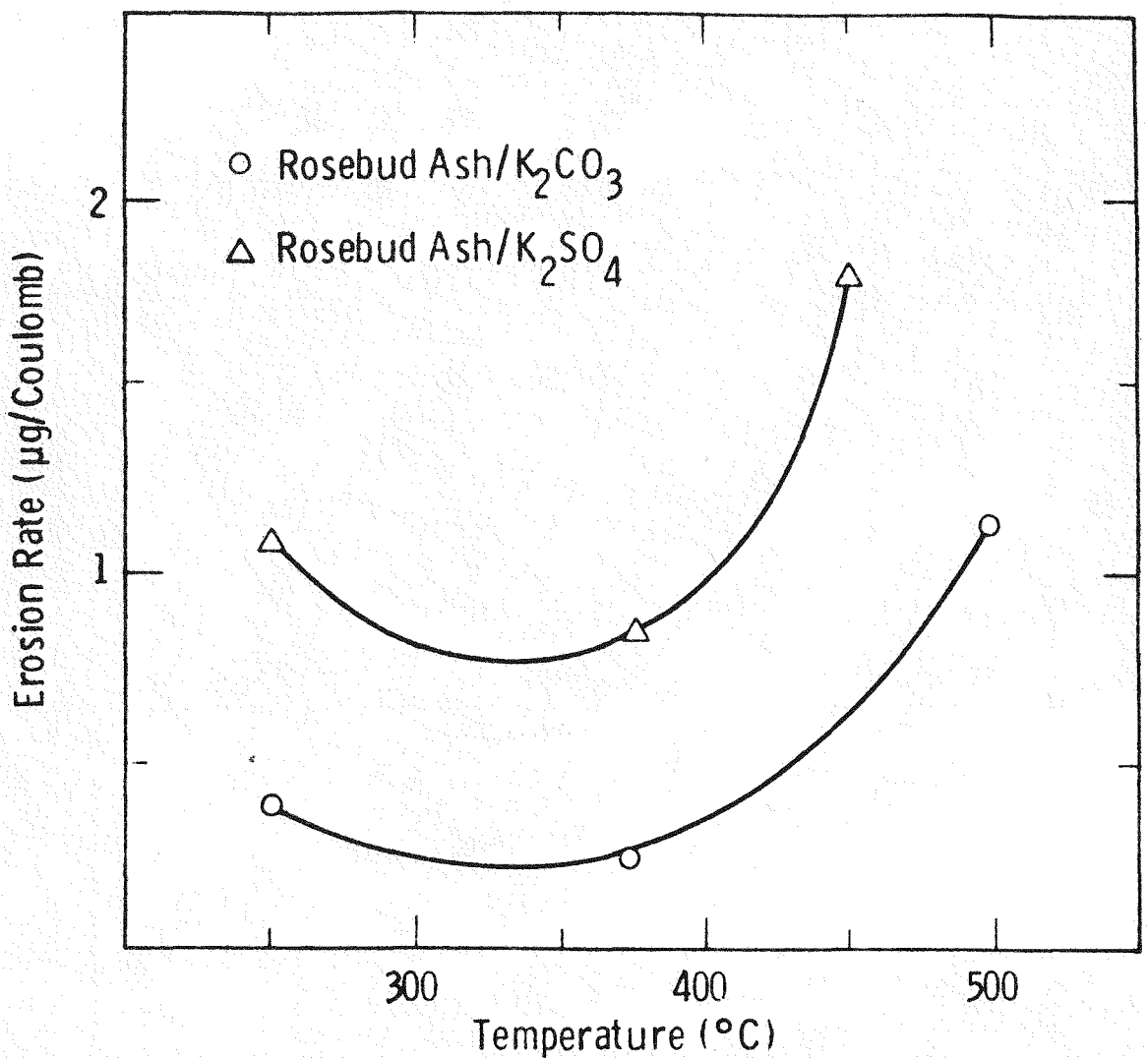

Figure 32. Erosion Rates of Platinum Anodes Coated with K_2CO_3 - and K_2SO_4-Rosebud Ash Mixtures

tests, (Reference 19, 29) would suggest that erosion rates would increase by an order of magnitude with use of K_2SO_4.

Comparison of copper from the arc test with copper anodes (Reference 28) run in WESTF show a similar visual appearance (see Figure 33). SEM examination of these samples indicates other similarities. In both cases, copper has been oxidized and subsequently dissolved into the slag near the anode surface. There are also spheres or droplets of copper metal in both arc test and WESTF anode samples (see Figure 34). These droplets are similar to platinum droplets identified by Bates (Reference 30). There is a difference in slag compositions between laboratory and test rig samples; the arc test samples show considerable loss of the volatile species (such as K and Si) in the slag. This is reasonable because the arc test does not have an atmosphere containing these species, while the MHD channel environment does.

The laboratory anode arc erosion studies are still at a stage where all the effects of experimental variables have not been assessed, so very little evaluation of candidate materials for use in the cold wall mode has been carried out. However, it is noteworthy to point out that a chemical vapor deposited coating of TiB_2 on copper showed an erosion rate very close to that of platinum on copper (see Figure 30). It will be the object of future tests to identify potential materials (most probably used as thin coatings on copper) that withstand the severe stresses created by anode arcs.

2.0 WBS 1.2 - ENGINEERING TESTS

2.1 WBS 1.2.1 - Test Engineering

2.1.1 Development Requirements

Preliminary test specifications are issued to initiate design activity on the channel for each test. Materials development/procurement and electrode systems development activities are initiated based on the Preliminary Test Specification. Final Test Specifications are issued after completion of all development activities and provide the basis for detail design of the channel and WESTF testing.

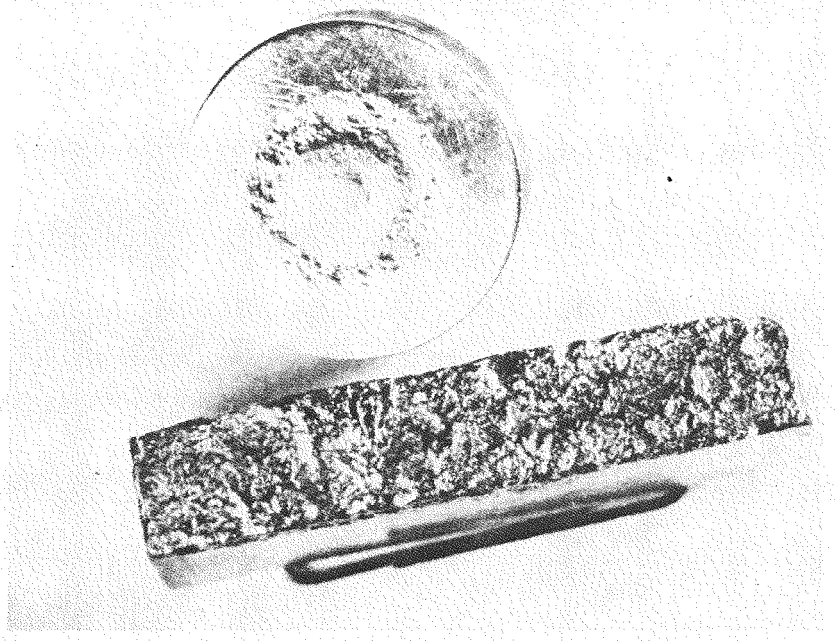

Figure 33. Comparison of Copper Anode Arc Sample (Top) and Copper Anode Run in WESTF (Bottom) 1-3/2X

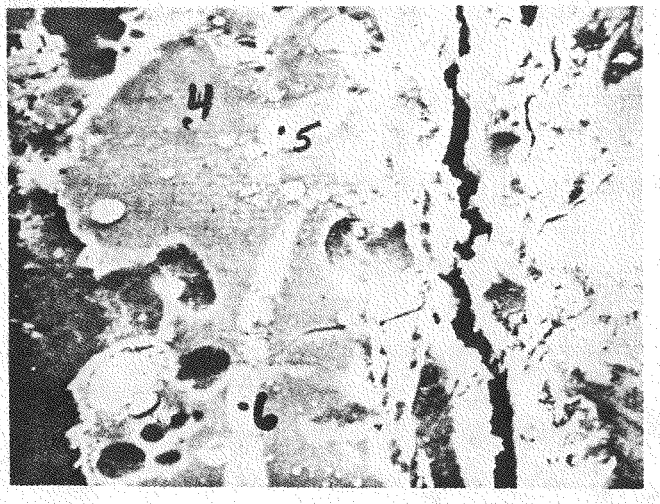

930X

(A)

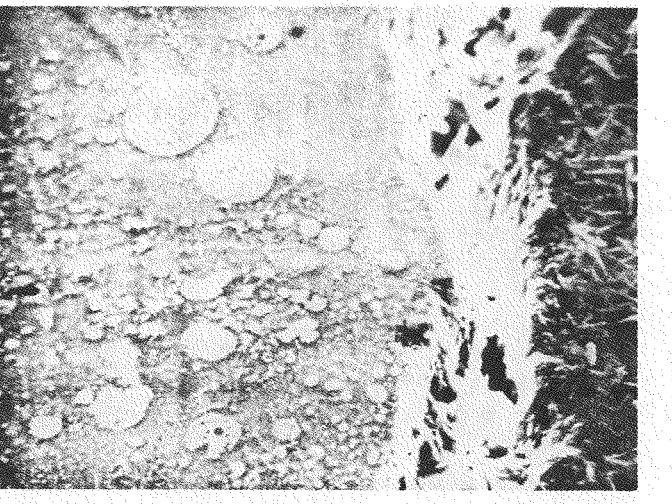

1000X

(B)

Figure 34. Comparison of Microstructure of Slag/Copper from Anode Arc Test (A) and WESTF Anode (B). Copper is on right and Slag is on the Left. In both (A) and (B) Spherical Particles in Slag are Molten Copper Globules.

During this quarter, an addendum for Run 4 of WESTF Test 40 (copper electrodes), revision 1 to the WESTF Test 41 (AVCO electrodes) Final Test Specification, and a revised Preliminary Test Specification for WESTF Test 43 (Pt-Fe Electrodes) were issued. A redesign and rebuild of the major components of the WESTF Test 41 channel is in progress. The reiterative design process was completed for WESTF Test 42 (coupon test) and is continuing on WESTF Test 43.

WESTF Test 40

An addendum for Run 40-4 was issued with the same objective as Run 40-3, i.e., to further investigate the electrical characteristics of the channel and to examine the effect of electrically isolating the exit end of the channel from ground. The difference between the two runs was that the silicone rubber gasket used at the exit end of the channel was eliminated due to a tendency to overheat and was replaced by the original metal/asbestos gasket. The channel for Run 40-4 was isolated from ground by replacing the downstream stainless steel spray flange with a non-conductive Micarta spray flange that was more effective in isolating the channel from ground.

WESTF Test 41

Revision 1 of the Final Test Specification for WESTF Test 41 was issued. The significant items affected by this revision are the following:

- Defining the initial test duration as 15 hours with the option of continuing to 50 hours without interruption.
- Reducing the cathode cooling water flow rate from 150 gph to 30 gph (made possible by modifying the cooling water flow passage).
- Reducing the thickness of the spinel insulation in the duct to limit the slag/spinel interface temperature to 900°C.
- Defining the electrical loading scheme to be used during the test.

Most of these items will be discussed in greater detail in other sections of this report.

The initial run of WESTF Test 41 was terminated after running for almost 14 hours at conditions because of a test section leak. Examination during

disassembly showed: loss of ceramic tiles from the insulating walls and transition section; excessive heating of boron nitride spacers used between the first electrode and the inlet transition section; and subsequent degradation of backing material which resulted in over-heating the G-10 wall and gasket. The surface condition of the electrodes was very good and, although some anode arc damage has been noted, the electrodes will be incorporated in a rebuilt test section.

Some redesign will be employed in rebuilding the test section not only to correct problems associated with Run 1, but to improve upon the overall design and performance of the test section.

- Interlocking ceramic tiles, Harklase refractory MgO, will be used to line the transition sections; MONOFRAX "A" Al_2O_3 tiles will line the insulating walls in the channel, and spinel brick will be relegated to use as a filler in the non-sensitive areas of the insulating walls. Insulating wall design temperatures will be 900°C maximum in the channel and 1600-1650°C maximum in the transition section.
- New G-10 electrode support walls will have to be made and hole locations will be shifted so that, instead of an ineffectively cooled 0.2 in. thick spacer on each end, a 0.4 in. water cooled spacer will be employed at the exit end of the walls. (The spacer is used to make up for differences in the AVCO electrode dimensions and the effective length of the Westinghouse electrode walls). New boron nitride interelectrode insulation will be machined and new tie rods will be prepared.
- The insulating walls will be redesigned. Diagonal heat sinks will be used in the center section and will be better insulated from one another and from the anode and cathode walls. The interlocking ceramic tiles, however, will extend beyond the electrodes (this feature will help hold them in place and provide better insulation). These changes will increase the

channel opening for this test to 1.08 x 2.36 in., so that appropriate adjustments in operating parameters will be made.

Every effort will be made to expeditiously rebuild WESTF Test 41 so that testing with Eastern flyash can be completed before embarking upon the next series of tests that require Montana Rosebud flyash.

WESTF Test 42

WESTF Test 42 is a test of "coupons" of selected zirconia-based materials under super-hot slag/seed conditions. The thermal design of the "coupons" is completely based on information presented in the Preliminary Test Specification. Engineering sketches of component parts for each coupon assembly will be prepared and fabrication activities initiated in parallel with the WESTF Test 41 rebuild. A final test specification will be issued.

WESTF Test 43

WESTF Test 43 is a first test of materials under hot slagging conditions with platinum anodes and iron cathodes. A new definitive preliminary test specification was issued to guide final design activities. Except for some parametric studies, the thermal design of the heat section is complete. Engineering sketches of component parts for this test section will also be prepared following the WESTF Test 41 rebuild. Some consideration will also be given to including the test section calorimeter in this run. After an overall design review, a final test specification will be prepared.

2.1.2 Experiment Design

WESTF Test 41

Insulating Walls

The thermal analysis required for the design of the revised insulating walls for WESTF Test 41 was completed.

A one-dimensional steady state thermal model was used to determine the maximum alumina thickness that would not cause the 900°C maximum surface temperature

specification to be exceeded. Alumina thermal properties used were those supplied by the manufacturer. The heat transfer coefficient reported in Reference 32 for Test 40 was employed in this analysis because the two tests are thermally similar with respect to heat transfer coefficient and because the heat transfer coefficient (0.11 w/cm^2K) appears to be conservatively high when compared to the limited available experimental data. An upper bound heat transfer coefficient is conservative when a maximum surface temperature is specified.

The surface temperature of the insulating wall alumina refractory will conservatively be below the 900°C design specification if its maximum thickness is 0.29 inches.

Transition Section

The thermal analysis necessary for the design of the transition section was completed.

Using the same thermal model as employed for the insulating walls, the maximum thickness of the Harklase magnesia refractory was conservatively computed to be 0.37 inches. This refractory thickness will result in a surface temperature less than the design specification upper limit of 1650°C.

WESTF Tests 42 and 44

WESTF Tests 42 and 44 are tests of "coupons" of selected materials under super hot slag/seed conditions. The primary objective of the tests is to evaluate and compare the behavior of selected materials in a super-hot MHD channel environment in the absence of electrical or magnetic fields. The general conditions are (Reference 33):

Operating Mode	Super Hot
Surface Temperature	1650-1850°C
Fuel Type	No. 2 oil
Ash	Rosebud and seed

Electrode Wall Materials	Selected ZrO_2 and HfO_2 based candidates
Insulator Wall Materials	Selection candidate materials from laboratory tests
Heat Flux	~60 W/cm^2
Current Density	0
Axial Voltage Field	0
Duration	8 hours

Since many different materials are being considered for the coupons, a parametric analysis was performed to minimize the anlysis effort and to allow the geometric sizing to be very straightforward. This analysis provides the dependent parameters (surface temperature, heat flux, nickel mesh, temperature, etc.) as a function of the independent parameters (electrode geometry, coupon thermal conductivity, and plasma mass flow rate) in graphical form.

The following sections present a description of the thermal model followed by the results of the parametric analysis. Specific geometric parameters will be given for the two coupon materials selected to date. Subsequent effort will define the information for programming the mini-computer to provide on-line surface temperatures and heat fluxes and the thermal design parameters for the transition section and insulating walls.

Thermal Model

From the general electrode design on Figure 35 the two dimensional model shown on Figure 36 was developed for the TAP A conduction code. This model employs 35 interior nodes and 43 surface nodes to represent one quarter of the electrode.

The major assumptions in this model are:

1. The heat transfer coefficient between the plasma and the electrode surface is computed from the Dittus-Boelter relationship using air properties from Reference 34. These air properties are extrapolated low temperature properties which are similar to "frozen" plasma

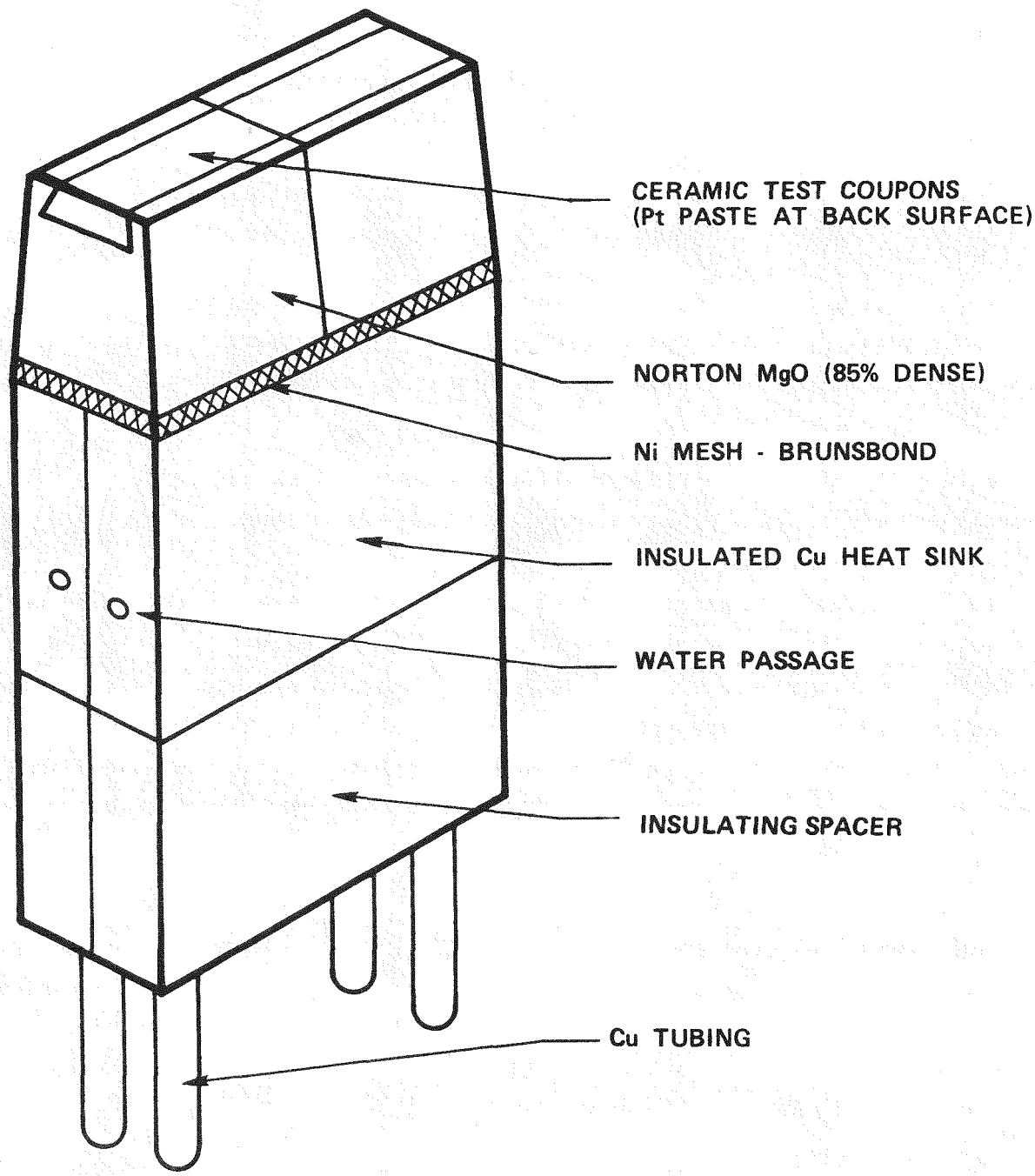

Figure 35. General Coupon Electrode

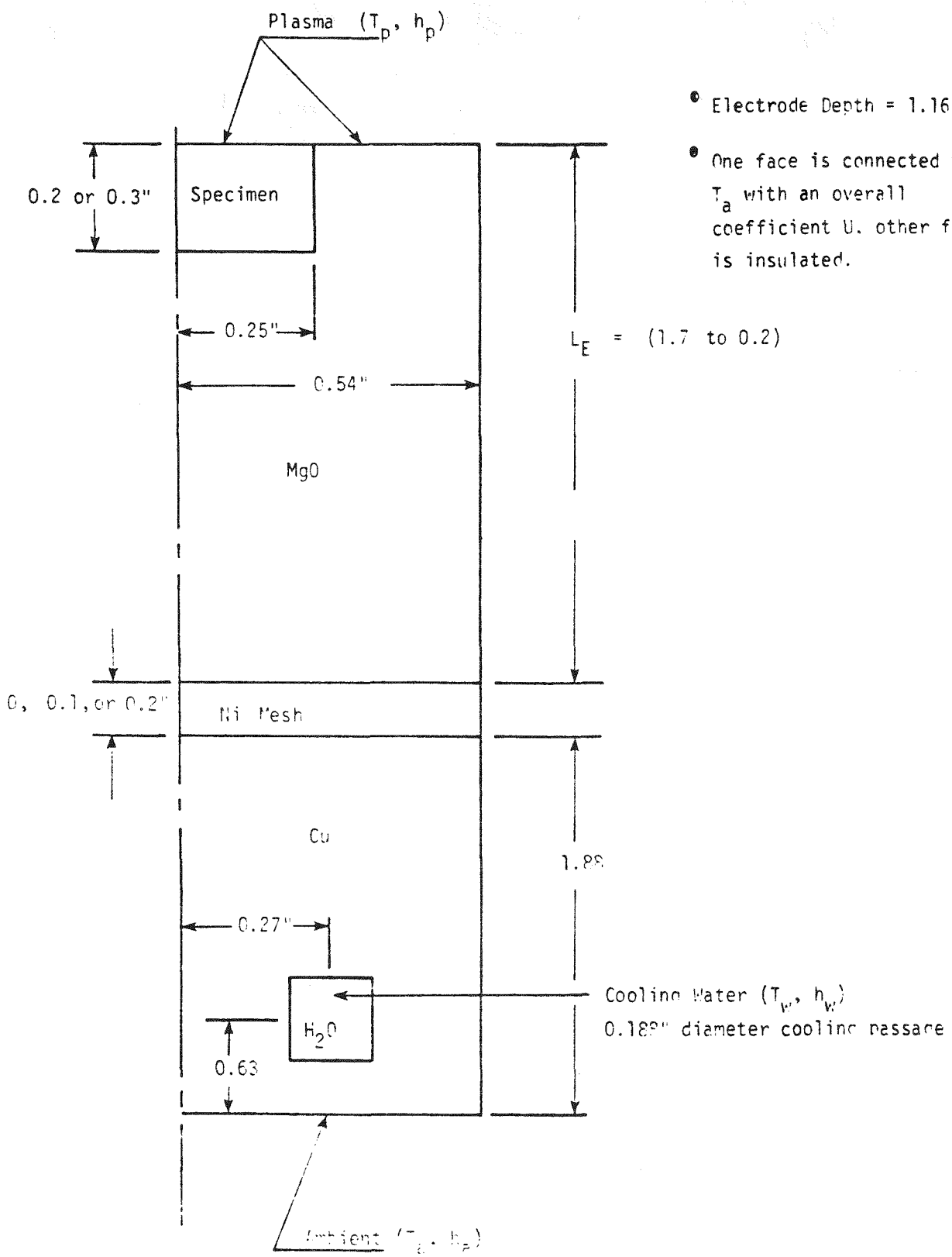

Figure 36. Coupon Electrode Model

properties. Frozen properties are proper because the time for chemical reactions to occur is longer than the boundary layer residence time.

2. Radiation heat transfer from the plasma to the electrode surface is not significant when compared to the convective heat flow.
3. To avoid complex three-dimensional analysis, an approximate relationship for heat losses from the electrode edges was employed.
4. The surface temperatures of other electrodes and insulators exchanging thermal radiation with the electrode in question through the plasma are equal to the electrode temperature. If not equal, their average temperature weighted by the radiant interchange factors are equal.

The net result of assumptions 1, 2, and 3 is a slight over prediction of electrode and insulator temperatures; however, because these effects are systematic, a slight reduction of the plasma temperature or flow rate from the design point will result in the desired temperatures.

Assumption 4 can be relaxed with additional analyses if it proves to be too restrictive.

The input data to the TAP-A electrode model are:

The plasma temperature was taken to be 2670 K. The plasma temperature change from channel entrance to exit is not significant ($\sim$10K).

The heat transfer coefficient was computed from the Dittus-Boelter correlation:

$$N_u = 0.023\ Re^{0.8}\ Pr^{0.4}$$

where

$N_u = h\ D_e/k$

$R_e = \rho V\ D_e/\mu$

$P_r = \mu C_p/k$

$D_e = 4\ A/C$

C = channel wetted perimeter

A = flow area

The plasma properties, which were extrapolated low temperature air properties, are (Reference 34):

$$\mu = 0.00064T^{0.68} \quad \text{(lb/ft hr)}$$

$$k = 0.00016T^{0.73} \quad \text{(Btu/ft hr } ^{o}\text{R)}$$

$$c_p = 0.103T^{0.13} \quad \text{(Btu/lbm } ^{o}\text{R)}$$

$$\rho = 0.019\ P/T \quad \text{(lbm/ft}^3\text{)}$$

where the temperature is in ^{o}R and P is in atmospheres. The resulting heat transfer coefficient as a function of mass flow rate is:

m (kg/s)	h(Btu/hrft^2 ^{o}F)
0.20	110
0.15	90
0.11	70
0.075	50

The water coolant temperature was taken to be 60^{o}F with a nominal flow rate of 12.5 lbm/min $\approx$ 100 cc/sec. The heat transfer coefficient was determined from the Dittus-Boelter relationship with the following properties:

$$\nu = 1.083 \times 10^{-5}\ \text{ft}^2/\text{sec}$$

$$k = 0.345\ \text{Btu/hr ft}^{o}\text{F}$$

$$Pr = 7.02$$

$$d = 0.188\ \text{in.}$$

with a resulting heat transfer coefficient of ~3500 Btu/hr ft^2 ^{o}F.

The heat loss from the edge of the electrode (one face in the two dimensional model) was estimated by considering an overall coefficient to the 60°F water cooled copper backing plate.

$$\frac{1}{U} = \left(\frac{L}{k}\right)_{\text{insulator}} + \left(\frac{L}{k}\right)_{\text{backing insulator}}$$

$$= \frac{0.15}{10} + \frac{0.2}{0.2}$$

$$U = 1.0\ \text{Btu/hr ft}^2\ ^{o}\text{F}$$

The thermal conductivities of the various electrode materials as provided in the Test Specifications (Reference 33) and:

MgO

$$k = (1.49 + 0.0142T)^{-1}$$

Copper

$$k = 220 \text{ Btu/hr ft } ^{o}F$$

Nickel Mesh

Temperature (K)	Thermal Conductivity (W/mK)
250	2.35
341	2.38
352	2.73
443	2.5
500	2.18
537	2.7
611	2.91
626	3.10
652	2.18
758	2.84
830	2.55
1000	2.5

where T is in ^{o}C and k is in $W/cm^{o}C$

Specimen

Thermal conductivities were parametrically varied to be 10, 7.5, 5.0, 4.0, 3.0, 2.0, and 1.0 W/mK.

The geometries assumed for the parametric runs are shown on Table 6 along with the corresponding plasma flow rates. With each of these geometries, the coupon thermal conductivity was varied from 1.0 W/mK to 10.0 W/mK. Cases were not run if the resulting temperatures were outside the range of interest.

Results

Results of the parametric analysis are given in Figures 37 through 40. The run number on these figures is identified on Table 8.

Figure 37 gives the coupon or specimen surface temperature as a function of specimen thermal conductivity, electrode geometry, and plasma flow rate for a 2670 K plasma temperature. Figure 38 gives the temperature at half the thickness

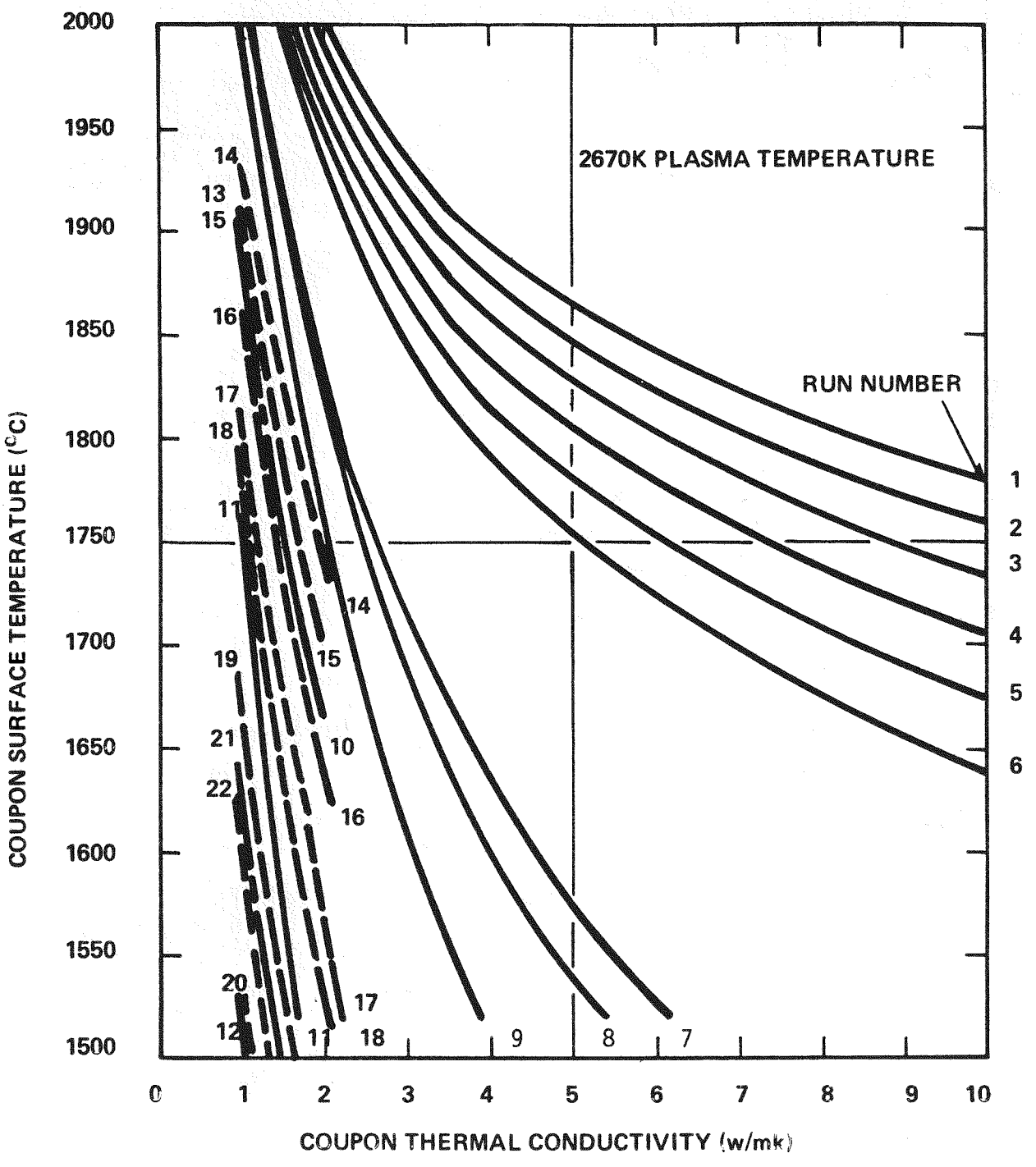

Figure 37. Coupon Surface Temperature

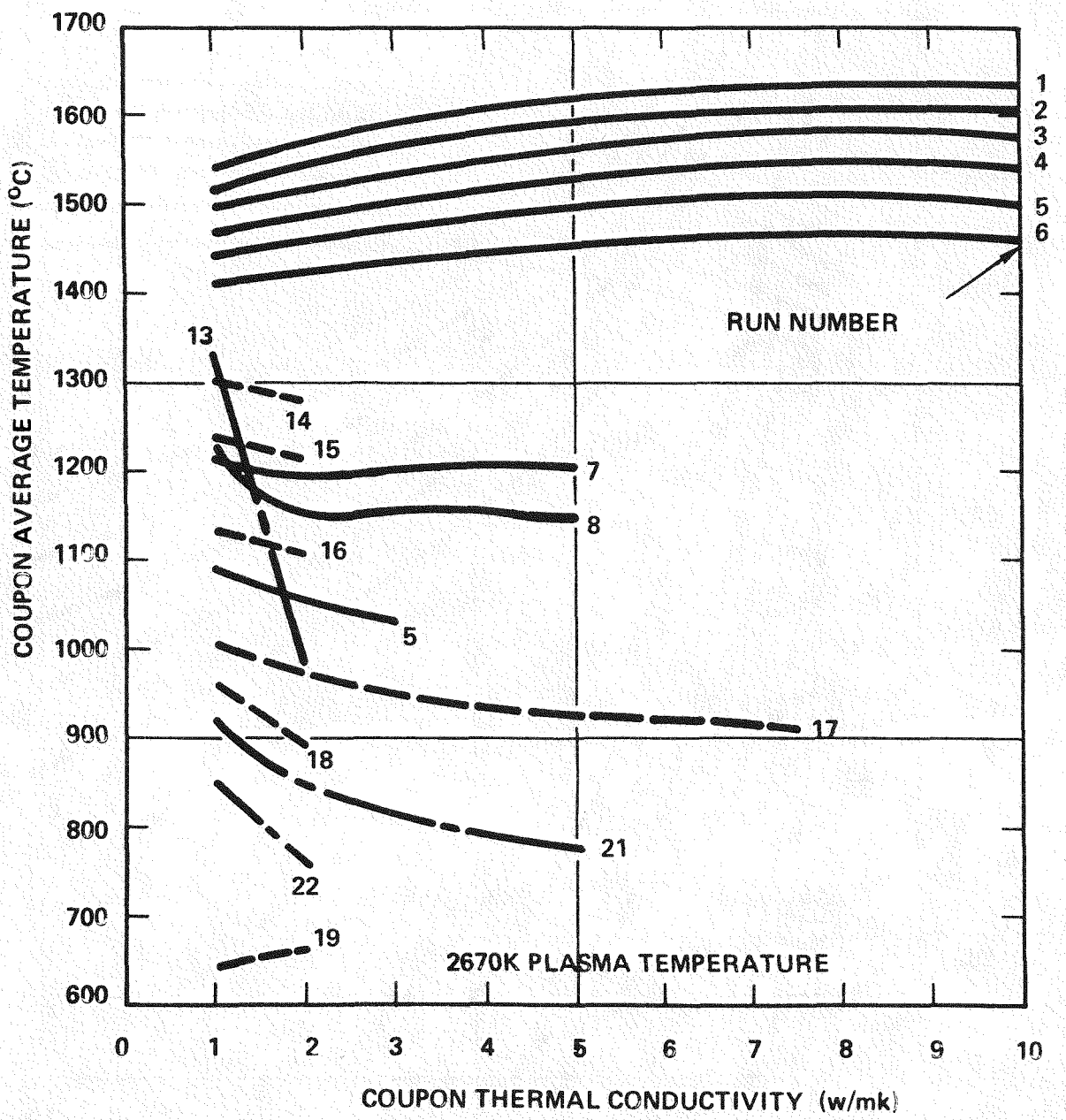

Figure 38. Coupon Average Temperature

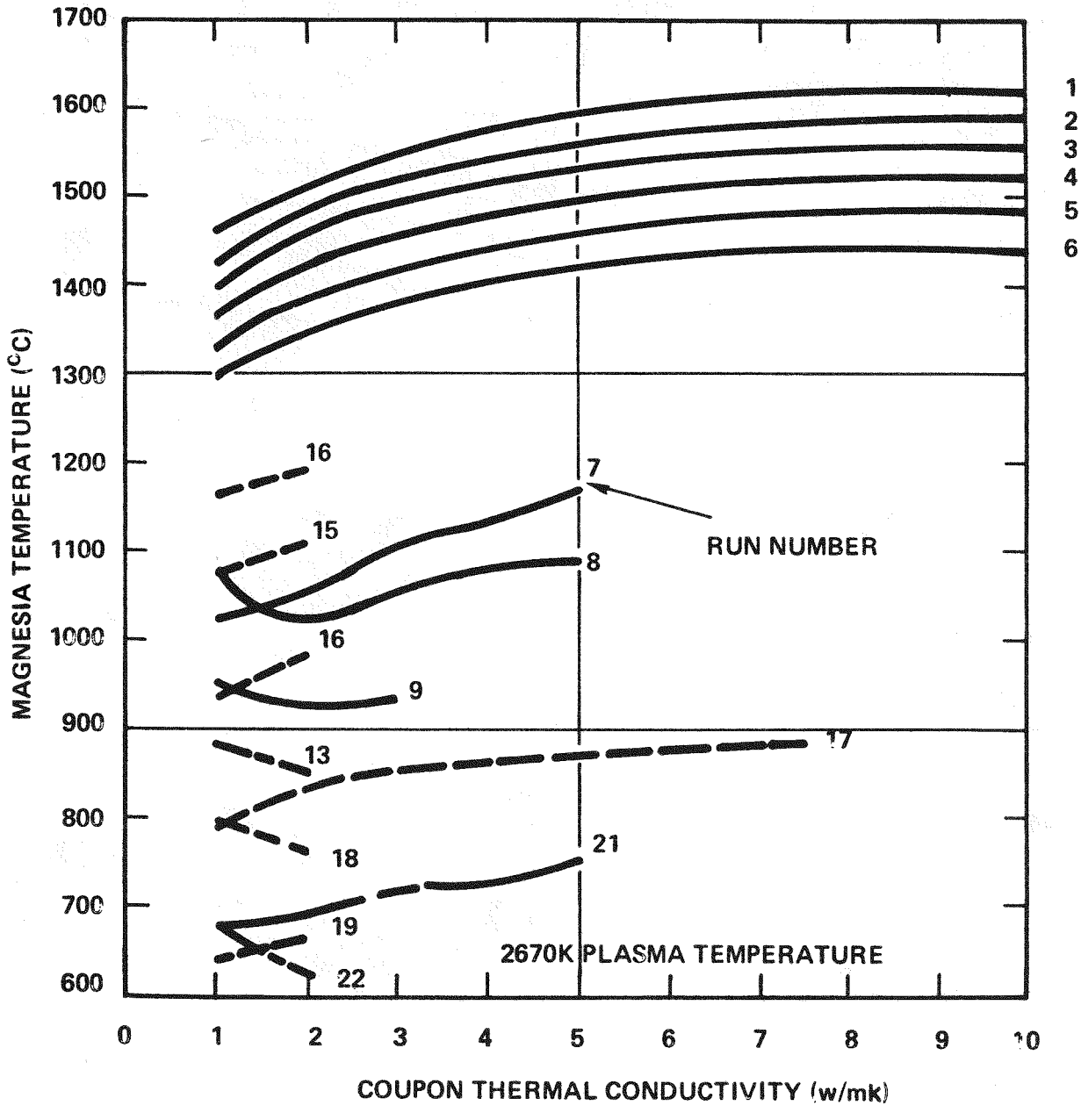

Figure 39. Magnesia Temperature - Thermocouple Location

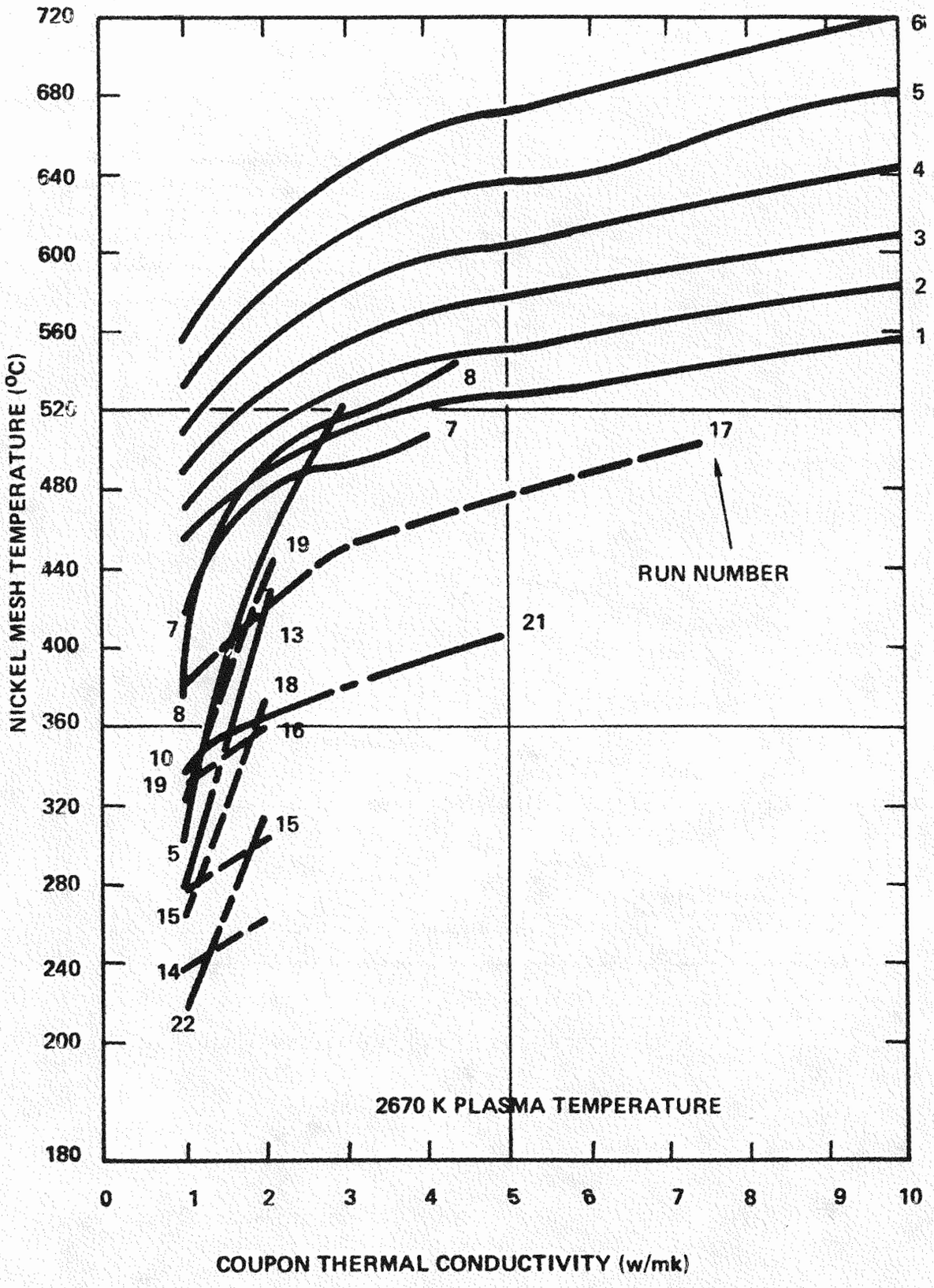

Figure 40. Maximum Nickel Mesh Temperature

TABLE 8

INDEPENDENT PARAMETERS FOR COUPON TEMPERATURE CALCULATIONS

RUN NUMBER	NICKEL MESH THICKNESS (IN)	COUPON THICKNESS (IN)	MgO THICKNESS BELOW COUPON (IN)	DISTANCE FROM SURFACE TO NICKEL MESH (IN)	PLASMA MASS FLOW RATE (kg/s)
1	0.2	0.3	1.4	1.7	0.20
2	0.2	0.3	1.2	1.5	0.20
3	0.2	0.3	1.0	1.3	0.20
4	0.2	0.3	0.8	1.1	0.20
5	0.2	0.3	0.6	0.9	0.20
6	0.2	0.3	0.4	0.7	0.20
7	0.1	0.3	0.3	0.6	0.20
8	0.1	0.3	0.2	0.5	0.20
9	0.1	0.3	0.0	0.3	0.20
10	0.0	0.3	0.0	0.3	0.20
11	0.0	0.2	0.0	0.2	0.20
12	0.0	0.1	0.0	0.1	0.20
13	0.1	0.3	0.0	0.3	0.15
14	0.1	0.3	1.4	0.3	0.11
15	0.1	0.3	1.0	0.3	0.11
16	0.1	0.3	0.6	0.3	0.11
17	0.1	0.3	0.2	0.3	0.11
18	0.1	0.3	0.0	0.3	0.11
19	0.1	0.2	0.0	0.2	0.11
20	0.0	0.2	0.0	0.2	0.11
21	0.1	0.3	0.3	0.6	0.075
22	0.1	0.3	0.0	0.0	0.075

of the coupon - the thermocouple location. This is also the temperature at which the coupon thermal conductivity should be evaluated. The MgO temperature at the same depth as the thermocouple location is in Figure 39. The maximum nickel mesh temperature is in Figure 40. The specimen surface heat flux is in Figure 41. A typical temperature distribution through the electrode is in Figure 42.

Linear interpolation between curves in Figures 37 through 41 is appropriate. Any errors introduced by this technique would be small compared to other analysis errors and to errors because of material property uncertainties.

Figures 37 through 41 were used to determine the electrode geometry and plasma flow rate for $0.12Y_2O_3 \cdot 0.88ZrO_2$ and $0.012Ce_2 \cdot 0.03Y_2O_3 \cdot 0.85ZrO_2$ - the only coupon materials selected to date. To achieve the desired surface temperatures of 1650°C, 1750°C, and 1850°C, the electrode dimensions were determined to be these in Table 9. The plasma flow rate should be 0.11 kg/s with a 0.1" thickness of nickel mesh interface material. Resulting dependent parameters such as temperatures at thermocouple locations and coupon heat flux, are in Table 10.

WESTF Test 43

Electrodes

The conceptual design thermal analysis was completed for the anodes and cathodes. The principal objective of the WESTF Test 43 is to operate the WESTF duct under hot slagging conditions ($<1500°C$) and to assess the durability and the performance of platinum anodes and low carbon steel (or iron) cathodes. The different material and temperature design constraints required for each electrode wall necessitated two separate designs and consequently, two separate numerical models. Among the principal asymetrical thermal and structural design considerations for this test were the surface and attachment region temperature requirements associated with the ceramic insulator-steel electrode cathode design and the platinum cap ceramic substrate anode design and the current leadout problem associated with both designs.

To satisfy the surface and interface temperature requirements of the cathode wall, the conceptual design in Figure 43 was developed from three dimensional

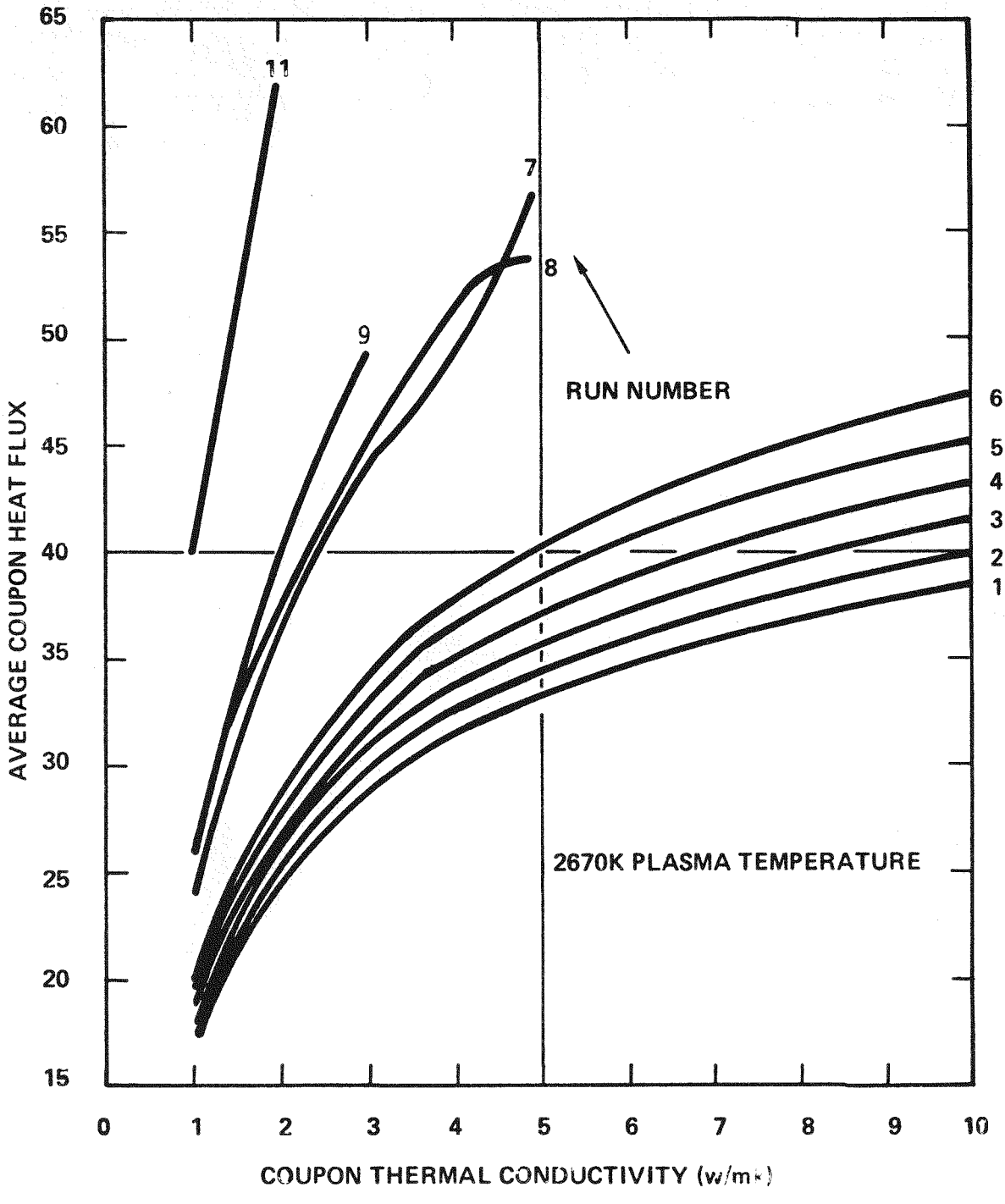

Figure 41. Average Coupon Heat Flux

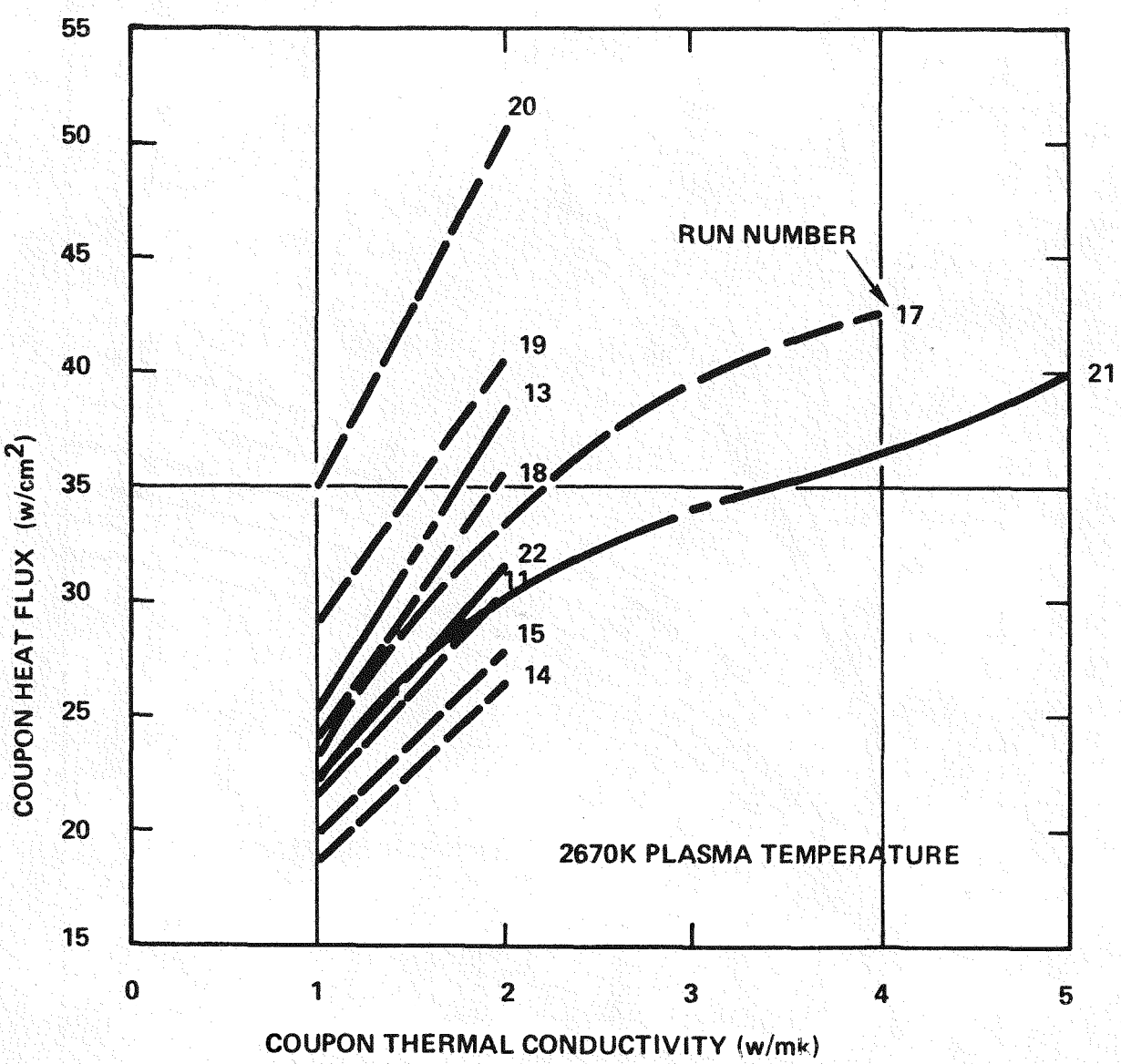

Figure 41. Average Coupon Heat Flux (Continued)

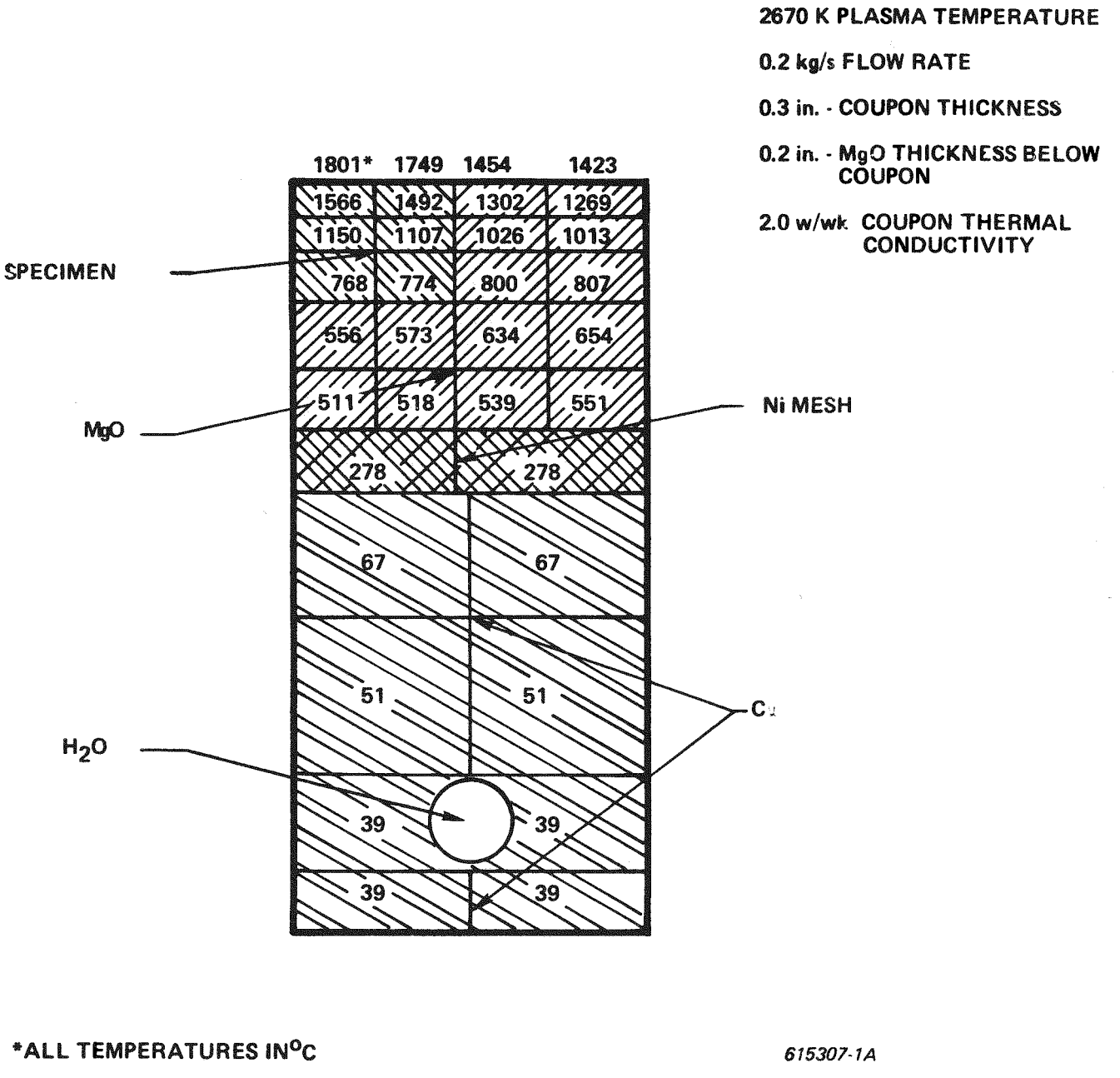

Figure 42. Coupon Electrode Temperature Distribution

TABLE 9

COUPON ELECTRODE GEOMETRY

	$0.12Y_2O_3 \cdot 0.88ZrO_2$	$0.12CeO_2 \cdot 0.03Y_2O_3 \cdot 0.85ZrO_2$
1650°C Surface Temperature		
Coupon Thickness (in)	0.25	0.27
MgO Thickness Below Coupon (in)	0.0	0.0
1750°C Surface Temperature		
Coupon Thickness (in)	0.30	0.30
MgO Thickness Below Coupon (in)	0.15	0.42
1850°C Surface Temperature		
Coupon Thickness (in)	0.30	0.30
MgO Thickness Below Coupon (in)	0.93	1.25

TABLE 10

COUPON ELECTRODE DEPENDENT PARAMETERS

	$0.12Y_2O_3 \cdot 0.88ZrO_2$	$0.12CeO_2 \cdot 0.03Y2\ O_3 \cdot 0.85ZrO_2$
1650°C Surface Temperature		
Average Coupon Temperature (°C)	800	855
MgO Thermocouple Temperature (°C)	715	740
Maximum Nickel Mesh Temperature (°C)	310	360
Coupon Heat Flux (W/cm^2)	28	30
1750°C Surface Temperature		
Average Coupon Temperature (°C)	985	1060
MgO Thermocouple Temperature (°C)	1030	795
Maximum Nickel Mesh Temperature (°C)	360	370
Coupon Heat Flux (W/cm^2)	25	24
1850°C Surface Temperature		
Average Coupon Temperature (°C)	1215	1270
MgO Thermocouple Temperature (°C)	1055	1140
Maximum Nickel Mesh Temperature (°C)	330	270
Coupon Heat Flux (W/cm^2)	22	21

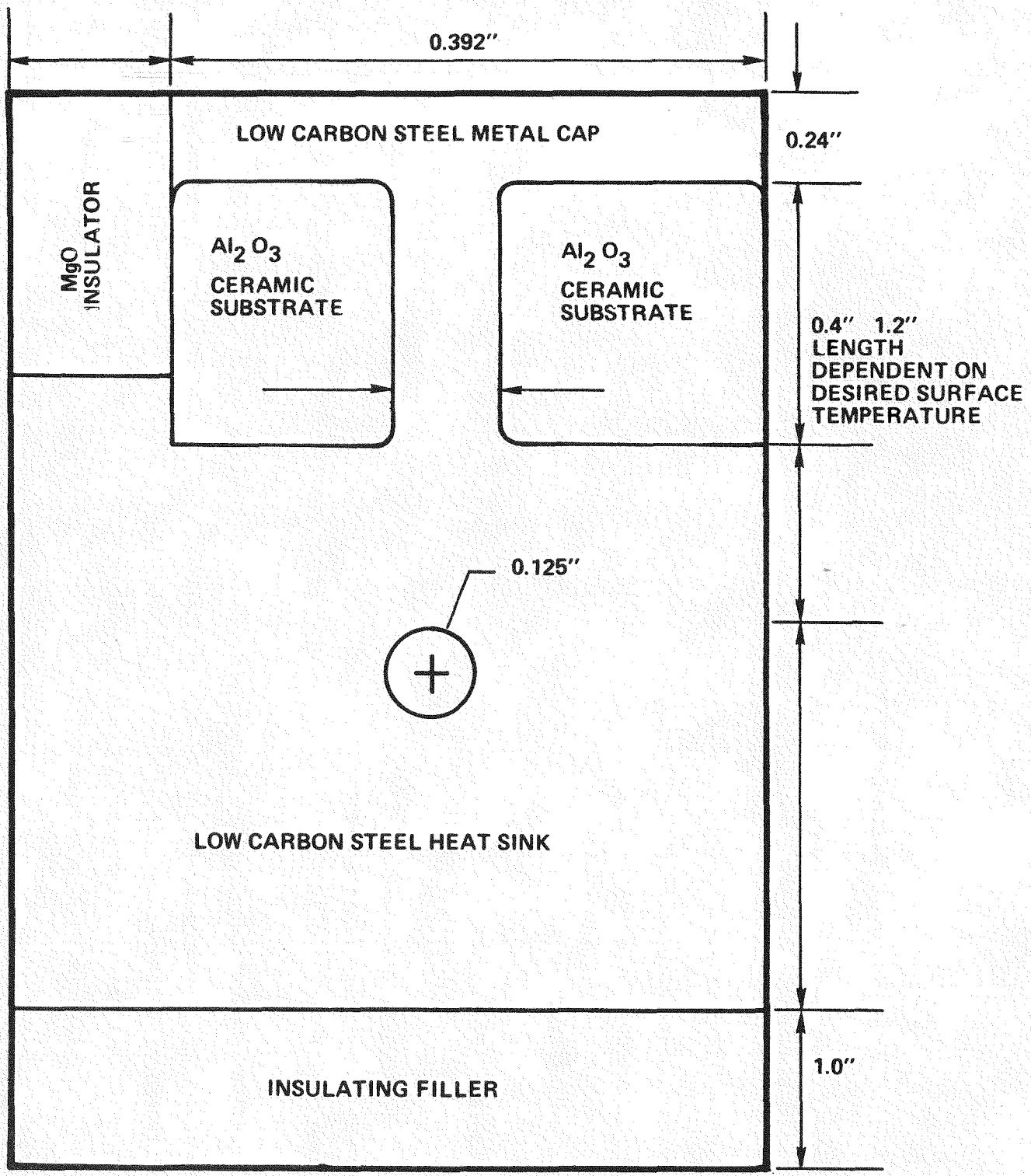

Figure 43. Conceptual Design Sketch-WESTF Test No. 43 Iron Cathode Wall/ Typical Electrode

finite difference modeling. The variations of the ceramic substrate length of between 0.4" and 1.2" will insure the surface temperature profile of approximately 950 - 1325°C from channel inlet to exit.

The anode wall surface and interface temperature requirements are satisfied with the conceptual design in Figures 44 and 45. The variation in the ceramic substrate length of between 0.2" and 0.6" will insure the surface temperature profile of approximately 1050 - 1425°C from channel inlet to exit.

For both walls, a flow rate of approximately 50 gallons per hour with 0.125" hydraulic diameter flow passage in the steel heat sink will provide adequate cooling for the entire electrode assembly and preclude any local boiling in any of the cooling passages. The hydraulic arrangement is to connect in a parallel-series arrangement no more than three electrodes per wall (i.e., there will be four such parallel-loops per electrode wall). During the next quarter the design of the Test 43 electrodes and cathodes will be finalized. Also, in the next quarter analysis will be completed to provide a thermal prediction summary for test operation and on-line data reduction.

Insulating Walls

The thermal analysis necessary for the design of the insulating walls was completed.

The thermal design specification for the Test 43 insulating walls is a maximum surface temperature of 900°C. Above this temperature molten potassium carbonate seed condensate would degrade the performance of the alumina insulator.

As the thermal specifications on Tests 41 and 43 are identical, the maximum refractory thickness will be the same as in Test 41. However, temperatures measured in Test 41 will be used to re-evaluate the insulating wall design procedure; and, if necessary adjustments will be made to the refractory thickness.

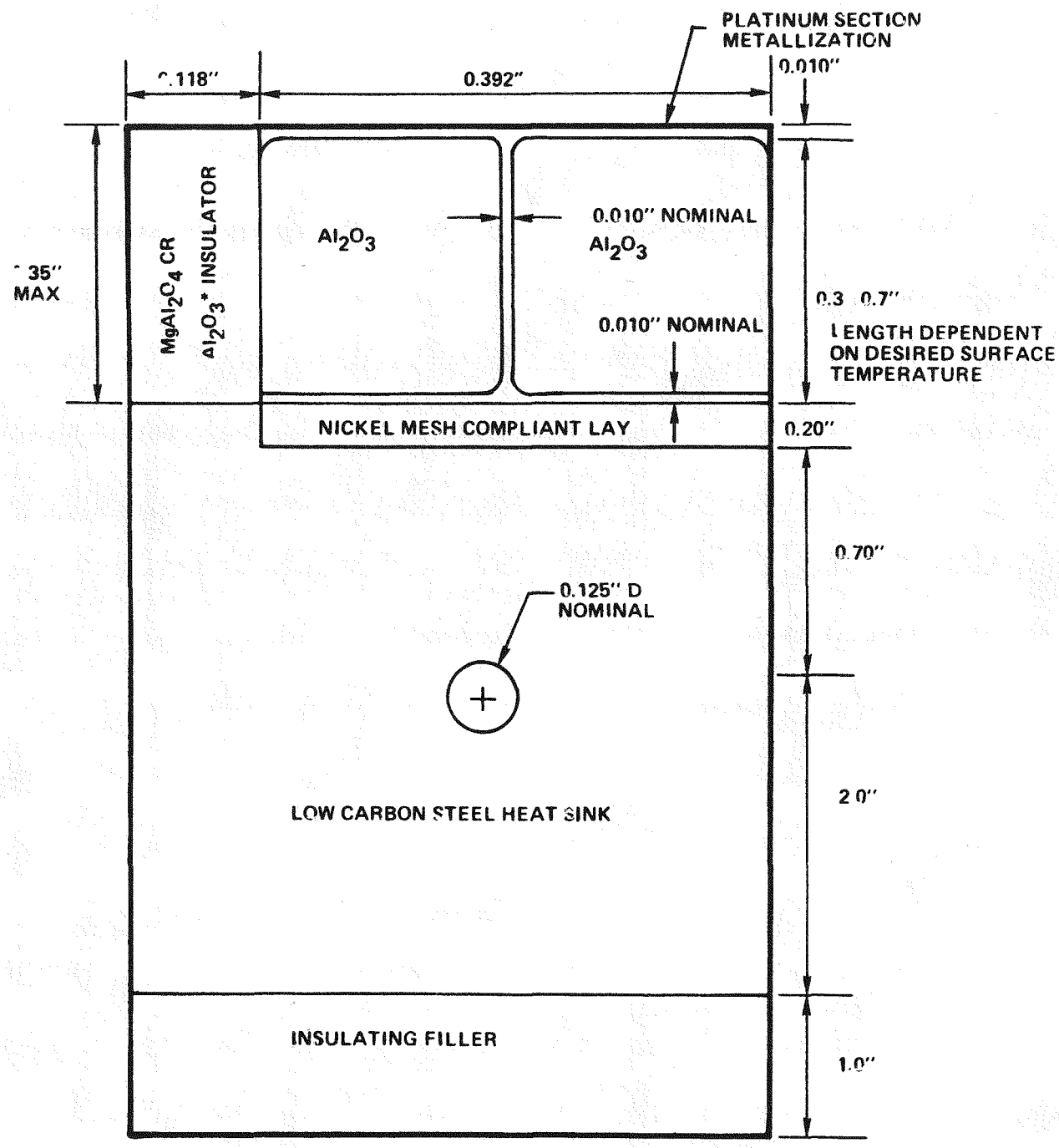

Figure 44. Conceptual Design Sketch - WESTF Test No. 43 Platinum Anode Wall/Typical Electrode

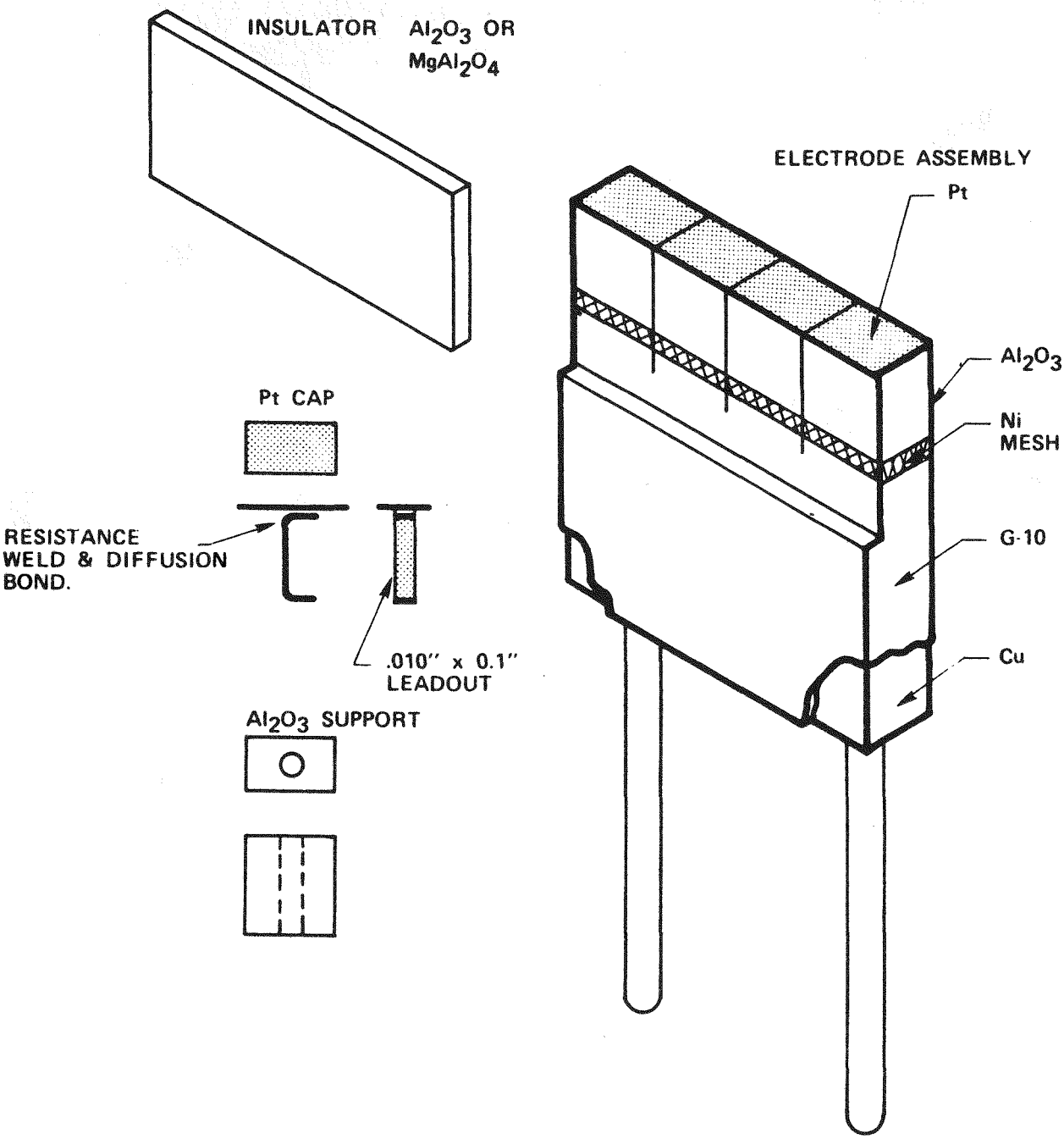

Figure 45. Test 43 Anode

Calorimeter Electrode

An accurate calorimeter electrode was designed to improve the measurement of surface temperature, heat flux, and heat transfer coefficient in the WESTF facility. Use of this calorimeter will provide a more accurate assessment of thermal conditions which will in turn lead to more effective material testing and electrode designs.

The calorimeter, shown on Figures 46 and 47, should be capable of determining, to accuracies of at least 15°C, 4% and 20% respectively, the surface temperature, heat flux, and heat transfer coefficient, which is a significant improvement over the current practice of analyzing electrodes. These accuracies are obtained by using guard sections, maintained at the same temperature as the central portion of the calorimeter assembly, and very good thermal insulation. The guard sections, with independently controlled heat sinks, function to eliminate heat losses or gains from all surfaces other than that exposed to the plasma. With the extraneous heat flows eliminated, water calorimetry is employed to accurately measure surface heat flux; the surface temperature is found by extrapolating interior temperature measurements. The calorimeter was designed using the materials shown to be most resistant to the MHD conditions in previous tests, and they will be interchangeable with the material test electrodes. Low carbon steel will be used for calorimeters with surface temperatures up to 1200°C. For higher surface temperatures, ceramic inserts will be employed (probably zirconia) to extend the temperature range of this basic design.

Fabrication of the first test calorimeter will begin during the next quarter with testing expected in the following quarter.

2.1.3 Post-Test Analysis

WESTF Test 40

Disassembly

The channel was disassembled at the test facility so that the data acquisition system could be used to provide data from electrical measurements made to determine areas of electrical leakage. The top insulating wall was removed first.

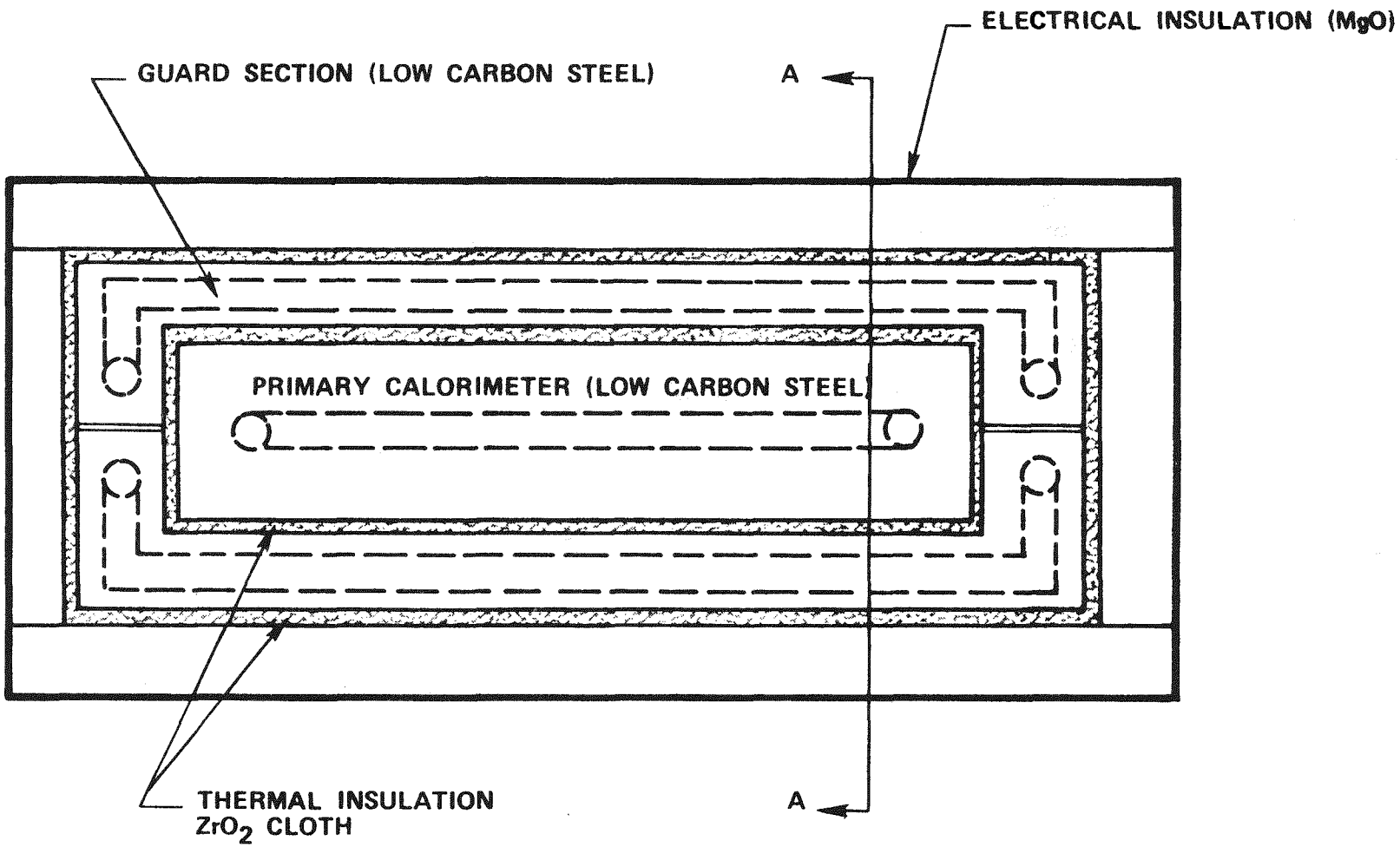

Figure 46. Design of Standard Calorimeter (Top View)

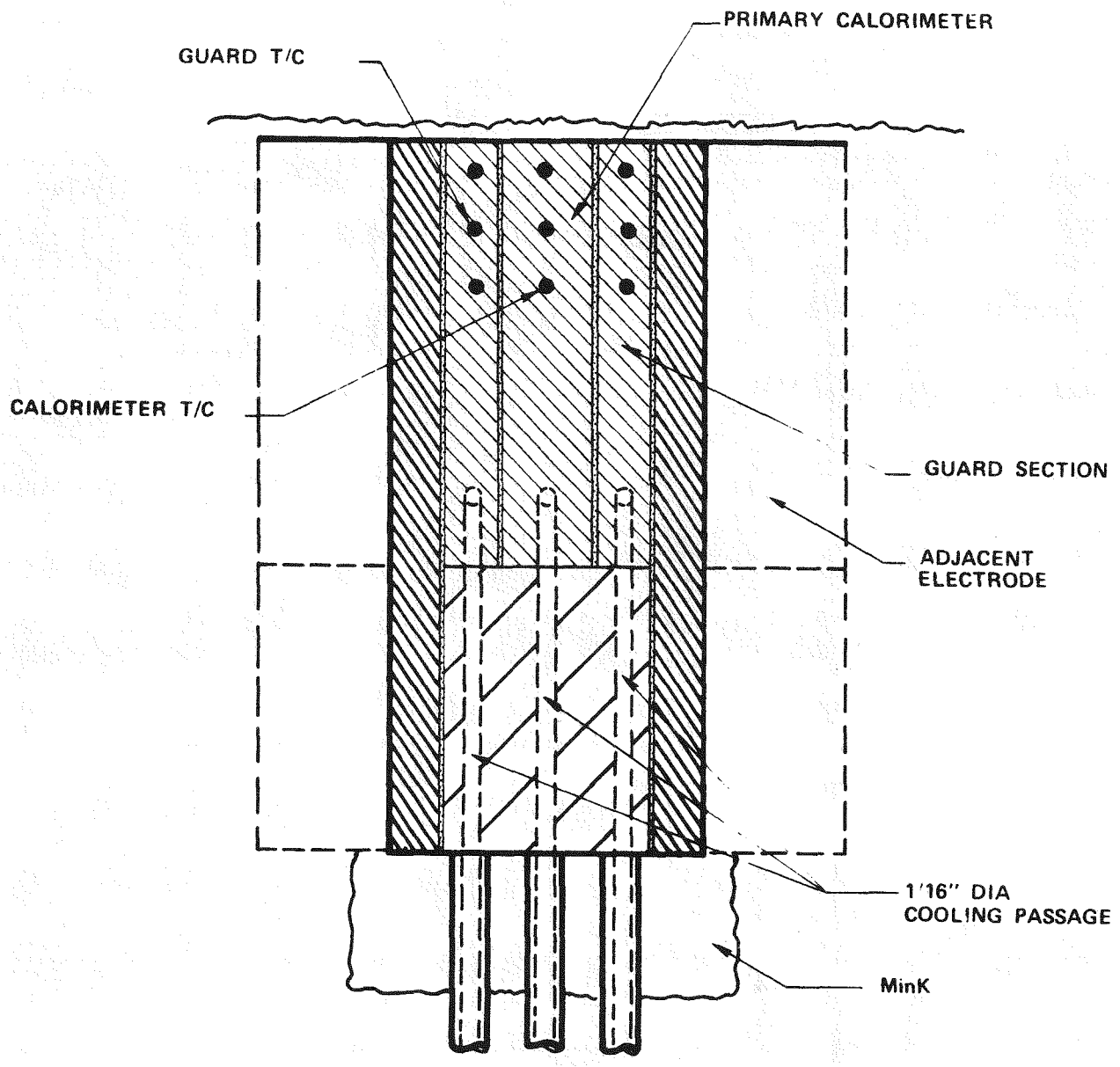

Figure 47. Design of Standard Calorimeter (Elevation)

With its removal the electrical characteristics changed drastically. A major area of electrical leakage appeared to be through the phosphate bonded cement between the electrodes and the top insulating wall at the exit of the channel. The G-10 insulating material at the inlet transition section from the electrodes was scorched at the top, indicating leakage of hot plasma at the channel inlet and a breakdown of the electrical insulation at that point.

The top slag layer was strong and adherent and stayed in place, bridging the anode and cathode walls, when the top insulating wall was removed. The slag adhered well to the anode walls, especially well to the interelectrode insulators, and to the bottom insulating walls and to the refractory lining the transition sections. The slag layer was less adherent to the cathodes because of hydrolysis of the high seed concentration in the cathode slag; it crumbled as the channel was dismantled into its major sub-assemblies. The surface appearance of the electrode walls after they were removed from the channel assembly is shown in Figure 48a.

Observations on the Free Standing Electrode Walls

The anode wall was nearly entirely coated with a 1.5-2.5 mm thick layer of brown colored slag. Flow lines and ripples in the slag could be readily discerned. Those areas of the anode electrodes where the slag had fallen off (most likely during disassembly) were characterized by thick black colored copper oxide scales overlayed with pockets of bluish colored copper salts. Extensive cracking of interanode insulators was evident.

The cathode wall had adhering slag covering about 20% of the total surface. These slag pockets were predominantly brown in color although there was considerable admixture of whitish potassium salts especially at the edges of the slag layer. The adhering slag which was $\sim$2.5-4.0 mm thick appeared to have experienced considerable swelling compared to the anode slag due, most likely, to seed hydration.

In fact, indications are that slag coverage on the cathode wall was complete upon conclusion of the test, but subsequently spalled off due to hydration reactions. A thin black-brown scale partially covered by blue crystalline material coated

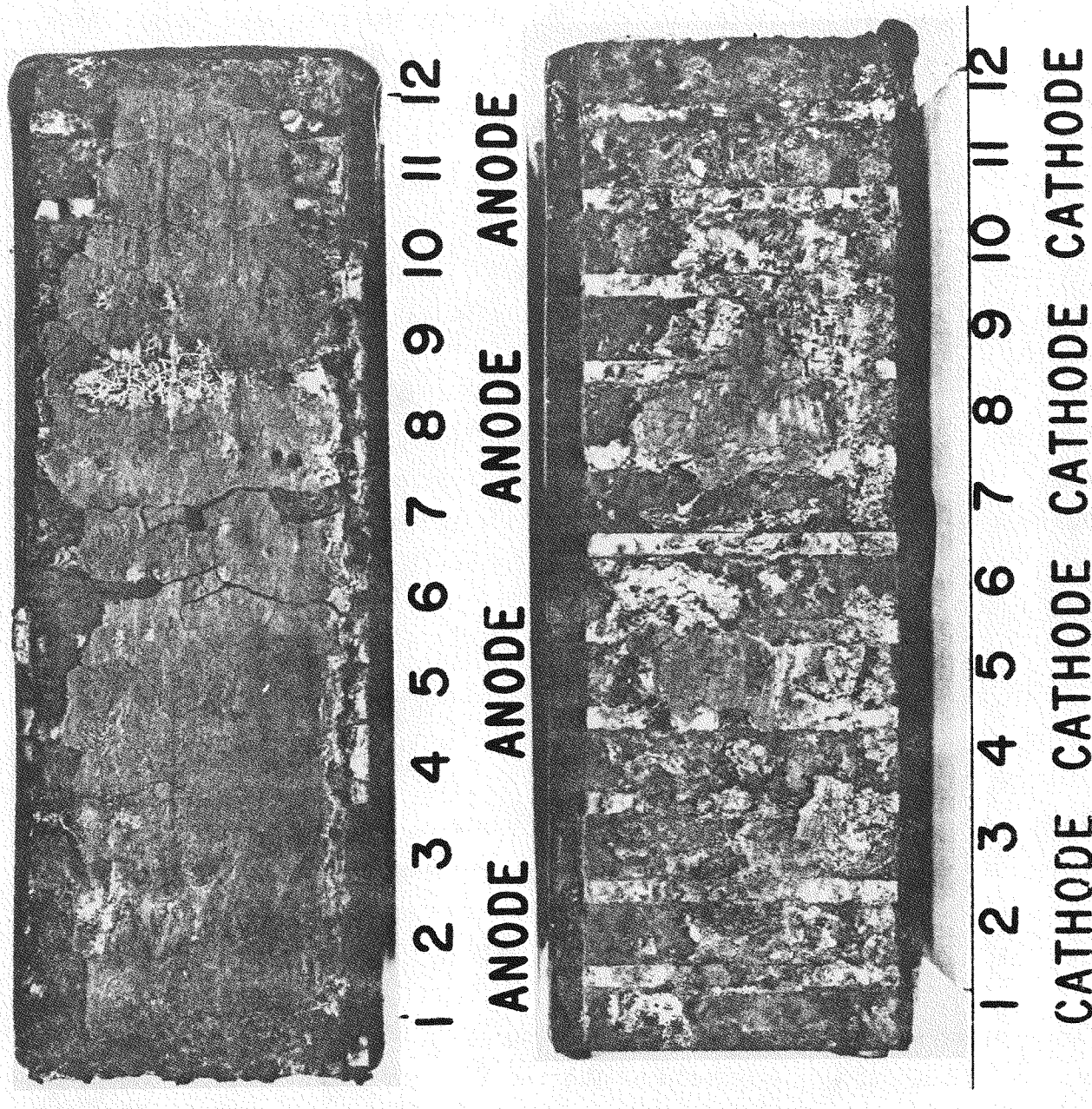

Figure 48a. WESTF Test 40 Electrode Walls After Removal from the Channel

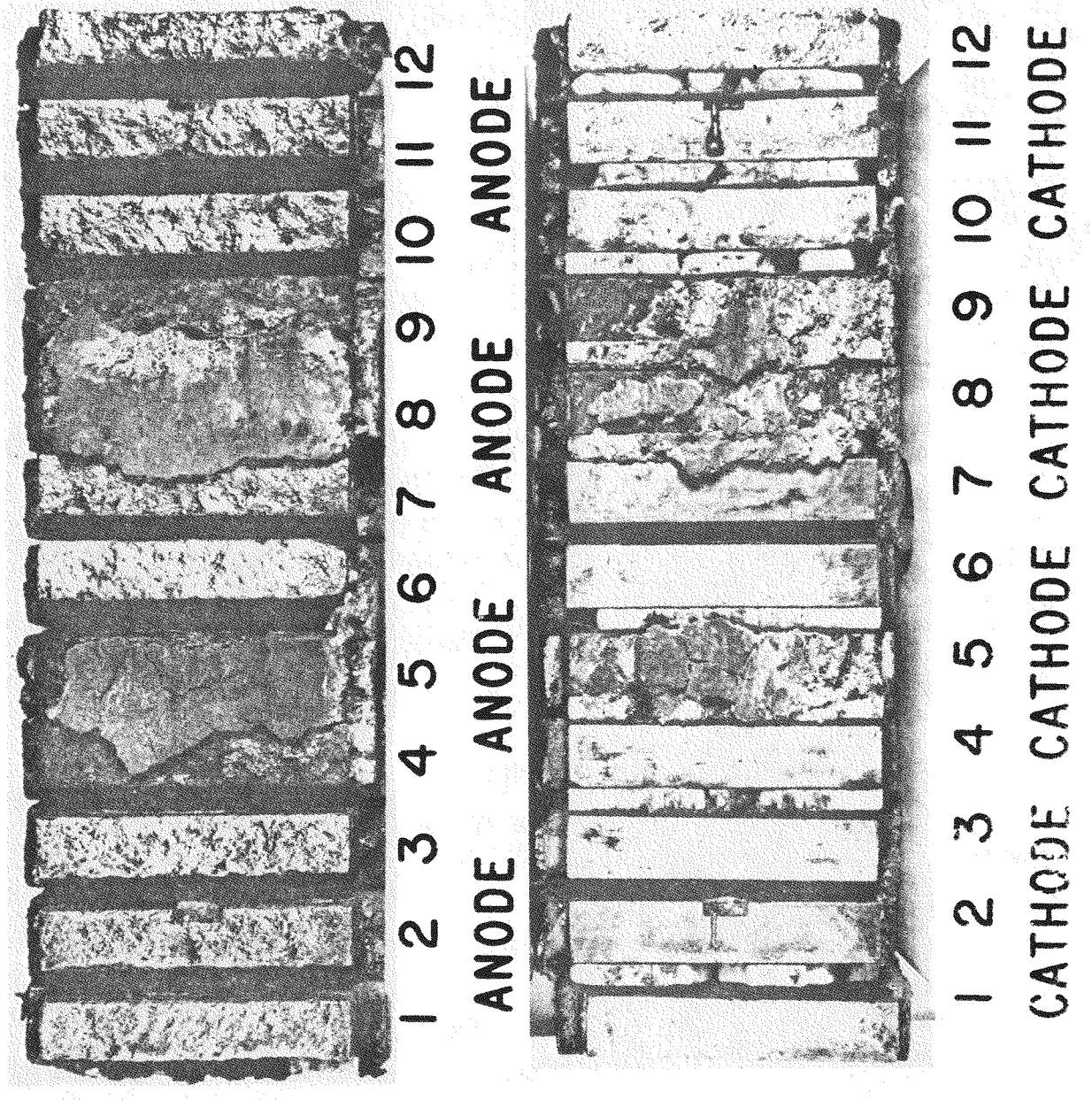

Figure 48b. WESTF Test 40 Electrode Walls After Separation and Partial Removal of Slag

the copper cathodes in those regions where slag was not present. The inter-cathode insulators were cracked but much less extensively than those at the anode.

Observations of Individual Electrodes

The electrodes were removed from the walls by sawing below the tie-rod level. They were then divided into groups 1-6 and 7-12, the tie rods removed, and then each electrode separated from its neighbor with care taken to retain slag on specific electrodes selected for metallography. The electrodes were placed side by side for the photograph shown in Figure 48b.

The .010" thick G-10 interelectrode sheet material used at the anode and cathode walls was burned away to a distance ~1/4" below the surface of the electrodes. The G-10 interelectrode tie-rods from electrodes 1-6 thermally degraded such that they had no strength and consisted of individual bundles of glass fibers with little binder material remaining.

Large differences in corrosion could be seen when selected anode and cathode electrodes were cleaned of their slag/seed layers by washing in water with a brass wire brush. The anodes experienced extensive material attack losing perhaps 1/8" of copper from the surfaces and edges. The electrode surfaces were heavily but uniformally pocked with overlapping craters. Especially deep craters occurred at those locations where thermocouples had originally been attached to the anode surfaces. Arcing-oxidation reactions appear to be responsible for the observed corrosion. Anode #12 was noticeably thinner (in the flow direction) than the other electrodes. The downstream side of this anode experienced extensive oxidation and arc damage, due perhaps to electrical leakage with downstream components. The washed anodes exhibited a golden brass-like color rather than the expected copper hue. In all cases, the interanode insulators crumbled and broke into numerous pieces during the washing and cleaning steps.

In contrast with the anodes, the washed cathode electrodes were relatively pristine exhibiting only very small and isolated arc craters. In general,

the intercathode insulators remained integral during the washing procedure, but it was noted that although the crack patterns on the long and short insulators differed, they always included the tie rod holes.

Slag Chemical Analysis

After WESTF Test 40 Run 1 was completed, a portion of the slag layer over the downstream section of the channel was removed and quantitatively analyzed. The analysis was compared to that of the as received flyash powder, as shown in Table 11. The major compositional difference was observed for MgO where there was an increase of approximately 30 w/o. This exceedingly large pickup can only be logically explained by assuming contamination of the channel area by the MgO refractories lining the upstream mixer section. All of the components upstream of the channel (the combustor, mixer, and transition section), were completely rebuilt with virgin insulating material prior to WESTF-40. It is reasonable to assume that some erosion of the refractories surface took place due largely to the settling of the newly reworked brick structure during the test run. A second analysis for MgO was made on the slag layer in the channel after WESTF Test 40-2. The percentage of MgO was found to be 11.68%, a substantial decrease from Run 1 but still indicative of some erosion of the mixer brickwork. Additional analysis of the slag composition will be made after future WESTF Tests to monitor this situation.

Post Test Materials Analysis

The evaluation of copper as an electrode material was not a primary objective of WESTF Test #40; however, post-test materials analysis of this test is instructive in providing a comparison of material degradation between WESTF, laboratory anode arc erosion, and MHD generator tests. In WESTF Test 40, an anode erosion rate of 47 μg/coulomb was calculated based upon the copper anode weight loss. Cathode losses were insignificant in comparison. This anode erosion rate (taken at approximately 200°C) can be compared to those calculated in MHD generator tests using eastern slag-K_2CO_3 (Reference 27) and eastern slag-K_2SO_4 (Reference 29) combinations. The WESTF rates are more than six times that reported by AVCO using the same New Hampshire flyash-K_2CO_3 seed mixture. The WESTF rates are close to UTSI's anode erosion rates using a Kentucky coal - K_2SO_4 mixture. The use of

TABLE 11

COMPOSITION OF COAL SLAG* USED IN WESTF-40 RUN 1 (WT%)

	SiO_2	Al_2O_3	FE_2O_3	CaO	MgO	SO_2	K_2O	Na_2O	P_2O_5	TiO_2	Others
As Received Flyash Powder	36.0	29.2	17.8	5.3	0.19	3.3	1.7	1.6	0.73	1.8	2.38
Solidified Slag (Taken off downstream channel wall)	25.9	25.5	11.1	3.7	29.9	0.10	1.5	0.1	0.05	0.91	1.24

*Flyash from Bow, New Hampshire steam plant - Western Kentucky Coal

K_2SO_4 should be much more corrosive to copper due to the stability of CO-S-O compounds, (Reference 23). These results suggest that anode erosion rates are much higher in WESTF than in either the AVCO or UTSI MHD generators. This difference could be related to the difference in arc characteristics caused by the presence or absence of a magnetic field or in differences caused by supersonic versus sub-sonic flow velocity. For example, larger, less mobile arcs in WESTF could account for the large degree of copper anode degradation.

A copper cathode and a copper anode from WESTF Test 40 was examined with the SEM to characterize slag/electrode condition. Comparisons were also made to copper samples from the anode arc erosion test.

Copper Cathode #5

Little slag adhered to the copper cathodes due to exfoliation of the slag layer or the hydration of potassium compounds upon cooling. The structure of a small piece of slag still adhering to the copper cathode (in far right) is shown in Figure 49. There is some variation in slag composition from one location to another; however, the composition at spot A (as shown by the bars in Figure 50) can be used in comparison with the initial New Hampshire flyash composition (dots in Figure 51). The channel cathode slag has picked up significant amounts of magnesium, most probably due to reactions with upstream MgO refractories. Dissolved copper oxide of the order of 10 percent is also present in the channel slag. Spots C and D which are away from the copper interface are much lower in copper content. The iron content of the channel slag is 1/2 to 2/3 of that of the flyash; the reduction in iron content is most probably due to the relatively higher volatility of FeO over other slag species. The Si/Al ratio is also lower for the channel slag; this also is due to the relatively higher volatility of SiO_2. The white areas in Figure 49, such as spot F, are regions of high potassium content. Most likely these areas are merely a layer of seed compounds on slag. Analysis of spot B, as shown by the dots in Figure 50, indicates that the copper matrix has picked up small amounts of sulfur, aluminum, calcium and iron.

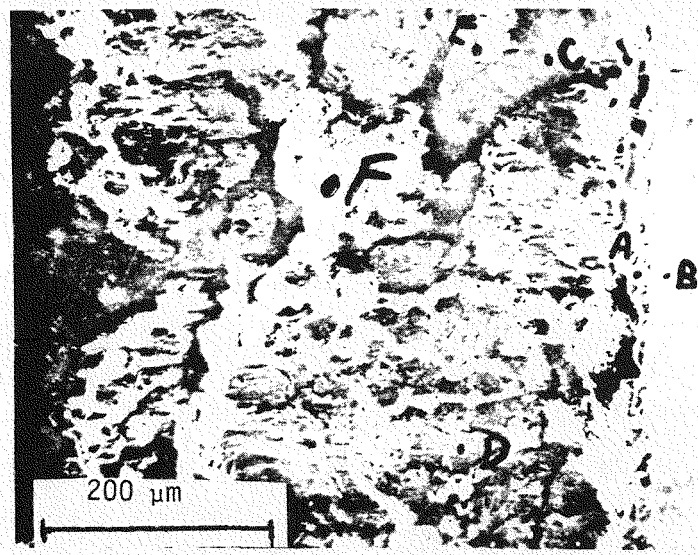

Figure 49. Microstructure of Slag Layer Coating Copper Cathode. Cathode is at Far Right.

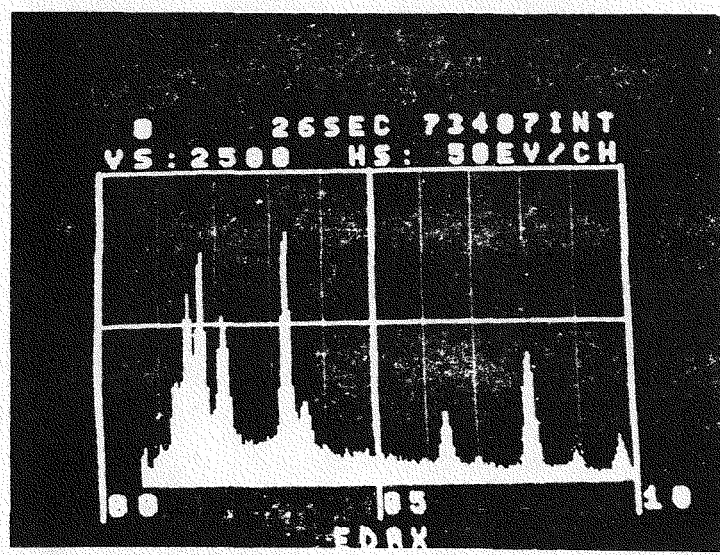

Figure 50. EDAX Display of Spot A (dots) and Spot B (bars) in Figure A.

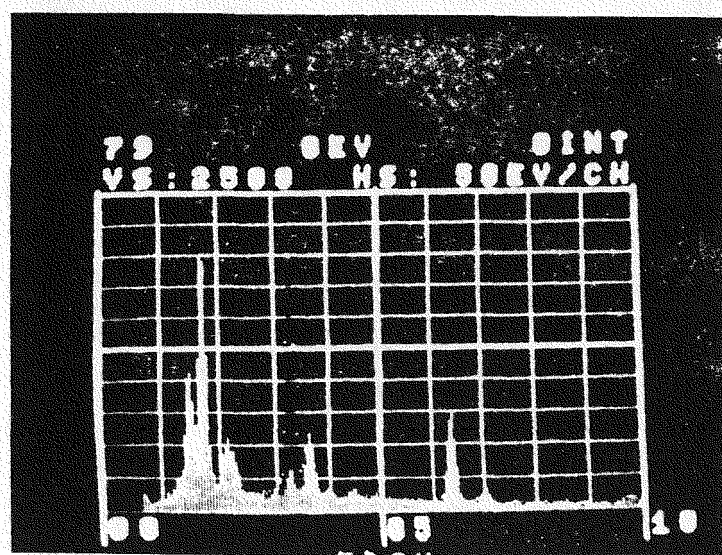

Figure 51. EXAX Display of New Hampshire Flyash (bars) and a Mixture of New Hampshire Flyash and $K_2 CO_3$ (dots)

Copper Anode #8

In contrast to the cathode wall, the slag layer on the anode wall was much more adherent. A cross section of an anode slag layer, approximately 2 mm. thick, is shown in Figure 52. A cross-section of the same area using SEM is shown in Figure 53. See Figures 54 and 55 for EDAX. The composition of the plasma side (spots J, K, and L) of the slag layer is highly enriched in potassium (compare with the composition of the original ash in Figure 51). In contrast the composition closer to the copper/slag interface at points such as E, F, and I is similar to that of the original flyash with pickup of insignificant amounts of magnesium and copper. In slag regions very close to the anode interface, such as area M in Figure 53, which is also shown in Figure 56, the copper concentration is very high (see EDAX display in Figure 57). The potassium content of the layer near the anode interface is significantly reduced. Metallic spherical globules are found in the slag to depths of approximately 0.5 mm from the anode interface. These can be seen in Figure 52 and 53 but are most obvious in Figure 56. These globules are either pure copper (spot C in Figure 56) or copper alloyed with a few percent iron and very small amounts of potassium and silicon (spots B and D in Figure 56). Also needle like compounds of potassium are found in the interfacial region between slag and copper (see right side of Figure 53).

Electrical Performance

The previous quarterly report included test data taken during Test 40, runs 1 and 2. Reference was made to a voltage threshold effect which was observed during Test 40-2. This effect can be observed in plots of I versus V_L for each electrode-pair of the channel. See Figures 58 to 60. The data shown in these figures were taken during the time interval between 1428 and 1530. Seed had been introduced into the channel at 1315. The data shown in the figures was obtained after the channel had been brought to 5 amperes per electrode pair. The chronology employed in taking the data for Figures 58 to 60 is listed in the plot for Electrode Pair #1 (EP1) in Figure 58.

Voltage threshold effects can be seen in the curves for the first five electrode-pairs and in the curves for electrode-pairs 8 and 12. The remaining electrode-pairs either have a less-pronounced voltage threshold or a voltage threshold is

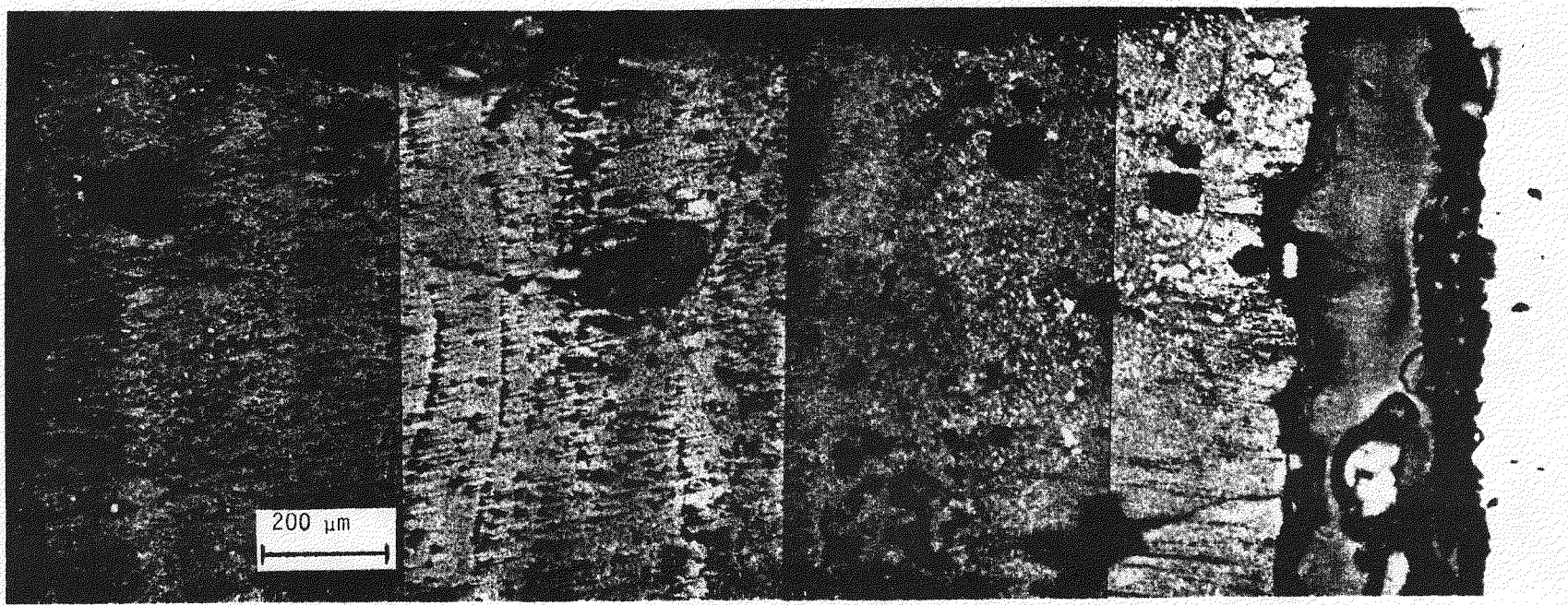

Figure 52. Cross-Section of Slag Layer Adhering to Copper Anode No. 8/WESTF Test No. 40

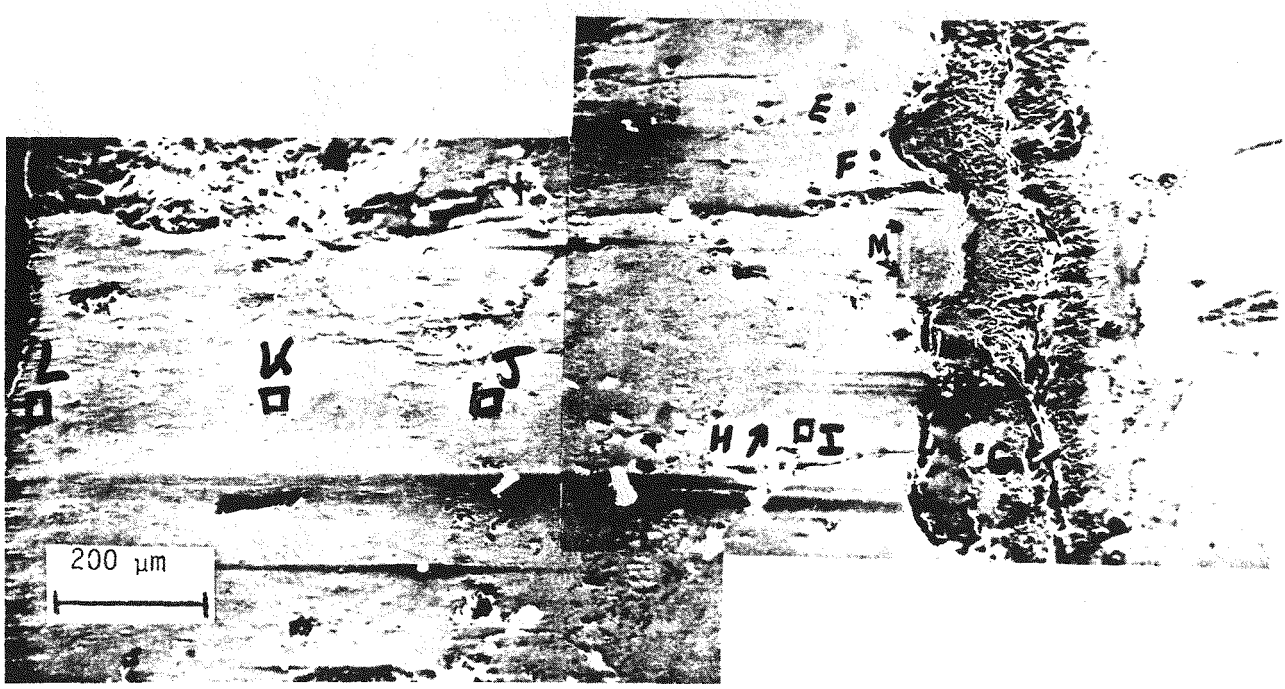

Figure 53. Cross-Section of Slag Layer on Anode #8 (WESTF Test #40)

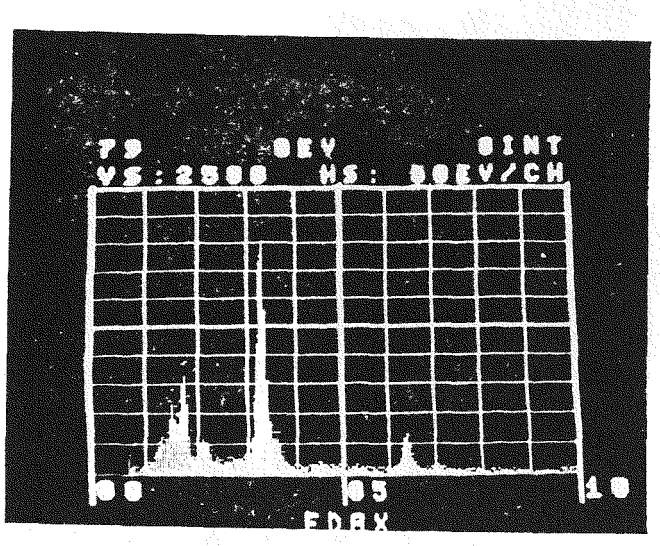

Figure 54. EDAX Display of Slag Composition at J,K (bars) and at L (dots) in Fig. 53.

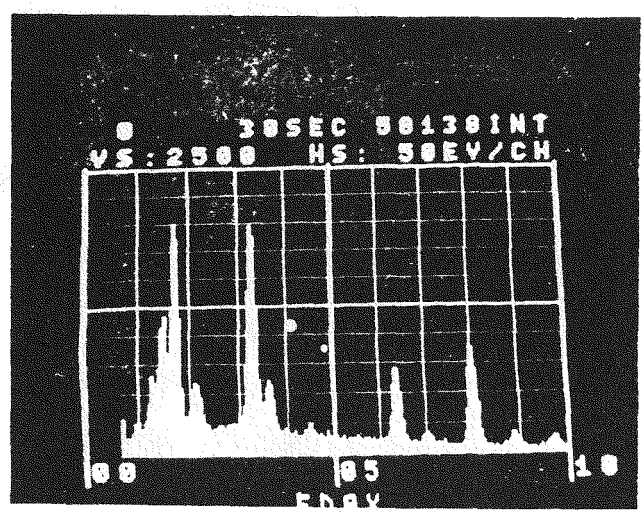

Figure 55. EXAX Display of Slag at I in Figure 53.

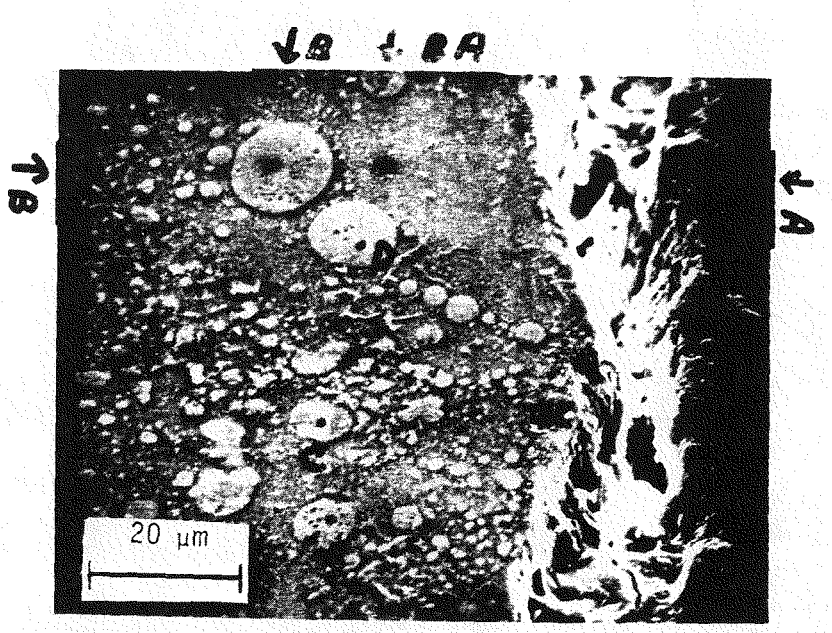

Figure 56. Slag Near Copper Anode 8. Shown as Area M in Figure 53.

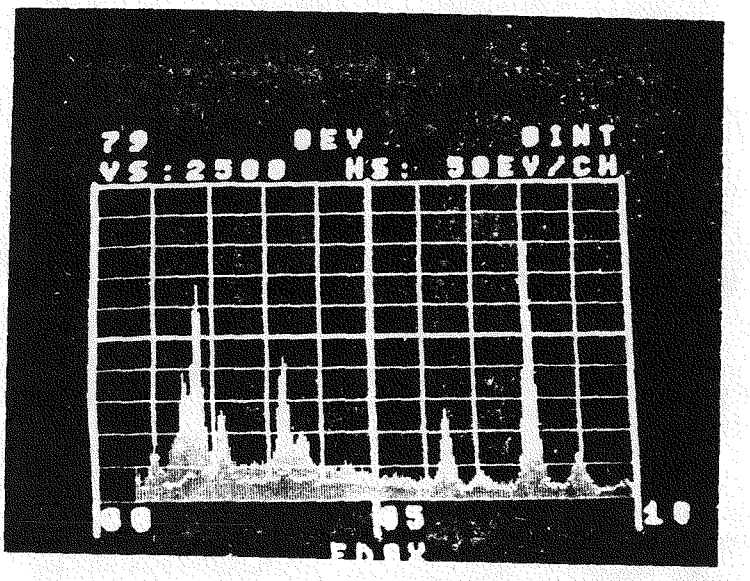

Figure 57. EDAX Display of Spots A (bars) and B (dots) in Figure 56.

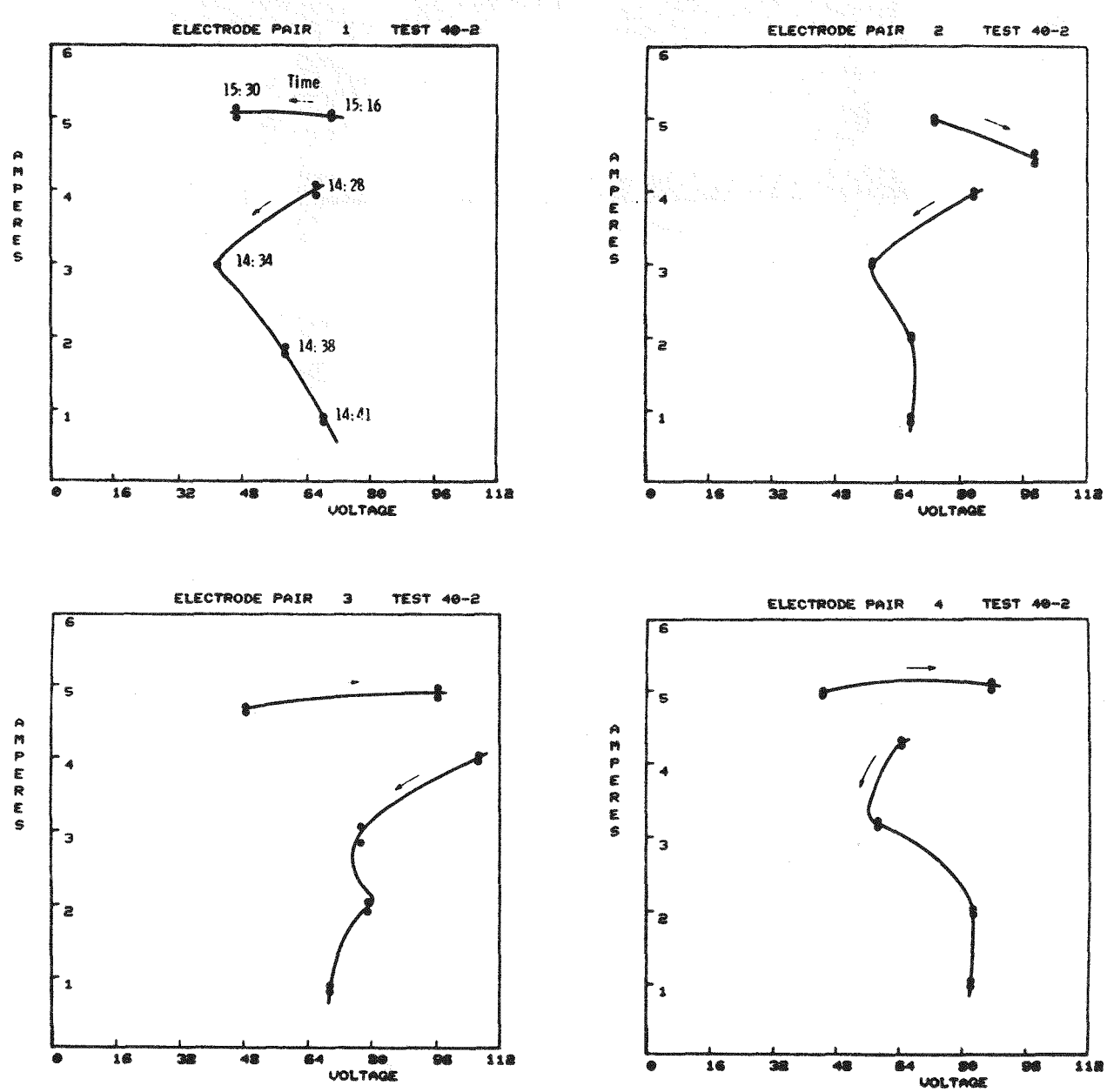

Figure 58. Amperes through Different Electrode-Pairs as Function of Impressed Voltage, Test 40 - Run 2

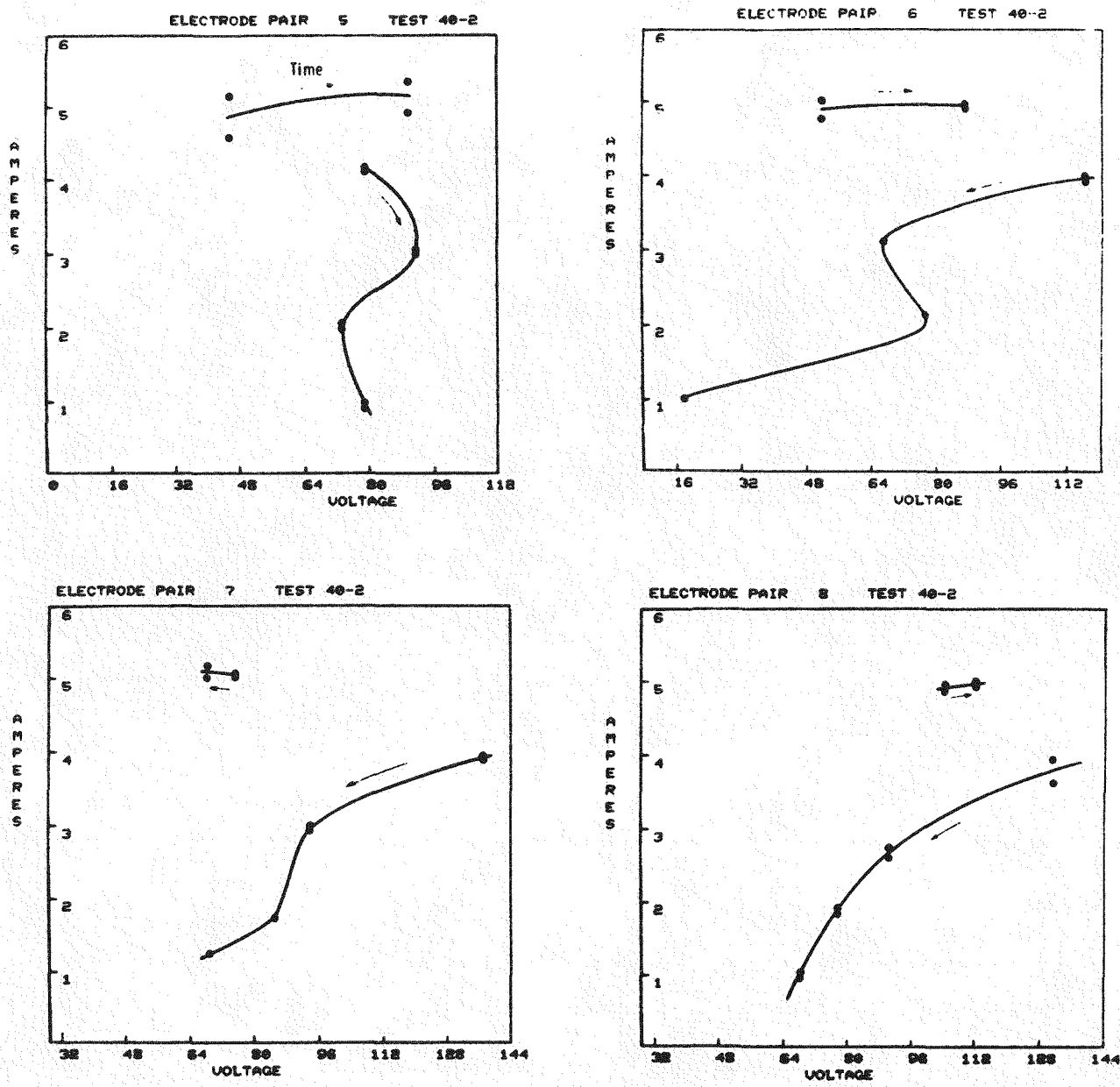

Figure 59. Amperes through Different Electrode-Pairs as Function of Impressed Voltage, Test 40 - Run 2

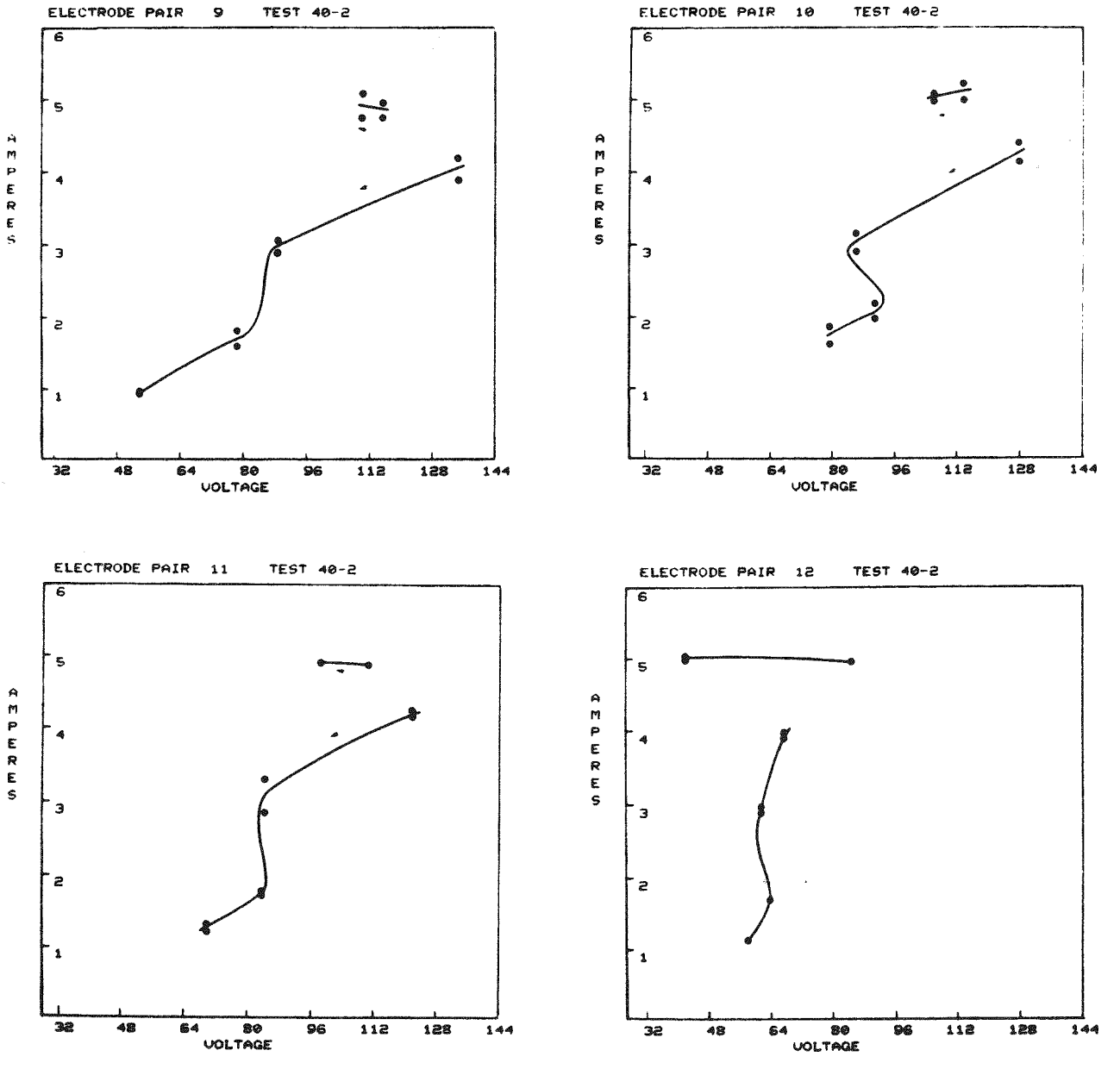

Figure 60. Amperes through Different Electrode-Pairs as Function of Impressed Voltage, Test 40 - Run 2

not present. Many of the curves have negative slopes or have "S" shaped curves. DC arc discharges characteristically have similar negative slopes, due in part to an increase in plasma temperature with increasing current. The presence of negative or vertical slopes in many of the curves indicates that the DC arcs extend from the cathodes to the anodes of the electrode pairs involved.

The 5 ampere points on the curves of Figures 58 to 60 were taken after the lower current points were obtained. The variation in the voltages required to impress 5 amperes through a given electrode-pair reveals that considerable fluctuation in the properties of the plasma occur as a function of time. All of the current versus voltage data were taken with the power supplies in the current control mode.

It is believed that the voltage threshold effects observed can be attributed to the insulating properties of the slag layer. It is possible in instances where voltage thresholds were not observed that a significant fraction of the electrode surfaces were not covered with slag thus permitting direct electrical contact. Leakage currents across the insulating walls would also tend to mask voltage threshold effects.

WESTF Test 40 - Run 3

WESTF Test 40-3 was run without making any changes in the structure of the channel . An attempt was made to disconnect the exit flange from any components which would tend to ground it. Insulating hoses were inserted in series with the water cooling connections; an insulating gasket was installed at the flange seal and the screws which held the flange seal together were insulated. However, the gasket seal tended to overheat during operation. The flange insulation, in practice, did not prove to be very effective. The C_nA_n electrical connection referred to in previous quarterly reports was used in the test. When this connection is utilized the power supplies are connected directly to the opposing electrodes of each electrode-pair.

Current through the generator became measurable within a few minutes after the seed was introduced at 1310. Typical voltage and current curves as a function of electrode-pair number during run 40-3 are shown in Figures 61 to 63 for

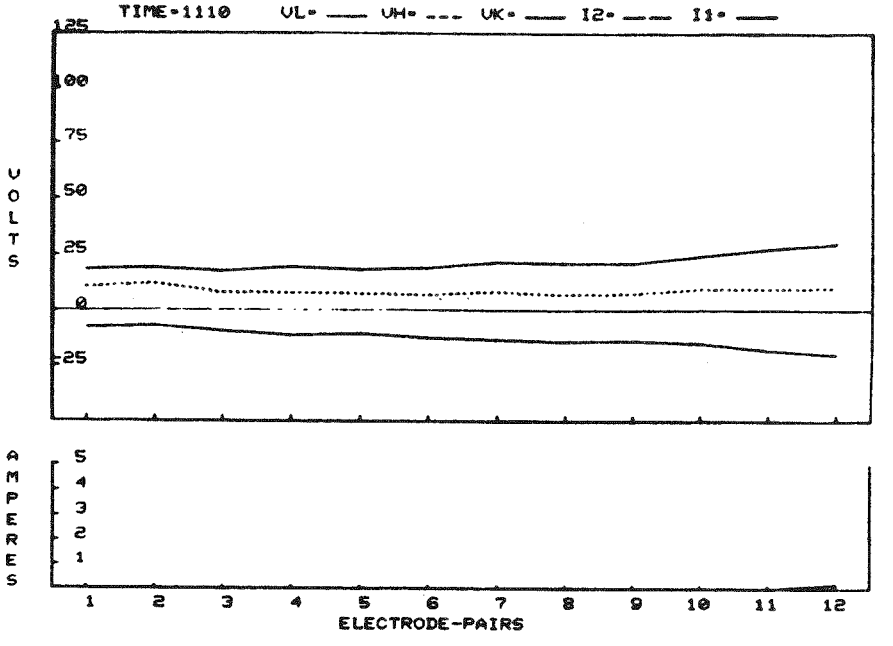

(a) Without Axial Voltage

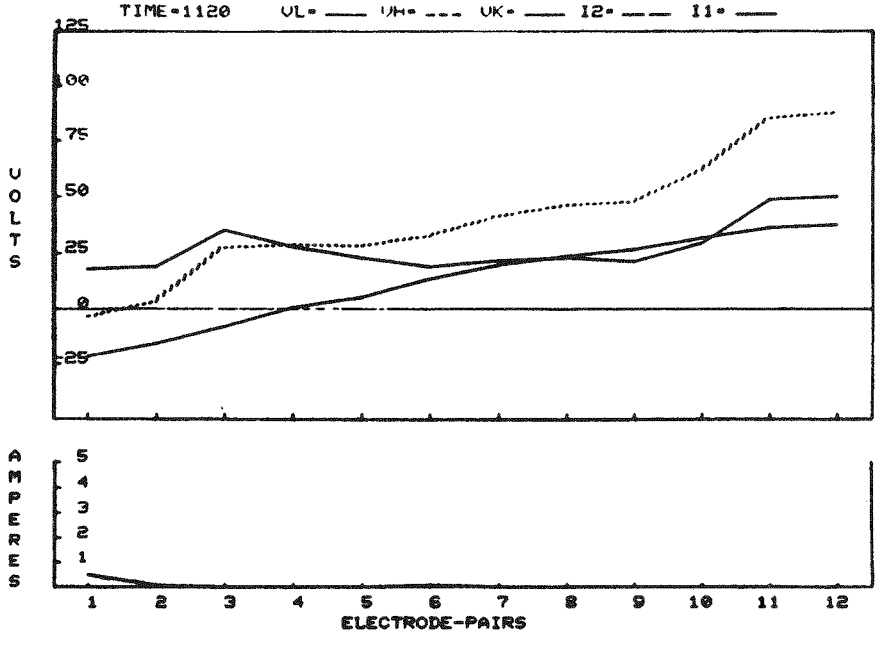

(b) With 91.3 V Axial Anode Voltage, 0.9 Amperes

Figure 61. Applied Voltages and Currents, WESTF Test 40 - Run 3

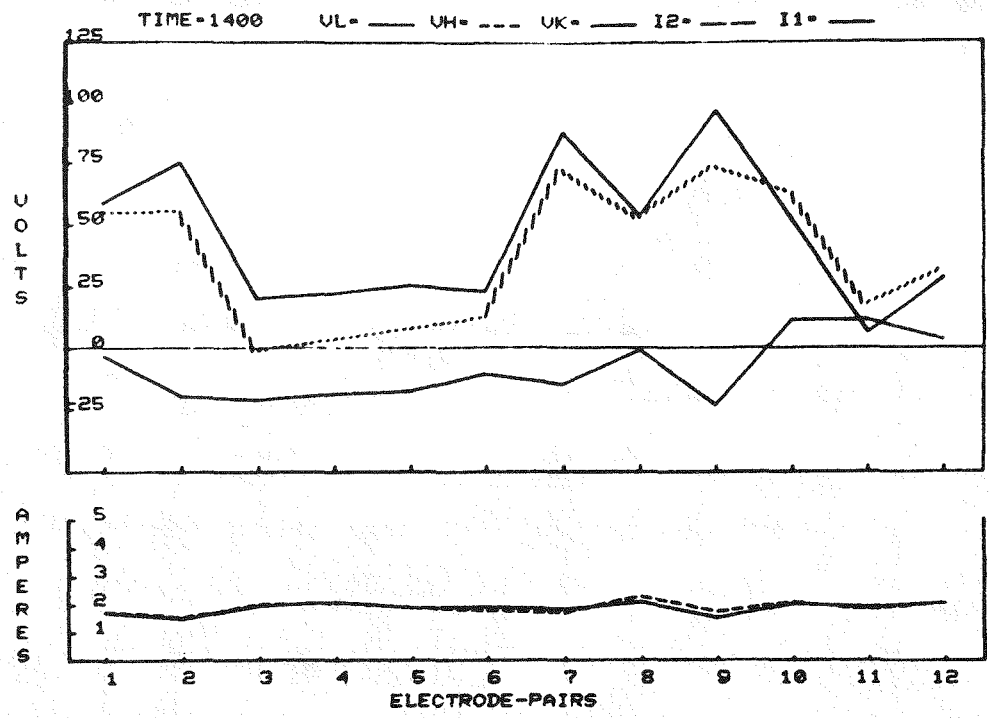

(d)

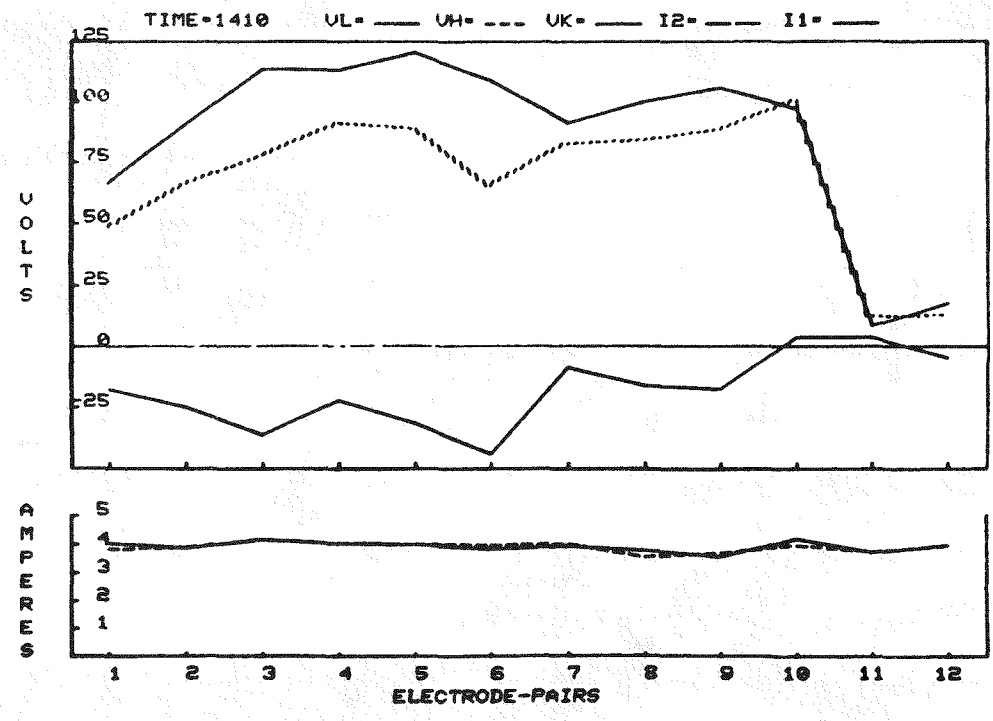

Figure 62. Applied Voltages and Currents, WESTF Test 40 - Run 3, No Axial Voltage

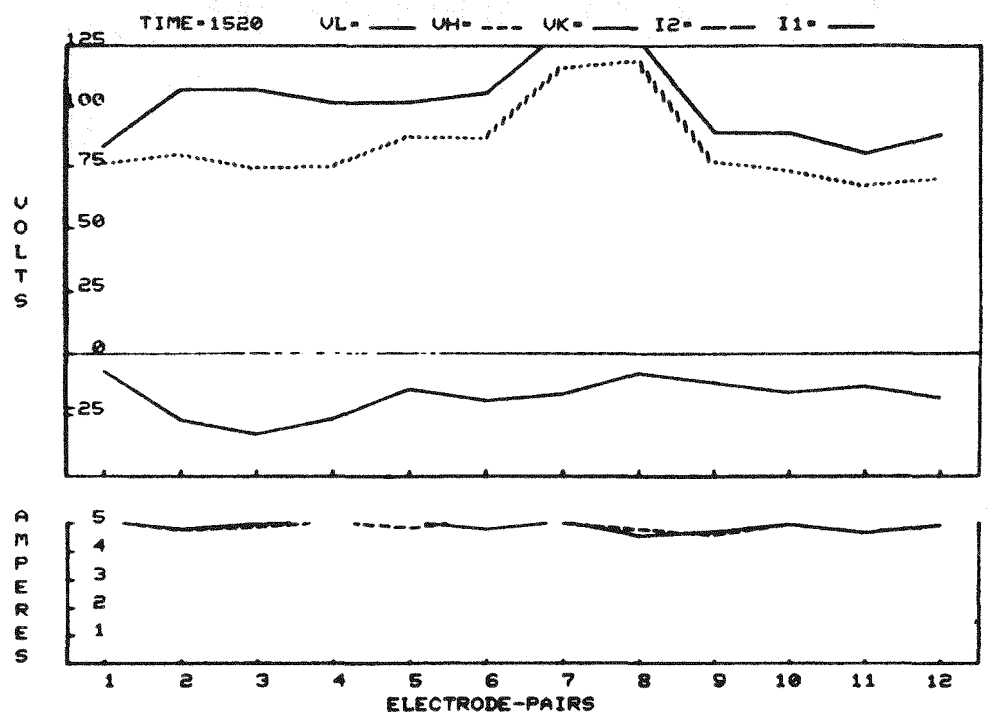

(a)

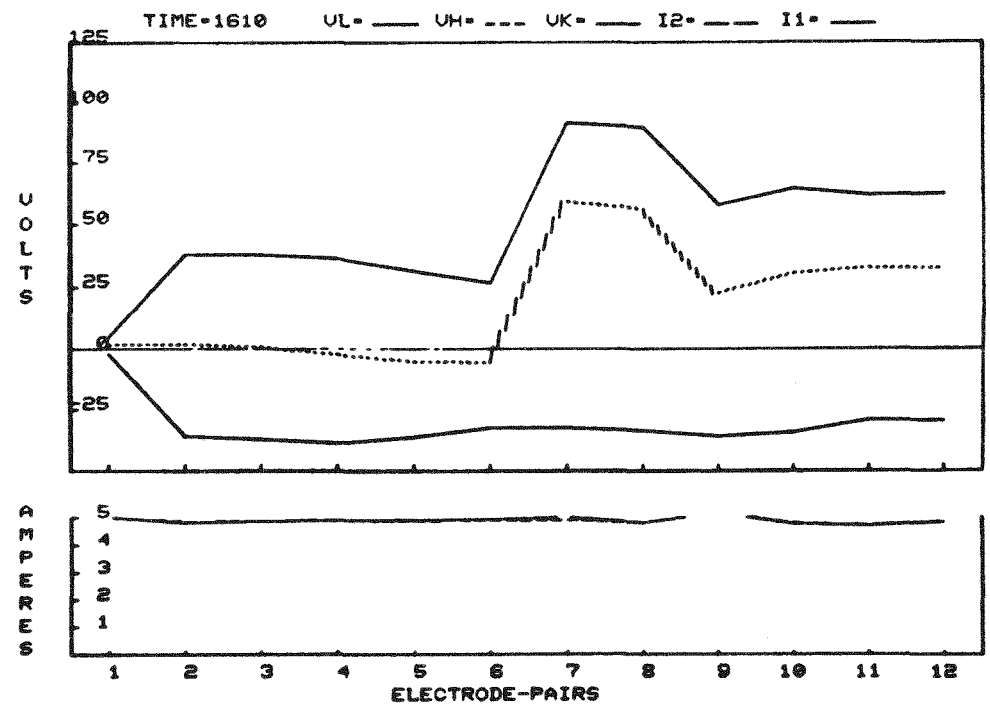

Figure 63. Applied Voltages and Currents, WESTF Test 40 - Run 3, No Axial Voltage

different times during Test 40-3. The curves on Figure 61 were taken some 2 hours before the introduction of seed while the generator was being brought up in temperature. A very slight current was evident in EP12 at 1110, see Figure 61 (a). When an anode axial field was applied, the shift in electrode potentials was in the anticipated direction. See Figure 61 (b) taken at 1120. The current which shows up at EP1 at this time is a measure of the circulating current produced by axial interelectrode leakage across the cathode insulation due to a combination of impressed voltages between the cathode of EP1 and the anode of EP12. The leakage current was probably by way of a path through EP12 (which had previously, at time 1110 demonstrated leakage current) and the cathode insulation interposed between the cathodes of EP12 and EP1.

Due to the location of the current sensors this leakage current does not read in the circuit of EP12, but will read in the circuit of EP1. The magnitude of the anode leakage current is read directly by means of current sensors in series with the axial power supply which applies a simulated Hall voltage between the anodes of EP1 and EP12. The magnitude of the anode leakage current which is listed on Figure 61 (b) compares to an anode leakage resistance between the anode SgEP1 and EP12 of about 100 ohms. The presence of significant axial leakage across both the anode and cathode interelectrode insulation at the low temperatures at which the channel was operated at an early stage in the run appears to be the result of residual seed in the channel left over from WESTF Test 40-2.

As the temperature of the channel was increased the currents through the different electrode-pairs of the channel initially increased, then decreased. The currents recorded may have been produced as the result of volitalization of seed left over from WESTF Run 40-1. These currents rapidly became negligible, apparently due to transport of seed from the channel and the absence of a seed replenishment process. Current in the channel initially showed up in the electrode-pairs at the beginning and end of the channel, apparently due to high leakage currents to the end flanges.

The axial anode leakage current tended to increase with time, compare Figure 61 (b) with Figure 63 (a). The anode axial voltage was impressed

between the anode electrodes of EP1 and EP12. Since both the input and output flanges of the channel were effectively at ground potential, leakage currents could proceed either by way of the intermediate insulation along the anode side of the channel, or by way of leakage to the adjacent grounded flanges. In order to determine whether significant leakage by way of the grounded flanges was occurring, the anode axial voltage was applied between the anodes of EP2 and EP11. This change of electrical connection as can be seen in Figure 63 (b), resulted in a substantial decrease in leakage current, corresponding to a leakage resistance of 18.4 ohms instead of 9.4 ohms. This observed decrease in leakage resistance encouraged the hypothesis that leakage by way of the grounded flanges played a significant role in the leakage effects noted.

Within a period of approximately 10 minutes after the change in connection, the axial current increased to its former values. Similar effects were noted when the anode axial voltage was impressed along quarter lengths of the channel, as between EP4 and EP9.

The mechanism for the decrease in leakage resistance noted requires further testing. Possible mechanisms for this effect are discussed later in this report.

The application of axial current was discontinued because of the high leakage currents. The channel load current during the run was gradually increased to 5 amperes. The substantial change in channel characteristics with time as the load current was increased can be seen in Figures 61 to 63. From these figures it is apparent that the voltage required to impress a given current across the channel is significantly lower at the extremities than it is in the center of the channel. The voltage required to pass 5 amperes through the different electrode-pairs of the channel varied markedly with time. In general it tended to decrease over long periods of time. The electrode-pairs near the ends of the channel usually had lower voltage drops due to the leakage currents by way of the end flanges.

In order to provide a better picture of the change in channel characters with time, the data obtained during Test 40-3 in the form of curves like Figures 61

to 63, can be plotted as a function of time for each electrode-pair of the channel. Typical curves are shown in Figures 61 and 65. The shut-down noted at 1455 was due to a preheater problem. The data were taken at discrete intervals and the curves plotted by connecting the experimental points taken at these times. The curves thus are a close but not exact indication of the change in channel parameters with time. Over the course of Test 40-3 the voltage required to impress 5 amperes varied from over 150 volts to less than 50 volts.

The voltage versus current curves taken during run 40-3 differ significantly from those taken during run 40-2. The curves shown in Figures 66 to 68 were obtained as the current was increased from 2 to 5 amperes. There is less evidence of the marked voltage threshold noted on similar curves taken during Test 40-2. Some "S" shaped curves and curves with vertical slopes are still evident, however.

The very steep slopes at EP11 and EP12 on Figures 68 may be due to initially very low resistance leakage paths at the exit flange. The increase in resistance evidenced by the change in slope of the curves as current is increased is possibly due to volitalization of materials from the connecting path (probably seed) due to heating losses as current was increased.

The seed was turned off at 1638. Resistance measurements taken using an ohmeter at 1642 in general showed resistances of the order of 100 to 200 ohms between anode and cathode, and somewhat lower values of resistance between the cathode and ground. Resistances between the anodes and ground generally were in the range between 1 and 2 ohms per the first 6 anodes and between 9 and 16 ohms per the last 6 anodes more than an order of magnetude lower than the resistances between the cathodes and ground. Similarly, the interelectrode resistances between adjacent anodes, which were less than one ohm per the first 6 anodes, were more than an order of magnitude lower than the corresponding interelectrode resistances on the cathode side.

Previous tests on hot electrode channels generally resulted in lower cathode than anode leakage resistances. Further investigation is needed to determine

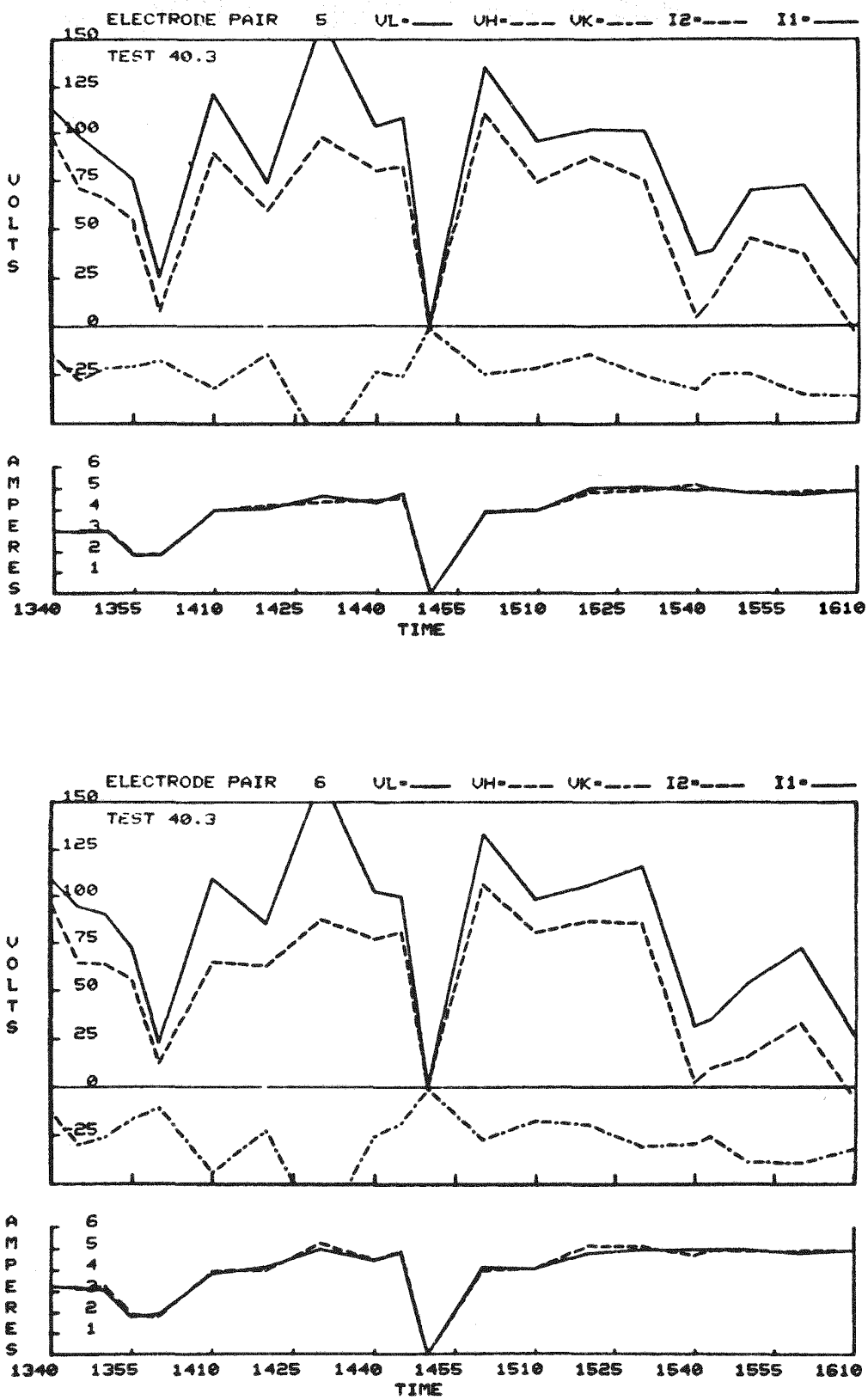

Figure 64. Voltages and Current through Different Electrode-Pairs as Function of Time, Test 40 - Run 3

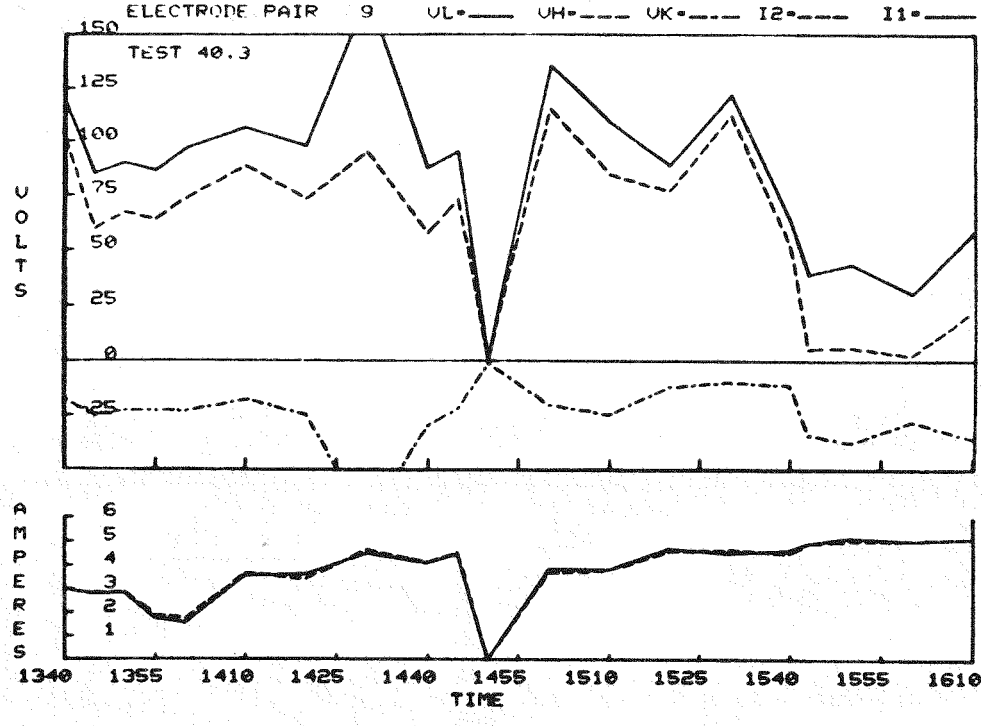

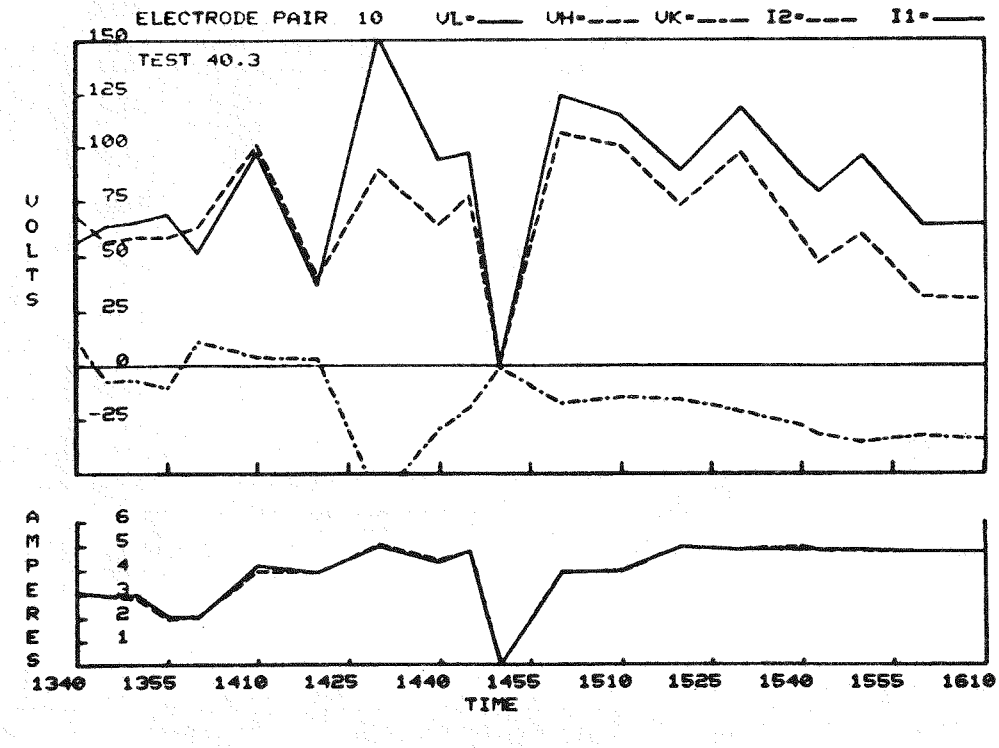

Figure 65. Voltages and Current through Different Electrode-Pairs as Function of Time, Test 40 - Run 3

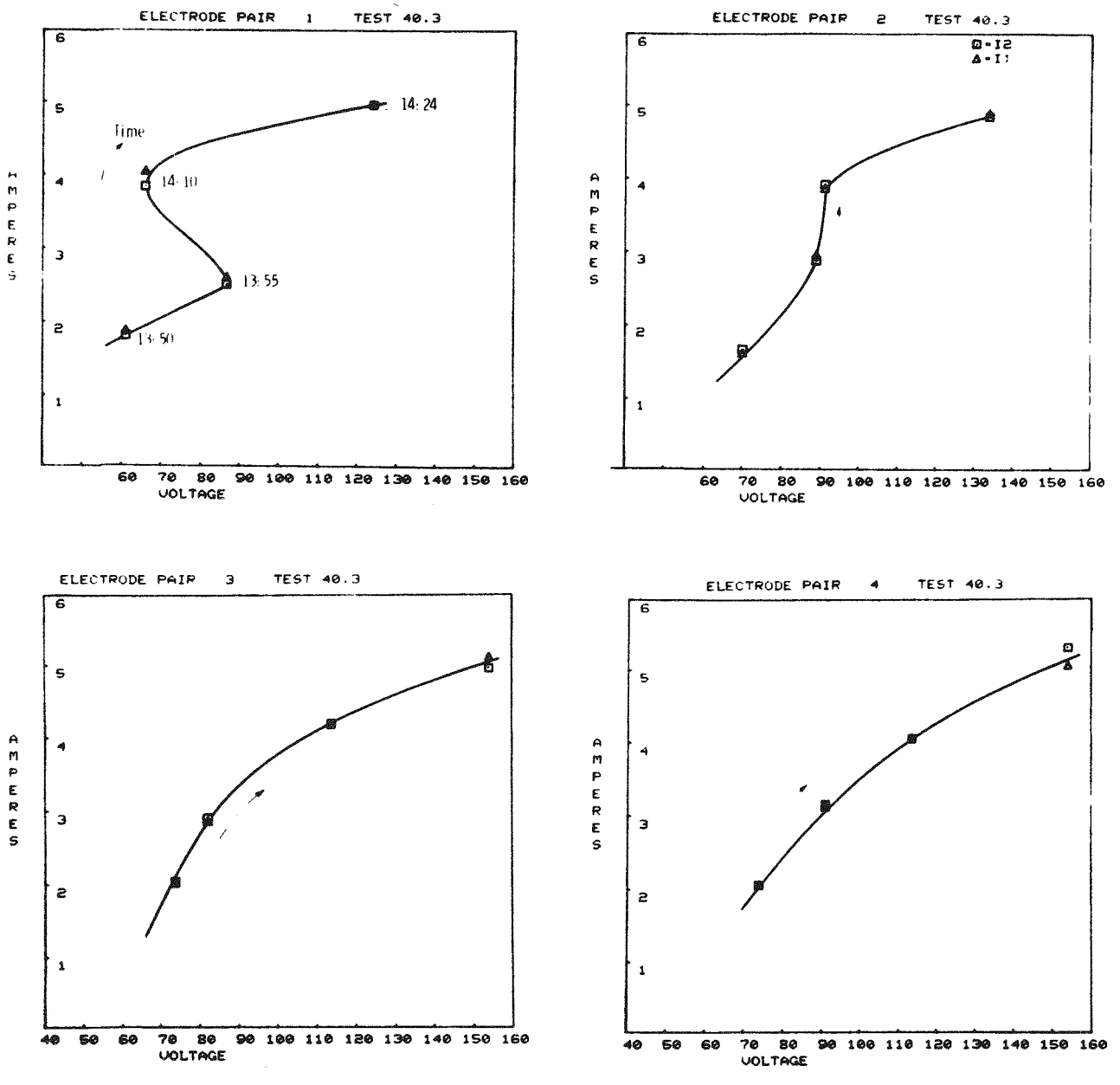

Figure 66. Currents through Different Electrode-Pairs as Function of Impressed Voltages, Test 40 - Run 3, 1350 to 1424 Hours

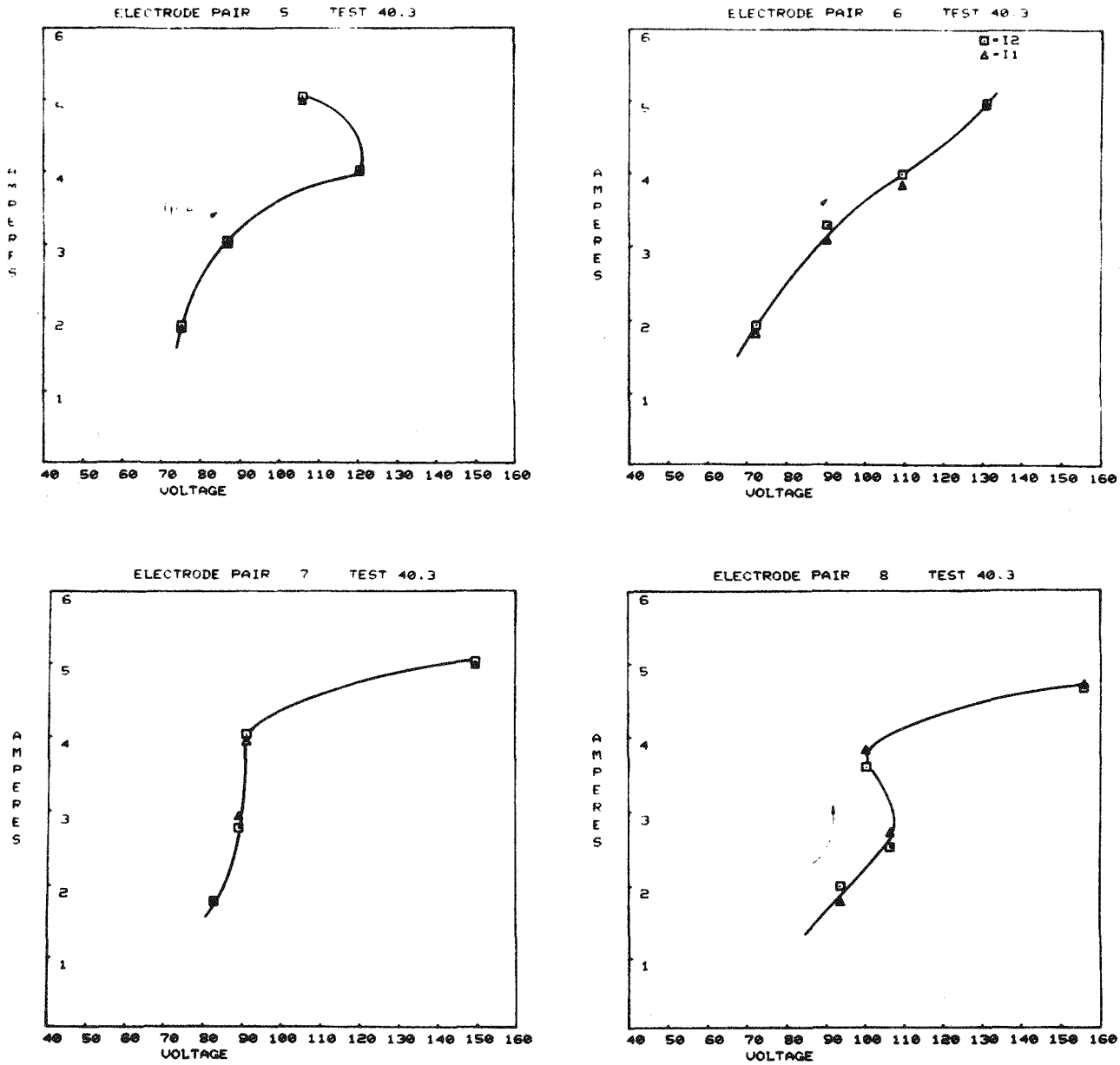

Figure 67. Currents through Different Electrode-Pairs as Function of Impressed Voltages, Test 40 - Run 3, 1350 to 1424 Hours

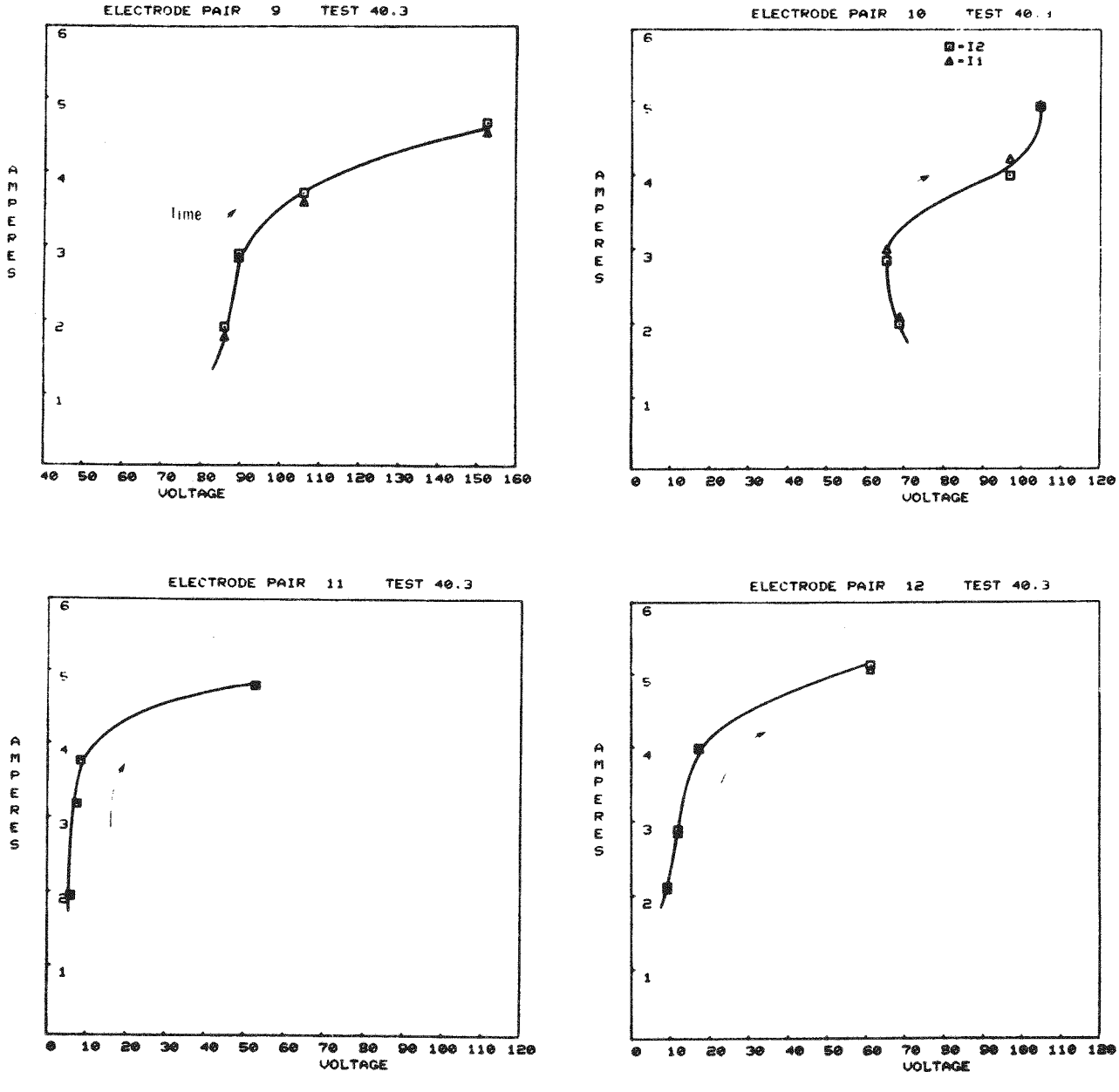

Figure 68. Currents through Different Electrode-Pairs as Function of Impressed Voltages, Test 40 - Run 3, 1350 to 1424 Hours

whether the lower anode leakage resistance noted in tests on channel 40 resulted from the imposition of anode axial fields, or whether it is related to higher anode erosion associated with the loads impressed on the generator under arcing conditions.

Test 40 Run 4

Test 40-4 was conducted without making any channel modifications. The insulation between the flange at the outlet side of the channel and ground was improved by inserting a micarta section within a pair of flanges supporting a final water cooling spray attachment mounted a couple of yards downstream from the channel. At the beginning of the test, the resistance between the flange and ground was greater than 200 ohms. The C_nA_n electrical connection was also used in Test 40-4. Representative plots of the potential of the positive electrodes, V_H, the negative electrode V_K, the applied potential V_L, and the electrode currents versus electrode-pair number at different time intervals during the run are shown in Figures 70 to 74. Seed was injected at 1253. At the bottom of each of these figures are separate curves in which the potentials of water-cooled copper heat sinks which back the top insulating wall of the channel are superimposed on the same plots of anode and cathode potentials versus electrode-pair number which appear in the graphs at the tops of the figures.

A key to the terminology used in identifying the locations of the heat sinks on on the top insulating wall is shown in Figure 69. As indicated in this figure the top insulating wall is divided into 5 sections on the anode side labeled TA1 to TA5, 5 comparable sections on the cathode side labeled TC1 to TC5, and 5 central sections labeled T01 to T05. Slabs of 3.5 mm thick spinel, which had the same dimensions as the heat sinks, were attached to the heat sinks with a conductive epoxy. Adhesive strips of 10 mil thick G-10 and RTV silastic adhesive were used to insulate the heat sinks from each other.

Figure 70 shows such a pair of characteristic curves taken about an hour before seed was injected as the channel was heating up. The leakage currents evident at several locations in the generator at low temperatures were the result of seed deposits laid down during Test 40-3. The higher leakage currents resulting

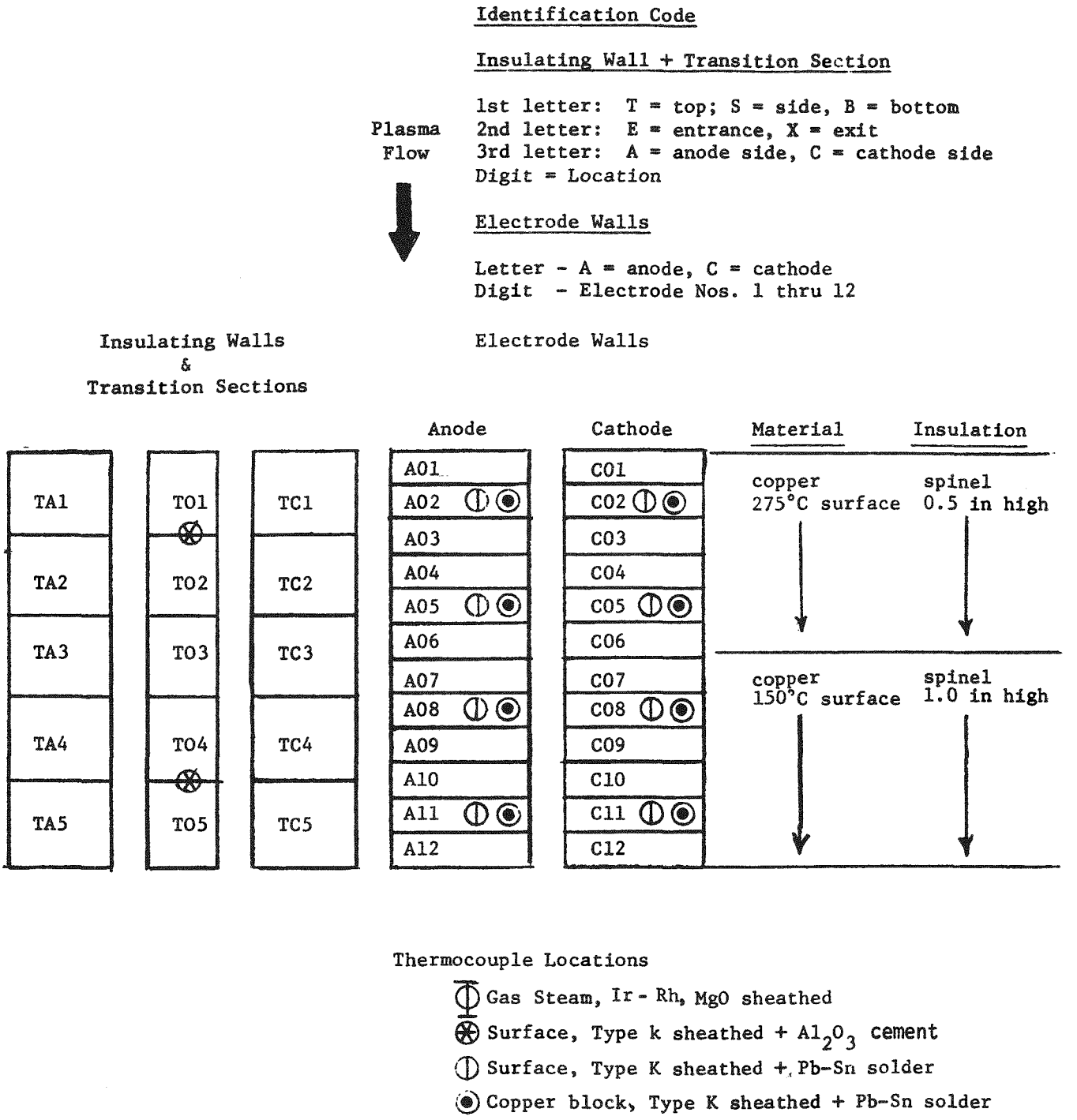

Figure 69. Channel Schematic - Test 40

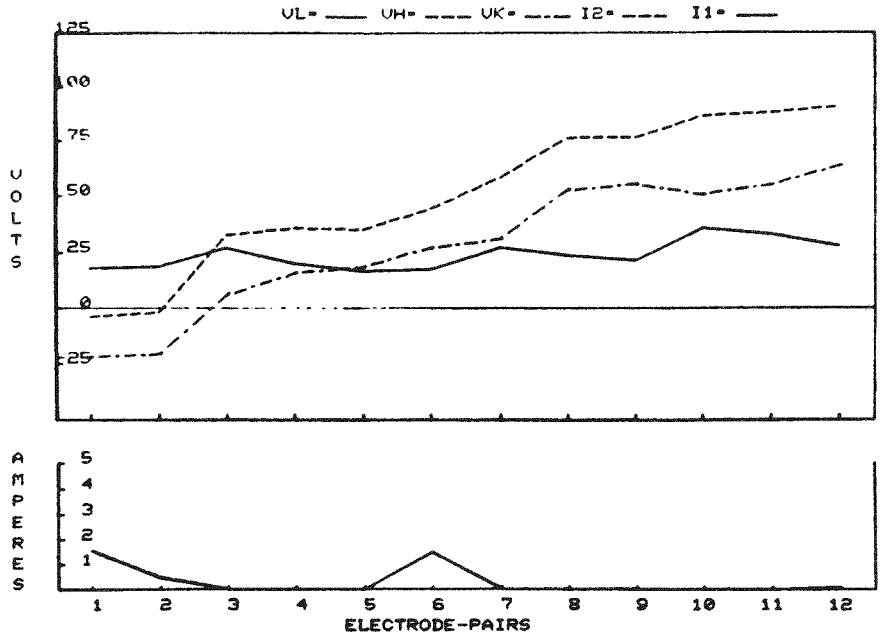

(a)

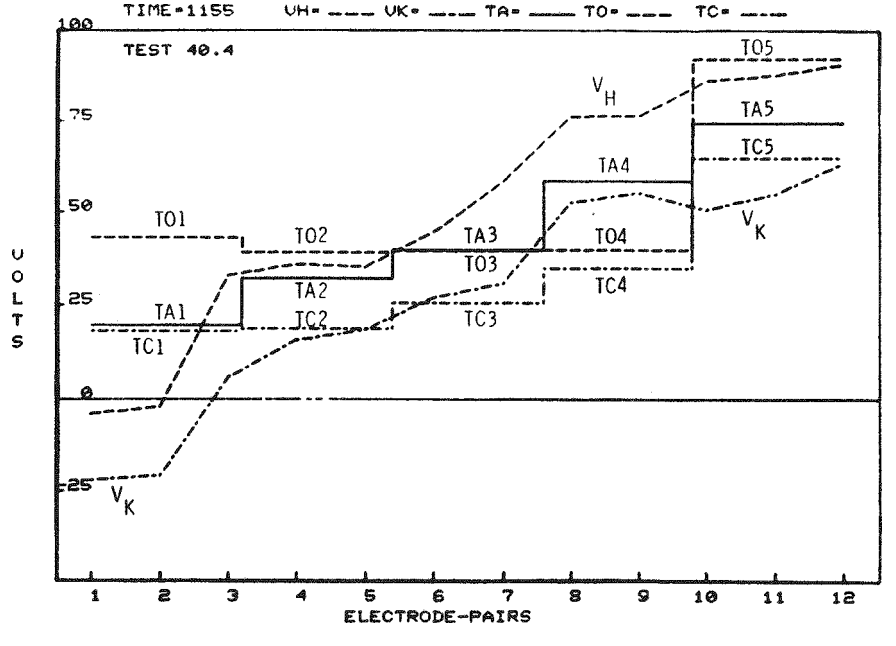

(b)

Figure 70. Applied Voltages, Currents and Floating Potentials of Water-Cooled Copper Heat Sinks in Top Insulating Wall, with Anode Axial Voltage of 98.2V, 5.3 Amperes, Time 1155, Test 40 - Run 4

from the residues of the previous run is also evidenced by the 5.3 ampere leakage current drawn when an axial voltage was impressed between the anodes of EP1 and EP12. This current corresponds to a leakage resistance of 18.5 ohms.

It is evident in the absence of appreciable plasma within the generator that leakage tends to cause the potentials of the heat sinks in the top insulating wall roughly to follow the axially impressed field. It will be noted that TO1, however, tends to be more positive than the potential of the neighboring heat sinks or electrodes. This higher potential is an indication that there is a low resistance path between TO1-TO2-TO3 and TO4. Expressed another way, the resistance along the TO1-TO4 line is small compared to the resistance between the TO line and the TA and TC lines of insulators at least at the upstream end of the channel.

The imposition of a cathode axial field at this time resulted in a somewhat higher leakage current on the cathode side of channel, corresponding to a 12.7 ohm leakage resistance.

As noted earlier the magnitude of anode leakage currents tends to be read on the power supply across EP12 per axial fields impressed on the cathode. When anode axial fields are used, the axial leakage current through the cathode electrodes tends to be read on the ammeters in series with the EP1 power supply.

The generater electrical characteristics taken in the absence of an axial field are shown at 1300 in Figure 71, 7 minutes after seed was introduced. At this time all of the heat sinks in the vicinity of TA4, TO4 and TC4 appear to have low leakage resistance connections to each other. As can be seen in Figure 72, the anode leakage resistance as measured at 1324 using an anode axial field dropped to 6.4 ohms. The insulating wall segments all appeared to have low leakage resistance connections of the anode as compared to the leakage resistance to the cathode electrodes.

When an axial field was impressed on the cathode side at 1330, see Figure 73, the cathode axial leakage resistance dropped to 4.7 ohms. The insulating wall elements still exhibited low resistance connections to the anode electrodes.

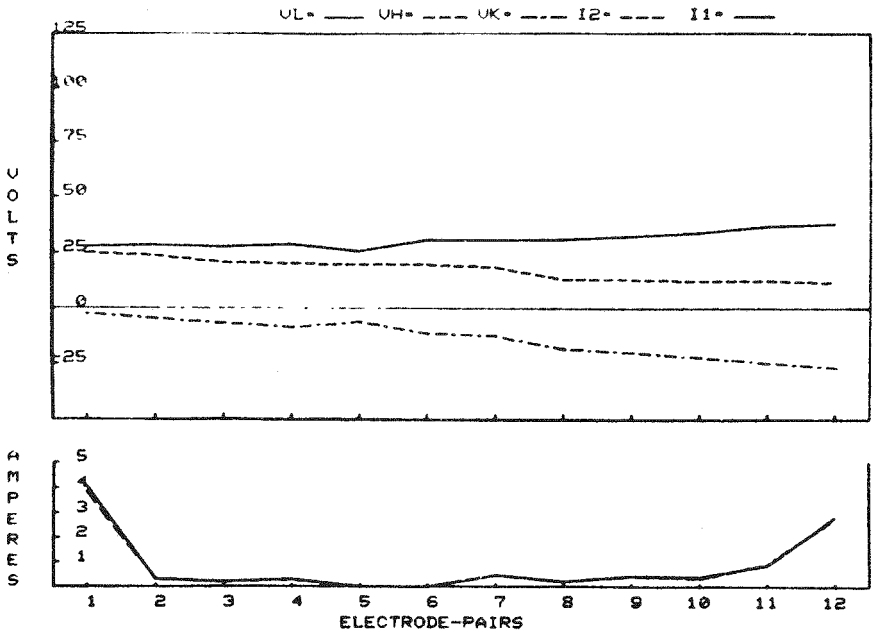

(a)

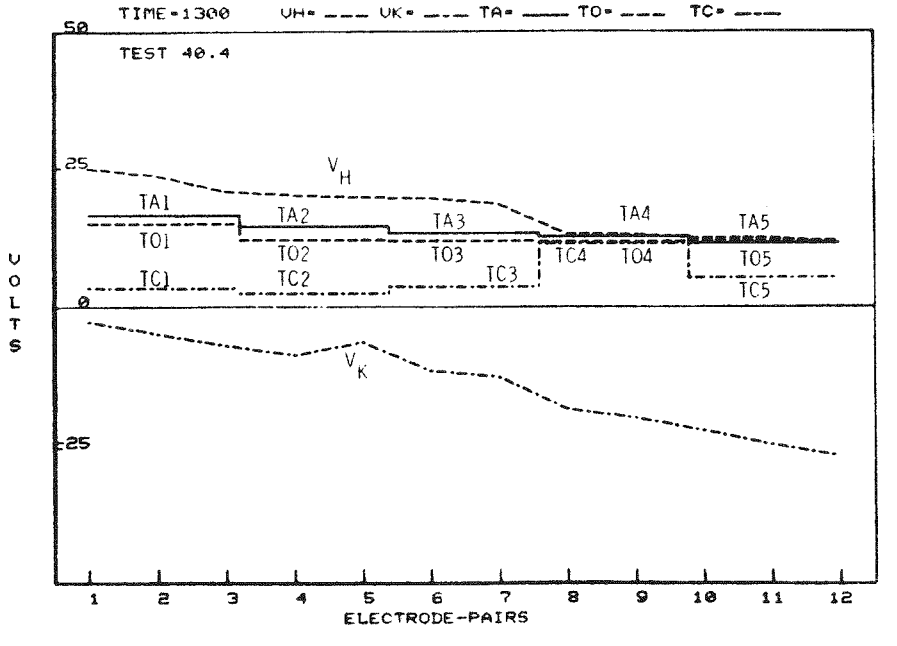

(b)

Figure 71. Applied Voltages, Currents and Floating Potentials of Water-Cooled Copper Heat Sinks in Top Insulating Wall, No Axial Voltage, Time 1300, Test 40 - Run 4

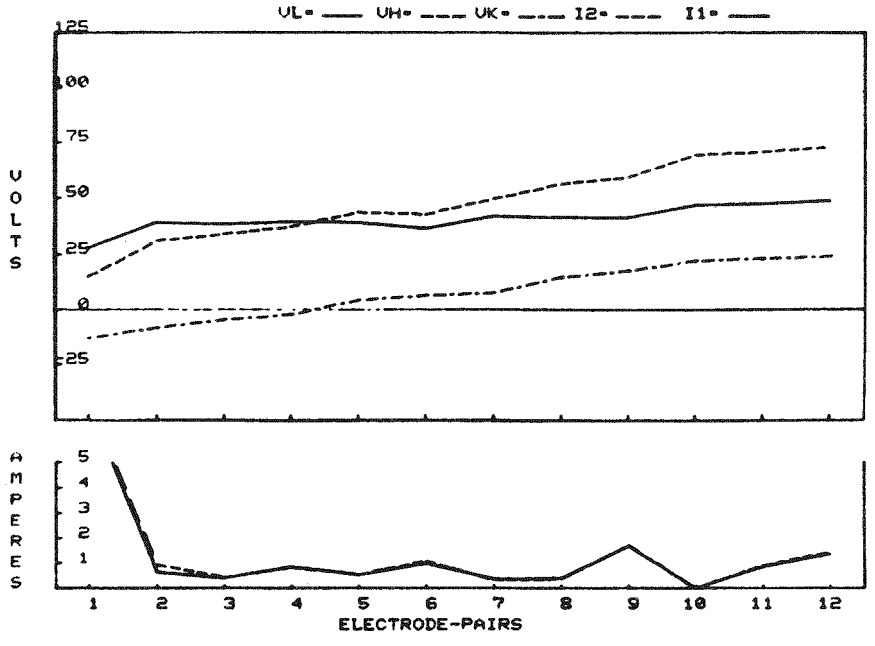

(a)

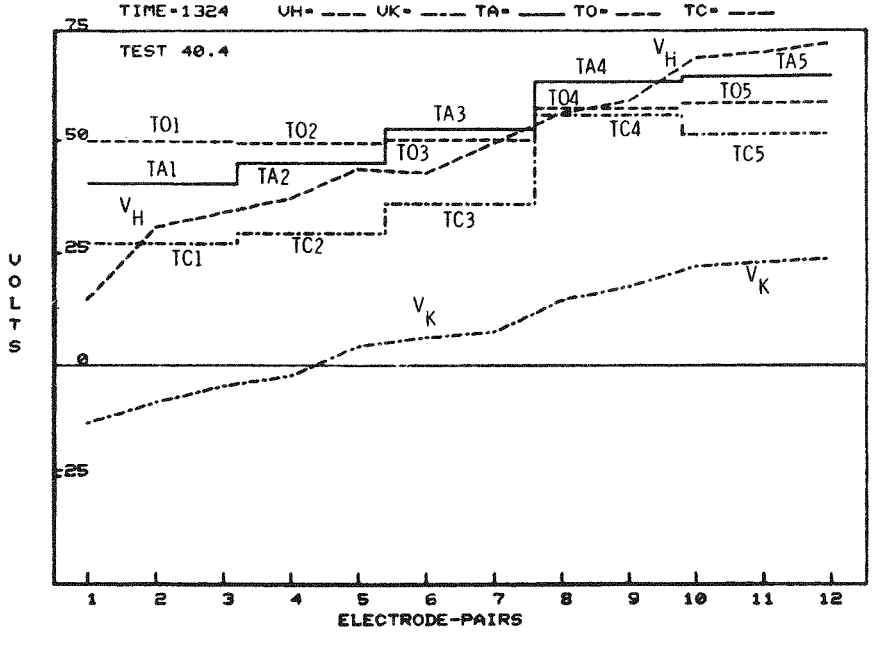

(b)

Figure 72. Applied Voltages, Currents and Floating Potentials of Water-Cooled Copper Heat Sinks in Top Insulating Wall with Anode Axial Voltage of 55.9V, 8.8 Amperes, Time 1324, Test 40 - Run 4

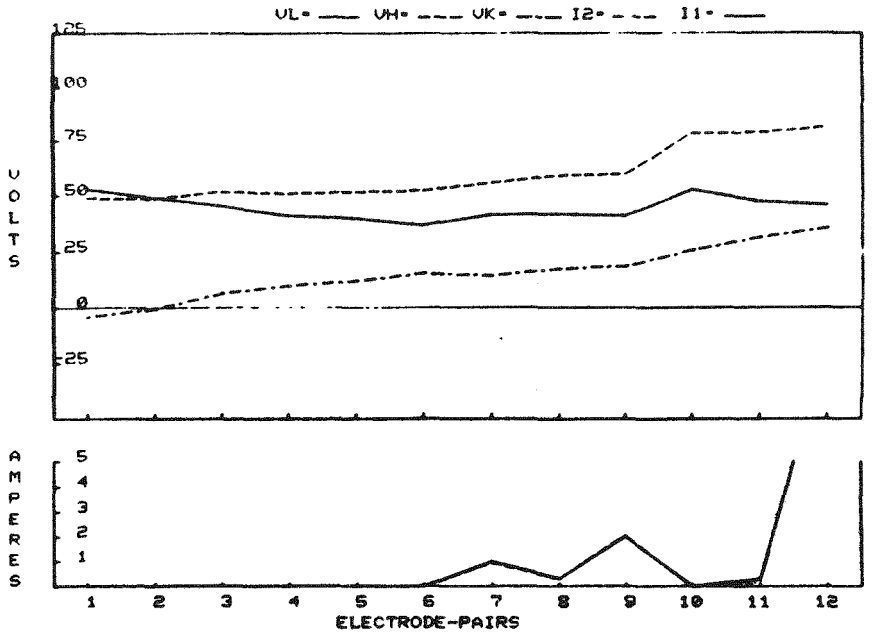

(a)

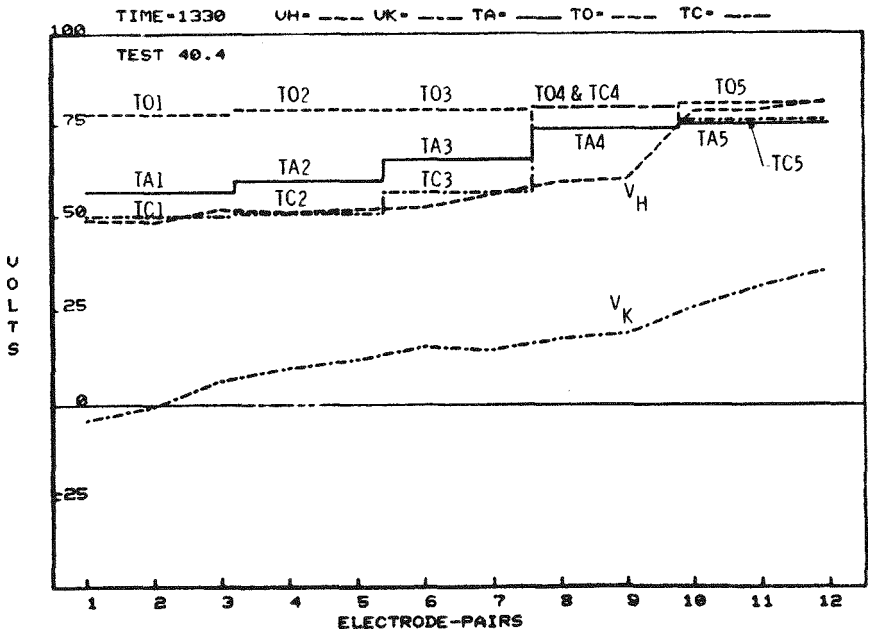

(b)

Figure 73. Applied Voltages, Currents and Floating Potentials of Water-Cooled Copper Heat Sinks in Top Insulating Wall with Cathode Axial Voltage of 39.4V, 8.3 Amperes, Time 1330, Test 40 - Run 4

The application of axial fields was discontinued because of the very high axial leakage currents experienced. Once the axial fields were terminated and the load currents through the generator brought over 2 amperes, the pattern of insulating wall potential changed in the direction of exhibiting lower leakage resistance to ground than to either anode or cathode electrodes. Figure 74 is representative of the change in electrical characteristics which took place.

During a one hour period between 1440 and 1538, the generator was operated at loadings between 4 and 5 amperes. The voltage required to achieve these currents was generally between 50 and 75 volts for electrode pairs 3 to 8. Electrode pairs 9 to 12 generally required voltages less than 50 volts. Electrode pairs 1 and 2 tended to require intermediate values of voltage.

Figures 75 and 76 are representative curves showing the electrical characteristics of different electrode-pairs as a function of time and loading. By comparing the voltages necessary to impress 5 amperes across different electrode-pairs on such curves it is easy to verify that lower voltages are required at the extremeties of the channel. It is likely that the current paths at the extremities of the channel are shunted by the end flanges.

Once the current had been brought to 5 amperes in Test 40-4 the current in each electrode-pair was slowly dropped to 0.5 ampere and then slowly increased back to 5 amperes. This dip in load is evident between 1404 and 1440 in the curves of Figures 74 and 75.

Ampere versus volts curves, representative of those obtained, are plotted in Figure 77 with the currents decreasing and in Figure 78 with the current increasing. Most of the curves taken with the current decreasing had the reverse or mirror image of a "C" shape. All of the curves taken with the current increasing had the "C" form.

Referring to the curve for EP5 on Figure 78, it seems very probable as the current is increased above 1.5 amperes that heating of the plasma occurs. The

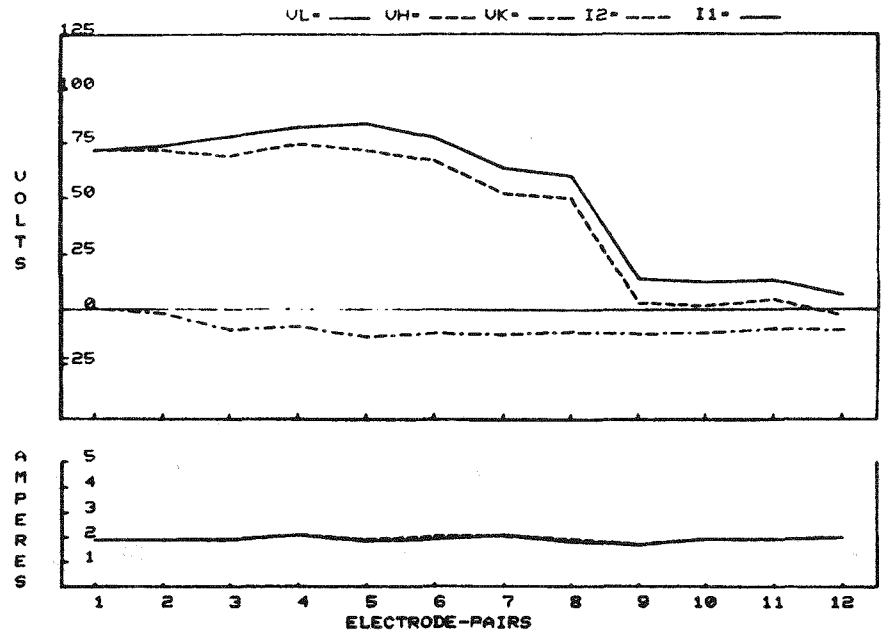

(a)

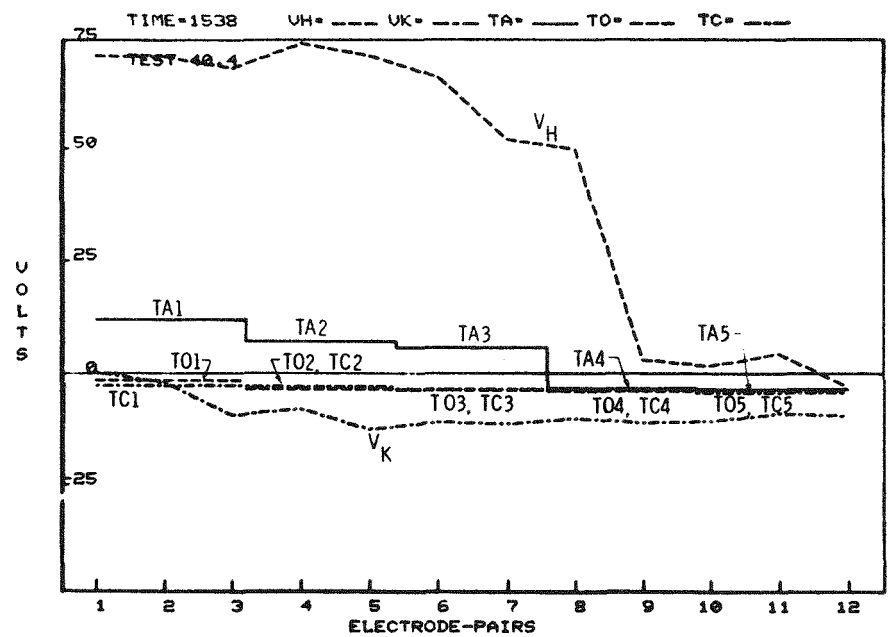

(b)

Figure 74. Applied Voltages, Currents and Floating Potentials of Water-Cooled Copper Heat Sinks in Top Insulating Wall, No Axial Voltage, Time 1538, Test 40 - Run 4

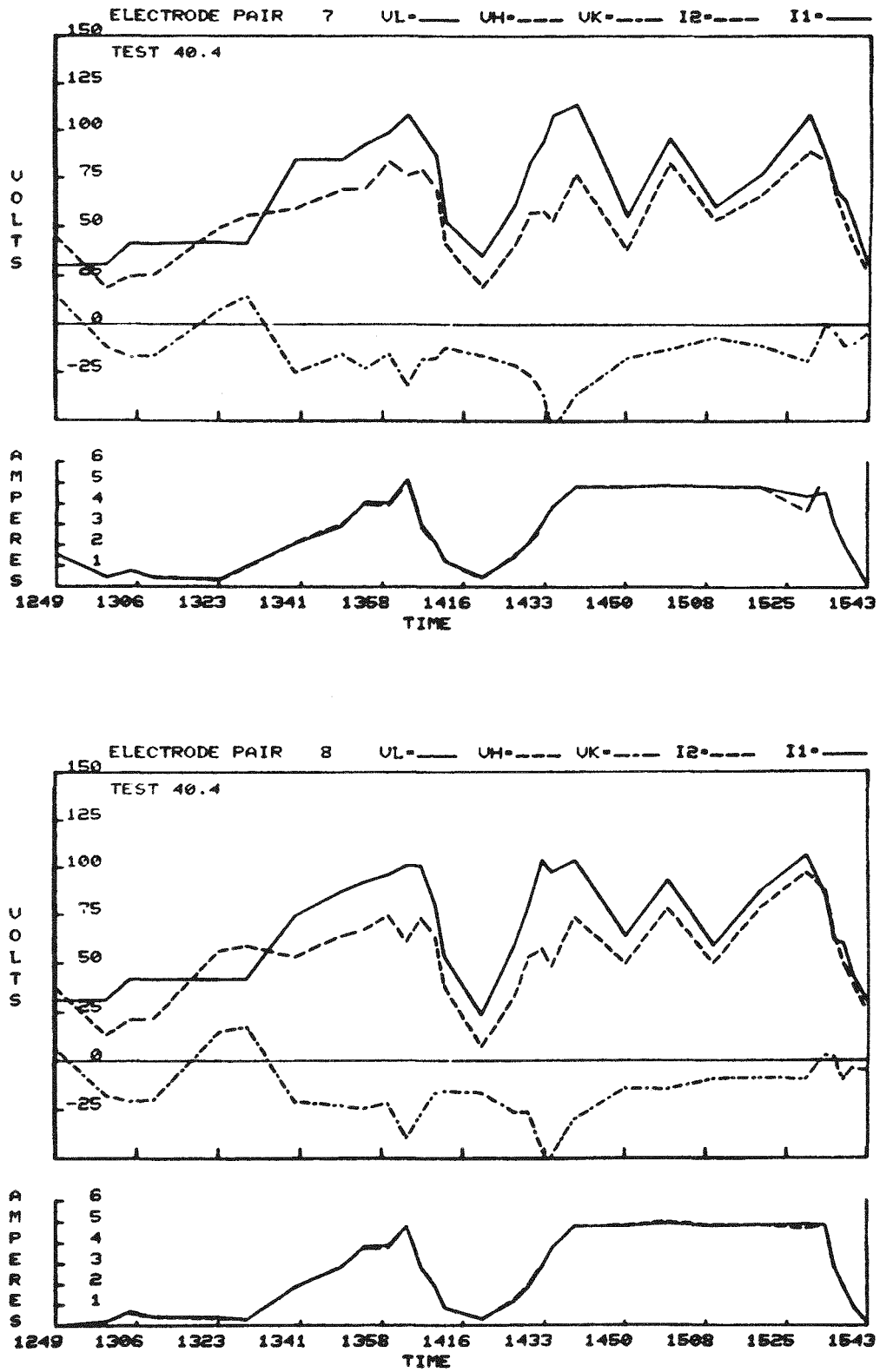

Figure 75. Voltage and Current Characteristics of Different Generators

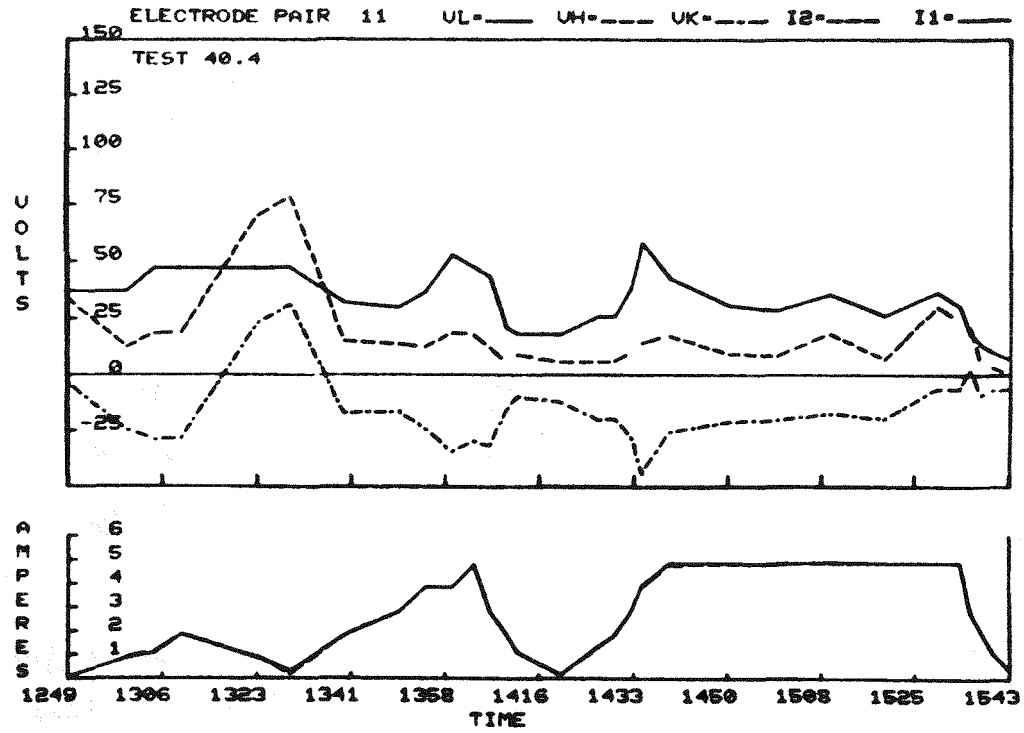

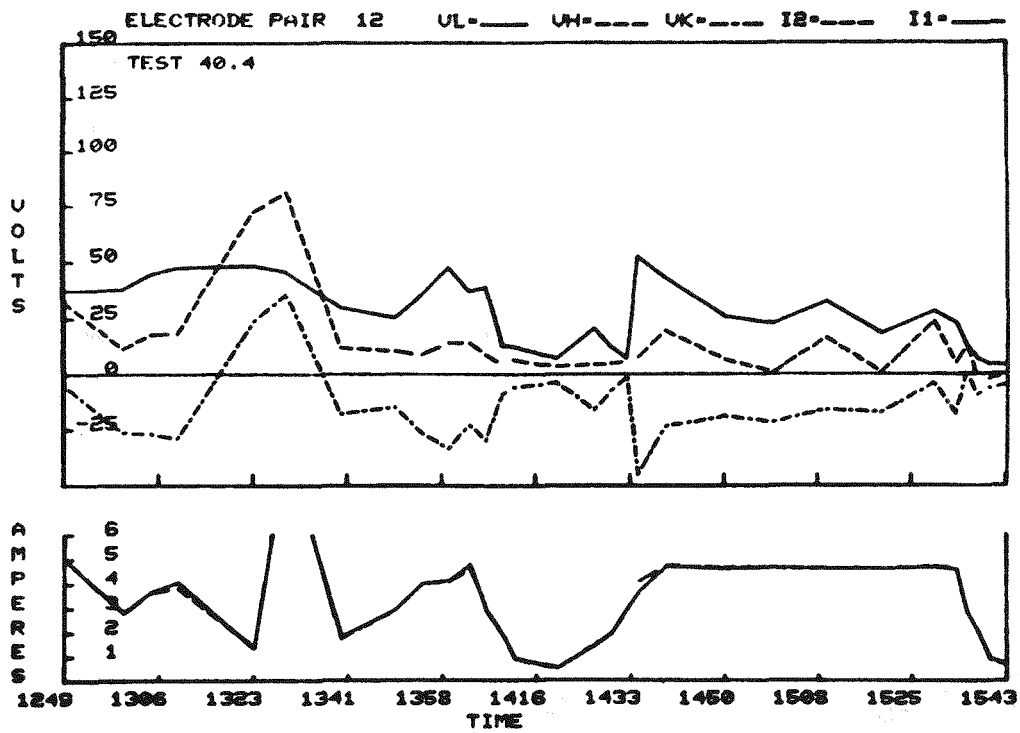

Figure 76. Voltage and Current Characteristics of Different Generators

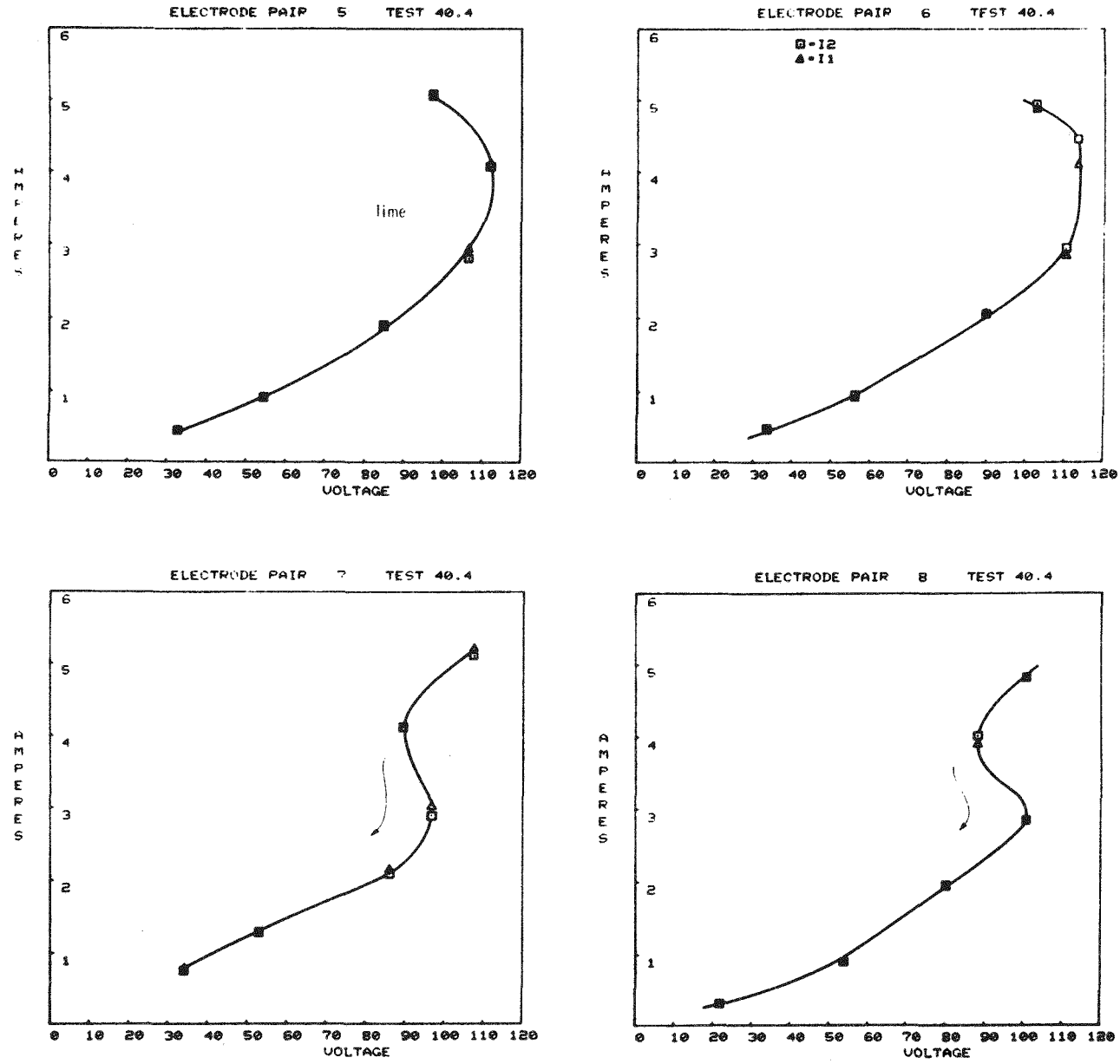

Figure 77. Currents through Different Electrode-Pairs as Function of Impressed Voltages, Test 4 - Run 4, Time 1404 to 1416 Hours, Current Decreasing

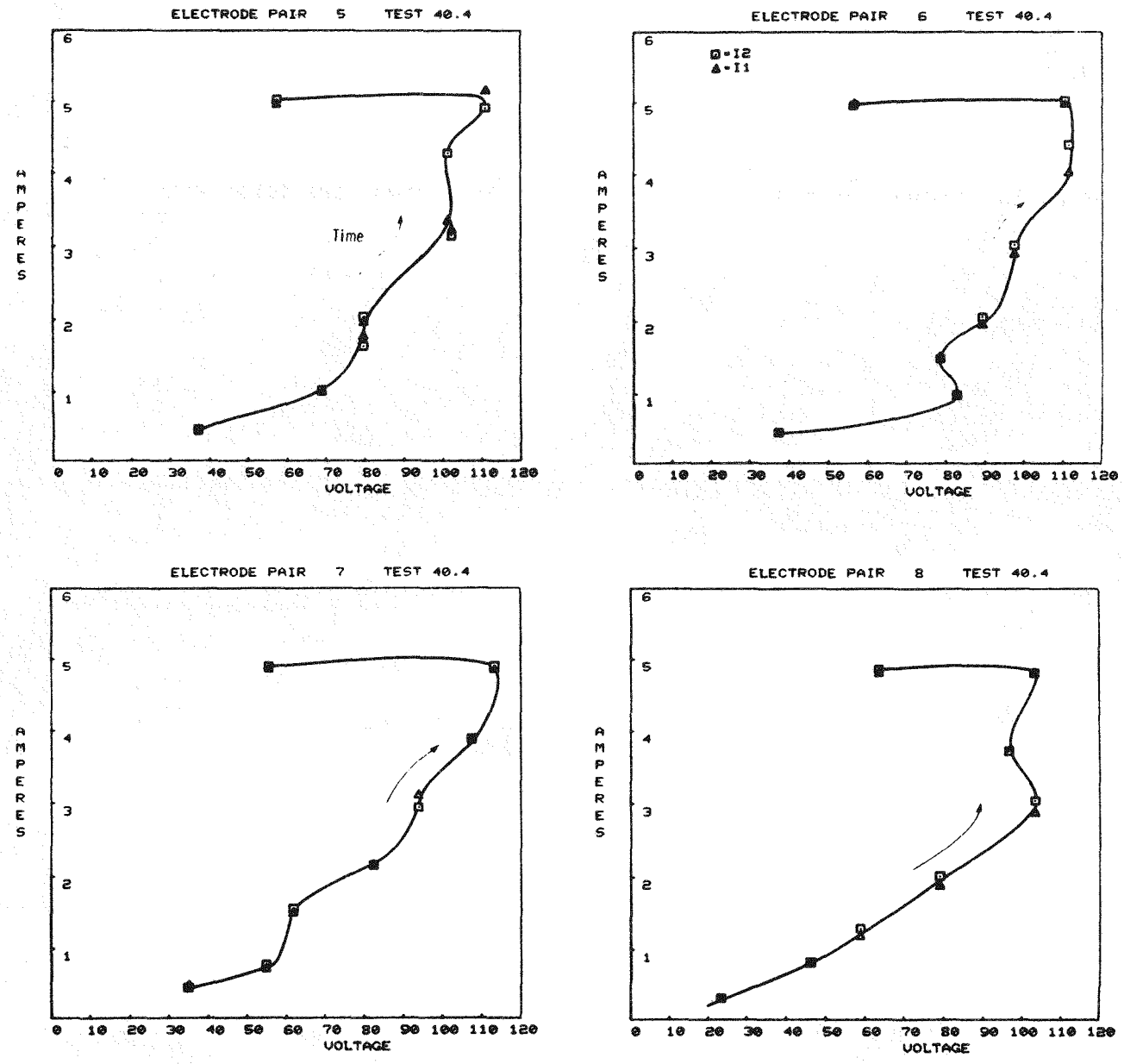

Figure 78. Currents through Different Electrode-Pairs as Function of Impressed Voltages, Times 1420 to 1451, Increasing Current, Test 40 - Run 4

resultant increase in plasma conductivity lowers the voltage required to impress the higher currents. Once the 5 ampere level has been reached the plasma heating which takes place over the 5 minute interval between 1448 and 1451 tends to lower the voltage required to pass 5 amperes.

It should be stressed that these curves, and in fact most of the electrical data taken on the channel once appreciable currents are drawn, are taken with the voltage supplies in the current control mode. If these data were taken in the constant voltage mode, from the shape of these curves it seems clear that the plasma conductivity increase with time would result in destructive breakdowns and consequent electrode overheating.

As indicated previously, the increase in plasma conductivities with increase in current is responsible for the negative slopes attributed to the usual volts versus amperes arc characteristic curves.

At low currents the voltage threshold effects noted in Test 40-2 are absent in almost all cases. It is likely that a voltage threshold effect is present but it is masked by the relatively high leakage currents resulting from the deposition of seed on the insulating walls of the channel during the course of the 4 runs. Possibly the threshold value of current conduction, in the sense that it was observed in Figures 58 to 60, occurs in Figures 77 and 78 at the region of the curves where the sharp transition occurs between the shallow almost linear curve of I versus V_L at low currents and the sharp increases which occur at intermediate levels of current.

Electrical Leakage Dismantling Test

After Test 40-4 was completed and prior to dismantling of the channel, anode and cathode axial fields were applied successively and the leakage currents across the total length of electrode insulation on the anodes and cathodes sides of the channel were determined at room temperature. The top insulating wall was then removed and similar measurements repeated. The results, which are summarized in Table 12, show that removal of the top insulating wall resulted in a very substantial decrease in axial leakage current. The anode axial

TABLE 12

AXIAL ROOM TEMPERATURE CHANNEL LEAKAGES AFTER TEST 40-Run 4
BEFORE AND AFTER REMOVING TOP INSULATING WALL

TEST CONDITIONS	VOLTAGE (Volts)	I_1 (Amperes)	I_2 (Amperes)	RESISTANCE (ohms)	REMARKS	STATUS TOPWALL ON OR OFF CHANNEL
Anode Axial	224	.35	.34	649	Floating	ON
Anode Axial	104	.79	.20	533	Floating	ON
Anode Axial	117	.02	.02	5,850	Floating	OFF
Cathode Axial	122	0.46	0.47	262	Floating	ON
Cathode Axial	106	0.0	0.0	10,000	Floating	OFF

leakage resistance increased from the order of 500 or 600 ohms to 5850 ohms, and the cathode leakage resistance increased from about 260 ohms to over 10,000 ohms.

From the results of this test, it is concluded that a significant part of the axial leakage current occured by way of the insulating walls. The electrical contact from the electrodes to the heat sinks in the insulating walls may have been by way of a rounded field of slag and condensed seed which was observed to be present at the corners between the insulating and electrode walls.

Discussion of Results of Test 40, Run 1-4

Because of our preheater problems and a reduced level of oxygen, plasma temperatures were low during Test 40-1 and it was not possible to draw significant load currents. Once these various problems were corrected, it was possible during the next three runs to bring each of the 12 electrode-pairs of Test 40 to 5 amperes, which corresponds to a loading of 1 ampere/cm^2 per electrode.

During Run 40-2 each electrode-pair was operated for a total of 4.4 ampere-hours. The electrode-pairs in Test 40-3 were operated for a total of 9.4 ampere-hours, and in Test 40-4 a total of 7 ampere-hours.

A total of 20.8 ampere-hours of loading per electrode-pair was drawn in Tests 40-2, 40-3, and 40-4, corresponding to 74,900 coulombs of load per electrode-pair. About 3.5 grams of copper was lost from each anode, corresponding to a rate of loss of copper per anode of 47 μ grams/coulomb. The loss of weight from the cathodes was negligible. The average load density during the three runs was of the order of 0.8 amperes/cm.

The relatively uniform loss of copper from the anodes is taken as a fairly reliable indication that the current transport during Tests 40-2, 40-3, and 40-4 occurred by way of the plasma discharge. The impressed voltage required to pass a given current varied substantially during the tests, possibly due to variations in plasma conductivity or to variations in the character of the plasma discharge. For example, during Run 40-3 with the load current at 9.0 amperes the lowest voltage across any electrode-pair in the channel at any given time varied from

30 to 80 volts. The highest voltage required to transmit 5 amperes varied from 92 to 133 volts. The end electrode-pairs were excluded from the above considerations.

The voltage to produce a loading of 5 amperes was substantially lower for most of Test 40-4. The highest voltage required to pass 5 amperes varied from 60 to 108 volts. The lowest impressed voltage at any given time varied from 4 to 37 volts.

The shape of the ampere versus voltage curves and the uniform anode erosion which occurred appear to indicate that the arcing which took place during the loading of test 40 extended from anode to cathode electrodes directly across the channel. The upper sections of the mirror image "C" shaped curves discussed previously, see Figures 77 and 78, is apparently the direct result of the heating of the intervening plasma.

The striking change in shape of the I versus V_L characteristics with time during Tests 40-2, 40-3 and 40-4 appears to be the result of the leakage resistance across the channel decreasing as the test progressed. For example, early in the life of the channel, see Figure 58, a very definite voltage threshold between 60 and 80 volts was noted. Apparently this voltage was required to produce electrical breakdown of the slag layer. At this stage of channel life, the leakage resistance across the channel was relatively low. In Figures 77 and 78 there was still evidence of the voltage threshold, the slope of the near linear part of the low current part of the graph, which for an ohmic resistance is equal to $(\frac{1}{R})$, corresponds to an initial leakage resistance across the channel of roughly 50 to 60 ohms.

Once the impressed voltage becomes high enough to establish a plasma discharge only about 50 or 60 volts was required to impress the 5 ampere load current through a given electrode-pair. These values of voltage and current correspond to an effective resistance of the order of 10 ohms. If the cathode and anode potential falls at the surface of the electrodes are neglected, a 10 ohm value of resistance corresponds to a plasma conductivity of about 5 mhos/meter. Thus it would appear that the estimated conductivity of the plasma under a loading

of 5 amperes was substantially greater than 5 mhos/m. The decrease in plasma conductivity with current indicates that some ohmic heating of the plasma was occurring.

Because of the high axial leakages experienced it was not possible to determine plasma conductivities by application of axial fields as performed in earlier tests with hot electrodes.

The sharp decrease in axial leakage currents which occurred when the top insulating wall was removed apparently indicates that a substantial fraction of the axial leakage was carried by longitudinal currents along the length of the insulating walls. It seems evident that the insulation between the end of the electrode and the side walls needs to be improved. In addition the inter-electrode insulation and the insulation between the end electrodes and the terminating flanges of the duct should be strengthened.

The erosion rate of 47 μgrams/coulomb from the anode is somewhat higher than the anode erosion rate reported by AVCO (Reference 27) of 7.5μ grams/coulomb. It is believed that the higher erosion rate experienced in WESTF is probably related to the difference in the nature of the arc discharge. As noted earlier from the shape of I versus V_L curve it was surmised that the arc discharge extended directly across the WESTF channel which is only 2.5 cm wide. The basic source of damage for the AVCO channel was breakdown between the core gas and the anode electrode, rather than across the channel between the cathode and anode electrodes, which for the AVCO channel is greater than 15 cm.

The increase in axial leakage current or decrease in axial leakage resistance with time noted during these tests has also been noted by Demirjian, Petty and Solbes (Reference 25). They observed that with continued operation the slag layer impedance on the cathode wall slowly decreases with time. They also observed a healing process that occurs during power interruption in which the resistance of the slag layer increases. They expressed the view that the effect may be due to evolution of a slag species composition or disturbance due to the passage of current. In our tests we have noted that these effects occur on both the anode and cathode electrode walls.

There are several possible explanations for the effect. The decreased axial resistance with operation may be due to ohmic heating of the relatively cool combination of seed and slag adjacent to the electrodes. Alternately, it may be due to an electrolysis effect in which potassium or iron ions are released. The combination of the two processes could also be involved. Both of these effects would be expected to be reversible.

The association of the axial leakage current with the slag layer gives definite credence to the hypothesis that a significant fraction of the axial leakage currents observed travel along the surface of the electrodes by way of the slag-seed layer.

WESTF Test 41, Run 1

Disassembly

This run was terminated after approximately 14 hours at conditions due to a gas leak in the test section. The leak occurred in the area of the first cathode where the top insulating wall is joined to the electrode wall. The channel was dismantled at the test facility where a preliminary examination was made.

The top insulating wall was removed first. The center channel section of the wall was free of insulating tiles. There were isolated spots of slag (approximately 1/2 in. dia. x .08 in. thick) on the bare copper; and the edges of the copper blocks showed arcing damage. The silicone rubber gasket at the inlet side was burned out from the corner of the cooling blocks toward the edges of the wall.

When the cathode wall was removed, the slag remained behind. The slag was less than .04 in. thick, and had lines of boron nitride where it came in contact with the electrode wall. The cathode surfaces showed no damage, but some of the boron nitride insulators were cracked or had irregular surfaces. The G-10 spacer backing up the first cathode was badly burned and had several holes through it. The boron nitride spacer used between the first electrode and the inlet transition section was distorted due to overheating. The slag coverage on the anode wall was 2 to 3 times heavier than that on the cathode

wall, and even though it was more adherent, part of it remained with the bottom insulating wall when the anode wall was removed. The spacers associated with the first electrode showed damage similar to that seen on the cathode wall. The general surface condition of the anodes is very good; there was a concentration of arc damage near the base of the wall.

The bottom insulating wall had heavy slag coverage that appeared to be more firmly attached near the exit end. The spinel insulating tiles that remained in the center section of the bottom wall showed signs of slag penetration and fluxing away of the grains. The same was true of the exit transition section. The inlet transition section lost most of its insulators and had virtually no slag coverage.

Figures 79 and 80 show the anode and cathode walls surface condition upon removal from the channel and after removal of slag from the surface. The conditions of the electrodes is such that they will be incorporated in a rebuilt test section.

Electrical Analysis

A description of channel 41 is given in Section 1.2.2. Figure 81 shows the configuration of electrodes, insulating wall components and the code used for identifying them. In order to take advantage of the additional anode axial insulation afforded by the 18 anode/9 cathode construction, an effort was made to power as many of the anodes as possible using separate circuits and separate individual power supplies. A total of 16 power supplies were available for the test. The C_nA_{n+1} configuration was chosen as being a reasonable compromise between the available options. This configuration provides a diagonal field, which as presented in an earlier report (Reference 36), is more compatible with the application of axial simulated Hall fields than the C_nA_n circuit.

The circuit diagram shown in Figure 82 was utilized. Power supply 16 was connected between electrodes A3 and A17,A18 to provide anode axial fields, and between C1 and C8 for cathode axial fields. As shown in the figure electrodes A1 and A2 and C9 were allowed to float. The floating potentials of these electrodes were recorded by the D. A. system during the periodic routine scans.

FLOW DIRECTION →

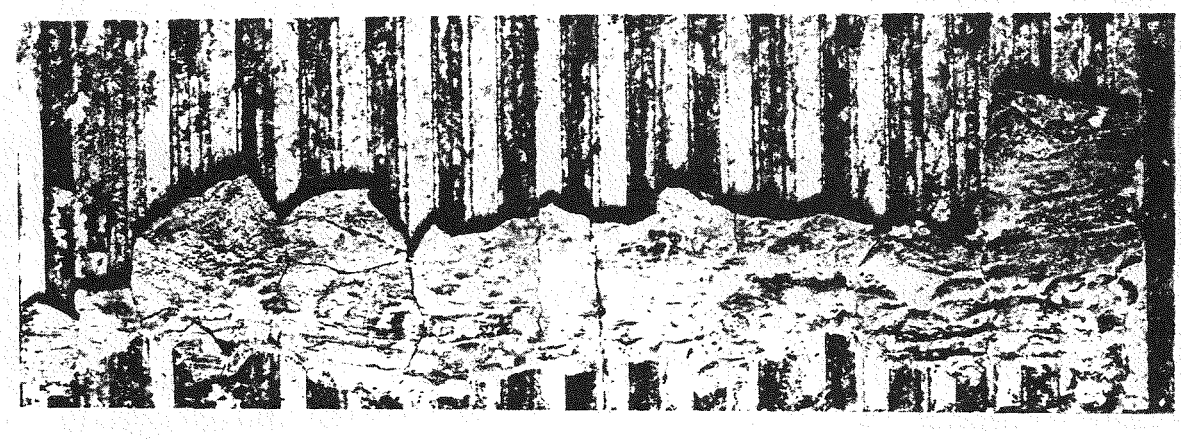

A) Upon Removal from Test Section

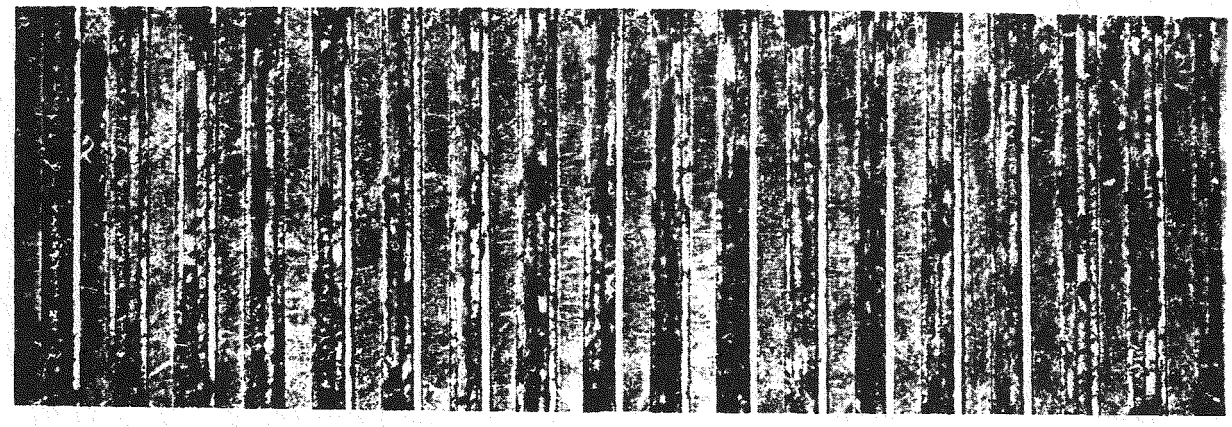

B) After Removal of Slag Layer

Figure 79. Condition of Anode Wall after WESTF Test 41, Run 1

FLOW DIRECTION →

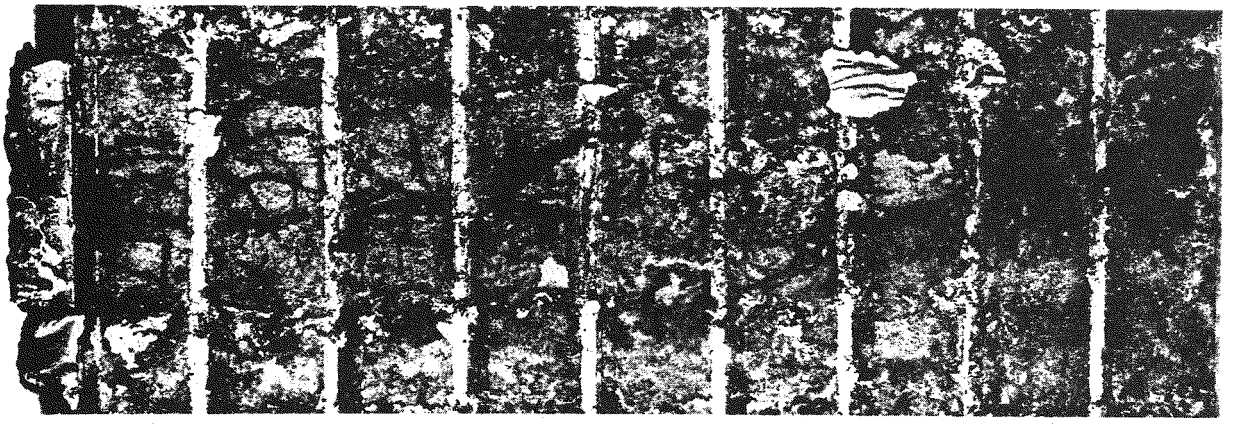

A) Upon Removal From Test Section

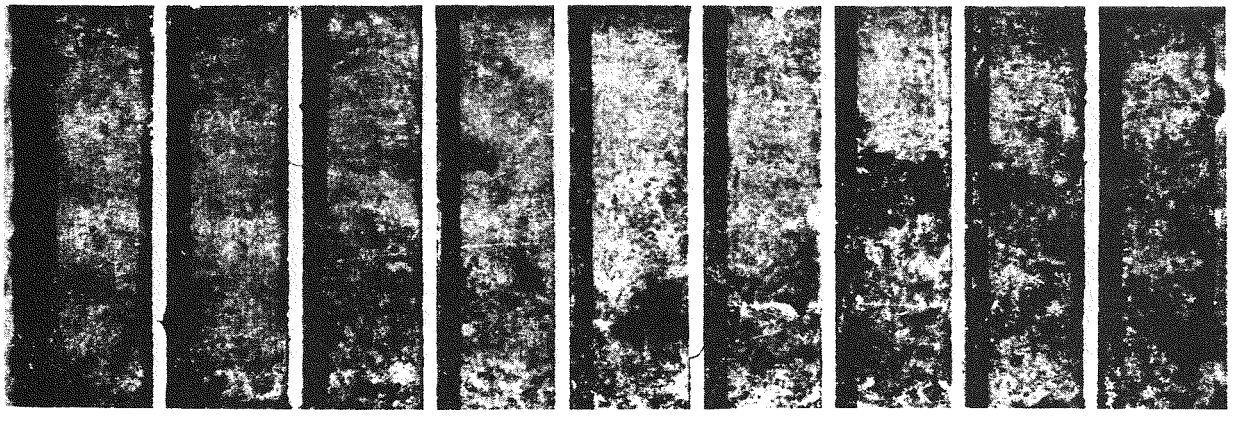

B) After Removal of Slag Layer

Figure 80. Condition of Cathode Wall After WESTF Test 41, Run 1

A special effort was made to isolate the exit flange, from electrically grounded plumbing at the exit sections of the duct. The potentials at which the exit flange operated were automatically recorded.

The circuit shown in Figure 82 was used exclusively during the test. However, the use of axial fields was discontinued roughly half way through the test because of the high leakage currents which developed during the course of the run. Provisions were made to record the potentials of all 36 of the top and bottom wall water-cooled copper backing elements defined in Figure 81.

Test 41-1 was initiated on March 5, 1979 and seed was introduced at 1415. Representation plots of the applied voltages and current which were taken at various times during the test are given in Figures 83 to 85. The electrode-pair numbers indicated in the figures were derived on a sequential basis from Figures 82. EP1 corresponds to the C1-A3 connection shown in the figure. EP2 corresponds to C1-A4, EP3 to C2-A5 connection, etc.

As can be seen from Figure 83, more than one hour was required after the introduction of seed before appreciable current was observed. This time is considered to be the time required for the slag layer to build up. Fifteen minutes after seed was introduced the anode axial leakage resistance was about 1200 ohms. One half hour later it had dropped to 28.5 ohms, see Figure 83 (a). The transverse current through the generator started to build up during the next half hour. During the same time interval the anode axial leakage resistance dropped to 13 ohms. The test schedule called for a loading of 1 ampere/cm^2 over the cathode surface or an 8 ampere loading for each individual cathode. Since there were two anodes per each cathode this loading schedule required a load current of 4 amperes per electrode-pair. As can be seen in Figure 84 at the beginning of the run, voltages of the order of 150 volts were needed to impress 3 amperes through each electrode-pair of the channel.

In order to initiate the passage of load current it was usually necessary to bring the voltage up to a "breakdown" voltage. Once breakdown was initiated the voltage required to impress a given current tended to drop. Electrode pairs

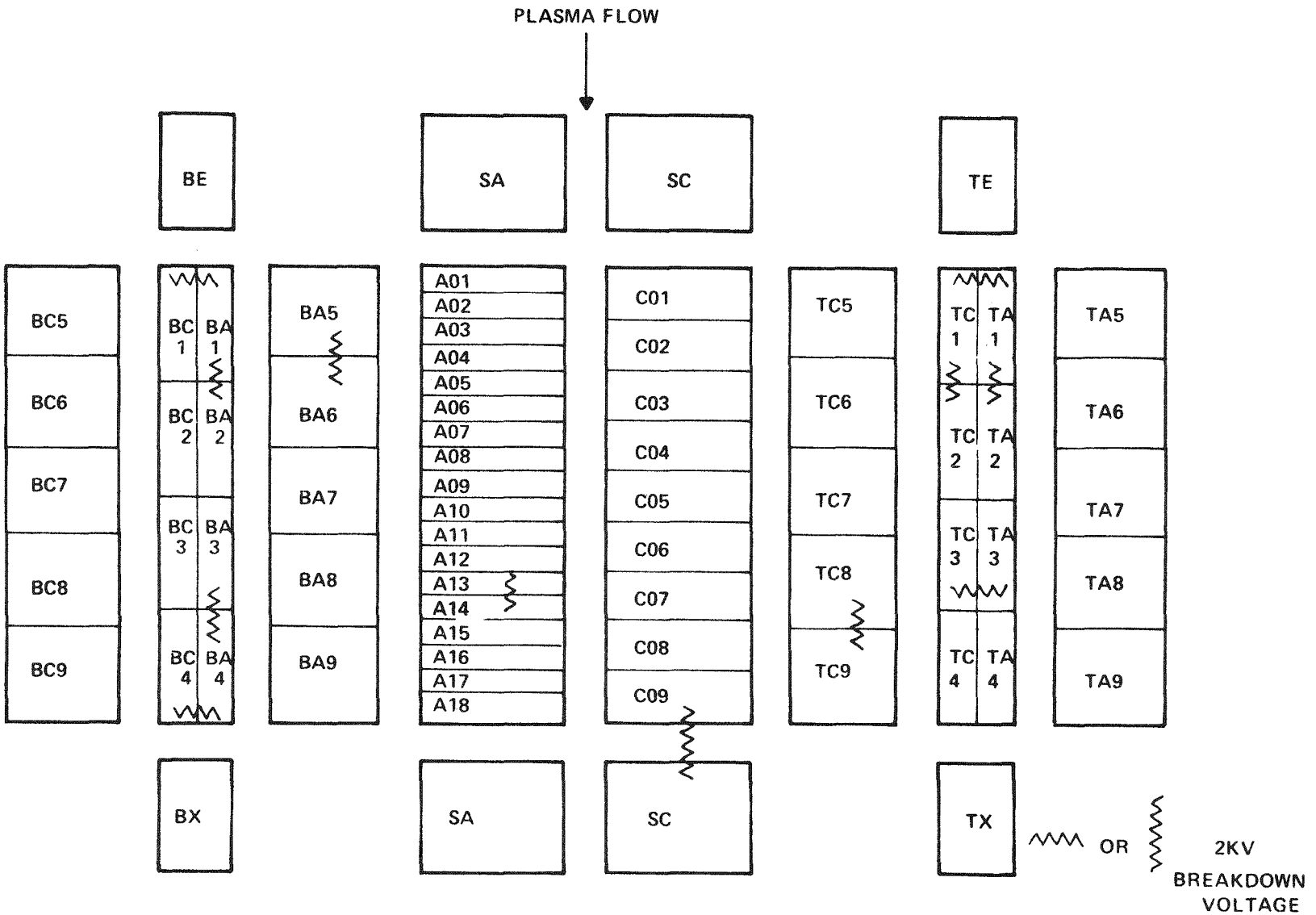

Figure 81. Channel Schematic - Test 41

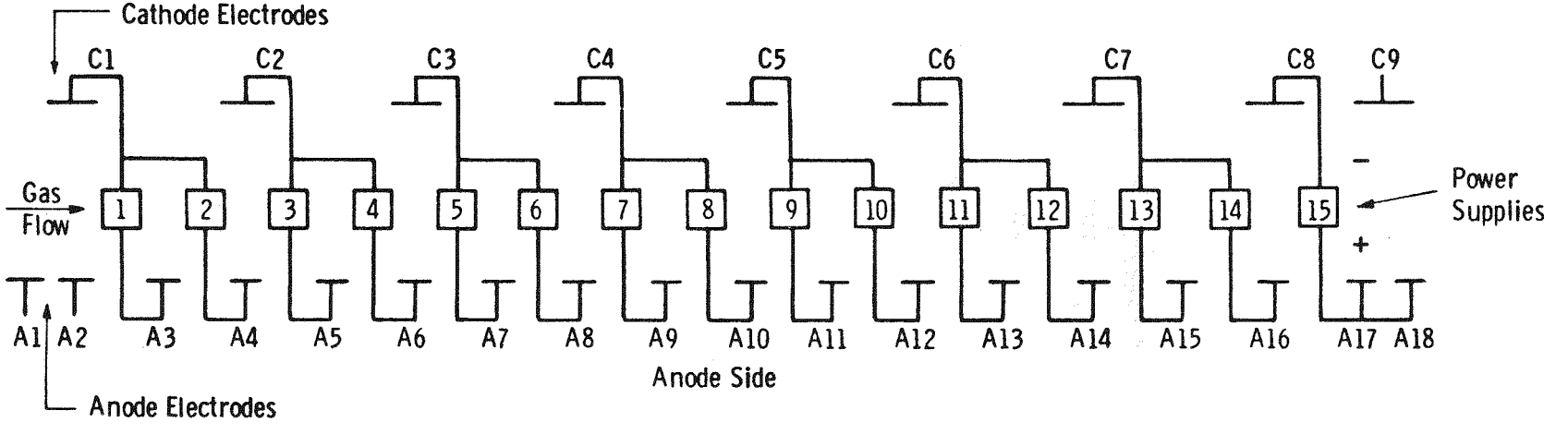

Figure 82. Electrical Circuit Used for Test 41 - Run 1

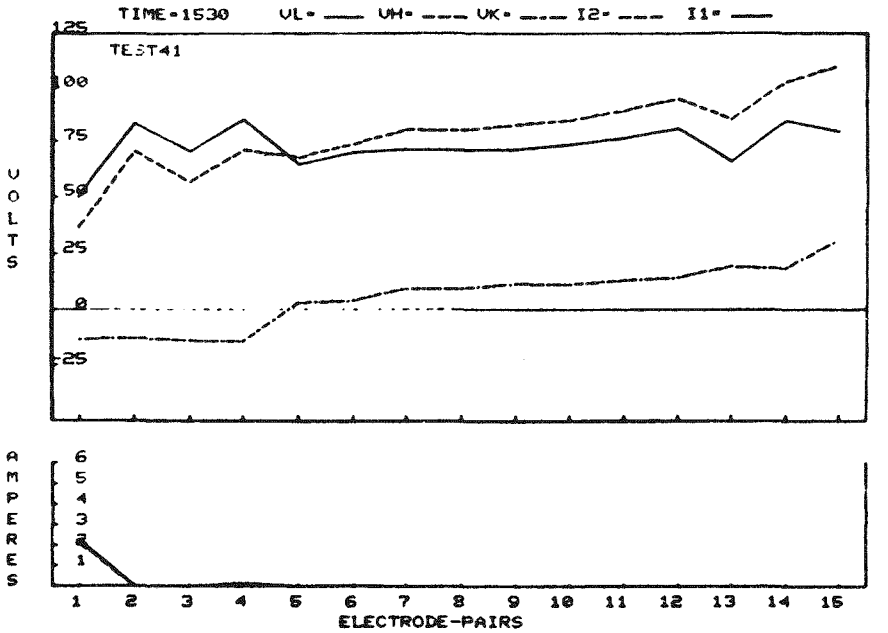

(a) Anode Axial Voltage, 62.6 Volts, 2.2 Amperes

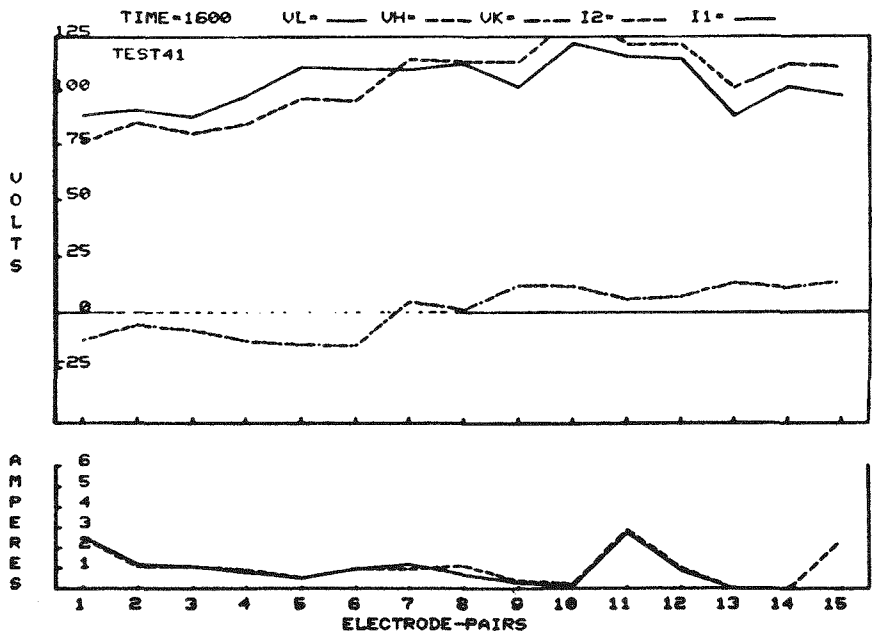

(b) Anode Axial Voltage, 31.2 Volts, 2.4 Amperes

Figure 83. Applied Voltages and Currents For Test 41 - Run 1

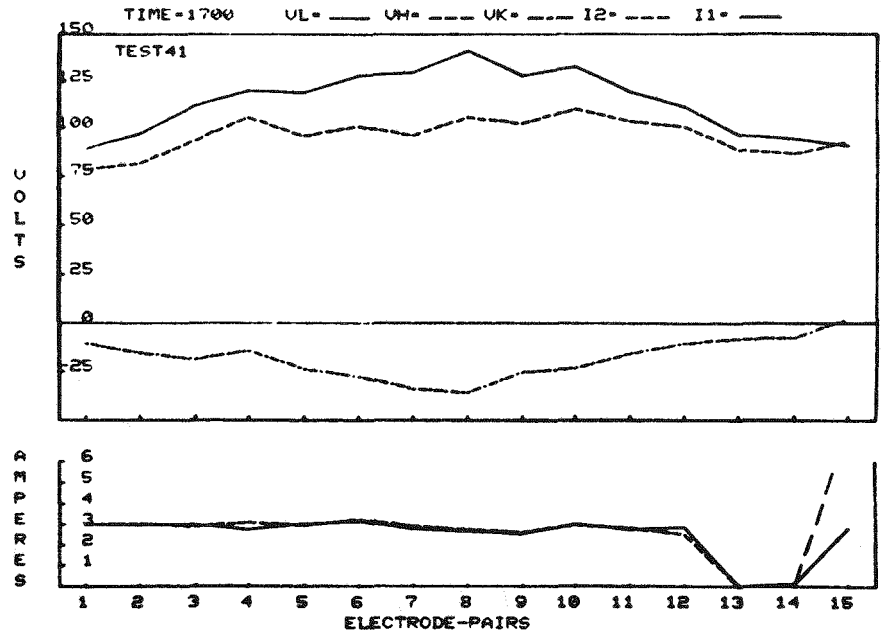

(a) Anode Axial Voltage, 7.5 Volts, 4.8 Amperes

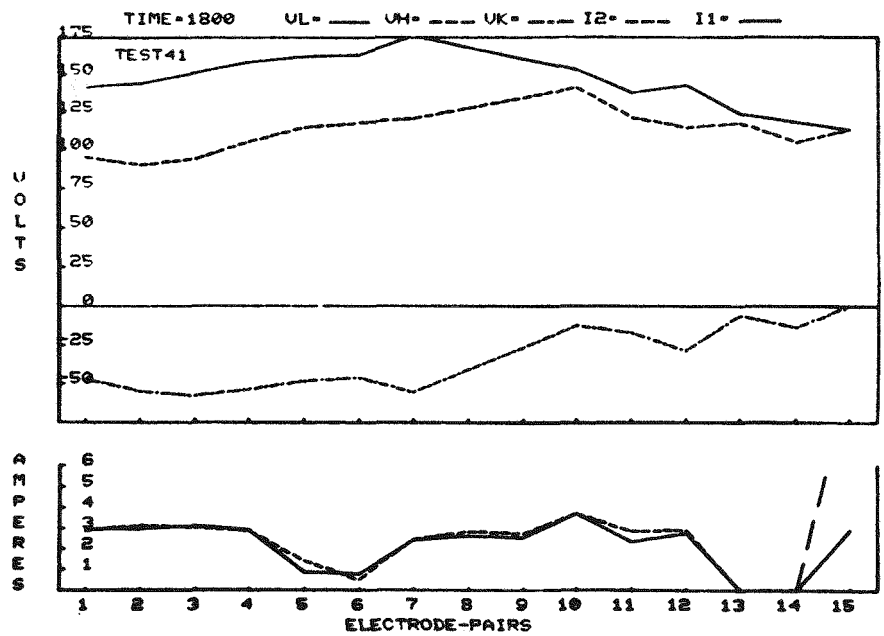

(b) Anode Axial Voltage, 110.0 Volts, 7.7 Amperes

Figure 84. Applied Voltages and Currents for Test 41 - Run 1

13 and 14, however, had power supplies having a maximum rating of 80 volts. From Figures 83 and 85 it is evident that there were time periods when it was not possible to exceed the "breakdown" voltage required to initiate load current.

Once the voltages required to impress 3 amperes dropped below 125 volts, the load current was increased to 4.0 amperes per electrode-pair. At 2140 all of the electrode-pairs in the channel including EP13 and 14 were operating satisfactorily at 4.0 amperes. By 2240, as can be seen in Figure 85, the characteristics of the channel had changed to the extent that the load through EP14 dropped to zero. At this time, within the limits afforded by the voltage available from power supplied 13 and 14, it was not possible to restart the discharge currents through EP13 and EP14.

Representative curves as the currents and impressed voltage of Run 41-1 are shown in Figures 86 and 87 as a function of time for general electrode-pairs circuits of Figures 82. The relatively slow decrease in voltage required to impress a particular load current through a given electrode-pair is evident on these figures. Comparing Figures 86 and 87 with Figures 64/65 and 75/76 it is evident that during the early stages of Test 41-1 the voltages required to impress given currents were significantly higher than the voltages required during Tests 40-3 and 40-4.

The tendency in Run 41-1 for higher voltage to be required to obtain given current loadings is also evident in the representative I versus V_L characteristics shown in Figures 88 to 90.

These curves show a tendency to assume the mirror image "C" shape noted in runs 40-3 and 40-4. However, the voltages required to pass maximum currents tended to be higher.

It is interesting to note in Figure 90 that both EPC7A15 and EPC7A16 (EP#13 and 14) extinguished as the current was being increased back to the original load of 4 amperes. The result was that the voltage output of the power supplies increased to the maximum voltage they could deliver, or roughly 90 volts. At this particu-

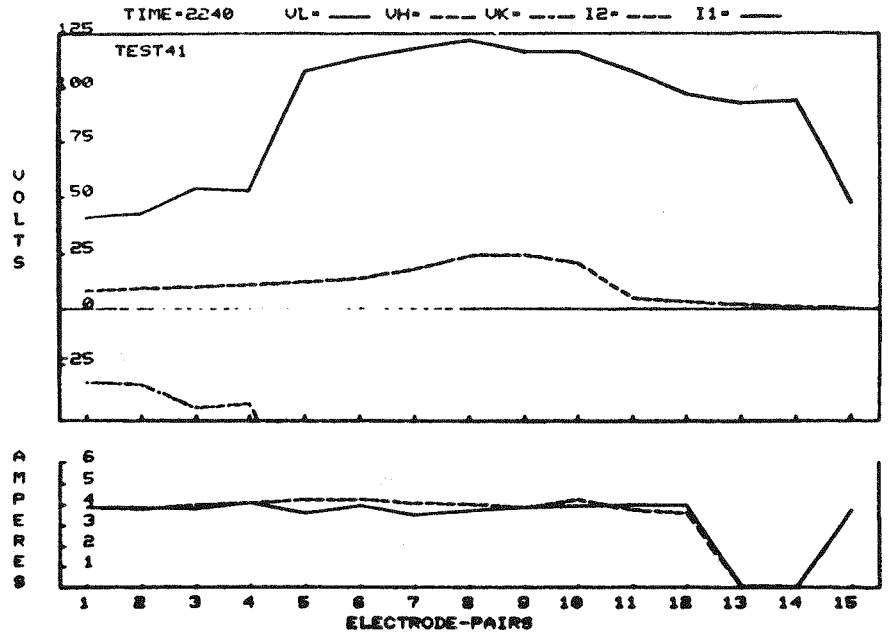

(a)

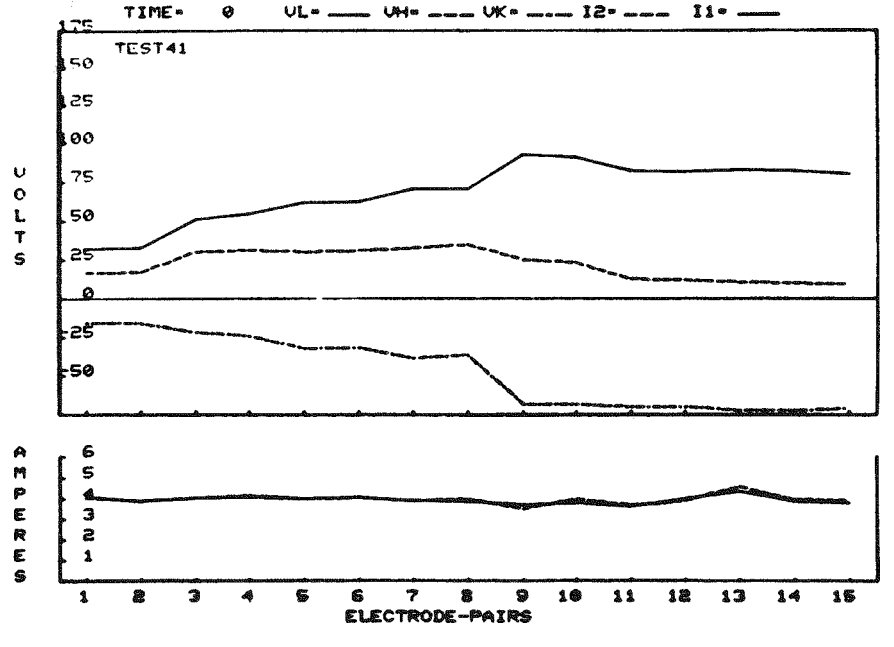

(b)

Figure 85. Applied Voltages and Currents for Test 41 - Run 1, No Axial Voltage

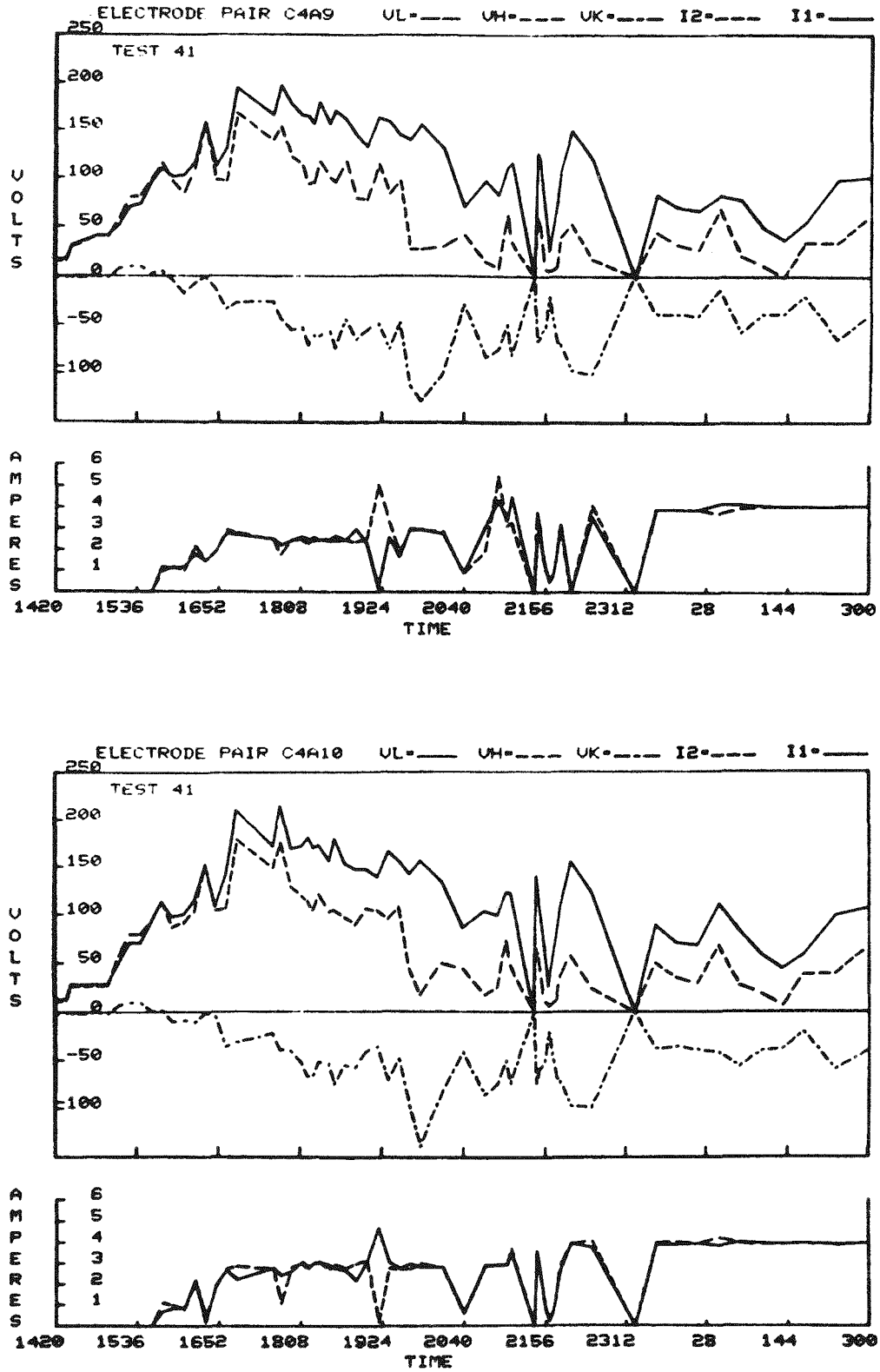

Figure 86. Applied Voltages and Currents as Function of Time for Test 41 - Run 1

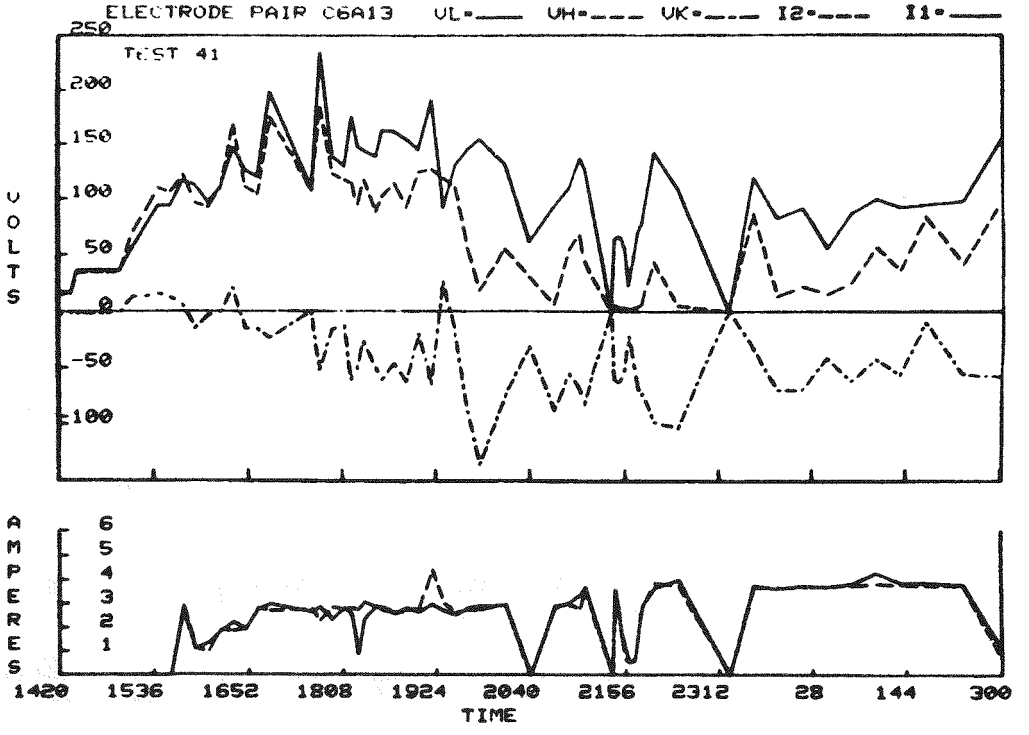

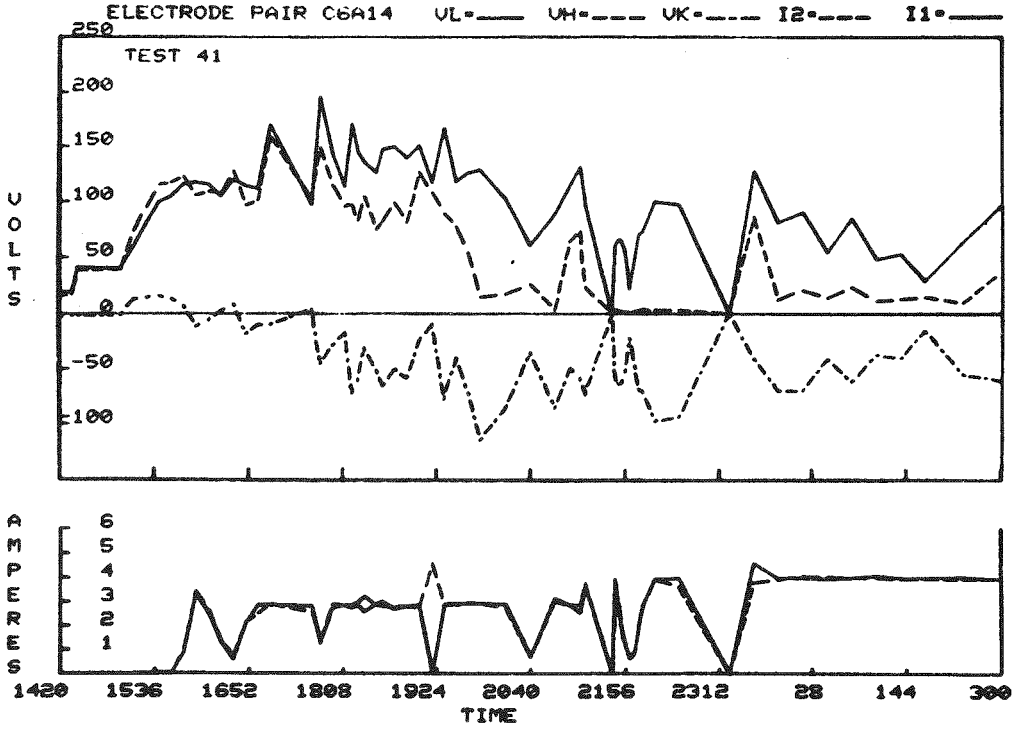

Figure 87. Applied Voltages and Currents as Function of Time for Test 41 - Run 1

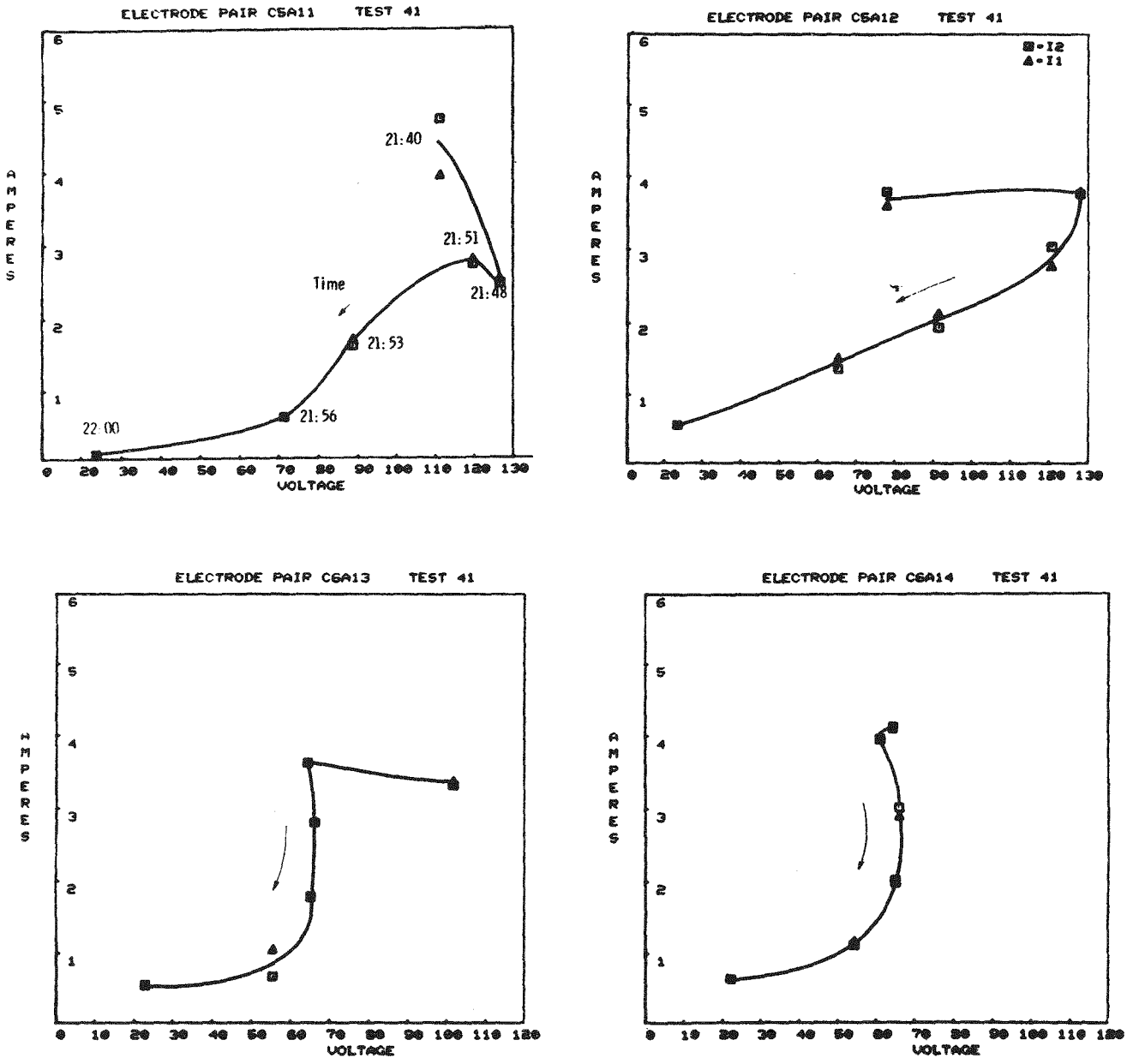

Figure 88. Amperes Versus Volts for Different Electrode-Pairs, Currents Progressively Decreased with Time, Test 41 - Run 1

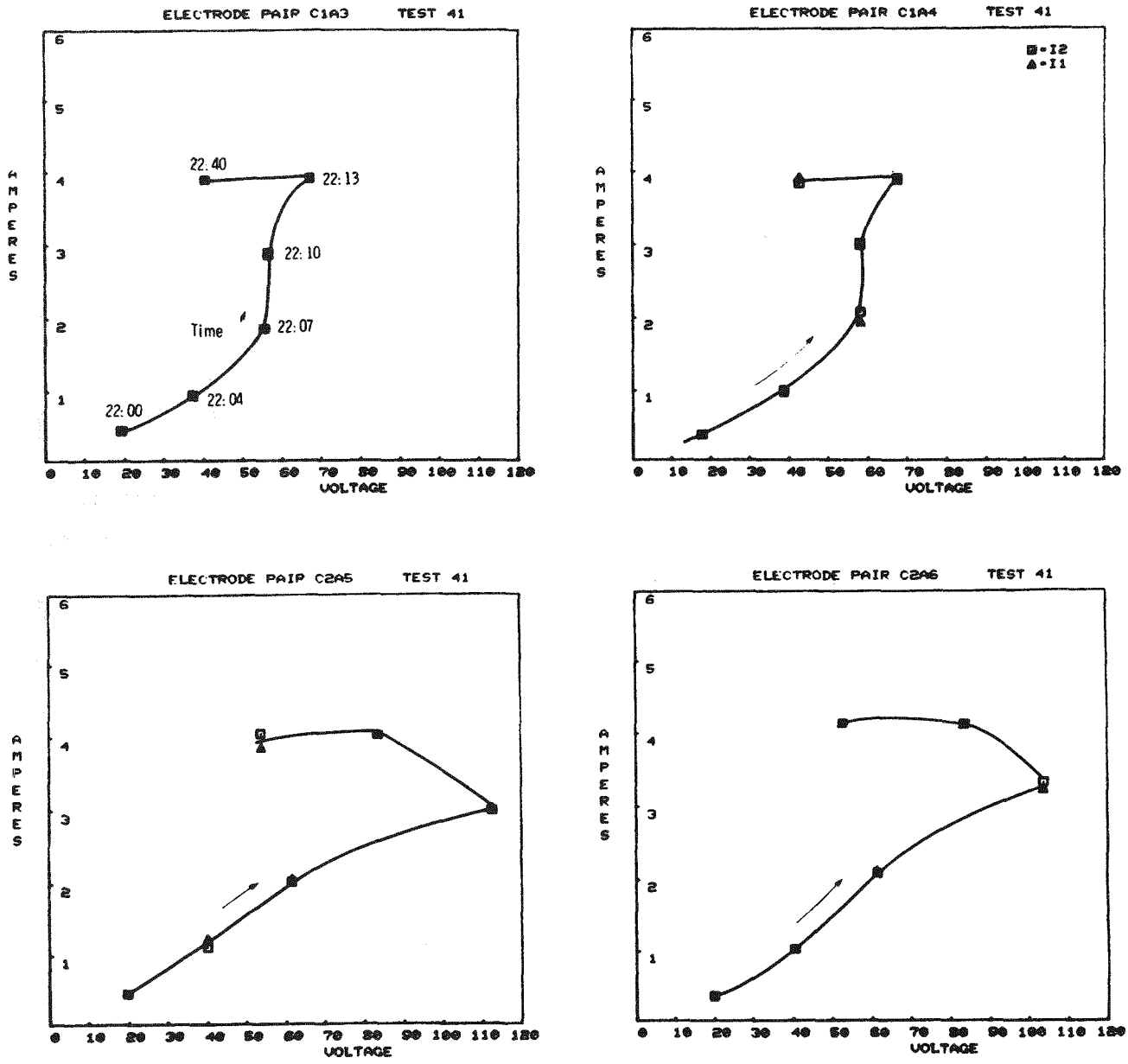

Figure 89. Amperes Versus Impressed Voltage for Different Electrode-Pairs, Currents Progressively Increased with Time, Test Run 41 - Run 1

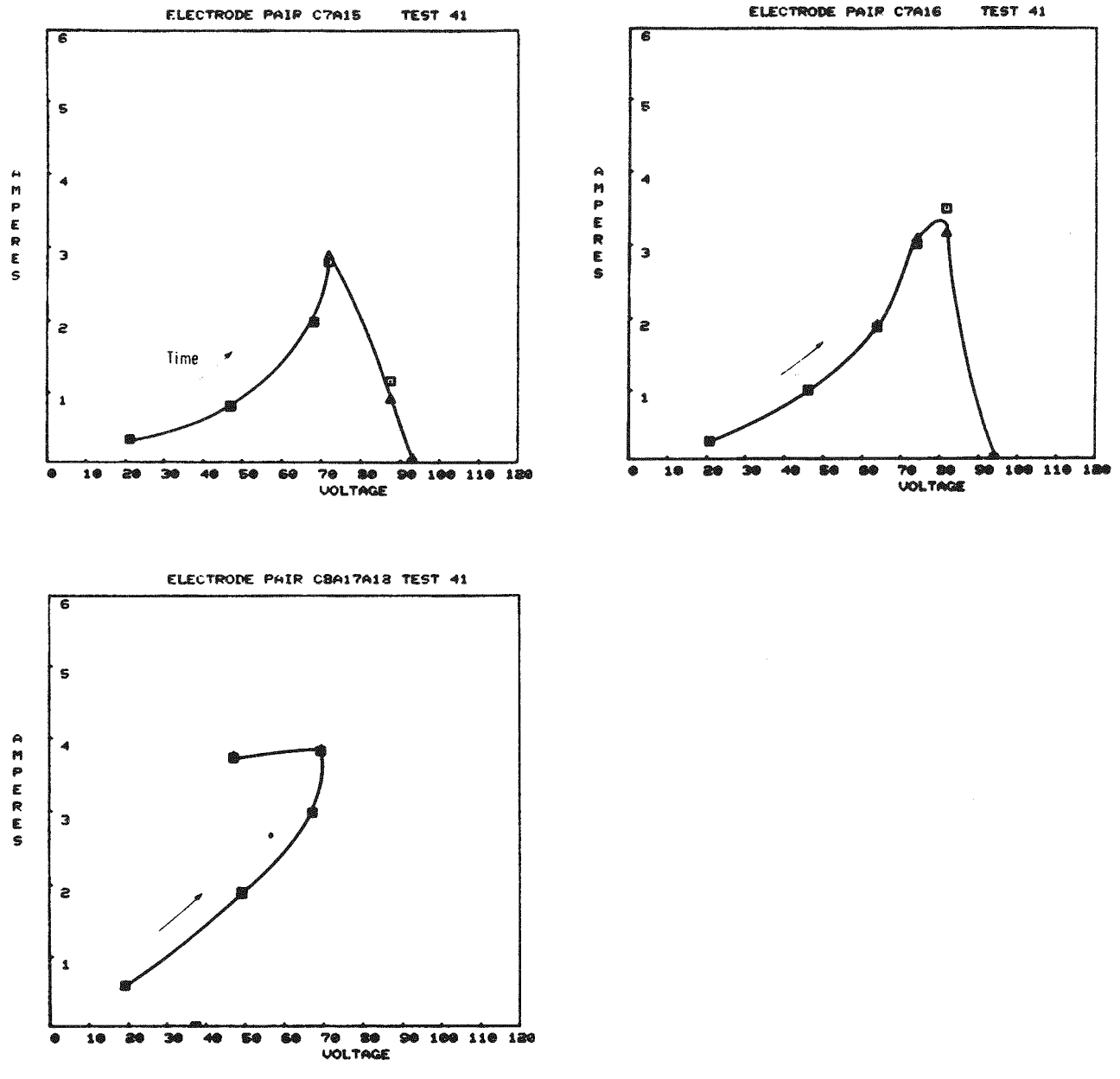

Figure 90. Amperes Versus Impressed Voltage for Different Electrode-Pairs, Currents Progressively Increased with Time, Test 41 - Run 1

lar time interval in the life of the channel the maximum deliverable voltages which could be delivered by power supplies 13 and 14 were not high enough to produce reignition.

An integrated total of about 37 ampere-hours was obtained during Run 41-1, which amounts to 133,000 coulombs, or almost double the ampere-hours accumulated during Run 40. The axial field was energized for the first 5-1/2 hours and off for the last 5-1/2 hours.

When the channel was opened up after the test, the evidence of anode erosion was extremely small compared to the erosion which occurred during WESTF Test 40. Arc erosion at the lower end of the wall could be seen indicating that some of the current going from cathode or anode travelled by way of the bottom insulating wall. The platinum protection on the anode showed little evidence of damage. However, the copper grooves on anode electrodes were severly eroded. The cathode electrodes were also relatively undamaged.

The spinel insulation at the top and bottom insulating walls of the channel had been stripped during the run and the copper heat sinks were exposed. The loss of insulation from the top and bottom wall naturally brings up the question as to when during the test was the wall insulation lost and how did this loss affect the electrical properties of the channel.

Sounds of objects traveling down the channel were heard early in Test 41-1. On the other hand, the voltage necessary to impress 3 amperes through the channel started to decrease at approximately time 1800. Graphs like Figures 70 to 74 which give the potentials of the heat sinks in the insulating wall at various times during the run as a function of distance along the channel were not available at the time of writing. These plots may shed some light as to the time interval during which the spinel insulation was lost.

The data on hand appears to indicate that the effect of the loading which occurred during Run 41 was not as hard on the electrodes as the loading which occurred in Test 40 despite the greater number of ampere-hours of operation and the somewhat

higher apparent loading of Run 41-1. It is likely that a significant fraction of the discharge travelled between the anode and cathode by way of the "insulating" walls. This topic is still being studied and will be discussed in the next quarterly report. It should be noted that steps have been taken to improve insulation of the insulating wall for Test 41-2 (see Section 2.1.1).

2.2 WBS 1.2.2 - Test Assembly Fabrication

WESTF Test 41

Several modifications were made to test section components before they were assembled into a channel for WESTF Test 40, Run 1. These modifications included: (a) incorporating annular flow restrictions in the cathode water passage increasing flow velocity to maintain an electrode surface temperature of 150°C; (b) reducing the thickness of ceramic on the insulating walls to reduce surface temperature to well below that of liquid slag condensation; and (c) applying a silicone adhesive film (and reducing tackiness with a dusting of fine aluminina powder) to the interior metal surface of the transition sections to eliminate possible electrical leakage to ground.

The brazed plug covering the .25 in. diameter flow passage in each of the nine electrodes on the assembled cathode wall were drilled into and tapped so that a machined plug, .128 in. diameter with a #10-32 threaded end could be inserted concentrically along the length of the flow passage. RTV silicone was used as a thread sealant. The cathodes were then pressure checked at 150 psig and flow measurements were made. These data are compared with previous measurements made on the anodes and cathodes in Table 13. A heat transfer analysis, used to predict electrode surface temperatures as a function of water coolant flow rate, showed that at a design surface temperature of 150°C, the water flow requirements were reduced from 150 GPH to 30 GPH by the use of the flow modifying insert.

The spinel insulators in the center sections of the top and bottom insulating walls were reduced from .18 thick to .071 in. thick. The reduction in thickness was made to reduce the ceramic/slag interface temperature below 900°C, i.e.,

TABLE 13

MEASURED WATER FLOW RATES - TEST 41 ELECTRODES

Pressure Drop (psig)	Flow Rate (GPH)		
	Anode(1)	Cathode(2)	Cathode(3)
10	46.2	38.4	46.5
20	68.0	55.2	66.0
40	96.0	84.0	94.9

(1) Single electrode, 0.188" diameter flow passage.

(2) Single electrode, 0.250" diameter from passage.

(3) Single electrode, 0.250" diameter flow passage with 0.128" diameter concentric insert.

below the liquid seed condensation temperature, to reduce the electrical conductivity of the slag and minimize seed attack of the insulator.

In order to improve the electrical insulation of the transition section, DENSIL, a silicone transfer adhesive was applied in a 2 mil thickness and covered with a fine alumina powder to remove the tackiness. The surfaces were checked with an ohmeter at room temperature and were found to be effectively insulated.

Electrical resistance measurements were made on the individual walls prior to assembly. The insulating walls, in particular, showed low resistance due to retained moisture from the grinding done to reduce the thickness of the center insulators. After oven drying, infinite resistances were measured between adjacent components for all but two locations on the bottom insulating walls and these resistances were in excess of .5 megohm. The pre-test electrical measurements for this channel are given in Table 14 with the symbols referenced to the schematic diagram shown in Figure 81. These data show that the insulating wall is improved over that used in WESTF Test 40, but that further improvement can be made through redesign.

WESTF Test 42

Fabrication activities have been initiated with the machining of copper cooling blocks and the cutting of nickel mesh for WESTF Test 42. These materials are ready for brazing.

2.3 WBS 1.2.3 WESTF Operations

2.3.1 Pre-Test Activity

A water pump was installed in the electrode cooling system to increase the water flow to 50 gal/hr. for the anodes and 30 gal/hr. for the cathodes. The water cooling paths for groups of six anodes were connected in series. Thus, anodes 1-6, 7-12 and 13-18 were in series. Cathodes 1-3, 4-6, and 7-9 were maintained at a 30 gal/hr. water flow rate.

The mini-computer data acquisition system was reworked to include the electrode cooling water inlet and outlet temperatures. With the water flows held constant

TABLE 14

ELECTRICAL TESTS - ASSEMBLED CHANNEL FOR WESTF 41, RUN 1

Measured Points[1]	Resistance Megohms	Breakdown
Electrode Walls		
A13-A14	∞	350
C09-SC	∞	67
Bottom Insulating Wall		
BA1-BC1	.6	18
BA1-BA2	∞	1800
BA3-BA4	∞	1900
BA4-BC4	1.1	40
BA5-BA6	∞	1800
BC8-BC9	∞	1900
Top Insulating Wall		
TA1-TC1	∞	1300
TA1-TA2	.05	1.4
TC1-TC2	∞	1800
TA3-TC3	∞	800
TC8-TC9	∞	1900

[1] Showing low resistance or breakdown voltages of less than 2,000 volts.

the computer is now able to calculate and tabulate the heat fluxes through the electrodes at each scan of data.

The electrical loading circuits were revised to accomodate the 18 anodes and 9 cathodes. Up to this time provisions were available for measuring the electrical loading of 8 electrode pairs using 16 power supplies. The circuits were rearranged as shown in Figure 82.

2.3.2 Test Operation

WESTF Test 41, Run 1

This test was of electrodes designed and fabricated by AVCO and equivalent to CDIF Reference channel #2 electrodes. Number 2 diesel oil was used as fuel with injected potassium carbonate seed and eastern flyash. The average conditions achieved are shown in Table 15 as well as the test chronology.

The test ran for 15.2 hours between seed on and the final seed off. At 0315 the seed line clogged due to the loss of atomizing air. The lines were cleaned and the seed was back on at 0425. The total time of operation with seed on was then 14.1 hours. At intervals during the tests sounds of material impacting metallic surfaces were heard. These noises were apparently the insulator walls ceramics pulling loose and hitting the back pressure valve. Pieces of ceramic were later found in the exhaust tubing. The test was terminated when the gasket between the insulating wall and the electrode wall leaked and allowed the escape of combustion gases.

Data scans were output by the computer on the graphics terminal which permitted quick analysis of channel conditions. The only limitation of the system was the failure of thermocouples as the test progressed. Electrical loading data was also instantly retrieved in tabulated and graphic form permitting the analysis of a large number of varied loading conditions.

TABLE 15

OPERATING CONDITIONS AND CHRONOLOGY

Operating Conditions Achieved

Gas Temperature	~2550 K
Static Pressure	2 atm.
Plasma Velocity	600 m/sec
Plasma Mass Flow	0.22 kg/sec
Seed Concentration (K_2CO_3)	0.9% K
Flyash Concentration	0.002
Heating & Cooling Rates	20°C/minute
Electrode Cooling Water	
Anodes	50 gal/Hr.
Cathodes	30 gal/Hr.

Chronology

Condition	Date	Time	Elapsed Time
Air Preheat On	3/5/79	0900	0
Combustor On	3/5/79	1130	2.5
Seed On	3/5/79	1413	5.2
Seed Off	3/6/79	0525	20.4
Combustion Off	3/6/79	0555	20.9
Air Preheat Off	3/6/79	0710	22.1

3.0 WBS 1.3 WESTF MODIFICATIONS

Initial room modifications for WESTF have begun. The control room has been enlarged by removal of internal walls and relocation of auxiliary equipment in the room. Relocation of the remaining equipment required to support the magnet installation will not begin until the facility planning group completes the floor plans and work schedules required to do a complete and expeditious job. These plans will include the installation of the magnet, power supply, and controls and the relocation of the test hardware and the gas analysis center, which is presently situated where the power supply will be located.

Magnet

Bids on a 3 tesla magnet suitable for making conventional MHD operation available in WESTF have been obtained. These bids have been based both on modifying the Waltz Mill magnet, and on the construction of a new magnet. On the basis of substantially lower cost and power supply requirements, the decision has been made to restructure the Waltz Mill magnet. The modification involves shortening the coils of the magnet. The two coils will then be electrically connected in series. The power supply requirements taking into account the decrease in coil lengths will be 500 V/1200 amperes, or 600,000 watts. A new 4160V feeder will have to be brought from the site sub-station to Building 301, the building in which WESTF is located.

The new magnet, which will essentially incorporate one of the three components of the Waltz Mill magnet H frame, will be mounted with the magnetic field in the horizontal direction to enable mounting on rollers. The capability of separating the two halves of the magnet will greatly facilitate installation and removal of experimental channels. The capability of testing experimental channels under normal MHD conditions, and at will subjecting the components of the channel to the simulated conditions which have been used in WESTF should substantially contribute to the understanding of factors affecting performance of MHD electrodes and insulation. Simultaneous use of the two modes of operation will permit operation of the generator under overload conditions and facilitate accelerated life tests.

4.0 WBS 1.4 - PROJECT MANAGEMENT AND DOCUMENTATION

The following required project documentation was issued during the reporting period:

Quarterly Report for the Period October-December 1978

In addition, the Project Management Summary Report previously submitted is being revised to reflect programmatic changes in the contract effort. Resubmittal of this document is expected shortly after completion of contract negotiations.

General program meetings were held with DOE personnel in January 1979 and with DOE and Dynatrend personnel in February 1979.

5.0 REFERENCES

1. Development, Characterization and Evaluation of Materials for Open Cycle MHD, Quarterly Report Ending June 1978, Batelle Pacific Northwest Laboratory, Contract EY-76-C-06-1830.
2. Karr, Jr., C., Waldstein, P., and Kovach, J.J. "Composition of Flyash from a Coal-Fired MHD Generator with Potash Seed,' Jn of Inst. of Fuel, September 1974.
3. Bowen, H. K. "MHD Channel Materials Development Goals," NSF-OCR Workshop on MHD Materials, November (1974).
4. Yoldas, B. E. "Preparation of Glasses and Ceramics from Metal-Organic Compounds," J. of Materials Science 12 (1977) 1203-1208.
5. "Development, Testing and Evaluation of MHD Materials and Component Designs", Quarterly Report, July - Sept. 1978, DOE Contract EX-76-C-01-2248, Westinghouse Electric Corp., Dec. 1978, FE-2248-22.
6. MHD Electrode Development, Quarterly Report, Oct-Dec. 1978 on ERDA Contract DE-AC-01-79-ET-15529, Westinghouse Electric Corporation, January 1979, FE-15529-1.

7. M. T. Simnad et al, J. of Metals. TAIME, p. 1386, Dec. 1954.

8. D. A. Dukelow and G. Derge, TAIME, 218, 1960, p. 136.

9. W. R. Dickson and E. B. Dismukes, TAIME, 224, 1962, p. 136.

10. J. K. Koester and R. A. Perkins, "Discharge and Corrosion Characteristics of Slagging Metal Electrodes," Fourth US/USSR Colloquium on MHD Electrical Power Generation, Washington, D. C., Oct. 5-6, 1978.

11. R. A. Perkins, "Electrode Materials for Coal-Fired MHD Generators, "Lockheed, LMSC-D628284, June 1978.

12. T. B. King and P. Korus, TAIME, 224, p. 299, 1962.

13. L. H. Cadoff et al, "The Evaluation of Electrode Materials for Slag Coated MHD Channels," Proc. of 16th Sym. on Eng. Aspects of MHD, Pittsburgh, PA, March 1977.

14. D. D. Marchant et al, "Electrochemical Studies of MHD Channel Materials in Molten Potassium Salt and Coal Slag," Proc. of 17th Sym. on Eng. Aspects of MHD, Stanford, CA, March 1978.

15. This work.

16. J. W. Patterson, "A Useful Model for Understanding the Performance of Solid Oxide Electrolyte Fuel Cells," Proc. Workshop on High Temperature Solid Oxide Fuel Cells, Upton, NY, May, 1977. BNL-50756

17. W. R. Cannon et al, "Properties and Test Results of Super-Hot Wall Electrode Materials" Proc. of 17th Annual Sym. on Eng. Aspects of MHD, Stanford, CA, March 1978.

18. J. L. Bates, "Electrical Conductivity of Molten Coal Slags Containing Potassium Seed," Proc. of 16th Sym. on Eng. Aspects of MHD, Pittsburgh, PA, March 1977.

19. "Development, Testing and Evaluation of MHD Materials and Component Designs," Quarterly Report, April-June 1978, DOE Contract EX-76-C-01-2248, Westinghouse Electric Corp. August 1978, FE-2248-20.

20. R. Pollina and R. Larsen, "MHD Slag Electrical Conductivity Studies," Proc. of 17th Annual Symposium on Engineering Aspects of MHD, Stanford, CA, March 1978.

21. L. H. Cadoff et al, "Electrochemical Corrosion of Ceramic Materials in MHD Slag/Seed," Fourth US/USSR Colloquium on MHD Electrical Power Generation, Washington, D.C. Oct.5-6, 1978.

22. L. H. Cadoff et al, "Electrochemical Corrosion of MHD Electrodes in Slags," Proc. of 17th Sym. on Eng. Aspects of MHD, Stanford, CA, March 1978.

23. "Electrodes and Insulators," Chapter 7 in Open Cycle MHD Power Generation, Ed. by J. Heywood and G. Womack, Pergamon Press, 1969.

24. S. Petty, et al, "Electrode Phenomena in Slagging MHD Channels," 16th Sym. on Eng. Aspects of MHD, Pittsburgh, PA, May 1977.

25. A. Demirjian et al, "Electrode Development for Coal Fired MHD Generators," 17th Sym. on Eng. Aspects of MHD, Stanford Univ., March 1978.

26. J. E. Fenstermacher et al, "Progress in the Testing of Refractories for Directly-Fired MHD Air Heater Service." Proc. of 15th Sym. on Eng. Aspects of MHD, Philadelphia, PA, May 1976.

27. S. Petty, AVCO Everett Research Laboratory, Personal Communication, 1979.

28. "MHD Electrode Development," Quarterly Report Westinghouse Electric Corp. Dept. of Energy Contract No. DE-AC-01-79-EP-15529, April, 1979.

29. M. Beaton et al, "Insulator Performance and Anode Recession Rate in a Direct Coal Fired Copper Diagonal Conducting Wall MHD Generator," 17th Sym. on Eng. Aspects of MHD, Stanford Univ., March 1978.

30. L. Bates, "Evaluation of Metal Electrodes from 250-Hour Test at AVCO," Battelle Pacific Northwest Laboratories, Report to Dept. of Energy, July 1978.

31. J. Dilmore et al, "Design and Operation of the Westinghouse Electrode Systems Test Facility (WESTF)", 17th Sym. on Eng. Aspects of MHD, Stanford Univ., March 1978.

32. J. W. Sadler, et al, "Development, Testing and Evaluation of MHD Materials and Component Designs," Quarterly Report AESD FE-2248-20. July 1978.

33. J. W. Sadler, "Test Specification - WESTF Test #42," PCR Sk-1058-11, January 5, 1978.

34. J. L. Hobbs and M. E. Lapides, "Physical Properties and Flow Characteristics of Air," General Electric, APEX 527, 1956.

35. D. A. Hofer and D. Meeker, "Development of Combustion Gas Properties Simulation Expressions," DRM-CDIF 039, July 22, 1978.

36. S. Petty, R. Rosa: G. Enos, 6th International Conference on MHD Electrical Power Generation, Washington, D. C. p. 245, 1975.

V. SUMMARY PLANS NEXT REPORTING PERIOD

Summary plans covering significant activities in the next reporting period are presented below according to the Work Breakdown Structure primary tasks.

WBS 1.1 - ELECTRODE AND INSULATOR MATERIALS

- Continue anode arc erosion tests including evaluating implications of specimen thermal design on test results.
- Continue electrochemical corrosion tests.
- Complete material development activities in support of WESTF Tests 43, 44 and 45.
- Continue evaluation of interelectrode insulator and insulating wall materials.

WBS 1.2 - ENGINEERING TESTS

- Continue test planning activities and issue Preliminary Test Specifications for WESTF Tests 44, 45 and 46; finalize Test Specifications for WESTF Tests 42, 43, 44 and 45.
- Complete detail design activities for WESTF Tests 44 and 45.
- Complete fabrication of channels for WESTF Tests 41 (Rebuild), 42 and 43.
- Complete WESTF Test operations for WESTF Tests 41 and 42.
- Initiate detailed design of revised test section, compatible with WESTF magnet.
- Complete fabrication of WESTF Calorimeter.
- Initiate detail design of WESTF-"Mini test section".

WBS 1.3 - WESTF MODIFICATION

- Complete detailed planning and initiate procurement/ installation activities to support addition of WESTF magnet.

WBS 1.4 - PROJECT MANAGEMENT AND DOCUMENTATION

- Complete technical, schedular and budgetary planning and issue Project Management Summary Baseline Report for DOE approval.
- Issue January-March 1979 Quarterly Progress Report.

VI. CONCLUSIONS

WESTF Tests 42/44 will include 'coupons' of candidate electrode materials, zirconia and hafnia based, judged promising for use under non-slagging super-hot conditions. Specific zirconia based materials to be included in WESTF are:

(1) 85 m/o ZrO_2-15 m/o $(Mg_{.625}Ca_{.375})O$

(2) 88 m/o ZrO_2-12 m/o Y_2O_3

(3) 88 m/o ZrO_2-12 m/o Y_2O_3 (U-02 Phase I)

Processing parameters as well as pre-test characteristics have been defined for these materials. The hafnia based materials will be defined by BNW.

As a result of laboratory studies of the mechanisms of electrochemical corrosion between liquid coal slag and ionically conducting zirconia based electrodes an anlytical model has been derived. This comprehensive model permits detailed analysis of the role of slag properties as well as electrode polarization on the nature of electrochemical reactions under hot slagging conditions. Based on this work $ZrO_2(Y)$ or $ZrO_2(Ca)$ and perhaps by extrapolation HfO_2, are serious candidate materials, especially for use as hot slagging anode wall electrodes with Montana Rosebud slag.

☆ U.S. GOVERNMENT PRINTING OFFICE: 1980-640-258/2153